Okinawa Institute of Science and Technology
Graduate University

Thesis submitted for the degree

Doctor of Philosophy

Light-Induced Interactions using Optical Near-Field Devices

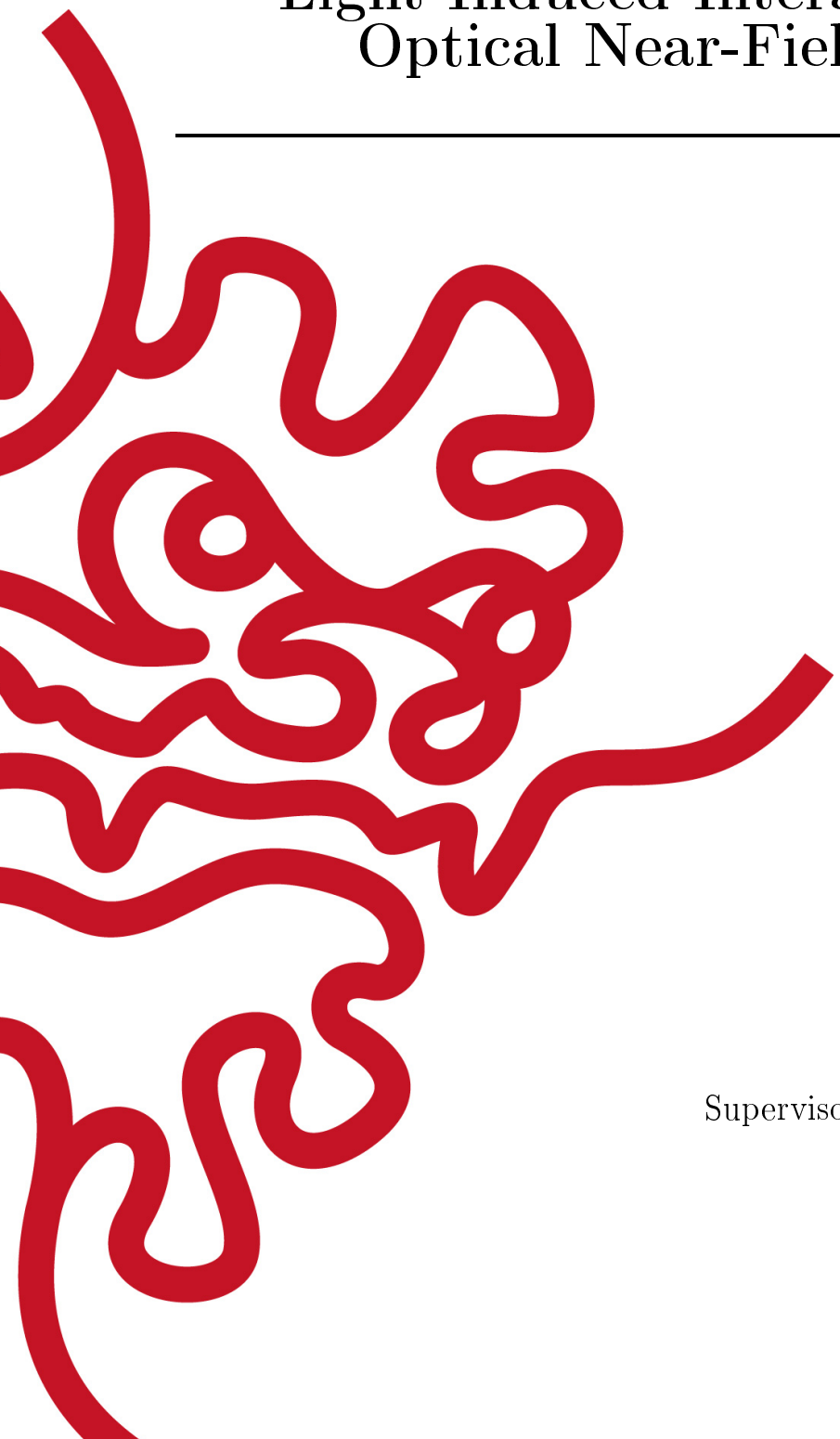

by

Mark Daly

Supervisor: **Prof. Síle Nic Chormaic**

October, 2016

Declaration of Original and Sole Authorship

I, Mark Daly, declare that this thesis entitled *Light-Induced Interactions using Optical Near-Field Devices* and the data presented in it are original and my own work.

I confirm that:

- This work was done solely while a candidate for the research degree at the Okinawa Institute of Science and Technology Graduate University, Japan and the University College Cork, Ireland.
- No part of this work has previously been submitted for a degree at this or any other university.
- References to the work of others have been clearly attributed. Quotations from the work of others have been clearly indicated, and attributed to them.
- In cases where others have contributed to part of this work, such contribution has been clearly acknowledged and distinguished from my own work.

Date: October, 2016

Signature:

Light-Induced Interactions using Optical Near-Field Devices

Optical near-fields are generated when light passes through components with wavelength, or subwavelength features. The near-fields generated at the surfaces of devices are often neglected, in part because the far-fields have more applications and are more readily accessible. Near-fields, as one might expect, occur very close to the surface of the material through which the light passes. However, near-fields present an interesting method of overcoming Rayleigh's diffraction limit. For example, the evanescent field at the surface of a prism or ultrathin fibre rapidly decays, but can exist in sub-diffraction limited areas. Similarly, the field generated by a subwavelength aperture or a plasmonic particle can have local field distributions with minute dimensions, allowing one to confine light to areas otherwise unattainable, extremely close to the surface of the material in question. By exploiting this aspect of optical near-fields we apply them to problems in atom and particle trapping.

Our main focus is on ultrathin optical fibres. These fibres differ from telecommunications fibre due to their lack of cladding material and their wavelength-scale dimensions. These two factors combine to produce a significant evanescent field at their waist. This field is readily accessible and can be used to trap particle or atoms through the optical forces which arise in such light-matter interactions. We can also use such devices to passively collect light which is emitted into the available guided mode. Here, we demonstrate how an ultrathin fibre can be used as a probe to determine the temperature of a cold atom cloud.

Ultrathin fibres, while extremely useful, have some limiting factors related to the strength and distribution of their evanescent fields. To improve upon the design, we also investigated how one can nanostructure an optical fibre using focussed ion beam milling techniques or combine optical fibres with gold dimer arrays to produce localised field enhancements. We used nanostructured fibres to trap 100 and 200 nm dielectric spheres within the structured region. Various numerical techniques were employed to characterise

both the nanostructured fibre and the plasmonic-enhanced fibre.

Aside from optical fibres, we also briefly discuss how an array of Fresnel microlenses can be packaged with other atom chip designs to produce a device which could trap atoms microns away from a gold surface. We discuss the theory and fabrication technique for such a Fresnel microlens array atom chip.

Acknowledgement

After many years of PhD research there is a seemingly uncountable number of people of whom I need to acknowledge. But, I would like to start with perhaps the most important person during my research career so far, my supervisor, Prof. Síle Nic Chormaic. She has guided my research for so many years, both as part of the Quantum Optics Group in Ireland, and as part of the Light-Matter Interactions group in Japan. I am extremely thankful for all her help and support, and especially her patience, during my PhD years. I hope that she will continue to guide many more students in the years to come.

During my time as a PhD student I had the pleasure to work with many people from all over the world. For many of these people it is difficult to pinpoint how exactly they helped me throughout my career, but I'll begin by thanking all of the group members I have worked with, past and present, for their support both academically and personally. Thank you Aili, Ramgopal, Ravi, Mary, Ivan, Marios, Ciarán, Michael, Vu, Laura, Eugen, Krishnapriya, Thomas, Peter, Alex, Amy, Yuqiang, Vibhuti, Vandna, Yong, Kristoffer, Aysen, Metin, Elaine, Alan, Bishwajeet, Sunny, Nitesh, Sho, Tridib, Jinjin, Wenfang, Xue, Fuchuan, Ratnesh, Ali (Seer), Sanele, Sahar, Cindy, Yuta, Lisa, Jan, Christiane, Vikraman, and Tushar. I'd like to especially thank Dr. Kieran Deasy, Dr. Viet Giang Truong, and Dr. Jonathan Ward for working closely with me throughout my PhD and providing me with invaluable advice and information. And I must also acknowledge Emi Nakamura for the incredible amount of work she has done for me throughout the years.

I must also acknowledge the technical support staff from OIST, UCC, and the Tyndall National Institute who have assisted me in both my technical training as well as producing

high quality devices when required. I would especially like to thank Dr. Laszlo Szikszai and Dr. Toshio Sasaki who were instrumental in my technical training at OIST. I must also thank the academic support staff at UCC and OIST. Margaret Bunce helped me many times at UCC, and the Student Support staff at OIST have always provided me with a friendly face to speak with despite bringing them an increasing number of problems to deal with. I'd also thank Dr. Kishan Dholakia for his support during my thesis proposal; his advice following my exam was extremely beneficial. I also thank Dr. Thomas Busch for being my mentor during my time at OIST, his wonderful sense of humour helped to improve my mood on many occasions.

I would also like to thank Dr. Jonathan Dorfan for his role as the president of OIST during its formative years. His phone call a week following the interview process allowed me to continue my work in physics to this day.

Aside from the technical support, I would also like to thank all of my friends, both from the past and the many new ones I have made during my PhD. It is safe to say that I would not have made it through my PhD without their support and company.

Finally I would like to thank my parents, Josephine and Mark, my sister Sarah-Jane, and my wonderful girlfriend Emily for the years of support, fun, and love that they have supplied me with, as well as my extended family who have always been supportive of my studies.

Abbreviations

AOM	Acousto-Optical Modulator
DAQ	Data Acquisition
EDS	Energy Dispersive X-ray Spectroscopy
FIB	Focussed Ion Beam
EBID	Electron Beam Induced Deposition
STOF	Slotted Tapered Optical Fibre
FDTD	Finite Difference Time Domain
FEM	Finite Element Method
HE	Hybrid Electric
ITO	Indium Tin Oxide
MNF	Micro/nanofibre
MOT	Magneto-Optical Trap
MST	Maxwell Stress Tensor
LP	Linearly Polarised
LSPR	Localised Surface Plasmon Resonance
PD	Photodiode
PSD	Power Spectral Density
SLM	Spatial Light Modulator
TE	Transverse Electric
TM	Transverse Magnetic
OMA	Orbital Angular Momentum

R-S	Rayleigh-Sommerfeld
SAS	Saturated Absorption Spectroscopy
SEM	Scanning Electron Microscopy
SIBA	Self-Induced Back Action
SPCM	Single Photon Counting Module
SPP	Surface Plasmon Polariton
STOF	Slotted Tapered Optical Fibre
TOF	Time-of-Flight
UHV	Ultra High Vacuum

Nomenclature

c	Speed of light ($2.997\ 924\ 58 \times 10^{8}$ ms^{-1})
$\hbar$	Reduced Planck constant ($1.054\ 572\ 66 \times 10^{-34}$ Js)
k_{B}	Boltzmann constant ($1.380\ 658 \times 10^{-23}$ JK^{-1})
ϵ_0	Permittivity of free space ($8.85418782 \times 10^{-12}$)
μ_0	Permeability of free-space ($4\pi \times 10^{-7}$ Hm^{-1})
$n_{air/vacuum}$	Refractive index of air (1)
n_{water}	Refractive index of water (1.33)
n_{silica}	Refractive index of silica (1.45591)
λ	Wavelength of light
ω	Frequency of light
$\vec{k}$	Wave vector of light
β	Propagation constant of light in a waveguide
$\vec{E}$	Electric field
$\vec{D}$	Electric displacement field
$\vec{B}$	Magnetic field
$\vec{H}$	Magnetic intensity ($\vec{B}/\mu_0$)
ρ	Charge density
j	Current density
J_n, K_n	Bessel functions of the first and second kind, respectively
$\sigma_{\pm}$	Circularly polarised light with positive and negative handedness
^{85}Rb	Rubidium isotope with 85 neutrons

$\mathbf{F}$	Total atomic angular momentum
$\mathbf{J}$	Total electronic angular momentum
$\mathbf{I}$	Nuclear angular momentum
T_{D}	Doppler-limited temperature
γ	Scattering rate
s_0	Saturation parameter
I	Intensity of light
I_s	Saturation intensity
μ'	Magnetic moment of atom
C_3	C_3 parameter of the Lennard-Jones potential

If desired, an optional and short dedication may be included here.

Contents

Declaration of Original and Sole Authorship ii

Abstract iii

Acknowledgement v

Abbreviations vii

Nomenclature ix

Contents xii

List of Figures xvii

List of Tables xxi

1 Introduction 1

1.1 Applications 3

1.2 Optical Trapping Regimes 4

1.2.1 Rayleigh Regime 5

1.2.2 Mie Solutions and Discrete Dipole Approximation 7

1.2.3 Other Forces 9

1.3 Optical Tweezers with Free-Space Laser Beams 9

1.3.1 Optical Tweezers Basics 10

1.3.2 Dual Beam Optical Tweezers 14
1.4 Trapping via Integrated Optics 16
1.4.1 Channel Waveguides 17
1.4.2 Optical Micro-Nanofibres 19
1.4.3 Slot Waveguides 20
1.4.4 Photonic Crystal Cavities 23
1.4.5 Microlenses 26
1.5 Plasmonic Based Devices 26
1.5.1 Surface Plasmon Polaritons and Localised Surface Plasmons 27
1.5.2 Scalability 29
1.5.3 Self-Induced Back Action 30
1.5.4 Super Resolution Optical Trapping 32
1.5.5 Gratings 34
1.5.6 Plasmonic Nanorods and Ultrathin Fibres 35
1.5.7 Subwavelength Apertures 37
1.6 Conclusion 41

2 Fundamentals of Optical Fibres and Optical Trapping 43
2.1 Ultrathin Optical Fibres 44
2.1.1 Maxwell's Equations and the Wave Equation 46
2.1.2 Optical Fibre Modes in MNFs 47
2.1.3 Fibre Pulling 48
2.2 Optical Forces 50
2.2.1 Maxwell Stress Tensor 51
2.2.2 Dipole Approximation 53
2.2.3 Mie Scattering 54
2.2.4 Minkowski Force Density 56
2.3 Atom Trapping 58

2.3.1 Energy Levels in ^{85}Rb . . . 59
2.3.2 Cooling and Trapping . . . 60
2.4 Plasmonic Enhancement . . . 63
2.4.1 Quasi-static Approximation . . . 63
2.4.2 The Dipole Hybridization Model . . . 65
2.5 Conclusions . . . 66

3 Forced Oscillation Temperature Measurement Using an Ultrathin Fibre 68
3.1 Alternative Measurement Techniques . . . 70
3.1.1 Time-of-Flight . . . 70
3.1.2 Release and Recapture . . . 71
3.1.3 Forced Oscillation Method . . . 71
3.2 Sub-Doppler Temperature Measurements using an Ultrathin Fibre . . . 74
3.2.1 Ultrathin Optical Fibres in a Vacuum Chamber . . . 75
3.2.2 Experimental Setup . . . 76
3.2.3 Timing and Triggering . . . 80
3.2.4 Results . . . 82
3.3 Conclusions . . . 86

4 Slotted Tapered Optical Fibre for Atom Trapping 89
4.1 Guided Modes of the System . . . 91
4.1.1 Optical Mode Distributions . . . 91
4.1.2 Mode Definition . . . 95
4.2 Trap Design . . . 97
4.2.1 Surface Interaction Potential . . . 97
4.2.2 Optically Produced Potential and Atom Trapping . . . 99
4.2.3 Trapping Potential . . . 101
4.2.4 Atom Trap Viability . . . 109
4.3 Slot Endface Geometry . . . 110

4.4 Conclusion 114

5 Particle Trapping using Ultrathin Optical Fibres 117

5.1 STOF Fabrication 121

5.1.1 Tapering Process 122

5.1.2 Coating Process 122

5.1.3 Etching Process 124

5.1.4 Alternative Approaches 126

5.2 Transmission Characteristics of STOFs 127

5.3 Experimental Setup 128

5.3.1 Ultrathin Optical Fibres and Slotted Tapered Optical Fibres 128

5.3.2 Field Distribution 128

5.3.3 Experimental Outline 130

5.3.4 Polarisation Preparation 133

5.4 Numerical Analysis 134

5.5 Additional Considerations 138

5.5.1 Multiple Particle Scattering 138

5.5.2 Thermophoretic Forces 140

5.6 Results and Trap Analysis 142

5.7 Conclusion 146

6 Plasmon Enhanced Ultrathin Fibres 148

6.1 Design and Fabrication 149

6.1.1 Electron Beam Induced Deposition 151

6.1.2 FEM Simulations 152

6.2 Characterisation 154

6.2.1 SEM Imaging 154

6.2.2 Energy-Dispersive X-ray Spectroscopy and Oxygen Plasma Treatment 156

6.2.3 Absorption Measurements 158

6.3 Conclusions 160

7 Fresnel Microlens Array for Atom Trapping 162

7.1 Fresnel Atom Microlens 163

7.1.1 Wave Diffraction Optics 163

7.1.2 Atom Potential 164

7.1.3 U- & Z-chips 166

7.1.4 Fabrication 169

7.2 Reflection Spectra 172

7.3 Conclusion 173

Conclusion 177

8 Conclusion 177

8.1 Thesis Summary 177

8.2 Impact and Future Work 178

8.3 Final remarks 180

A Solutions to the Scalar Helmholtz Equation — Mie Scattering 182

B Relevant Code and Model Files 185

Bibliography 186

Published articles 213

List of Figures

1.1 Mie interference effects 8
1.2 Gaussian beam optical tweezers 11
1.3 Detectable position change vs. trap stiffness 13
1.4 RNA polymerase step-size measurement 15
1.5 Channel waveguide for particle propulsion 18
1.6 Sorting using counter-propagating fields in a fibre 21
1.7 Slot waveguide for particle trapping 22
1.8 Tapered photonic crystal cavity 24
1.9 Photonic crystal cavity trap 25
1.10 Channel waveguide with gold nanopads 30
1.11 Plasmonic nano-aperture array 31
1.12 Self-induced back action in plasmonic apertures 32
1.13 Gold nanoblocks for plasmonic trapping 33
1.14 Bowtie nanoantennas for optical trapping 35
1.15 Plasmonic bottle beams 36
1.16 Polymer embedded gold nanorods 37
1.17 Gold nano rod exciting whispering gallery mode of ultrathin fibre 38
1.18 Double-nanohole 39
1.19 NSOM tip with BNA 40

2.1 Refractive index profiles of step-index fibres 44

2.2 Fibre Pulling Rig 50
2.3 Polar plot of dipole scattering. 57
2.4 D_2 transitions in rubidium 85 59
2.5 Optical Molasses Diagram 61
2.6 Zeeman shifting of energy levels and atom trapping 62
2.7 Sketch used in determining the quasi-static approach 64

3.1 Diagram of anti-Helmoltz coil 77
3.2 B-field of an anti-Helmoltz coil 78
3.3 Atom cloud oscillation diagram 79
3.4 Timing scheme for temperature measurement 81
3.5 Flow diagram of the timing scheme used in the temperature measurement . 82
3.6 Sinusoidal fit to SPCM output 83
3.7 Oscillation frequency versus phase difference 84
3.8 CCD image of atom cloud 85
3.9 Oscillation frequency vs. phase difference for varying pump beam detunings 86
3.10 Atom cloud temperature versus pump probe detuning 87

4.1 Schematic of the slotted fibre for a vacuum-fibre system 92
4.2 The electric field distribution at the slot region of a STOF 94
4.3 Electric field distribution for the symmetric and anti-symmetric modes . . 95
4.4 Graphic comparing circular sectors and circular segments 96
4.5 Analysis of single- and multi-mode operation regions 96
4.6 Normal L-J potential function compared to interpolation QED calculation 98
4.7 Observation of the van der Waals potential near inner STOF surfaces . . . 99
4.8 Combination of blue-detuned and vdW potentials 102
4.9 Surface plot of STOF potential at the slot center 103
4.10 Two-colour trapping potentials for various power combinations 104
4.11 Contributions to the two-colour trap inside and outside the slot section . . 105

4.12 Effect of power on the trapping potential 106
4.13 Trap depths for varying slot widths 106
4.14 Trap depths at fibre surface vs. slot width 107
4.15 Optimisation plots for STOF parameters 108
4.16 First four modes of a nanostrucutured fibre 111
4.17 Tapering profiles for nanostructured fibre 112
4.18 Propagation of first two excited modes for a tapered slot geometry 113
4.19 FDTD simulation of an untapered and tapered slot 114

5.1 Slot milling procedure 121
5.2 SEM images of STOFs fabricated using Helios Nanolab^{TM}650 125
5.3 SEM images of STOFs fabricated using FIB-SEM Helios G3 UC 126
5.4 3D rendering of a STOF. 129
5.5 Fraction of the field travelling in the core and cladding portions of an ultrathin fibre and a segment of circle 131
5.6 Optical setup for trapping 200 nm silica particles with a STOF 132
5.7 FDTD analysis of STOF. 135
5.8 Forces on 200 nm particles in a STOF. 136
5.9 FDTD simulation for 200 nm particle in a STOF. 138
5.10 Interaction force between two particles 139
5.11 Time series of images showing the effect of thermophoresis 141
5.12 Time series and histogram of STOF trap 143
5.13 Trap measurement of slotted tapered optical fibre trap 145
5.14 SEM images of fluorescent particles 146

6.1 Elongated gold nanodisk dimers patterned on the surface of an MNF . . . 150
6.2 Elongated gold nanodisk dimer array layout 151
6.3 Layout used for FEM simulation 153
6.4 COMSOL simulation of a gold dimer on silica substrate 154

6.5 SEM images of the GNR on an ultrathin optical fibre taken immediately after fabrication . . . 155
6.6 SEM images of the GNR on an ultrathin optical fibre . . . 156
6.7 SEM images of the GNR on an ultrathin optical fibre with defects . . . 156
6.8 Energy-dispersive X-ray spectroscopy measurement on an ultrathin fibre plasmonic structure . . . 157
6.9 Absorption spectra for the gold nanodisk array on the surface of an ultrathin fibre . . . 159
6.10 Absorption spectra for the gold nanodisk array on the surface of an ultrathin fibre . . . 159
6.11 Spectrum of light scattered from gold dimer. . . . 161

7.1 Schematic of Fresnel microlens traps . . . 163
7.2 Fresnel atom trap potential along central axis . . . 166
7.3 Fresnel atom trap potentials at various z-planes . . . 167
7.4 Diagram and fields from U- and Z- chips . . . 168
7.5 B-field components for from U- and Z-shaped wires . . . 169
7.6 B-field along the z-axis for a U-shaped chip for two models . . . 170
7.7 Atom chip design . . . 171
7.8 SEM images of final devices . . . 173
7.9 Packaged Fresnel microlens atom trap with U- and Z-wires . . . 174
7.10 SEM images of final devices . . . 175
7.11 Reflection spectrum of Device 7 . . . 175

List of Tables

4.1 Parameters used in trapping potential models. 101

4.2 Trap parameters found by varying P_r with respect to P_b, which was fixed at 30 mW. Values were obtained for a fibre width of 1 μm and a slot width of 350 nm 110

5.1 Parameters for ITO sputter process 123

5.2 Trap stiffnesses for varying input powers 144

7.1 Device parameters 171

Chapter 1

Introduction[1]

The idea that particles could be influenced by the radiation pressure from light has existed as a concept for a very long time; almost 400 years ago Johannes Kepler published a treatise entitled "De cometis libelli tres" [2], wherein he proposed that solar rays were the cause of the deflection of a comet's tail. However, it was not until much later, when James Clerk Maxwell formalised his theory of electromagnetism, that this force could be quantified. In 1906, John Henry Poynting, in relation to the force induced by radiation pressure, stated that "even here, so minute is the force, that it only need be taken into account with minute bodies" [3]. The next major milestone on the road to harnessing radiation pressure came with the discovery and invention of the laser in 1960 [4].

Just over two decades after the first operational laser was created, Ashkin et al. [5] published their seminal paper in 1986 in which they proposed and demonstrated how a laser could be used to trap and manipulate micron and submicron dielectric particles by considering the total conservation of momentum in a light-particle system. The initial design for the "optical tweezers", as the design based on Ashkin et al.'s work came to be known, required very few optical components, with the laser source being the most costly. While Ashkin pioneered the work [6], other research groups quickly began to improve upon the design to make it more versatile. Modern optical tweezers allow for

[1] This chapter is adapted from M. Daly et al. [1]. M. Daly wrote the majority of the text and S. Nic Chormaic guided the work. All authors reviewed the paper

a high degree of control over several trapping parameters, such as particle location and trap strength. This has been achieved by including components such as acousto-optical deflectors, servo-controlled mirror arrays, etc. to create multiple trapping sites and/or to provide control over the particle's motion in the 2D focal plane of the optical tweezers. Spatial light modulators allow for particle manipulation in the third (axial) direction. Optical tweezers are capable of performing high resolution measurements when it comes to sensing small displacements of the trapped objects. This property has made the technique of interest to the life sciences where, typically, such small measurements of displacement or force are required, necessitating the use of optical techniques.

In more recent years, the field of optical trapping has benefitted greatly from advances in other optics-related areas. To overcome limitations imposed by the diffraction limit of free-space laser beams, the research direction of many optical manipulation groups has shifted to devices that exploit optical near-fields. Optical near-fields, unlike far-fields, can create subdiffraction-limited spot sizes. Near-field devices range from the super-resolution lens as described by Pendry [7] to the use of surface plasmons [8, 9] created by the coherent oscillation of electrons near the boundary of a metal dielectric system. Both of these designs are capable of creating electric field 'hotspots' that can greatly enhance the field strength locally.

In the introduction to this thesis we seek to outline the current state of the field while focussing mainly on methods that can be employed to shift optical trapping into the nanometre regime through the use of methods and techniques that are not overly complex in design. The scope of the field of optical trapping makes a complete review an almost impossible task. Instead, we touch on many aspects of optical trapping which relate, in some shape or form, to the research presented in this thesis. The topic of this thesis is, for the most part, the interaction of light in the evanescent field of ultrathin optical fibres both in the presence of atoms and particles. In Chapters 3 and 4 some focus is placed on atomic systems, but the research direction moves towards colloidal particle systems and the total modification of ultrathin optical fibres in Chapters 5 and 6. The

enhancement of ultrathin fibres through surface or bulk modification is a major point in this thesis, and the work performed by other groups, outlined in this section, served as inspiration for many of the approaches we attempted. For more extensive reviews of the biological applications of optical tweezers, or more in-depth discussions about how optical tweezers can be improved by algorithms or diffractive elements, the reader's attention is drawn to other works [10–12]. Since biological applications are not a core part of this thesis, we do not discuss them in depth.

1.1 Applications

The field of optical trapping, as with many scientific fields, is motivated by the potential applications that can stem from it. The high degree of control and precision with which one can trap and localise particles using optical tweezers, or other similar trapping systems based on optical forces, is impressive by itself, but it is the ability to then apply these techniques experimentally with incredible resolution that is of interest to scientists.

One of the most common applications of optical tweezers is the strong confinement and manipulation of small objects. For example, Waleed et al. [13] used optical tweezers to spatially localise plasmid-coated microparticles that were then optically inserted into MCF-7 cells. The cells were optically perforated using a femtosecond laser to guarantee transfection. In this work, the versatility of the optical tweezers is shown since, not only were the optical tweezers used to manipulate the particle's position, but they were also used to experimentally determine the focal length of various laser sources.

Other work has been done using optical tweezers to measure exceptionally minute position changes with high resolution. Examples include measuring the step sizes of kinesin proteins along microtubules [14], determining the distance between adjacent base pairs via determination of the step sizes of DNA polymerase [15]. More recently, unwinding/rewinding dynamics in P-fimbriae [16]. Some of these applications will be discussed in more detail later.

The application of forces to trapped particles can also be achieved using an optical tweezers and this has been exploited to analyse biological systems. By incorporating optical tweezers with Förster resolved energy transfer (FRET)[2] [17], conformational dynamics of Holliday junctions and the folding dynamics of DNA hairpins have been measured. Integrating optical tweezers with other spectroscopic and microscopic techniques is a vital step in the furthering of their applications in the life sciences. This has led to the integration of optical tweezers with techniques such as Raman spectroscopy and stimulated emission depletion (STED) fluorescence microscopy [18–20]. All of these modifications have served to further increase the effectiveness of optical tweezing techniques in many fields.

Moving from manipulating 'large', i.e. micron-sized, particles to smaller, nanoscale particles opens up a vast array of applications. The previous examples, which certainly involved the investigation of nanoscale objects such as DNA, were only possible via the use of micron-sized spheres. Much research in this field is, therefore, focussed on overcoming this size limitation. Eventually, we can expect that trapping small particles, such as bacteria and viruses, will become routine. This would be an excellent achievement for the nanobiology world [21] and some progress in this direction has already been made. For example, influenza viruses, of about 100 nm size, have been individually manipulated using optical forces alone [22]. Here, we aim to discuss some of the progress made in these applications, commencing with the introduction of the more well-established techniques in the field.

1.2 Optical Trapping Regimes

The first applications of light to trap particles utilised a technique that came to be known as optical tweezing. By employing a tightly focussed Gaussian beam, particles can be trapped near the focus due to the gradient force induced by the momentum exchange

[2]The mechanism which describes how energy is transferred between two light-sensitive molecules.

of photons with the dielectric particles. Ashkin proposed the application of focussed Gaussian beams for both particle [6] and atom trapping [23] using radiation pressure, albeit almost a decade apart. The description of how a particle behaves in a light field can be understood using different models that depend on the particle's size in relation to the wavelength of the light used for trapping. For example, if the particle is large in comparison to the wavelength, a ray-optics approach can be used. Since this chapter focusses on the transition between the micro- and nano-worlds of optical trapping, the details of the ray-optics approach will not be discussed. However, the simple ray-optics explanation does provide a somewhat intuitive model for how trapping occurs and should not be discarded as an invalid approach to describing the optical forces on particles.

1.2.1 Rayleigh Regime

For particles with sizes smaller than or equal to the wavelength of light, an electromagnetic model is required to adequately represent the forces at play in a particle–light system. To assist the reader, we provide a brief description of the forces here, but a more thorough derivation is given in Chapter 2. This solution can range from a more complete theory, which uses the Mie solutions to scattering problems involving spherical or elliptical objects, to a simpler case when the particle size is much smaller than the wavelength of the trapping light and is made from a linear, isotropic material. This allows for the use of the dipole approximation in the calculations. The polarisability of a particle in this case gives rise to a dipole moment, $\vec{p}$ [24], with

$$\vec{p} = \alpha \vec{E}, \tag{1.1}$$

where $\vec{E}$ is the electric field. The electrostatic potential, U, generated by a dipole in an electric field is related to this dipole moment via $U = -\vec{p} \cdot \vec{E}$. Hence, the force, $\vec{F}$, which

is the negative gradient of the potential, can be determined

$$\vec{F} = -\nabla U = \nabla(\vec{p} \cdot \vec{E}) = \alpha \nabla |\vec{E}|^2. \tag{1.2}$$

Because of this polarisability dependence, metallic nanoparticles, which, over wavelengths of interest in particle trapping have a much higher real component of their polarisability compared to silica or polystyrene particles of the same size, are often used as targets for trapping at the nm-scale since they require the use of lower optical powers. Taking the time average of the field into account and using the Clausius-Mossotti relationship for a spherical dielectric particle, the so-called gradient force,$\vec{F}_{grad}$, a particle feels is finally given as

$$\vec{F}_{grad} = \frac{2\pi n_0 r^3}{c} \left(\frac{m^2 - 1}{m^2 + 2} \right) \nabla I(\vec{r}), \tag{1.3}$$

where r is the particle's radius, c is the speed of light, n_0 is the refractive index of the medium, m is the dielectric contrast, i.e. the ratio of the particle's refractive index to the medium's refractive index, and $I(\vec{r})$ is the time averaged intensity as a function of position, $\vec{r}$. A more in-depth derivation is given in Chapter 2. The dielectric contrast plays a role in the trapping strength of an optical tweezers, but, more interestingly, changing the value of this property can cause the sign of the force to be reversed. If particles of a lower index than their surrounding medium are used, i.e. $m < 1$, as is the case for air bubbles in water, the sign of Eqn. 1.3 is seen to change and different trapping schemes involving vortex beams are required for trapping [25]. The origin of the term "gradient force" should now be evident from Eqn. 1.3; it is a force that is linearly dependent on the gradient of the intensity and tends to attract particles to regions of higher, or lower, intensity depending on the value of the dielectric constant.

Stable trapping occurs when the net force on a particle is zero and any small displacements from this stable position result in an optical force that resists the motion of the particle away from this position. Typically, traps with a potential depth greater than the

thermal limit, i.e. a few $k_{\mathrm{B}}T$, are required for stable trapping, where k_{B} is the Boltzmann constant and T is the particle's temperature in Kelvin. A potential depth of $10k_{\mathrm{B}}T$ is often used as a threshold value for stable particle traps.

To complete the discussion on optical forces, one must also include the scattering force, $\vec{F}_{scatt}$, felt by a particle that is being bombarded by a flux of photons of wavenumber k. Under the Rayleigh approximation, along with the Clausius-Mossotti relationship (see Appendix A), this is given as

$$\vec{F}_{scatt} = \frac{8\pi n_0 k^4 r^6}{3\ c}\left(\frac{m^2-1}{m^2+2}\right)^2 I(\vec{r})\vec{z}. \tag{1.4}$$

Again, these forces are discussed in more detail in Chapter 2, where a full derivation is given.

1.2.2 Mie Solutions and Discrete Dipole Approximation

For particles of intermediate sizes, between that of the ray optics and Rayleigh regimes, one can apply the Mie solutions [26, 27]. These solutions are the complete solutions to the Helmholtz equation that take the form of an infinite series. The Mie solutions are very important in this size regime. In the Rayleigh regime, the force scales as the cube of the particle's radius and this can be shown to be incorrect for larger particles in the ray-optics regime. The Mie solutions help to bridge this gap between the two regimes, while also introducing some new phenomena which would otherwise be unnoticed in the theory. In a paper by Stilgoe et al. [28], a detailed calculation of the trapping forces on particles of varying radii and refractive indices using different numerical apertures is described. A phenomenon known as a Mie resonance occurs in intermediate-sized particles and this is more prominent in particles with a higher refractive index contrast between them and the medium. The presence of Mie resonances strongly changes the trap strength of optical tweezers, as can be seen from Fig. 1.1 [28], and should be taken into account when developing tweezers to work at such particle sizes in order to maximise its effectiveness.

As can be seen in Fig. 1.1(b), interference effects can cause the trap strength to oscillate between trapping and nontrapping regions as the particle size is changed, an effect that is absent in the Rayleigh regime.

If the high accuracy of Mie solutions is not required, but work is being performed at or near the boundary between the Rayleigh and Mie regimes, the dipole can instead be approximated as a discrete sum of dipoles to reduce the errors arising from the single-dipole approximation. Again, a more mathematical description of Mie scattering and the forces at play in light-particle systems is given in Chapter 2.

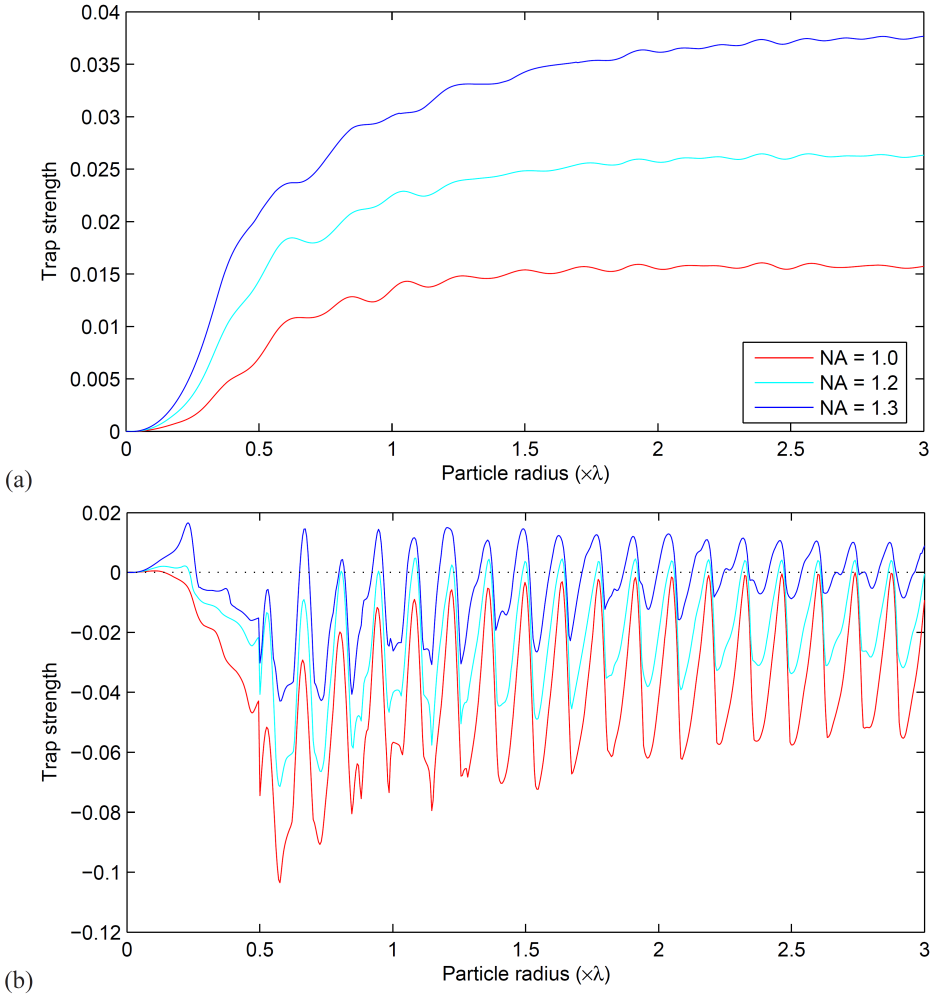

Figure 1.1: Dependence of trapping force for (a) polystyrene and (b) diamond particles for a fixed numerical aperture and particle radii varying from 0 to 3 λ. Note the pronounced interference effects present in the higher refractive index diamond particles. Reproduced with permission from [28].

1.2.3 Other Forces

To fully model an optical manipulation system, other forces must be considered. These forces include the Stokes' drag of a particle and the force due to the random Brownian motion. A further discussion of Brownian motion can be found in Section 5.6. The Stokes' drag present in a system can be quite complicated to determine due to the influence of nearby surfaces. For optical tweezers, Faxen's law [23, 29] is often used to include the influence of nearby planar surfaces, such as coverslips, in an experiment. Often, these effects can be solved in experiments by modelling the system as a damped harmonic system and calibrating accordingly.

1.3 Optical Tweezers with Free-Space Laser Beams

Optical tweezers epitomise optical trapping. They were the first devices to be used for optical trapping and were quickly adapted for use in other fields. A discussion of optical trapping would, therefore, be incomplete without mentioning optical tweezers. By analysing shortcomings of such devices the motivation behind some of this thesis work is evident. Modular optical tweezers using free-space Gaussian beams are highly versatile tools that have high trap stiffness when dealing with micron and, to some degree, submicron objects. This is a necessary requirement for precise trapping. They also have incredible resolution with respect to position or force measurements on trapped objects. It is this resolution that makes optical tweezers invaluable in the life sciences. Applying this type of optical tweezers to the problem of trapping dielectric particles does have two drawbacks when it comes to trapping smaller particles. The first arises from the diffraction limit, which limits the waist size of a Gaussian beam refracted through a lens. The second drawback is, admittedly, also a side-effect of the diffraction limit; particles of increasingly smaller size require larger gradient forces to trap them. Photons directly exchange energy with particles via scattering; this force is typically called the scattering force and, on average, acts in the direction of beam propagation. In the Rayleigh regime,

the ratio, R, of the magnitude of the gradient force to the scattering force yields an inverse cube dependence on radius. Taking this value at the position of maximal axial intensity gradient yields [5]

$$R = \frac{F_{grad}}{F_{scatt}} = \frac{3\sqrt{3}}{64\pi^5} \frac{n}{\left(\frac{m^2-1}{m^2+2}\right)} \frac{\lambda^5}{r^3\omega_0^2} \geq 1, \tag{1.5}$$

where ω_0 is the focal spot size, n is the refractive index of the trapped particle, and m is again the refractive index contrast. This puts an upper limit on the particle size, since the gradient force must dominate. However, the time needed for a particle to be trapped must also be longer than the diffusion time out of the trap to ensure efficient trapping. Trapping objects in the nanometre regime requires laser powers which can quickly destroy or denature the samples being trapped. Despite this, optical tweezers systems using focussed Gaussian beams remain invaluable tools.

1.3.1 Optical Tweezers Basics

The term 'optical tweezers' has become a term which refers to any optical system that is capable of confining a particle in all three dimensions. The most commonly available system involves the use of free space optical beams to provide a gradient force trap in all directions. Recently, commercial, self-calibrating optical tweezers systems have become available, indicating the rise of interest in the field.

Free-space optical tweezers exist in many different varieties due to their high customisability. As mentioned previously, optical tweezers typically use focussed Gaussian beams, Fig. 1.2, combined with a mechanism that can deflect or otherwise steer the light beam in and out of the focal plane of the tweezers. Some examples include: galvanometer mounted mirror arrays to create multiple trapping sites by rapidly moving the trap centre around the focal plane [30]; holographic optical tweezers that include a spatial light modulator (SLM) to create different trapping patterns; acousto-optic deflectors; and even diffractive or polarizing elements. Each variation of optical tweezers has advantages and disadvan-

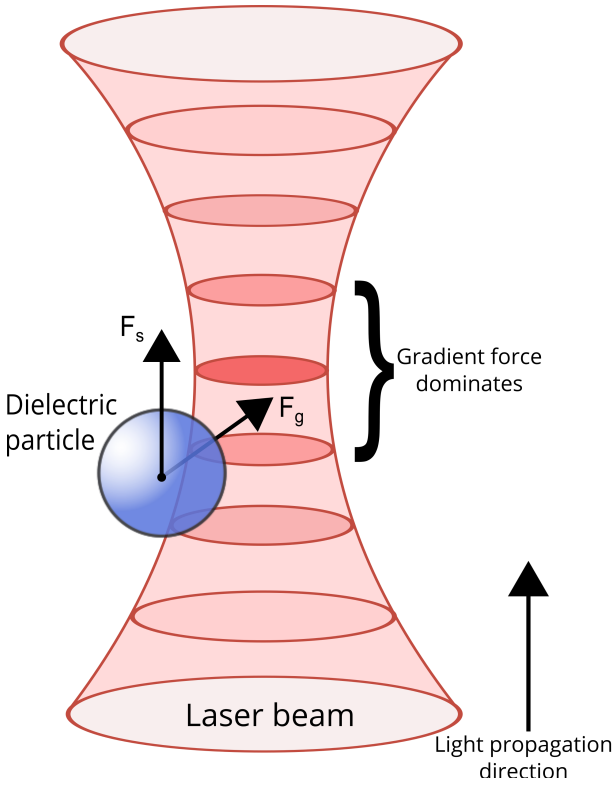

Figure 1.2: Schematic of a Gaussian beam optical tweezers. The darker shades of red indicate regions of higher intensity.

tages. For example, SLMs allow for a higher degree of control and customisability, but have typically slow response times [31–33]. Both continuous-wave (CW) or pulsed lasers can be used in optical tweezers [34].

The operation of optical tweezers is typically chosen to be in the near-infrared region, primarily because light of wavelength greater than 800 nm is poorly absorbed by most living matter and, as one moves further into the far infrared region, absorption from water molecules becomes an issue [35]. For these reasons, light from an Nd:YAG laser at approximately 1064 nm is commonly used for optical trapping. Optical tweezers are capable of resolving subnanometre motion and measuring pN of force [15, 36].

For optical tweezers in viscous media, the motion of the trapped particle can be well described by an overdamped Langevin model, often termed the "Einstein–Ornstein–Uhlenbeck theory of Brownian motion" [37]. In this overdamped regime, the inertia terms in the Langevin equation become negligible and the power spectrum of the system can be more

easily interpreted. To put it simply, the fundamental operational limit for measurements using optical tweezers, or indeed in any of the systems that will be discussed herein, is due to Brownian noise. This noise is always present and, unlike other measurement-based errors such as laser noise, shot noise, imaging errors, etc., it cannot be circumvented. The motion of a particle while trapped in optical tweezers can be described as a harmonic oscillator. Therefore, we may equate the energy of the particle's Brownian motion to the trap's energy using the equipartition theorem, i.e. $\frac{1}{2}k_{\mathrm{B}}T = \frac{1}{2}\kappa\left\langle x^2\right\rangle$ [38], where k_{B} is Boltzmann's constant, T is the temperature, κ is the spring constant of the system, and $\langle x^2\rangle$ is the particle's mean squared displacement from equilibrium. This can be used to determine the fundamental measurement limit for experiments based on optical tweezers. By defining the square root of the mean squared displacement as $\sqrt{x^2} = \sqrt{k_{\mathrm{B}}T/\kappa}$, the minimum detectable limit can be determined, as shown in Fig. 1.3. Therefore, if one wishes to measure a displacement, the displacement itself should be larger than the Brownian motion. In Fig. 1.3, the two lines correspond to motions which are one (blue solid) and three times (orange dashed) the Brownian motion, with their corresponding detection efficiencies given in the caption. To measure the trap stiffness, a simple Lorentzian function can be fitted to the power spectrum, but this gives errors of 10–20%. Further studies have shown how to increase the accuracy of such a measurement via modification of the Lorentzian fit [39].

The assumption that one can work at this Brownian noise limit is, of course, untrue, as there will always be sources of error that cannot be entirely eradicated. One can, however, work extremely close to this limit. Attempts have been made over the years to reduce noise and increase trapping times in optical tweezers. These approaches range from the use of laser feedback control algorithms to reducing the average laser power and, hence, the associated noise, to the use of interferometric techniques to enhance sensitivity [14, 40].

Although not discussed in detail here, it is worth mentioning that the problems of noise for optical tweezers in vacuum, such as that associated with optically levitated particles,

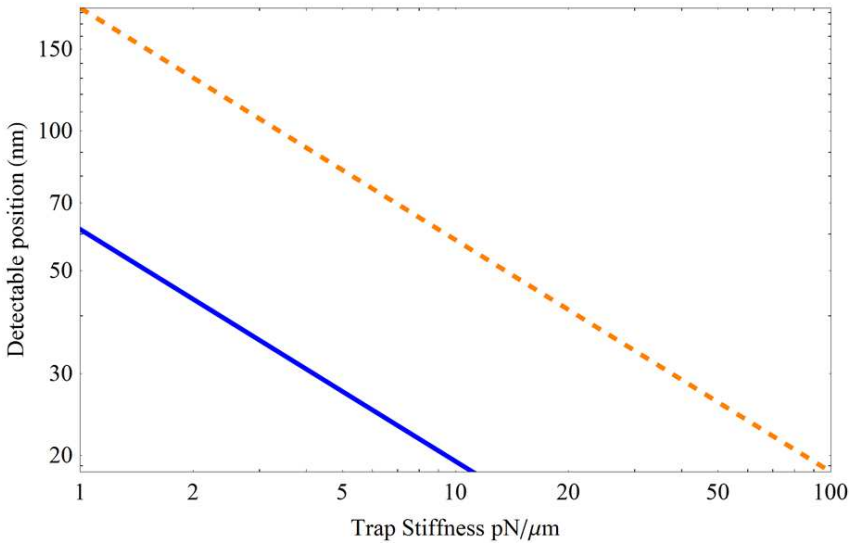

Figure 1.3: Log-log plot of detectable position change versus trap stiffness at the thermal limit (blue solid line), which corresponds to 68.5% detection efficiency, and three times the thermal limit (orange dashed line), which corresponds to 99.7% detection efficiency.

are different. Earlier, we discussed an overdamped system, but, in vacuum, the system is underdamped as there is no viscous medium to interact with the trapped particle. A recent demonstration of this comes from Dholakia's group where they optically levitated a particle in vacuum [41]. Aside from the other effects that this has on optical trapping, it also means that the measurement limit now becomes a problem more strongly related to the laser intensity, or, rather, the photon flux. Recoil energy is directly imparted to the particles via interaction with the photons in the laser beam. This is, in many ways, similar to laser cooling of atoms in a magneto-optical trap, where the thermal limit comes not from any interaction with residual gases in the vacuum, but rather from the recoil energy of the laser photons.

An influential demonstration of optical tweezers was performed in 1993 by Svoboda et al. [14]. They concluded that kinesin, a type of motor protein found in eukaryotic cells, moved in 8 nm steps. In this early application of optical tweezers, silica beads were coated with kinesin in such a way as to allow only a single active molecule per bead. These beads were then attached to microtubules along which kinesin can move and measurements of

the step size were made using overlapping beams from a Wollaston prism. Phase objects, such as silica beads, placed in the overlapping region caused varying degrees of ellipticity in the recombined beam and this effect was used to determine fine movements of the objects. This extra step was required to achieve the 8 nm resolution reported and helped show the versatility of optical tweezers in biology.

1.3.2 Dual Beam Optical Tweezers

Single-beam traps are at a disadvantage when compared with dual- or multiple-beam optical tweezers since only one particle can be steered or guided at any given time, unless Bessel beams or other optics are used to produce multiple trapping planes [42, 43]. Multiple-beam traps can be created numerous ways, such as the time sharing of a single beam using galvonometric mirror arrays, or the splitting of a single beam via polarisation elements to create two individual trapping potentials [44]. A particle suspended in the optical gradient of a beam is somewhat decoupled from the environment, but measurements generally require that a second object, which is directly coupled to the environment via some physical stage or mount, be used. This second particle is subject to many forms of external noise, such as stage drift, that often dominate the noise spectrum.

Dual-beam optical tweezers are systems that, effectively, combine two single-beam optical tweezers. This allows one to simultaneously trap two objects and perform differential detection measurements, thereby improving the attainable spatial resolution [36]. Traps of this form existed as early as 1993, although large improvements in stability occured a decade later. Comparing the 8 nm resolution previously obtained [14] to a more recent measurement using a dual-beam trap where a resolution of 3.7 Å was achieved [15], an impressive leap in measurement accuracy can be seen, though admittedly, this jump was not entirely due to the dual-beam configuration itself.

In 2005, base-pair stepping by RNA polymerase was measured and step sizes of 3.7 Å were distinguishable [15]. This level of high resolution was made possible both through the use of a dual beam tweezers, as well as isolating the system from external air currents via

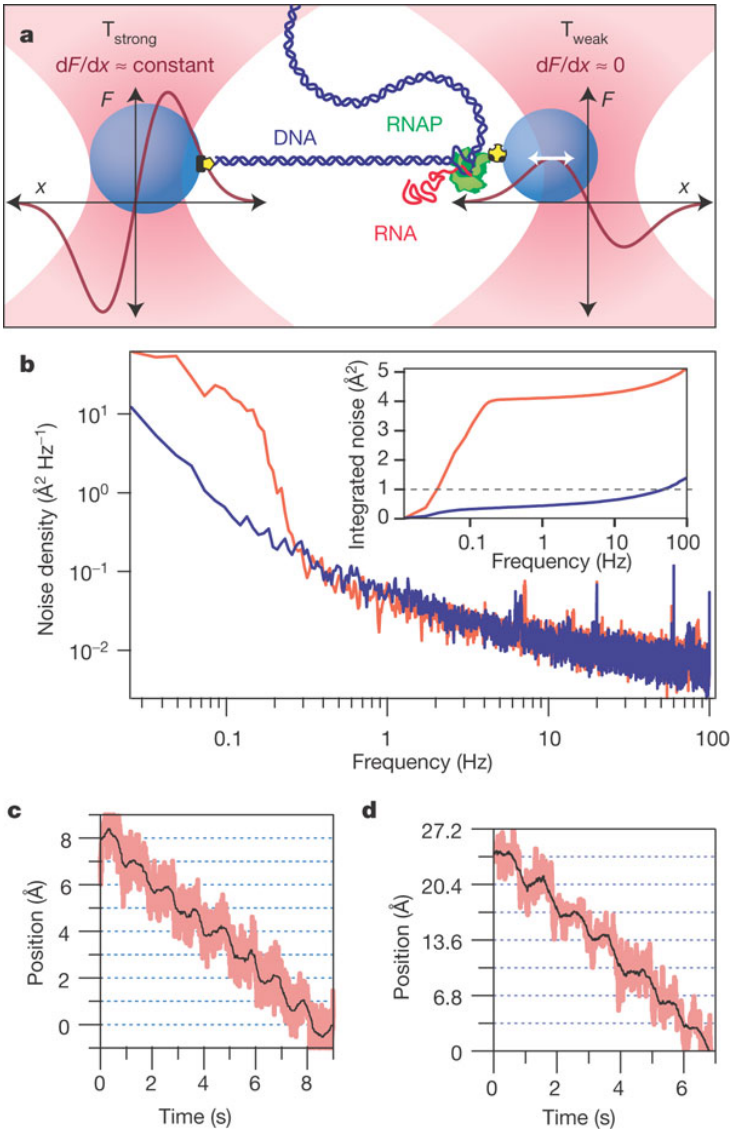

Figure 1.4: RNA polymerase immobilised using a dual beam optical tweezers and polystyrene beads. T_{strong} and T_{weak} are names given to the traps which refer to them having high and low spring constants respectively. (b) Noise density for helium enclosure, blue, and the unenclosed system, red. (c) Steps resolved for a stiffly trapped bead moved in 1 Å increments at 1 Hz. (d) 3.4 Å steps by using a bead-DNA-bead tension of 27 pN then moving T_{strong} in 3.4 Å increments at 1 Hz. Reproduced with permission [15].

the use of a helium-filled enclosure. By immobilizing both sides of the RNA polymerase with separate optical tweezers, the noise induced by the motion of the stage was effectively removed. The improved signal-to-noise ratio of dual-beam traps has been quantified by Moffitt et al. [45]. The system behaves like a three-spring system consisting of two optical tweezers and a DNA strand as the extra spring. Autocorrelations in the motions of two spheres tethered by a DNA strand, as illustrated in Fig. 1.4(a), were measured to determine the 3.7 Å step size. This study showed strong agreement between theory and experiment over the chosen parameter range.

Optical tweezers are also used to apply forces. One such example is the combination of an optical trap with a three color FRET process. In a FRET system, the energy transfer is strongly dependent on the distance between donor and acceptor chromophores [46], which allows one to measure the changes in fluorescence during the application of force and hence infer information about the internal dynamics of the system.

Although we only discussed the application of Gaussian beams which have uniform phase-fronts, there have been many successful optical trapping experiments using non-standard beams. Interesting mode configurations, such as Bessel beams, have been used and in more recent years the ability to tailor the phase of light using SLMs or DMDs (deformable mirror devices) has begun to appear in the literature. This is of particular interest to physicists as it allows us to investigate the effects of spin and orbital angular momentum through their effects on dielectric particles, potentially providing us with some new insight into the fundamentals of light. More information can be found in the review paper upon which this chapter is based [1].

1.4 Trapping via Integrated Optics

Trapping nanoparticles, or submicron particles, in subdiffraction-limited regimes can be achieved by using optical near-fields. These can provide high electromagnetic field gradients near dielectric surfaces, opening up attractive avenues of research for optical trapping.

Optical near-fields generally take the form of evanescent fields that decay exponentially from their point of origin. The first work that made use of the evanescent fields produced by a dielectric channel waveguide was published in 1996 by Kawata and Tani [47]. Here, the authors used only the evanescent field to propel latex particles of 5.1 µm in diameter along the length of a channeled waveguide at a speed of approximately 5 µm s^{-1} using only 80 mW of input laser power. While the particles propelled were of a relatively large size, it was the first work that highlighted the applicability of evanescent fields to particle trapping. Some of the following applications can be classified as tweezers, since they allow for full 3D confinement of the particle, while others only provide confinement in fewer dimensions.

The work in this section resonates strongly with the focus of the work in this thesis and the work of the Light-Matter Interactions unit as a whole. Near-field devices, in the form of ultrathin fibres are used in a variety of configurations. This section introduces a number of topics which ultimately led to the development of the devices discussed in later chapters.

1.4.1 Channel Waveguides

Evanescent fields that extend beyond the boundary of light carrying structures, such as waveguides, become more intense as the dimensions of the waveguide approach the wavelength of the guided light or become smaller [48]. This arises due to the wave nature of light that imposes certain boundary conditions on the structures in which they can exist. Evanescent fields play an indirect role in many plasmonic structures, primarily because they are used to excite SPPs via the Kretschmann configuration [49]. However, there are many structures where the evanescent field can be accessed directly to trap particles. The evanescent field from a single beam propagating in an evanescent waveguide provides a gradient force that attracts particles towards the surface, while a simultaneous scattering force is applied in the direction of beam propagation. Hence, single-beam evanescent field traps are useful for guiding particles along the surface of a waveguide, making them ideal

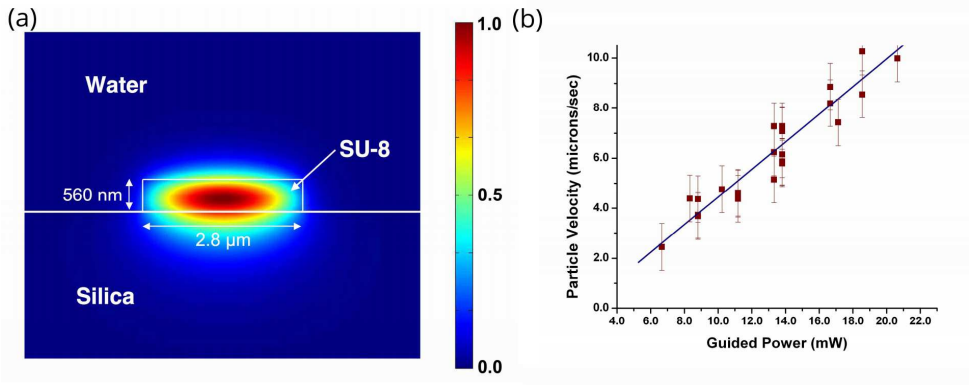

Figure 1.5: (a) E-field intensity plot of the channel waveguide. (b) Particle velocity versus guided power of a 3 µm particle trapped and propelled along a waveguide. Reproduced with permission [50].

for integration with microfluidic systems.

An example of a microfluidic/evanescent system is described in a paper by Schmidt et al. [50] where they demonstrated how particles could be trapped and propelled using channel waveguides in conjunction with microfluidic channels. An illustration of the channel waveguide used is given in Fig. 1.5. This work provided a clear and concise explanation of the physics at play in optofluidic systems, as well as displaying the trapping and propulsion of particles of varying size. Similarly, Yang and Erickson [51] have analysed optofluidic particle trapping near waveguides. Building on these works, Ng et al. showed that gold colloidal particles as small as 17 nm could be propelled along a channel waveguide [52]. Using branched channel waveguides, or branched microfluidic channels, other groups have been able to extend these ideas to particle sorting [53, 54]. The attractiveness of these approaches comes from the fact that microfluidic channels and channel waveguides can run parallel to each other, or even inside each other. Simple waveguides can also be arranged such that they produce resonating structures. Lin et al. [55] showed how microparticles can be trapped above a planar silicon microring resonator with large trapping depths of 25 $k_{\mathrm{B}}T$.

There is a current trend in scientific research to encourage the development of "lab-on-a-chip" devices. Channel waveguides perfectly fit the requirements of a lab-on-a chip

device as they operate at the correct scale, can be mass produced, and are easily integrated with many existing technologies [56].

1.4.2 Optical Micro-Nanofibres

Optical micro- or nanofibres (MNFs), or ultrathin optical fibres, are optical fibres with micron or submicron diameters that do not operate in the weakly guided regime. They are sometimes used to trap particles in their evanescent fields [57–60]. MNFs are, generally, manufactured from standard communication-grade optical fibres by heating them until they became malleable, at which point a force is applied from either side to elongate and taper the heated region until the central (waist) region of the fibre has a diameter less than or equal to 1 µm. A more detailed description of this heat-and-pull procedure can be found in the literature [61, 62]. In contrast, channel waveguides typically need to be grown on a substrate, which allows for complex geometries to be fabricated, but somewhat limits their versatility. For example, some studies in neurobiology require a probe that can reach deep inside tissues in vivo. Very recently, optogenetics has come to the fore in neuroscience and relies heavily on the use of optical fibres due to their ability to guide light into areas that are inaccessible using other methods [63]. While these techniques do not directly make use of the evanescent field or particle trapping, they emphasise the flexibility that is introduced once one moves from a platform consisting of rigid channel waveguide structures towards the use of fibres. Fibre-based waveguides are capable of trapping and guiding particles as efficiently as their substrate-grown counterparts [58, 64–66].

The use of a near-field scanning optical microscope to create a fibre optical tweezers (FOT) was realized by Xin et al. [67], and was used to reliably trap micron-sized particles. Experiments also showed that smaller particles such as yeast, bacteria, and 0.7 µm silica beads could be trapped, albeit with higher laser powers.

To realise a device that operates closer to that of optical tweezers, but with only the use of the evanescent fields produced by waveguides, one must consider counterpropagating laser beams [68–70]. Here, a standing wave can be formed that produces a potential

landscape that favours the trapping of particles at certain lattice sites defined by the wavelength of light used. In practice, a standing wave is not entirely necessary for successfully immobilising particles. Lei et al. [71] showed that, by varying the power of two counterpropagating beams, without the formation of a standing wave, particles with a diameter of 710 nm could be transported in either direction along a fibre. This was a useful study as it showed that standing waves are not necessary for the controlled guidance of micro- and nanoparticles along a tapered optical fibre.

Particle sorting using counterpropagating beams of different wavelengths relies on the scattering force's dependence on particle size, refractive index, and the wavelength of light used [72, 73]. Zhang and Li [72] used a subwavelength optical fibre with different wavelengths of light injected at either end (Fig. 1.6). The difference in scattering for various particle sizes resulted in the particles being sorted by size.

As is the case for optical tweezers, higher-order modes can be used to trap particles in waveguides. MNFs are an ideal platform for this, as they are capable of supporting many higher-order modes [74, 75], including Bessel-beams [76]. Higher-order mode trapping in straight, channel waveguides has been realised [77], but maintaining these modes in tapered fibres has proven to be a difficult process due to the fine degree of control required during the fabrication process, although it has been performed successfully using linearly tapered optical nanofibres [78]. Adiabaticity requirements impose important shape requirements on the taper profile and the dimensions of the fibre at the waist must also be considered. These combined conditions require a more complex tapering system [62] than is usually available to research groups. The use of higher-order modes in fibres for the purposes of atom trapping has been discussed elsewhere [79, 80].

1.4.3 Slot Waveguides

When two waveguides are placed in close proximity to each other, as is the case in slot waveguides, the evanescent fields of the two waveguides overlap, producing a region of increased intensity between them [81]. Yang et al. have published a series of papers [82, 83]

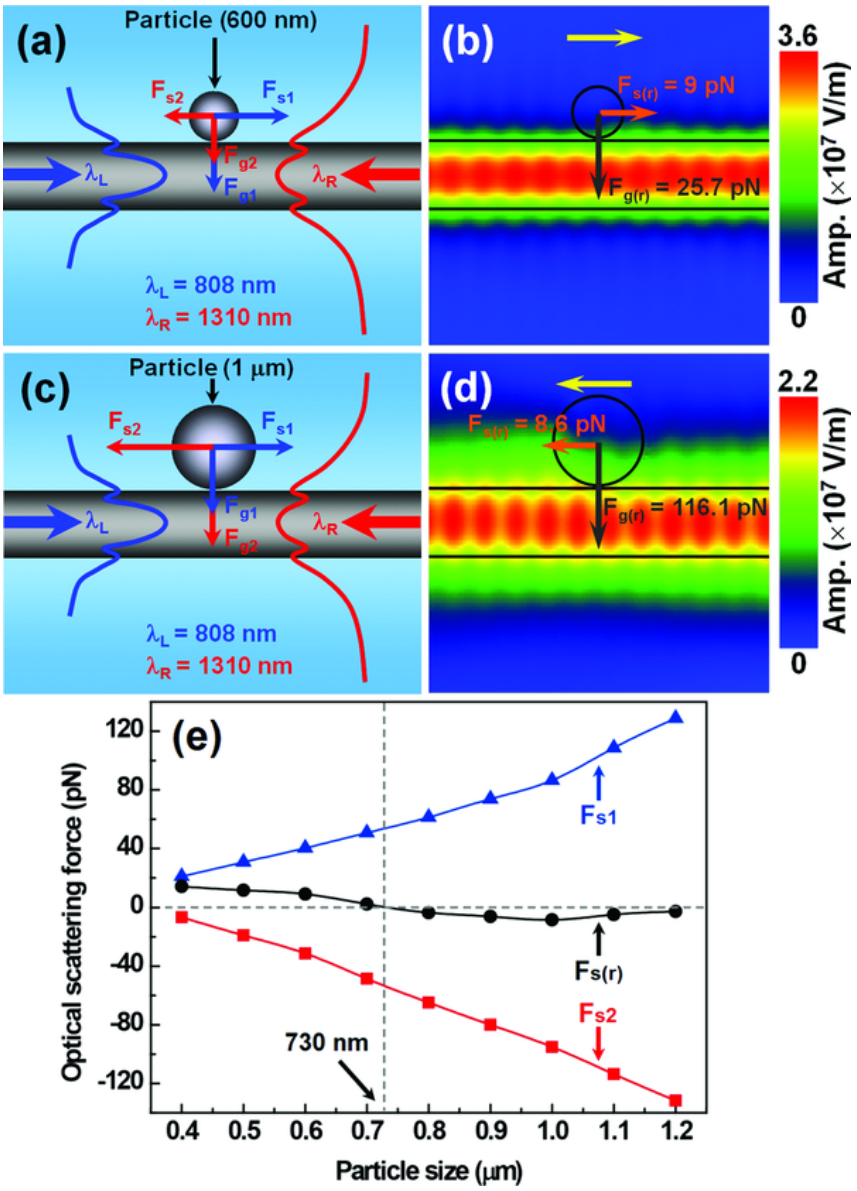

Figure 1.6: (a-d) Visualisation of the difference in the forces applied to 600 nm and 1000 nm diameter particles due to two different wavelengths counter-propagating along a tapered optical fibre. (b) and (d) are simulation results corresponding to (a) and (c) respectively. (e) A graph of the optical scattering forces on different particle sizes due to different wavelengths. Here, the blue line is the scattering from 808 nm light while the red line shows the scattering from the 1310 nm light, finally, the black line shows the contribution of both fields to the total scattering force acting on the particle. Reproduced with permission [72].

where polystyrene and gold particles are trapped in an optofluidic system consisting of a silicon slot waveguide grown on a glass substrate. The small waveguide separation, combined with the overlapping evanescent fields, provides a subdiffraction-limited trapping potential (Fig. 1.7). The authors were able to trap 75 nm dielectric nanoparticles and λ-DNA molecules using this waveguide system. Lin and Crozier [84] applied this technique to the problem of particle sorting. They used a channel waveguide that ran parallel to a slot waveguide. By introducing a defect, in this case a microsphere that had been fused to the channel waveguide, they were able to 'kick' smaller particles out of the potential formed by the channel waveguide and into the potential generated by the slot waveguide, which had a higher field confinement. Initially, 350 nm and 2 µm particles were guided along the channel waveguide. Upon reaching the defect, the 350 nm particles were pushed more than 250 nm away from the channel waveguide where they were then captured by the potential of the slot waveguide.

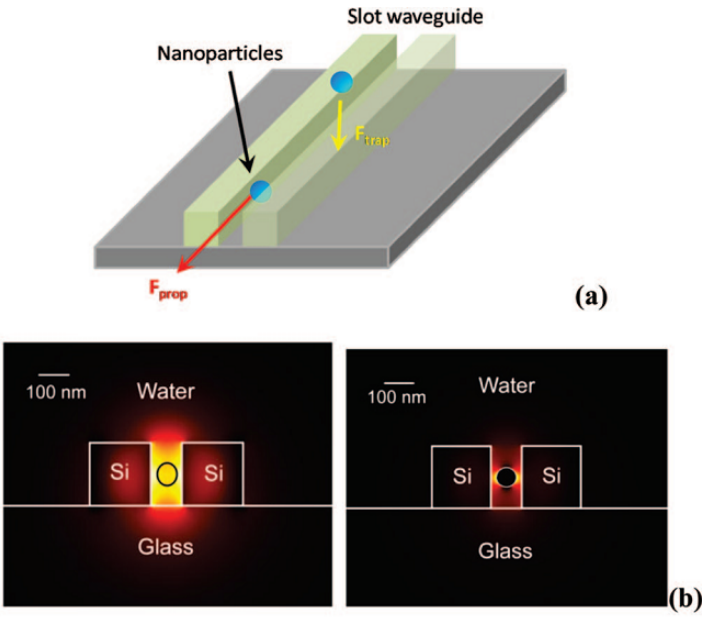

Figure 1.7: (a) Slot waveguide, (b) electric field intensity profiles for 65 nm polystyrene particles (left), and 100 nm gold particles (right). Reproduced with permission [82].

The use of evanescent devices to trap and manipulate micro- and nanoparticles continues to be of interest in the scientific community because of their versatility and customis-

ability. Channel waveguide structures can be incorporated into almost any device at the fabrication stage and are produced using common industrial techniques. This makes their potential uses in commercial products more likely than other, more specialised, devices which are produced by non-scalable, multi-stage techniques. The combination of a slot waveguide with an ultrathin fibre was one of the driving motivations behind the work in Chapters 4 and 5.

1.4.4 Photonic Crystal Cavities

With the goal of confining light to subdiffraction-limited sizes, many research groups have focussed their interest on photonic crystal (PC) cavities. Photonic crystal structures consist of a waveguide which has been periodically patterned to forbid the transmission of specific wavelengths. If, however, one introduces a defect to this periodic lattice, it is possible to create a region where frequencies that were previously forbidden are now allowed to propagate. By choosing the defect carefully, a cavity can be set up within the crystal structure [85, 86]. If the wave vector of this new cavity mode is chosen so that it is also a confined mode of the waveguide, both lateral and in plane confinement is possible [87]. Photonic crystal cavities have some interesting properties that are advantageous for trapping particles. Robinson et al. [88] showed that the modes present in such structures have "ultrasmall" mode volumes. This leads to extremely high field gradients over subwavelength dimensions; the confinement of the electric field is comparable to the defect size used to create the cavity.

Particle trapping using photonic crystal cavities was shown to be theoretically possible by Barth and Benson in 2006 [89]. They concluded that, not only could particles of varying sizes be trapped with a PC cavity, but the presence of the particles could shift the cavity resonance, a process known as self-induced back action (SIBA), which is discussed in more detail in Section 6.3. PC cavity devices have distinct advantages over other evanescent field-based devices. For example, Lin et al. [90] showed theoretically that, by tapering the angle of a PC cavity and including a slot, the gradient force could be significantly improved

over that given by a waveguide alone and that a high cavity quality (Q) factor can be maintained. Here the Q factor is a measure of how under-damped a cavity resonance is.

By tapering a PC cavity, as shown in Fig. 1.8, an interesting method of controlling a particle's position was achieved [91]. The angle with which such a device is tapered controls the distance along the z-axis at which different wavelengths are reflected. This, in turn, produces trapping potentials at different locations depending on the frequency of the laser light. Using a tuneable laser source, particles can be moved along the axis of a PC cavity waveguide by gradually varying the wavelength and allowing the trapped particle to follow the changing trap position. Some uncertainity in the particle's position is introduced since the potentials created have multiple minima. However, input powers of 7 mW could, theoretically, trap 50 nm particles stably. PC cavities have also been integrated into optical fibres via femtosecond laser ablation processes, as well as composite systems comprising of MNFs in optical contact with external nanostructured gratings [92, 93]. PC cavities offer an effective way of trapping dielectric particles. Recently, van Leest and Caro [94] were able to stably trap single bacteria of two different species with an inplane trap stiffness of 7.6 pN nm^{-1} mW^{-1}.

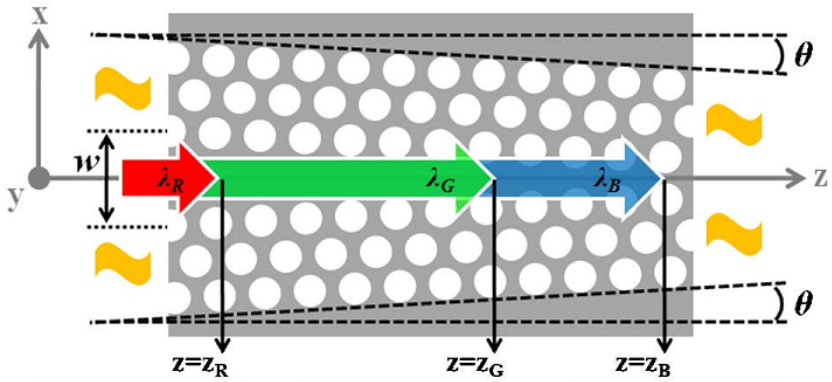

Figure 1.8: Tapered photonic crystal cavity. zR, zG, and zB are the locations where light of three different colours — red, green, and blue — are reflected. Reproduced with permission [91].

Surface traps have also been formed using photonic crystal structures that do not rely on the introduction of a defect. For example, Jaquay et al. [95] used a photonic crystal

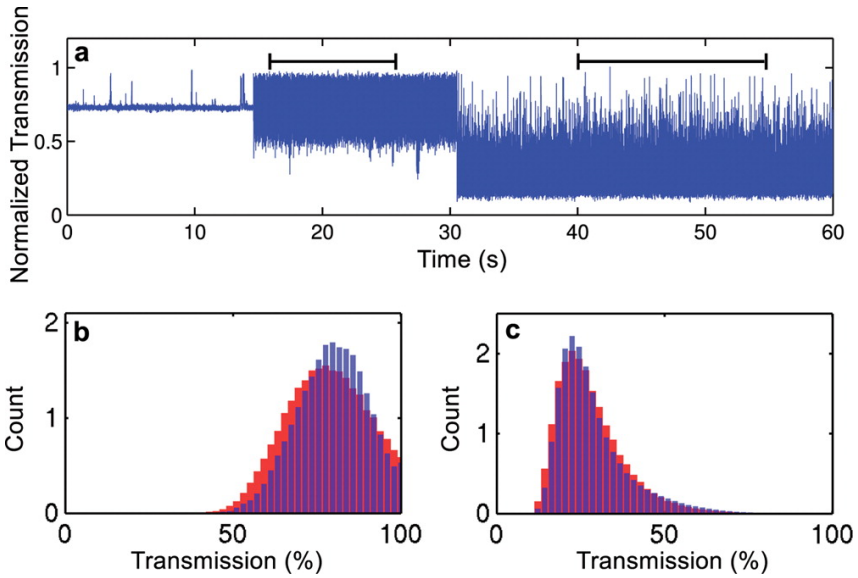

Figure 1.9: (a) Normalised transmission of the PC cavity system. (b) and (c) are histograms of the data highlighted with the horizontal bars at the left and right of (a), respectively. The histograms of the time series data (red) are given alongside the simulated histogram data (blue). Simulations were performed with a mean particle diameter of 24.8 nm (b) and 30 nm (c). Reproduced with permission [97].

structure where the light was incident perpendicular to the apertures. This produced a lattice potential that caused particles to congregate and form large self-assembled arrays, a process that they referred to as light-assisted self-assembly (LATS) [96]. Work performed by Mirsadeghi and Young [97] using PC cavities has shown that they are a useful tool for trapping nanoscale particles and providing a means by which the size of the trapped particle can be determined with nm precision. By introducing a single-mode channel to a PC structure, particles as small as 24 nm were trapped. Analysis of the transmission spectra obtained over a number of trapping events was used to determine the mean diameter of the trapped particles by assuming some variance in the particles' polarisabilities, as shown in Fig. 1.9. As a particle trapping device, PC cavities are promising and their integration into existing technologies makes them an attractive choice for future progress in the trapping of particles.

1.4.5 Microlenses

Microlenses with diameters greater than the wavelength of light can also be used to trap particles in regular arrays. Zhao et al. [98] used arrays of 22 µm microlenses to trap 3.1 µm polymer particles. The relative ease of operation and reliability of such a macroscopic device makes it of interest for applications in the life sciences where high optical alignment may not be available. More recently, a similar device was made using femtosecond laser ablation [99].

1.5 Plasmonic Based Devices

As particle sizes become smaller, problems associated with gradient force trapping arise. There are two options to enhance trapping at nanometre scales. One can choose to increase the power to further deepen the optical trap, but this is not usually viable as it is advisable to keep powers at a lower level to reduce noise and lessen power-induced damage to the trapped object. This means that one must increase the confinement of the laser light by some other means. Plasmonic structures have come to the fore in this size regime.

The effect of surface plasmons on metallic nanostructures of varying designs is being actively pursued for particle trapping [8, 100]. Nowadays, many research groups have access to a wide array of lithography techniques, allowing the creation of arbitrarily shaped designs. Furthermore, access to finite-element and FDTD software packages allow researchers to model how light interacts with plasmonic materials, photonic crystals, III-V semiconductors, etc., to a high degree of accuracy. With this arsenal of tools at hand, it is no surprise that the number of publications in the field has been rising rapidly in the last decade.

1.5.1 Surface Plasmon Polaritons and Localised Surface Plasmons

Using plasmonic techniques, light can be concentrated in areas that are significantly below the diffraction limit. Surface plasmons can be considered differently depending on the geometry of the substrate in question as either localised surface plasmons (LSPs), or as propagating surface plasmon polaritons. For brevity we will refer to the latter simply as surface plasmon polaritons (SPPs). Surface plasmons are the result of coherent electron oscillations on a metal's surface. SPPs are a means of quantifying how they behave on larger metallic surfaces that are capable of supporting propagating plasmon waves. SPPs cannot be directly excited with laser light since they exist as a wave propagating along the dielectric surface interface and their dispersion curves prohibit direct phase matching with an incident laser beam. Instead, they must be excited by an evanescent field. Currently, the most popular method of coupling to SPPs is called the Kretschmann configuration. This configuration makes use of total internal reflection through a glass prism. The required plasmonic structure need only be placed on one face of the prism, thus enabling it to be excited by the evanescent field generated by the reflection of the incident light passed through the prism at the critical angle. LSPs, on the other hand, define how surface plasmons behave on smaller surfaces where the boundary conditions cause confinement of the surface plasmon. LSPs are present in nanoparticles and wavelength-scale plasmonic geometries. Due to spatial confinement, phase matching is relaxed and, therefore, only light matching the correct LSP resonance frequency is required to excite them in a material. SPPs have a wide frequency range over which they can be excited, which is not the case for LSPs.

The form of an SPP is dictated largely by the geometry of the substrate and the input light field. That is not to say they are the only factors; of course, refractive indices and other material properties are important. A recent paper by Tsai et al. [101] showed how an SPP with a topological charge of 2, that is to say an SPP that contains orbital angular

momentum, could be produced by using circularly polarised light in combination with a unique surface geometry. By etching an Archimedes spiral into a gold film, they were able to both confine a particle, and impart angular momentum to the particle, causing it to rotate.

Heating, due to inevitable ohmic losses in the metal, is an intrinsic property of plasmonic devices, especially when devices based predominantly on the excitation of LSP modes are considered. The interaction between laser light and nanoparticles causes the generation of point-like heat sources at locations that depend on factors such as particle type, beam polarisation, and angle of incidence. Intense light fields generated near plasmonic nanostructures are often used to trap particles [102–104]. In some cases, the heat generated by the structures themselves was used to trap particles [105]. Because of this, analysing heating effects is important. Donner et al. [106] discussed how the plasmon-assisted optofluidics is influenced by the heat produced. In short, this paper concluded that, for isolated nanostructures below 200 nm, the influence of heating is negligible. The authors also state that, to increase the plasmon-assisted fluid motion from tens of nanometres to hundreds of nanometres, structures larger than 1 µm must be used. Larger structures are easily integrated with heat sinks to help quickly dissipate the accumulated heat [107].

A recent study by Roxworthy et al. [108] on the heating effects of a 9 by 9 array of gold BNAs (bowtie nanoantenna apertures) in a SiO2/ITO substrate has shown that heat-induced convection currents of greater than 1 µm s^{-1} can be created. The study gives both theoretical and experimental results that are quantitatively in agreement with each other. Seol et al. [109] showed that heating involved with the trapping of gold nanoparticles can also affect the spring constant of an optical trapping system. Because of this heating, they concluded that gold nanoparticles are not recommended when working with biological systems. Despite this, other authors have performed experiments with gold nanoparticles which seem to be in contradiction. For example, Demergis and Florin [110] showed ultrastrong binding of metallic nanoparticles via the optical binding force

and estimated that there was no heating, contrary to other reported studies on similar systems.

1.5.2 Scalability

Plasmonic activity on metallic surfaces sufficiently larger than the plasmon wavelength can be characterised as SPPs. Under these conditions, it can be assumed that the dispersion curve of the structure approaches that of an infinite metallic film [111]. This relationship is important as it shows that plasmonic-based devices cannot be scaled down *ad infinitum*. Devices that may work well at a few microns cannot be expected to work analogously at the nanometre scale. For example, in an experiment performed by Wong et al. [111], a dielectric channel optical waveguide was integrated with an array of gold micropads of 5 µm diameter and with a pitch of 15 µm. Figure 1.10 shows a schematic of the system. The authors trapped 5 µm polystyrene beads and yeast cells using an input beam power of 20 mW. This technique works well and relies on the formation of SPPs to create adequate trapping potentials above the discs. A paper by Righini et al. [112], where a prism was used to excite the SPPs, showed similar results. It should be obvious that simply downscaling the dimensions will not yield the same results. First, the plasmon will cease to be describable as a SPP once the pad size is reduced sufficiently in size, behaving instead as an LSP, and secondly, the viscous damping of suspended particles is greatly reduced due to the decreased cross-section of smaller nanoparticles.

Gold nanopads were used by Chen et al. [113] to trap 500 nm and 100 nm nanoparticles using the LSPs generated in subwavelength disk structures. A seven by seven array of four gold circular nanopads was patterned on an indium titanium oxide substrate and illuminated by a Gaussian beam (Fig. 1.11). The nanopads were 200 nm in diameter, which produced polarisation-dependent LSPs. This work was inspired by the earlier work in [114] and produced a similar washboard-type potential, thus drawing particles towards the centre of the plasmonic structure.

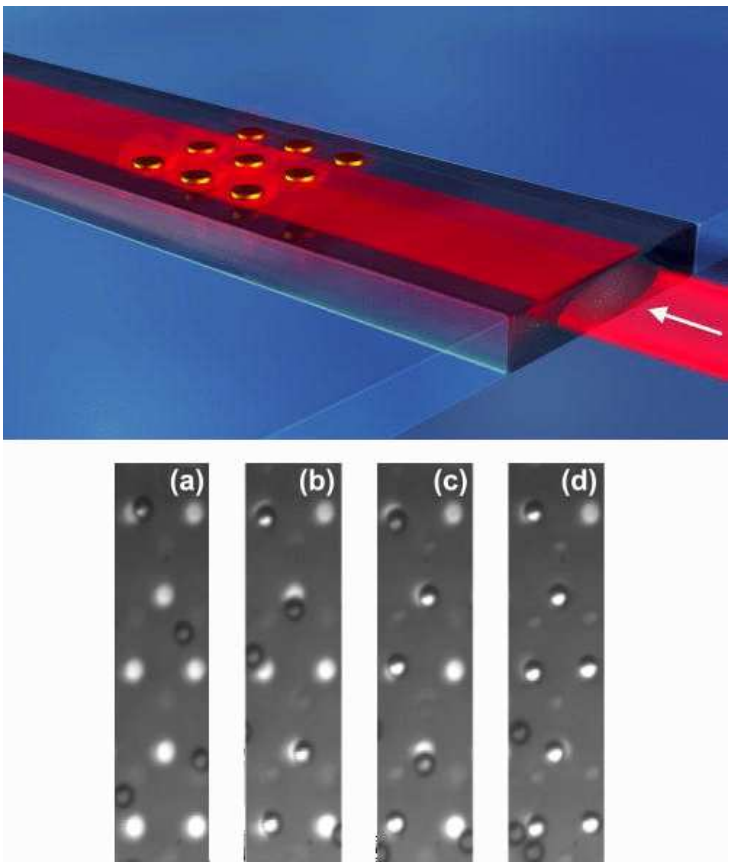

Figure 1.10: Channel waveguide incorporating a plasmonic gold micropad array. (a) – (d) are a time sequence of images showing the parallel trapping of 5 µm polystyrene beads. Reproduced with permission [111].

1.5.3 Self-Induced Back Action

Often, the calculation of the trapping capabilities of optical tweezers is done in the absence of any particles. In many cases this is an appropriate choice, as it both simplifies the physics, from a computational viewpoint, and gives quantitatively accurate results. However, as particle sizes becomes smaller, and lower optical powers are used, it is necessary to include the effect of the dielectric particle on the local electric field rather than relying on the Rayleigh approximation, especially when plasmonic effects are present. This is because the effect of the particle on the local refractive index distribution becomes important when calculating the fields due to the proximity of the particle to the nearby surfaces which do not arise in free space calculations. The effect of a single particle tends

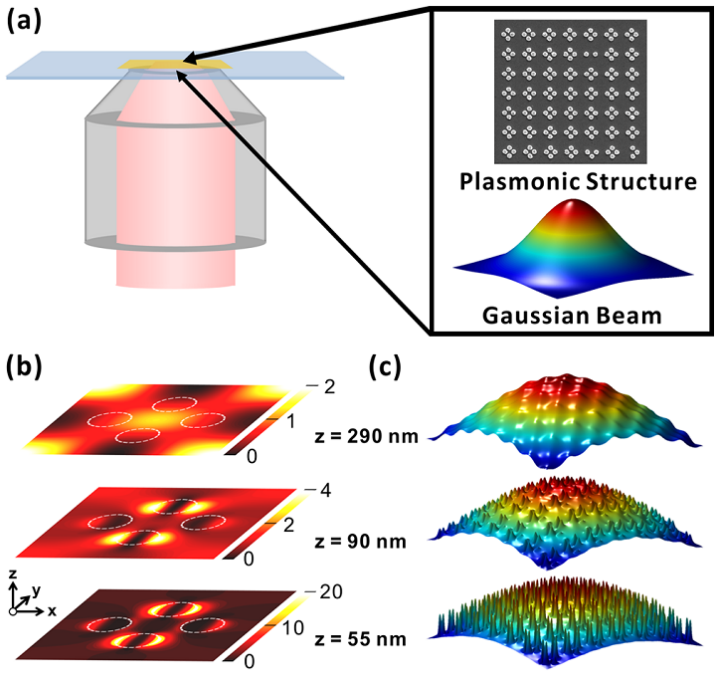

Figure 1.11: (a) Plasmonic disk array placed on an objective lens. (b) Light intensity at various heights above the disks. (c) Visualisation of the intensity profile at varying heights. Reproduced with permission [113].

to improve certain types of optical trapping via a mechanism called self-induced back action (SIBA). This effect has been studied in various systems, such as plasmonic and photonic crystal cavity systems, as mentioned earlier [115].

SIBA is especially relevant in many plasmonic structures as the effect plays a large role at the scales typically used. Juan et al. [115] trapped 50 nm nanoparticles using 2 mW of power with the help of SIBA. By cutting a 310 nm circular aperture into a 100 nm thick gold film a near-field was generated, which, in the presence of a dielectric particle, created a system that was sensitive to small position variations (Fig. 1.12). The particle present in the vicinity of the aperture effectively "saw" a larger hole due to the shifting of the cutoff wavelength, thereby causing higher transmission of light through the aperture. Deviations of the particle from the equilibrium position near the aperture either increased or decreased the net transmission of light through the aperture. The authors showed that the motion of the particle always served to create a force that pushed the particle back

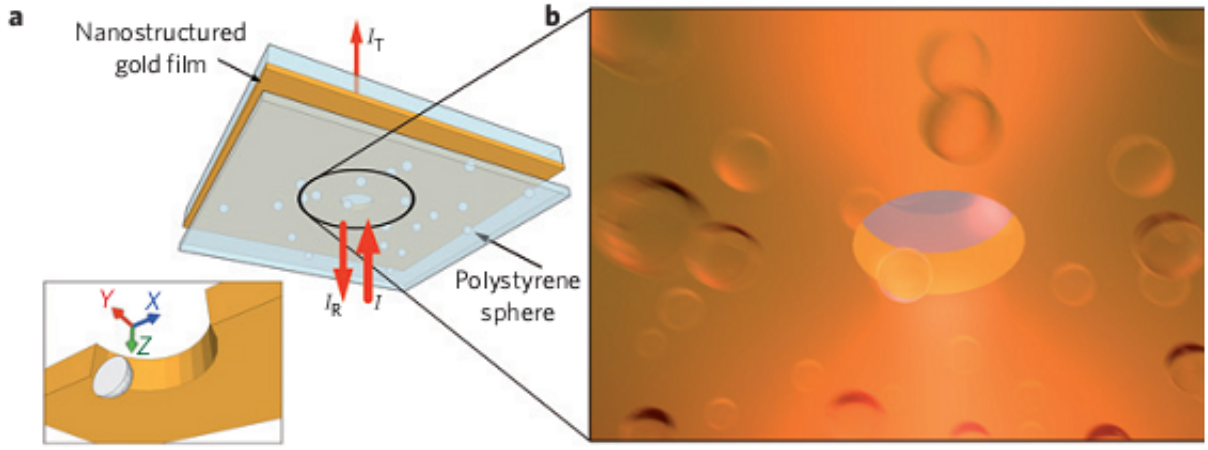

Figure 1.12: (a) An image showing the structure used to examine self-induced back action. (b) A closer view of the nanohole in the gold substrate. Reproduced with permission [115].

to its equilibrium position.

1.5.4 Super Resolution Optical Trapping

Localised surface plasmons can be used for enhanced trapping well below the diffraction limit. Tanaka and Sasaki referred to this ability as "superresolution optical trapping" [116]. Their plasmonic structure consisted of only two square gold nanoblocks, as shown in Fig. 1.13. This work is indicative of this subfield of plasmonic trapping, in so much as how it highlights the importance of the choice of polarisation in LSPs. Two important cases are considered, one parallel to the axis joining the two squares, and one at 90° to this. The two cases highlight the fact that the device has various available modes and, by changing the polarisation, specific modes can be excitied individually. The first configuration creates a single high-intensity spot between the two squares, whereas the latter allows for the creation of multiple trapping potentials with a subdiffraction limit separation. Using gold nanoblocks, the authors succeeded in trapping 100 nm polystyrene particles and observed double well potentials with 230 nm separation.

Gold bowtie nanoantenna apertures (BNAs) such as those created by Roxworthy et al. [102] allow for trapping using LSPs (Fig. 1.14). They created an array of BNAs

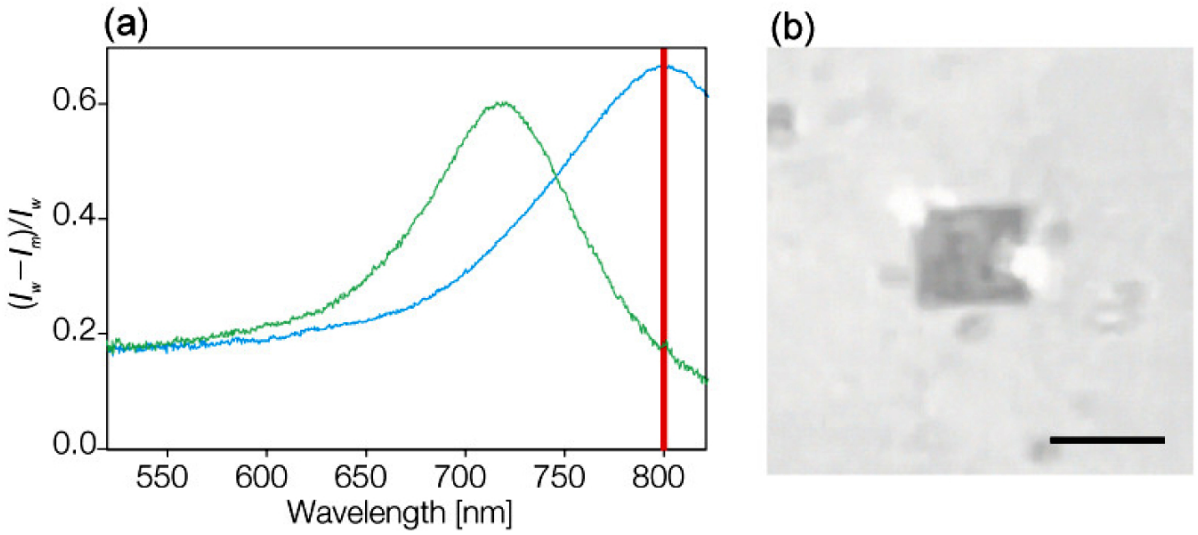

Figure 1.13: (a) Extinction spectra of a pair of gold nanoblocks with longitudinal (blue) and transverse (green) polarisations. (b) Plasmonic trapping of a 350 nm particle (bright region) using 80 nm × 80 nm × 40 nm nanoblocks as the polarisation is shifted between longitudinal and transverse. The red line shows the incident wavelength for the experiment. Scale bar = 3 µm. Reproduced with permission [116].

and, instead of using a standard continuous-wave (CW) laser source, they used a pulsed femtosecond (fs) laser source to trap dielectric and metallic particles. They observed increased trap stiffness over a CW approach while providing the ability to observe nonlinear effects in situ, such as two-photon absorption, second-harmonic generation, etc. The BNA arrays, however, coupled with the fs laser source, caused some of the spheres to adhere to the surface. The effect did not seem to be caused by the melting of the spheres, since the heat generated was not sufficient for this. Rather, the induced heating seemed to attract particles to the BNA surfaces. The authors acknowledged that a theoretical model for optical tweezing using fs laser sources did not yet exist and did not attempt to explain the dynamics of the interaction in such a way. The increased trap stiffness was attributed to the illumination spot size of the laser source. Many BNAs were illuminated at once allowing particles to 'see' the effect of multiple traps, which, in turn, caused the particle's motion within the trap to be describable as acting with an effective trap stiffness with multiple contributions. Once again, fs laser sources are an interesting choice since they

have the potential to reduce the overall power transferred to the trapped particles. A difference can be seen between the upright and inverted microscope setups. This is due to the lack of particle lensing effects while in the upright configuration, reducing the amount of second harmonic generation in the substrate. In this experiment, the power levels were three orders of magnitude lower than the optical damage threshold, as reported in [117].

Particles with a high polarisability are good for optical trapping, especially if a high refractive index contrast between them and the surrounding material can be obtained. J-aggregrates, or Jelley aggregrates to give them their full name, were discovered independently by Scheibe et al. [118], and Jelley in 1937 [119]. J-aggregrates are essentially dye clusters with an absorption band that can be shifted. Zamecnik et al. [120] showed that by functionalising these aggregrates onto plasmonic silver nanoparticles interesting effects could be seen. The authors considered a particular type of material, known as ϵ near-zero materials (ENZ). This is a branch of materials that has an effective ϵ value near zero when illuminated at certain wavelengths, thereby significantly enhancing the scattering cross-section. The permitivity of a medium, ϵ, is a measure of how much resistance it has to an external electric field, which leads to the electric displacement field encountered in Maxwell's equations. The authors targeted this property by combining silver plasmonic nanoparticles with J-aggregrates. By illuminating the particle near the plasmonic resonant wavelength, the electric field was confined within the J-aggregrate, creating a high field in a tightly confined area. The authors used this effect to perform surface-enchanced Raman spectroscopy.

1.5.5 Gratings

Gratings etched onto metallic surfaces allow coupling to SPPs since the additional grating vector of the system allows for mode matching of the SPP to the incident light. As we know, light fields can be combined to produce interesting electric field configurations, and SPPs, being a form of electromagnetic radiation, behave the same. Genevet et al. [121] showed how placing diffraction gratings on a gold surface can generate a plasmonic

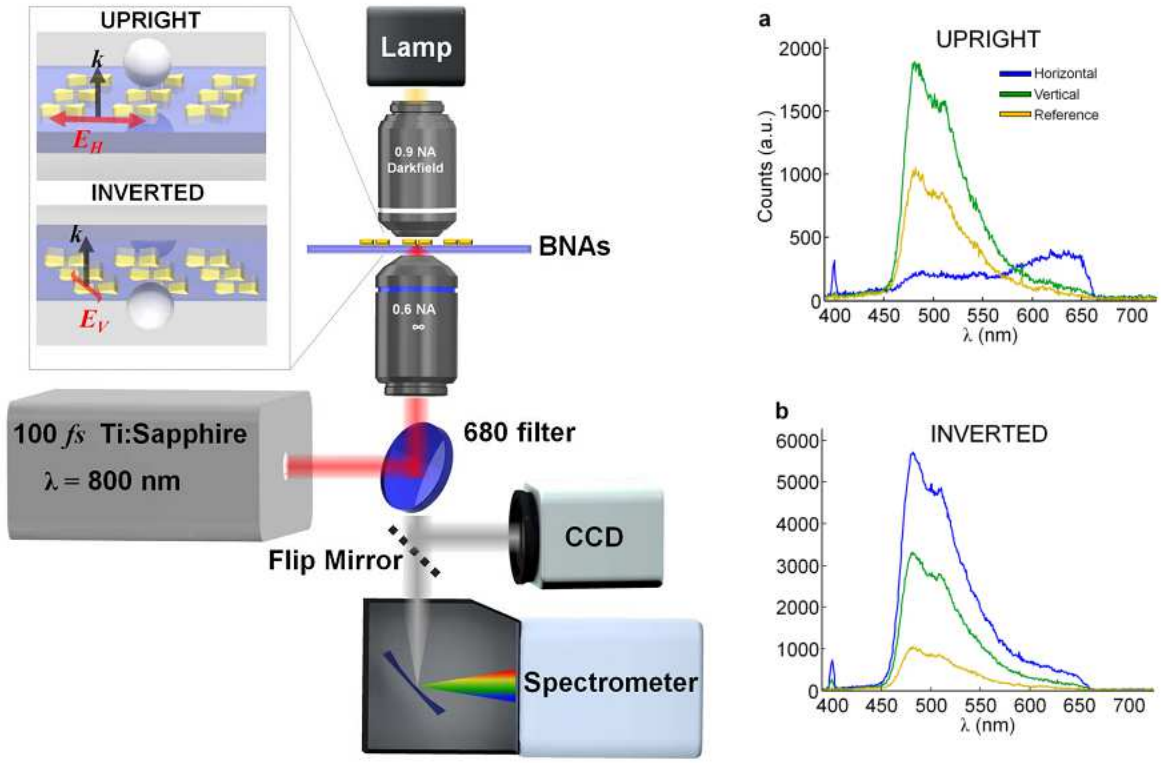

Figure 1.14: Au bowtie nanoantenna arrays in upright and inverted configuration and the associated experimental setup. Two-photon fluorescence measurements from a trapped fluorescent microsphere are given in (a) the upright orientation and (b) the inverted orientation. Blue and green curves represent the horizontally and vertically-polarised results, respectively. The yellow curve is a reference signal from a particle trapped on the glass substrate. Reproduced with permission [102].

bottle beam (Fig. 1.15). When two 2-dimensional planes with intersecting directions of propagation meet, what is known as a cosine Gaussian beam (CGB) is formed. CGBs are similar to Bessel beams since they have a nondiffracting nature in the direction of propagation. The authors applied this theory to SPPs. Using this property, they were able to create an intensity profile that could trap particles at the nodes of high intensity.

1.5.6 Plasmonic Nanorods and Ultrathin Fibres

Gold nanorods (GNRs) are cylindrical gold structures with dimensions of the order of a few to a few tens of nanometres. These rods are plasmonically active and exhibit different

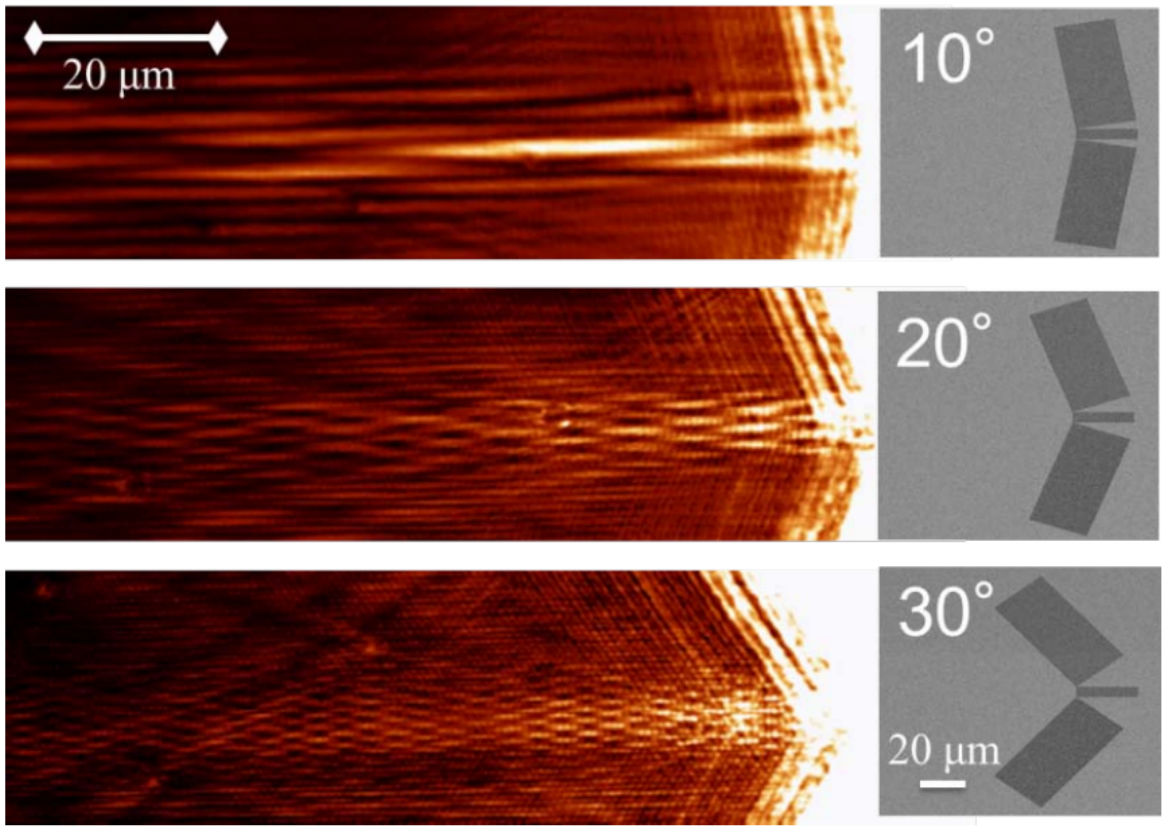

Figure 1.15: Near-field scanning optical microscopy images of plasmonic bottle beams generated at three different grating configurations. Reproduced with permission [121].

resonant peaks depending along which axis of the rod the polarisation lies. The plasmonic activity of such objects are described as LSPRs [122]. Some early attempts have been made to incorporate ultrathin fibres with plasmonic structures, but writing such a device directly to the curved, dielectric surface is quite difficult. Wang et al. [123, 124] have had success combining ultrathin fibres and gold nanorods in two different geometries. Their first work [123] involved dispersing gold nanorods throughout a polymer solution, which was then used to create polymer ultrathin fibres through an electrospinning-like technique see Fig. 1.16. Two samples were created with measured GNR densities of 0.8 and 0.2 μm^{-3} respectively.

Later, Wang et al. [124] improved upon the earlier experiment by locating a single GNR on the surface of a silica ultrathin fibre and then using this GNR to excite a whispering gallery mode of the fibre (see Fig. 1.17). Unlike the previous paper, where the

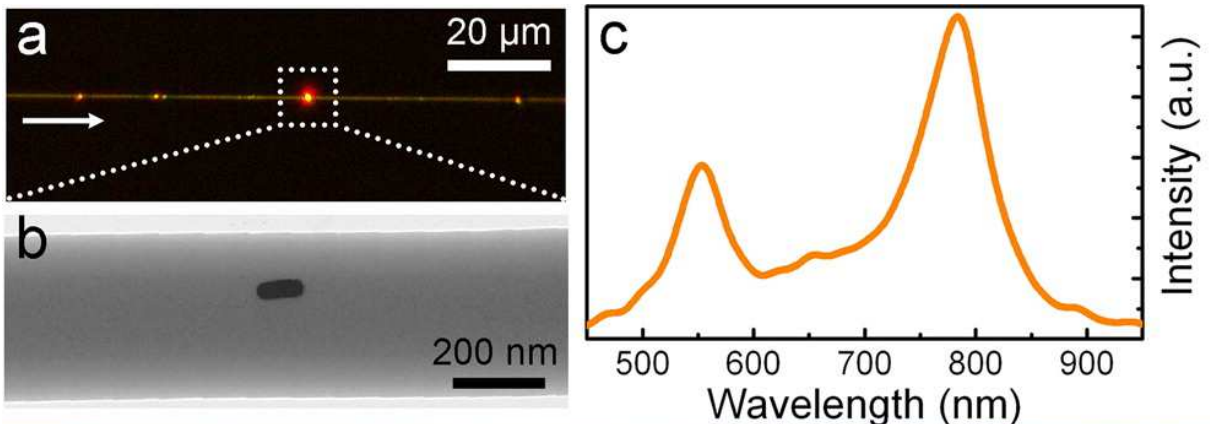

Figure 1.16: (a) Fluorescence from a gold nanorod which has been excited by light passing through the fibre, (b) TEM image of a GNR embedded in the fibre, and (c) Scattering spectrum of the GNRs. Reproduced with permission [123].

distribution of the GNRs was throughout the polymer fibre, here the GNRs were instead on the fibre surface, allowing better access to the enhanced electric field, while also enabling excitation of the whispering gallery modes in the fibre. While both of these papers are impressive, it is important to note that the position of the rods is non-deterministic and a technique which could place such structures on a specific fibre location is desirable. This idea was a driving motivation for the work presented in Chapter 6.

1.5.7 Subwavelength Apertures

Subwavelength aperture diffraction is, subject to debate, another area where plasmonics may play a role. Previously accepted theories, such as those by Bethe and Kirchhoff [125], were used to model the propagation of light through apertures in either perfectly conducting screens, or black opaque screens. Given certain conditions, these theories worked quite well, but did not provide an adequate explanation of how the light propagated through structures where the dimensions were below the cutoff for any mode to exist. A thorough review of previous and current theories on this type of diffraction is given by Weiner [126]. It was not until 1998 that a theory of plasmon-assisted transmission through subwavelength apertures was proposed by Ebbesen et al. [127]. The authors showed that Bethe

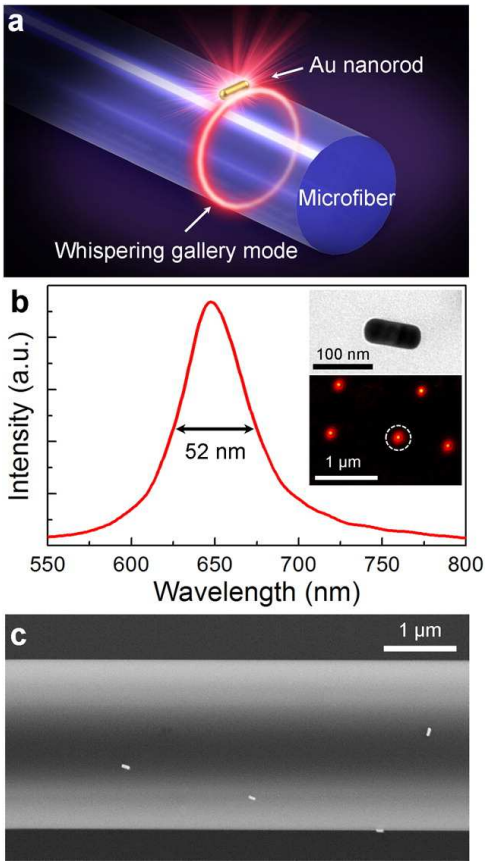

Figure 1.17: (a) Graphical representation of the system, (b) Typical scattering cross-section of the GNR with a 52 nm linewidth, (c) SEM image of the fibre with nanorods present. Reproduced with permission [124].

theory was wholly unsuitable to describe the transmission of light through subwavelength aperture arrays in a silver film. Surpisingly, they showed that transmission increased for wavelengths more than 10 times the diameter of the apertures and, in some cases, more light was transmitted than was directly incident on the apertures. These facts combined indicated that the apertures were more than just passive elements. The authors further showed that the behaviour seemed to be independent of hole size and material type, yet had a strong angular dependence that could only be explained by the presence of surface plasmons. While plasmonics may play a role in the transmission through apertures, and for the case of gold materials they most certainly play some part, they are not entirely required to explain the dynamics of light transmission though Bethe apertures and this remains a point of controversy.

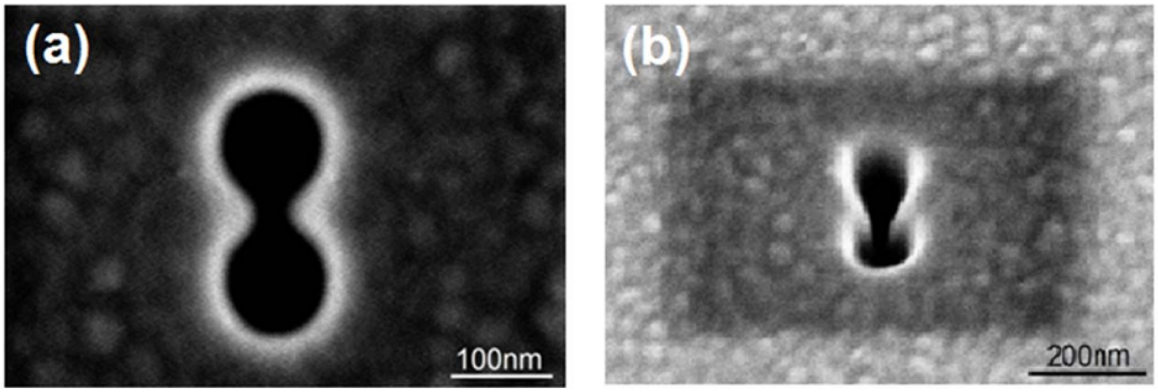

Figure 1.18: Double-nanohole created using a focussed ion beam in a gold layer. Reproduced with permission [128].

Baida and Van Labeke [129] performed work on annular aperture arrays that sought to increase the transmission of light via the same process as that described by Ebbesen et al. [127]. Plasmonic double-nanoholes deal with the problem of transmission through subwavelength apertures. A typical double-nanohole is shown in Fig. 1.18. Using such a system, Zehtabi-Oskuie et al. [128] trapped 20 nm polysterene particles using as little as 3.5 mW of input power. A later analysis of the trapping efficiency was also produced by the same group [130], where they compared the trap stiffnesses obtained for a double-nanohole trap with that of a standard optical tweezers and claimed that similar trap stiffnesses can be obtained, but for particles that are 10 times smaller.

Building on the work by Baida and Van Labeke [129] many groups have pursued coaxial plasmonic waveguide structures for trapping [132–134]. Rodríguez-Fortuna et al. [132] predicted that coaxial plasmonic structures arranged in an array could be used as a negative refractive index material. This property may be used to produce backwards travelling electromagnetic waves. Highly hybridised structures, such as the device proposed by Liu et al. [133], which combines gold annular aperture arrays with a photoresponsive liquid crystal, can also produce high field gradients in subdiffraction-limited regimes. All of these studies indicate progress towards a highly tuneable technique which has promising applications in particle trapping. Saleh and Dionne [135] published a theoretical paper

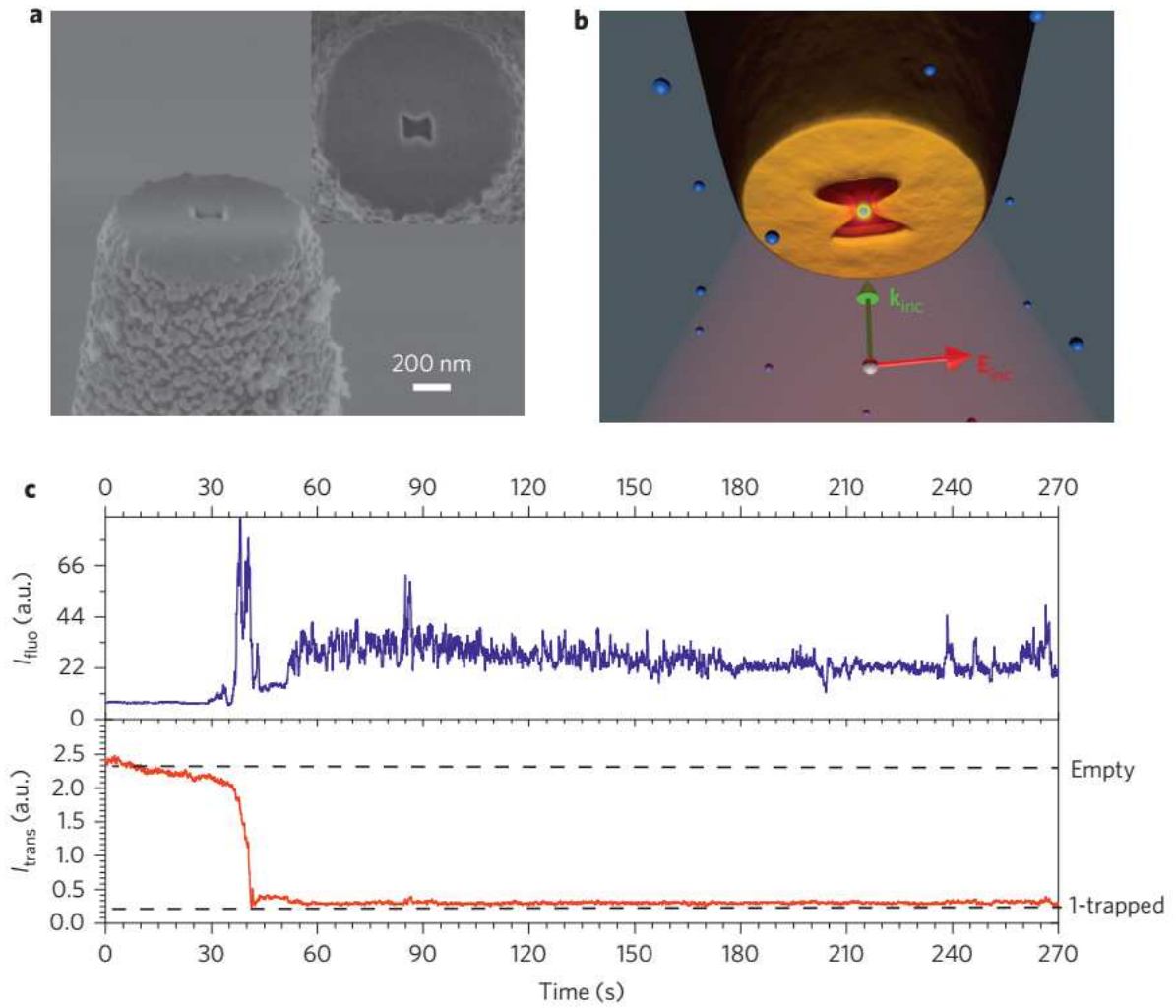

Figure 1.19: SEM image, (a), and schematic, (b), of an NSOM tip with a bowtie nanoantenna aperture located in the gold layer at the apex. (c) Time series of blue fluorescence from a dye doped bead (blue line) along with the trapping beam intensity (red). A trapping event occurs at 40 s. Reproduced with permission [131].

where a gold coaxial plasmonic aperture in a silica fibre could be used to trap particles with sizes less than 10 nm. They also showed that the creation of dual trapping potentials at a distance of 20 nm from the surface is possible.

Subwavelength apertures in gold films can also be used in combination with tapered fibres. For instance, Neumann et al. [136] proposed the use of tapered optical fibres with subwavelength apertures to allow the high transmission of light to subdiffraction-limited regions. The end-face of a near-field scanning optical microscope (NSOM) probe was coated with gold and a focussed ion beam was used to etch a 45 nm aperture into the gold layer. The NSOM taper was chosen such that it was near the cut-off diameter for the first excited mode. A more in-depth discussion of the transmission mechanism has been published by Gordon [137]. He showed that transmission through the NSOM was improved by two orders of magnitude. Later, Berthelot et al. [131] expanded on this idea by including a bowtie nanoaperture to the end face of a tapered optical fibre to allow three-dimensional manipulation of 50 nm dielectric objects (Fig. 1.19). The fields produced at the output of a half-tapered fibre, similar to an NSOM taper, are also capable of lensing light sufficiently to trap particles without any enhancements from plasmonic apertures.

1.6 Conclusion

Here we have outlined the state of the field of optical trapping while driving home some important points related to this field. While the trapping of larger, micron-sized particles has become somewhat routine, the trapping of smaller particles is an extremely active area of research. This thesis work aimed to combine some of the techniques used to further confine light and apply them to ultrathin optical fibres for use in atom and particle systems. Namely, we took inspiration from the areas of slot waveguiding and plasmonic trapping. Some preliminary work was done with standard ultrathin optical fibres, which is demonstrated in Chapter 3, and subsequently we explored the modification of such

fibres and how they could be adapted for use in atom and particle trapping.

This introduction, aside from outlining the current state of the field, serves as a motivation for many of the topics to follow. Chapter 2 contains much of the theoretical background required to understand the phenomena of particle and atom trapping. From there we move on to atom trapping in Chapters 3 and 4. These chapters cover an experiment showing how ultrathin optical fibres can be used to probe a cold atom system, and hence, measure the temperature of the trapped atoms. We also include a theoretical description of how one could use a nanostructured ultrathin fibre to trap atoms within a rectangular cavity etched at its waist. Chapter 5 discusses how we fabricated a nanostructured ultrathin fibre and also an experiment in dielectric particle trapping where 100 and 200 nm particles were trapped using this proposed device. Chapter 6 moves in a slightly different direction; rather than modifying the bulk of the fibres, we instead added to the fibres by using electron beam induced deposition to write plasmonic gold dimer arrays on the fibres' waists. Finally, in Chapter 7, we look at a near-field device incorporating Fresnel microlenses and how it could be used to trap atoms as well as fabricating such a device.

Chapter 2

Fundamentals of Optical Fibres and Optical Trapping

Optical near-field phenomena, such as evanescent fields, are especially effective in probing or otherwise interacting with microscopic and atomic objects. Devices which use this principle are excellent platforms for locally confining light fields since they do not suffer from the restrictions enforced by Abbe's limit, namely that a beam of light with wavelength, λ, travelling in a medium, with refractive index n, with a converging angle of θ, can produce, at best, a spot size of $\lambda/2n\sin(\theta)$. Near-field phenomena allow for devices with long interaction lengths as well as subdiffraction-limited spot sizes. To understand the motivation behind the work in this thesis we must discuss how near-field devices operate, as well as how one can harness the optical forces to perform useful work.

We shall begin, in Section 2.1, with a discussion of ultrathin optical fibres as they are central to this thesis and used in Chapters 3, 4, 5, and 6. Section 2.2 focusses on the optical forces induced in dielectric particles using classical electrodynamics. This is important in Chapter 5 where we demonstrate the trapping of dielectric particles. Section 2.3 discusses the problem of atom trapping, specifically the trapping of neutral ^{85}Rb atoms. This section is necessary to understand parts of Chapters 3, 4, and 7. Finally, in Section 2.4, a brief description of plasmonic enhancement in the form of localised surface plasmons is

given to help understand the device presented in Chapter 6.

2.1 Ultrathin Optical Fibres

Tapered optical fibres, or ultrathin optical fibres, being the main focus of this thesis, produce evanescent fields which extend significantly, often hundreds of nanometres, beyond their dielectric boundaries. To fully comprehend their usefulness, it is first necessary to understand the principles of their operation, beginning with a discussion of the differences between ultrathin fibres and untapered optical fibres.

Commercial grade, single-mode optical fibres have typical core diameters of about 6 µm and cladding diameters of 125 µm. With such a macroscopic dimension for the cladding it is reasonable to assume that the evanescent field at the fibre surface is negligible. Micro/nanofibres (MNFs), on the other hand, have overall diameters of a few micron or lower, and the surrounding medium instead becomes the cladding. This leads to a significant change in the refractive index profile, shown in Fig. 2.1

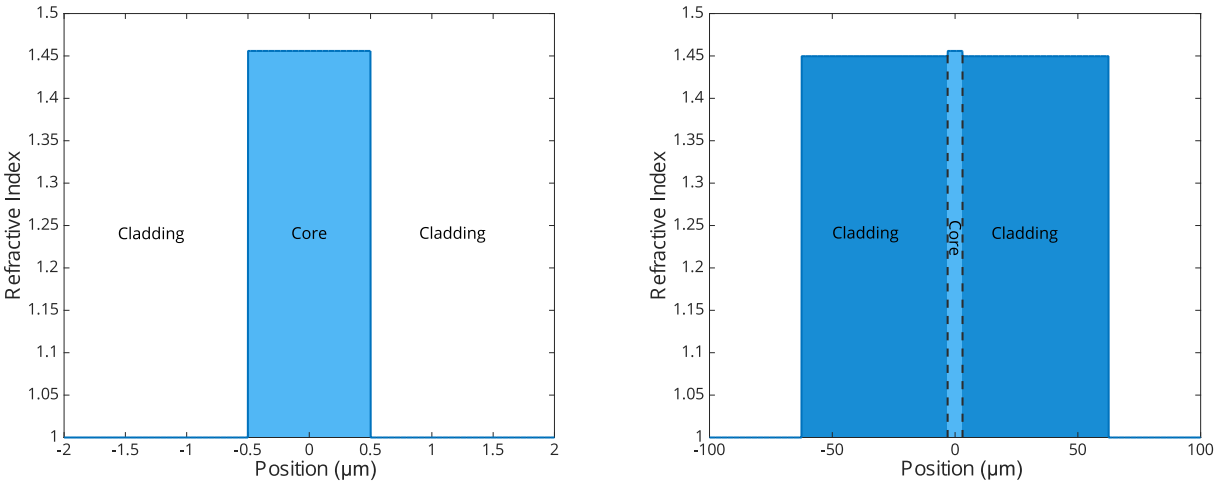

Figure 2.1: Refractive index profiles for (left) an MNF, and (right) a step-index optical fibre.

Here, we only consider step-index profile optical fibres, but there exist many different refractive index profiles. Some fibres have a radially varying index distribution, such as graded-index optical fibres, while others can have azimuthally varying distributions as is

the case for polarisation maintaining (PM) optical fibres.

For light to be guided in an optical fibre, a parameter known as the numerical aperture (NA) is crucial in determining the acceptance angle. The NA is used to determine an acceptance cone centred at $r = 0$ on the fibre axis for which light can enter and become guided into a fibre mode; light which enters outside of this cone will not be guided. The NA is determined by the refractive indices of the core and cladding. Experimentally, the main benefit for knowing the NA is that it allows one to choose appropriate lenses when coupling light from free-space into the guided fibre modes. A poor choice of lens will drastically reduce the coupling efficiency. The numerical aperture is given as

$$\sin(\theta_{max}) = \sqrt{n_{co}^2 - n_{cl}^2} = \text{NA}, \tag{2.1}$$

where θ_{max} is the acceptance angle of the fibre, n_{co} is the refractive index of the core, and n_{cl} is the refractive index of the cladding. The NA is also used in the definition of the V number [48]. The V number is a dimensionless quantity used to determine the modes which can propagate in a step-index fibre for a given set of radii, refractive indices, and wavelengths. The V number is normalised by the wavelength allowing us to see the behaviour of the modes without having to specify a particular wavelength. We will discuss the V number later when we solve for the fibre modes; it is given by

$$V = \frac{2\pi}{\lambda} a \sqrt{n_{co}^2 - n_{cl}^2}, \tag{2.2}$$

where a is the radius of the fibre. Despite the similar geometries between MNFs and standard optical fibres, the description of their optical modes is very different. Standard optical fibres operate in what is known as the "weakly guided regime" due to the low refractive index contrast between the core and the cladding. MNFs, on the other hand, operate in the "strongly guided regime" due to the large difference between their core and cladding regions. To fully understand this, we must consult Maxwell's equations.

2.1.1 Maxwell's Equations and the Wave Equation

Maxwell's equations form the foundation of classical electrodynamics [48]. They describe the relationship between electric and magnetic fields and also how charges and currents generate or affect the fields. The four Maxwell's equations given in differential form are:

$$\begin{aligned} \nabla \times \vec{E} &= -\frac{\partial \vec{B}}{\partial t}, \\ \nabla \times \vec{H} &= \vec{j} + \frac{\partial \vec{D}}{\partial t}, \\ \nabla \cdot (n^2 \vec{E}) &= \frac{\rho}{\epsilon_0}, \\ \nabla \cdot \vec{B} &= 0. \end{aligned} \tag{2.3}$$

Here, $\vec{E}$ and $\vec{H}$ are the electric and magnetic fields, respectively, μ_0 is the permeability of free space, ϵ_0 is the permittivity of free space, $\vec{j}$ and ρ are the current and charge densities of the system, and n is the refractive index. We assume nonmagnetic materials throughout. If we now consider the source-free version of these equations, which is appropriate for an optical fibre system, we can set ρ and $\vec{j}$ equal to zero leading to the much simpler forms

$$\begin{aligned} \nabla \times \vec{E} &= -\frac{\partial \vec{B}}{\partial t}, \\ \nabla \times \vec{H} &= \frac{\partial \vec{D}}{\partial t}, \\ \nabla \cdot (n^2 \vec{E}) &= 0, \\ \nabla \cdot \vec{B} &= 0. \end{aligned} \tag{2.4}$$

It is important to note that we have not assumed an isotropic refractive index at this

point. If we eliminate $\vec{H}$ from Eqn. 2.4 we get a less standard form of the wave equation

$$(\nabla^2 + n^2k^2)\vec{E} = -\nabla(\vec{E}.\nabla \ln(n^2)). \tag{2.5}$$

This is an important equation as it shows that solving for anisotropic systems is a nontrivial problem which can involve treating the anisotropy as a perturbation to the unperturbed Helmholtz equation, the solution of which may also be a nontrivial problem depending on the geometry. However, if we assume an isotropic medium, the right hand side of Eqn. 2.5 becomes zero, yielding the familiar Helmholtz form of the wave equation

$$(\nabla^2 + n^2k^2)\vec{E} = 0. \tag{2.6}$$

2.1.2 Optical Fibre Modes in MNFs

The modes which propagate within step-index optical fibres are easily determined due to their homogeneous, isotropic refractive indices and longitudinal invariance. For standard optical fibres, the refractive index contrast, Δn, is relatively small and can be used to simplify the final step of the solution leading to the degenerate mode sets. In the case of MNFs, this approximation is not valid, instead leading to the splitting of the degenerate linearly polarised (LP) modes into the constituent transverse electric (TE), transverse magnetic (TM) and hybrid electric (HE) modes. EH and HE modes correspond to cases when the z-component of the electric or magnetic fields, respectively, is dominant, as opposed to the transverse modes, TE and TM, which contain either no E_z or B_z component, respectively. The longitudinal geometry of the system leads us naturally to solutions to the Helmholtz equation (Eqn. 2.6) of the form:

$$\vec{E_T}(r, \phi, z) = \vec{E}(r, \phi)e^{i\beta z}, \tag{2.7}$$

where $\vec{E_T}$ is the total electric field solution. By substituting this solution into Eqn. 2.6, and solving the associated scalar form of the resulting vector equation, we can determine

the mode distributions of the MNFs. The theory behind the solutions is well documented [138], and a full derivation is not given here. The important transcendental equation that governs the propagation constants for the modes is:

$$\left[\frac{J_p'(u)}{uJ_p(u)} + \frac{K_p'(w)}{wK_p(w)}\right]\left[n_{co}^2\frac{J_p'(u)}{uJ_p(u)} + n_{cl}^2\frac{K_p'(w)}{wK_p(w)}\right] = \frac{\beta^2}{k^2}\left(\frac{1}{u^2} + \frac{1}{w^2}\right)p^2, \tag{2.8}$$

where J_p and K_p are Bessel functions of the first and second kind, J_p' and K_p' are the derivatives of the associated Bessel functions, β is the propagation constant, u and w are the normalised transverse wavenumbers inside and outside of the fibre, respectively, and p is the azimuthal index. If we let $p = 0$ we obtain the TE and TM solutions by placing either the first or second term of the left-hand side of Eqn 2.8 equal to zero.

Being a transcendental equation, the solutions cannot be solved for without using a numerical method. By plotting the left-hand side versus the right-hand side of Eqn. 2.8 with the same x axis we can determine the points of intersection and, hence, the allowed values of β. Plotting the β values versus the V number, we arrive at the often used mode diagram.

2.1.3 Fibre Pulling

To produce MNFs, two basic elements are required. These elements are a heat source and a linear translation mechanism. The most rudimentary combination of these two objects can produce submicron fibres with varying degrees of success and quality. However, higher quality tapers are produced when cleanliness and precision in the fibre pulling process are taken into account.

In the early work reported in this thesis, we used an oxygen butane (oxybutane) flame, which is a perfectly adequate candidate for producing simple taper geometries. A combustion yield for such a flame of 100% can never fully be realised and this leads to some of the carbon in the butane gas not being converted into CO_2 and deposits on the surface of the fibre as soot. This can dramatically reduce the transmission of the MNF

as well as acting as a hot spot when light is passed through the fibre leading to possible breakages when in vacuum.

In more recent work we used a hydrogen and oxygen flame. This type of flame burns cleanly and is a better candidate for a fibre pulling rig. The reaction is

$$2H_2 + O_2 = 2H_2O + Energy. \tag{2.9}$$

In some cases, we can forgo flame sources for resistive heating elements. These are not a significant fire hazard and are arguably more reliable, provided regular calibration is performed on the system; the physical heat element degrades over time requiring higher currents to produce the same temperature. They are, however, more difficult to work with since the fibre must be passed through a small aperture in order to reach the hot zone near the heating element. The high voltages and currents required add to the danger of using such a system, but a carefully constructed enclosure and strict training before use can reduce the risk.

The size of the hot zone of a static heat-and-pull rig alters the final taper since it determines its length. However, the method of pulling also has a large influence on the fibre taper. Two linear translation stages pulling at a constant rate produce MNFs with exponential taper profiles [61]. If more complex taper profiles are required, a flame-brushing rig can be used. Here, a third stage is used to translate the flame allowing us to dynamically control the hot zone size leading to different taper profiles. This helps us to achieve highly adiabatic fibres, which are low loss and support higher order fibre modes. Alternatively, one can hold the flame still while superimposing an oscillating motion to the translating fibre stages. A 3D rendering of the hydrogen oxygen pulling rig currently used in our lab is given in Fig. 2.2.[1]

An in-depth review of this fibre pulling rig is given by Ward et al. [62]. Cleanliness is an important factor as it impacts the fibre quality as well as any post-processing of the

[1] This rig was developed over several years with many contributors. This rig was used for the majority of the work presented in Chapters 4, 5, and 6.

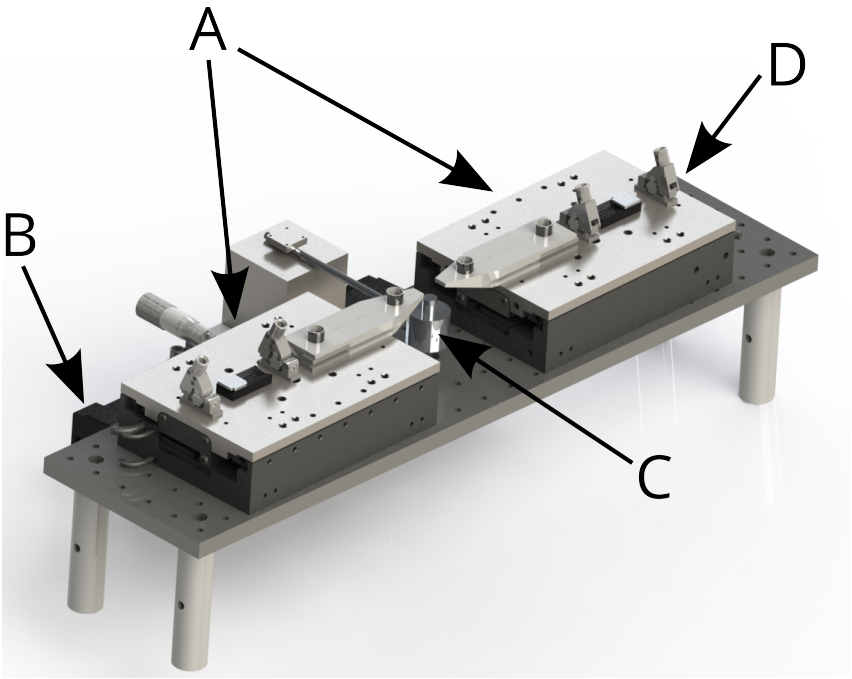

Figure 2.2: A hydrogen-oxygen fibre pulling rig. A) Primary pulling stages, B) Flame linear motorised stage [partially obscured], C) Flame nozzle, and D) Fibre clamps and V-grooves.

fibres. The most recent incarnation of the pulling rig was designed with cleanliness as the driving factor. A 24/7 flow box is used to keep the pulling rig enclosure free from dust and the entire room itself is kept clean through the use of air purifiers to collect dust.

2.2 Optical Forces

Describing the optical forces on a particle can be difficult. However, if we limit our scope to spherical particles, the problem is greatly simplified as we only need consider the particle's diameter. Hence, we can tailor our approach with respect to what is known as the size parameter, defined as $k_m d$, where

$$k_m = \frac{2\pi n_m}{\lambda_0}. \tag{2.10}$$

k_m is the light wavenumber in the medium, d is the diameter of the sphere, n_m is the refractive index of the surrounding medium, and λ_0 is the incident wavelength in vacuum.

This statement allows us to distinguish between three different regimes by altering our approach to the calculation of the optical forces according to the size parameter, defined as

$$k_m d \begin{cases} \gg 1 \\ \approx 1 \\ \ll 1 \end{cases} \tag{2.11}$$

For large particles it should be clear that a ray optics approach is sufficient to determine the optical forces; however, for particles with sizes close to and below the wavelength of light, different approaches are required.

2.2.1 Maxwell Stress Tensor

Rather than begin with a discussion on the optical forces where the approach is chosen based on the size of the particle in question, we instead begin with a discussion on the Maxwell stress tensor (MST) whose roots lie in classical electrodynamics without any size-dependant approximations which would limit its applicability. The interaction of charges and currents with electric fields is well understood and, beginning with the Lorentz equation we can perform some simple operations which result in the MST formalism. The MST formalism is a powerful tool which can also elucidate the interactions between light and matter. First, we consider the Lorentz equation, $\vec{F}_{Lor} = q(\vec{E} + \vec{v} \times \vec{B})$, for a particle of charge q, moving with a velocity $\vec{v}$, and transform this into an integral form to get

$$\frac{d}{dt}\vec{P}_{mech} = \int_V [\rho\vec{E} + \vec{j} \times \vec{B}]dV \tag{2.12}$$

where $d\vec{P}_{mech}/dt$ is the mechanical momentum, of the particles, ρ and $\vec{j}$ are the charge density and current contained in a volume V bounded by a surface S. Eliminating ρ and

$\vec{j}$ by applying Maxwell's relations (Eqn. 2.3) we obtain

$$\frac{d}{dt}\vec{P}_{mech} = \int_V \epsilon_0[(\nabla \cdot \vec{E})\vec{E} + \vec{B} \times \frac{\delta \vec{E}}{\delta t} - c^2\vec{B} \times (\nabla \times \vec{B})]dV \tag{2.13}$$

where c is the speed of light in vacuum. Using various trigonometric identities and appropriate substitutions we reach an explicit form for the conservation of total linear momentum, $\frac{d}{dt}(\vec{P}_{mech} + \vec{P}_{field})$

$$\frac{d}{dt}(\vec{P}_{mech} + \vec{P}_{field}) = \int_V (\nabla \cdot T_M)dV \tag{2.14}$$

with $T_M = \epsilon_0[\vec{E} \otimes \vec{E} + c^2\vec{B} \otimes \vec{B} - \frac{1}{2}(\vec{E} \cdot \vec{E} + c^2\vec{B} \cdot \vec{B})]$ where $\otimes$ is the tensor, or dyadic, product and T_M is the Maxwell stress tensor (MST). We have, of course, skipped a number of steps in this derivation, the most notable of which is where we define a field momentum, $\vec{P}_{field}$, related to the Poynting vector. Here, $\vec{P}_{field}$ refers to a component of the force which is a time derivative of the linear momentum density over the volume in question which appears on the right hand side of Eqn. 2.13 once ρ and $\vec{j}$ have been substituted for using Maxwell's equations. $\vec{P}_{field}$ can be see as the portion of the momentum which is contained within the electromagnetic fields themselves. In electrostatics this is zero since $\vec{B} = 0$, but for more interesting systems it is non-zero. Using Gauss' theorem, we can convert the volume integral in Eqn. 2.14 to a surface integral and we finally arrive at the more approachable expression

$$\frac{d}{dt}(\vec{P}_{mech} + \vec{P}_{field}) = \oint_S (T_M \cdot \hat{n})dS. \tag{2.15}$$

By taking the time average of Eqns. 2.15 and 2.14, we obtain the average force on a particle, given by

$$\left\langle \vec{F} \right\rangle = \oint_S (\langle T_M \rangle \cdot \hat{n})dS = \int_V (\nabla \cdot \langle T_M \rangle)dV \tag{2.16}$$

where the brackets $\langle\rangle$ denote the time average of the enclosed quantity. Here, we have the

MST formalism for determining the force on a particle. We can see from Eqn. 2.16 that the MST can be viewed as a form of momentum flux density. A field with no momentum flux will consequently experience no force. For a monochromatic plane this results in a force in only one direction due to the nature of the surface integral. The MST method is extremely useful in calculations but, perhaps, a more intuitive picture of the forces at play can be gleaned from an examination of those forces in the dipole approximation regime.

2.2.2 Dipole Approximation

The dipole approximation, i.e. the assumption that a field remains approximately constant across a particle at any moment in time, is equivalent to assuming that the particle size is significantly smaller than the wavelength of the incident light field (in the medium). This assumption is used extensively in many branches of physics. Here, we use it to help simplify the problem of optical trapping.

A dielectric particle which has a radius that is much smaller than the wavelength of the incident field has an induced dipole, $\vec{p} = \alpha\vec{E}(\vec{r})$, where α is the polarisability given by

$$\alpha = \frac{\alpha_0}{1 - i\alpha_0 k_0^3/(6\pi\epsilon_0)}, \tag{2.17}$$

with $\alpha_0 = 4\pi\epsilon_0 a^3(\epsilon - 1)/(\epsilon + 2)$. ϵ is the dielectric constant of the material and a is the radius of the particle. We include the radiation reaction correction, which takes into account the finite size of the dipole and α_0 is the Clausius-Mosotti polarisability in the absence of any radiation reaction corrections [139].

From classical electrodynamics, we know the force on a single dipole in an external field is $F = \vec{p}.\nabla\vec{E}$; we can therefore represent our time-averaged force as

$$\langle F(\vec{r})\rangle = \frac{1}{2}Re\left\{\sum_i p_i \nabla E_i^*(\vec{r})\right\} = \frac{1}{2}Re\left\{\sum_i \alpha E_i(\vec{r})\nabla E_i^*(\vec{r})\right\}. \tag{2.18}$$

Using Eqn. 2.3, along with the identities:

$$\begin{aligned} \sum_i E_i \nabla E_i^* &= (\vec{E}\cdot\nabla)\vec{E}^* + \vec{E}\times(\nabla\times\vec{E}^*), \\ -2iIm\{(\vec{E}^*\cdot\nabla)\} &= (\vec{E}\cdot\nabla)\vec{E}^* - (\vec{E}^*\cdot\nabla)\vec{E}, \end{aligned} \tag{2.19}$$

we transform Eqn. 2.18 to

$$\langle F\rangle = Re(\alpha)\{\nabla\frac{1}{4}\left|\vec{E}^2\right|\} + \sigma\{\frac{1}{c}\left\langle\vec{S}\right\rangle\} + \sigma c\nabla\times(\frac{\epsilon_0}{4\omega i}\vec{E}\times\vec{E}^*) \tag{2.20}$$

where σ is the definition for the total cross-section of the particle $k_0 Im(\alpha)/\epsilon_0$. Here, we can see three distinct components which contribute to the force. The first term on the right-hand side of Eqn. 2.20 corresponds to the gradient force since it is proportional to the electric field gradient. This is often the limiting term in optical systems. The second term is the familiar scattering force, which is proportional to the Poynting vector. The last term is a spin-curl force, which is often zero since excitation from single plane wave sources would cause the term to be identically zero. A non-homogeneous polarisation field would be required to produce force and, in these cases, the forces can often be negligible [29].

2.2.3 Mie Scattering

For particles with sizes approximately equal to the wavelength of light the simple dipole approximation begins to break down, although a distributed dipole approximation can still give excellent results provided some care is taken when choosing the appropriate element size for the individual dipoles [140].

To solve for the internal and external fields of a dielectric sphere in an external electric field we can once again fall back on the Helmholtz equation (Eqn. 2.6). When solving the Helmholtz equation for a cylindrical geometry we had the liberty of assuming a simple

form for the E_z components of the electric field because of the longitudinal invariance. For a sphere, however, this is not so simple. To reduce the associated Helmholtz equation to a more tractable form we can use intermediate vector functions as follows

$$\begin{aligned} \vec{L} &= \nabla\psi_{l,m} \\ \vec{M}_{l,m} &= \nabla \times \vec{c}\psi_{l,m} \\ \vec{N}_{l,m} &= \frac{1}{k_m}\nabla \times \vec{M_{l,m}} \end{aligned} \tag{2.21}$$

where $\vec{c}$ is some constant vector, $\psi_{l,m}$ is a scalar function, and k_m is the wave number in the surrounding medium. We can show that $\psi_{l,m}$ is also a solution to the wave equation via direct substitution into $\nabla^2\psi_{l,m} + k_m^2\psi_{l,m} = 0$. $\vec{M}_{l,m}$ and $\vec{N}_{l,m}$ are solenoidal vector functions which are analogous to the relationship between the $\vec{E}$ and $\vec{H}$ fields. $\vec{L}$, however, can be neglected as it represents a purely longitudinal solution.

By using this Helmholtz decomposition, we reduce the problem to a simpler, scalar problem which we can solve by using the separation of variables technique. The solution of this problem is somewhat lengthy and has been reproduced numerous times in textbooks so only the important results are included here, see Appendix A for a more complete solution.

The angular portion of the solution to the Helmholtz equation can be given in terms of spherical harmonics. These spherical harmonic functions contain the associated Legendre functions, which depend on integer numbers l and m. The radial portion has two linearly independent solution sets which are expansions of Bessel or Hankel functions. The asymptotic behaviour of these functions is significantly different and must be chosen appropriately, i.e. singularities are not allowed at the origin and the field must be zero at infinity.

The solution to the Helmholtz equation is, therefore, a multipole expansion. The

scattered field, $\vec{E}_s$, from a sphere of radius, a, can be expanded as

$$\vec{E}_s(r,\hat{r}) = E_i \sum_{l=0}^{\infty} \sum_{m=-l}^{m=l} A^{(1)}_{s,lm} \vec{H}^{(1)}_{lm}(k_m r, \hat{r} + A^{(2)}_{s,lm} \vec{H}^{(2)}_{lm}(k_m r, \hat{r})), \tag{2.22}$$

where E_i is the incident E-field, $A_{s,lm}$ are the associated amplitudes, and $H_{lm}(k_m r, \hat{r})$ are the **H** multipoles, which correspond to the radial solutions satisfying the radiation conditions at infinity. By taking boundary conditions regarding the continuity of various components of the field into consideration this equation can be solved completely to give the scattered fields of a spherical object under plane-wave illumination.

The multipole form of this equation helps us to understand the shift between the dipole approximation and Mie theory. For small particle sizes, only the lowest pole of the expansion contributes significantly, which reproduces a dipole-like scattering profile, as shown in Fig. 2.3. As we increase the particle size (or rather the size parameter, $k_m a$) we see the asymmetry of the scattering increase as more and more forward scattering dominates. Here, the higher order poles can no longer be ignored. In practice, it is necessary to truncate the infinite sequence at some value of l, as determined by the Wiscombe criteria [141, 142]. The Wiscombe criteria looks at the extinction coefficient and defines a minimum threshold value for when the higher order components become negligible. Choosing a suitable value for this threshold yields the following formula which can be used to truncate the sequence at an order N. $N = x + 4.05x61/3 + 2$, where x is the ratio of the particle's circumference to the incident wavelength with the given constraint that, $8 < x < 4200$. A complete discussion of these problem is given in [142].

2.2.4 Minkowski Force Density

The force on an object can be determined by a surface integral of the Maxwell stress tensor given by Eqn. 2.16. However, this is sometimes a problematic quantity to determine. The Maxwell stress tensor can be interpreted as a momentum flux density which is present not only on a particle in a field, but also in the medium of the field. If one considers

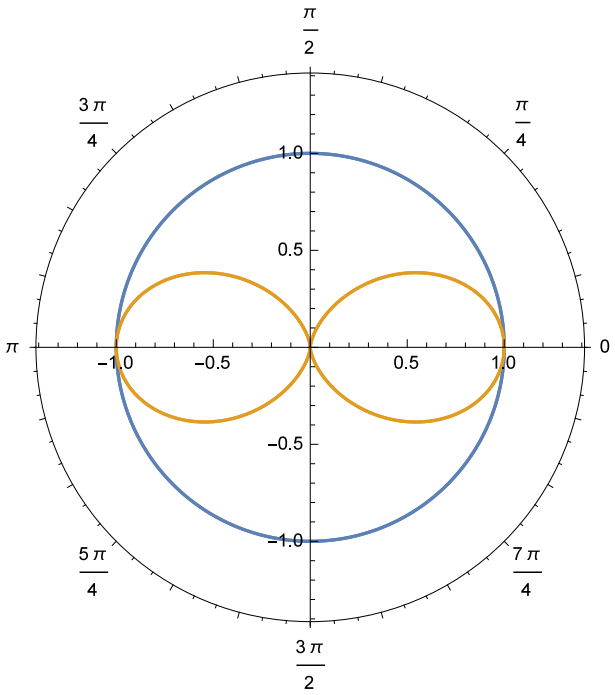

Figure 2.3: A polar plot of the intensity of the scattering from a dipole. The blue line indicates light polarised perpendicularly to the dipole's axis and orange line is light polarised parallel to the dipole's axis.

the no-slip boundary condition from fluid dynamics, it is apparent that a force applied to the fluid near a particle is also transferred to the particle. Often, researchers avoid this problem by integrating over a sphere slightly larger than the particle. For example, Yang et al. [51] used an integration volume which was always 120% larger than the target sphere to produce consistent force results. Finite element method (FEM) force analyses are often performed in such a way.

Alternatively, the Minkowski force-density approach can be used. A full derivation of the force-density along with some interesting comparison with Abraham's approach is provided by Mansuripur [143]. The force-density, $\vec{F}_M$, can be written as

$$\vec{F}_M(\vec{r},t) = \rho_{free}\vec{E} + \vec{J}_{free} \times \vec{B} - 1/2[\epsilon_0(\nabla\epsilon)(\vec{E}\cdot\vec{E}) - \mu_0(\nabla\mu)(\vec{H}\cdot\vec{H})] \tag{2.23}$$

where ρ_{free} and $\vec{J}_{free}$ correspond to the free charge and current, respectively. This formal-

ism can be used to determine the force on a particle in a field. The first two components of the right-hand side of this equation should be familiar as they represent the Lorentz force. Often we deal with situations where there are no free charges or current densities, but there are still forces present. With the Minkowski force-density we see that applying these conditions reduces the complexity of Eqn. 2.23, but does not eliminate all sources of force. Unlike the Maxwell stress tensor approach, where the forces are applied through a momentum flux density, here the origin of the forces due to spatial discontinuities in the electric permittivity or magnetic permeability can be visualised. By inspection of Eqn. 2.23, it is clear that only areas where these quantities vary contribute to the total force. Typically, this corresponds to boundaries between materials with different properties. Changing the contrast between the object's permittivity and the surrounding medium's permittivity can easily cause a change in the sign of the force. By integrating over an area of interest which fully encapsulates the object to be analysed, the force exerted by the field on the object can be unambiguously determined without having to control for the integration volume in a careful and consistent way between models. This method was employed in Chapter 5 to determine the forces on trapped particles.

2.3 Atom Trapping

The laser cooling and trapping of neutral atoms is a highly popular field with countless books and articles written on the topic [144, 145]. The description of laser cooling is also a highly complex subject, since it can be approached using a variety of approximations and simplifications. In the work reported in this thesis the ^{85}Rb isotope is used in the experimental work while ^{87}Rb was used in the theoretical work to reflect the species currently used in our group's cold atom experiments. Fundamentally, the cooling of atoms is mediated by momentum transfer with photons from a laser source. Rather than go through a rigid derivation of the theory of atom cooling, the important points required to describe the work in this thesis are highlighted. Experimental and theoretical work on

this subject is given in Chapters 3 and 4.

The cooling of an atom is a recoil process whereby an atom moving at a high velocity has its speed along an axis reduced by bombarding it with photons moving in the opposite direction along the same axis. The recoil generated by a great number of these collisions reduces the velocity and, hence, the temperature, of an atom. One can imagine slowing a bowling bowl as it moves towards you by repeatedly pelting it with a steady stream of tennis balls. To effectively cool an atom, this must be performed in three dimensions, or along six axes; a single beam would eventually push an atom moving towards it along the direction of the photon flux. Other considerations such as Doppler cooling, requiring that a velocity-dependent force be engineered, and magnetic trapping are also necessary for an effective laser cooling setup.

2.3.1 Energy Levels in ^{85}Rb

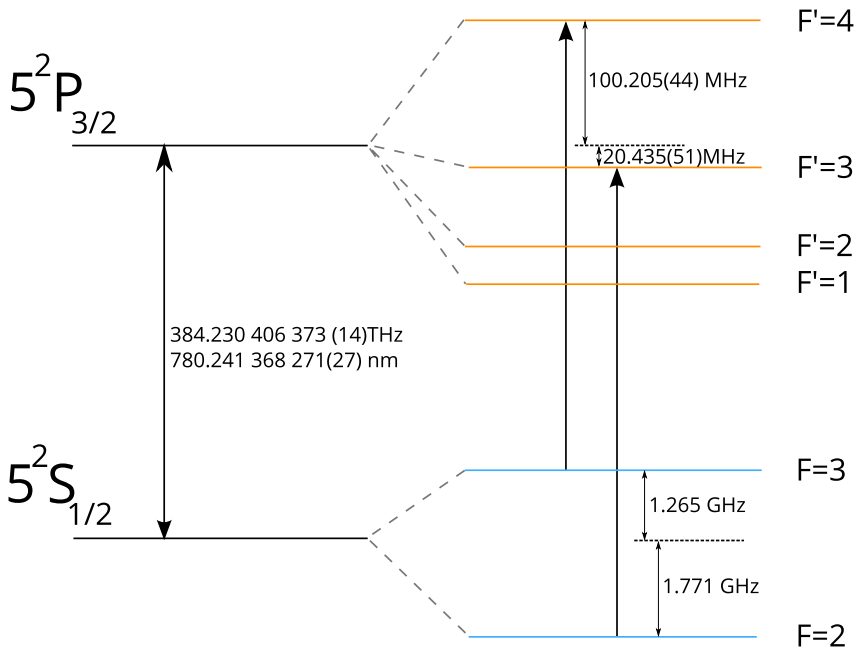

Figure 2.4: Energy level diagram for the D_2 transitions in ^{85}Rb.

To understand this process, we must first look at the energy levels and hyperfine splittings — we will consider ^{85}Rb as an example. Rubidium has a large number of available

energy levels, but for atomic cooling we only require a transition which is recyclable – that is to say that an atom can be excited and re-excited along a closed loop with little loss to other energy levels. Such a perfect cycle does not exist, but the D_2 transitions in ^{85}Rb closely approximate this, only requiring that a secondary repump laser be used to return the "lost" atoms to the correct ground state. The ground level, $5^2S_{1/2}$, has a total angular momentum of $\mathbf{J}$=1/2 while the excited level, $5^2P_{3/2}$, has a total angular momentum of 3/2. Interactions between the total angular momentum, $\mathbf{J}$, and the nuclear angular momentum, $\mathbf{I}$, (equal to 5/2 for the ^{85}Rb ground state) result in hyperfine energy level splittings. The total atomic angular momentum $\mathbf{F} = \mathbf{J} + \mathbf{I}$ has allowed values of F which range from $|J - I| \leq F \leq J + I$. The resulting energy level diagram for the hyperfine splitting known as the D_2 transition is given in Fig. 2.4.

Despite the rather large energy gap between the $5^2P_{3/2}$ and $5^2S_{1/2}$ levels, we can see from Fig. 2.4 that the separation of the F levels in the upper transition is only $\approx$ 120 MHz. To specifically target such an energy level without exciting neighbouring levels requires a narrow linewidth laser. Extended cavity diode lasers are typically used in such experiments due to their reduced linewidth.

Each of the hyperfine energy levels, F, has $2F + 1$ degenerate magnetic sublevels, identified by the quantum numbers $m_{g.e}$, where m_g is for ground state levels and m_e is for excited state levels. . In the presence of a magnetic field, the Zeeman effect causes these levels to split providing us with more energy levels to target, each with a specific set of requirements. This effect is exploited to provide a position-dependent force through the use of polarisation preparation in the cooling laser beams.

2.3.2 Cooling and Trapping

The effective cooling and trapping of neutral atoms requires a trap that is sensitive to changes in both velocity and position. It is necessary that atoms moving towards the laser beam be affected more strongly than atoms moving away from the beam. By detuning the cooling laser beams by an amount dictated by the Doppler shift of a moving atom ($-\vec{k}.\vec{v}$

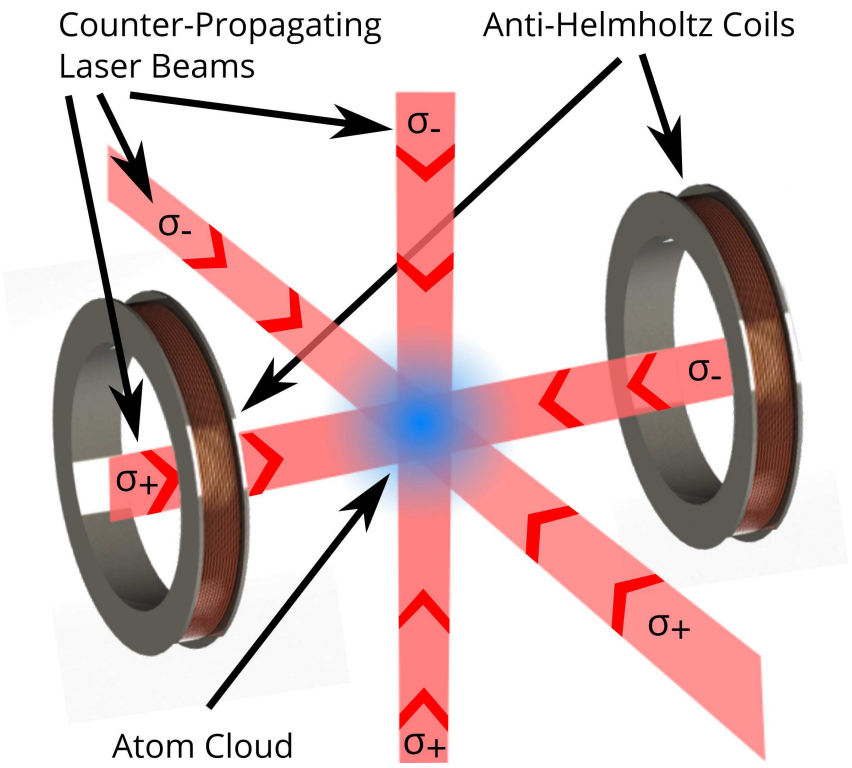

Figure 2.5: A simplified optical molasses setup combining anti-Helmholtz coils and three counter-propagating laser beams with opposite polarisations used to cool neutral atoms.

where $\vec{k}$ is the wave vector of the laser and $\vec{v}$ is the velocity of the atom) we can produce a three dimensional cooling scheme. A simplified optical molasses diagram is given in Fig. 2.5. Atoms moving towards a red-detuned beam feel a stronger force as they will be closer to the resonance condition than atoms moving away from the beam. Since the velocity distribution is Maxwellian this proves to be an effective technique. A magnetic quadrupole field can be used to induce a Zeeman shift in the energy levels which, due to selection rules, produces additional sublevels. If we assume an atom with $F = 0$ ground state and $F' = 1$ excited state, these three hyperfine sublevels ($m_e = -1, 0, 1$) are only accessible to light of a particular polarisation, namely σ^-, π, and σ^+. A diagram showing the Zeeman energy level splitting versus atom position in a quadrupole field (along z) is shown in Fig. 2.6.

For two beams of σ^+ and σ^- polarised light, with frequencies of ω_L, red-detuned from the $|m_e\rangle = |0\rangle$ hyperfine state by an amount δ, a position dependent magnetic field can

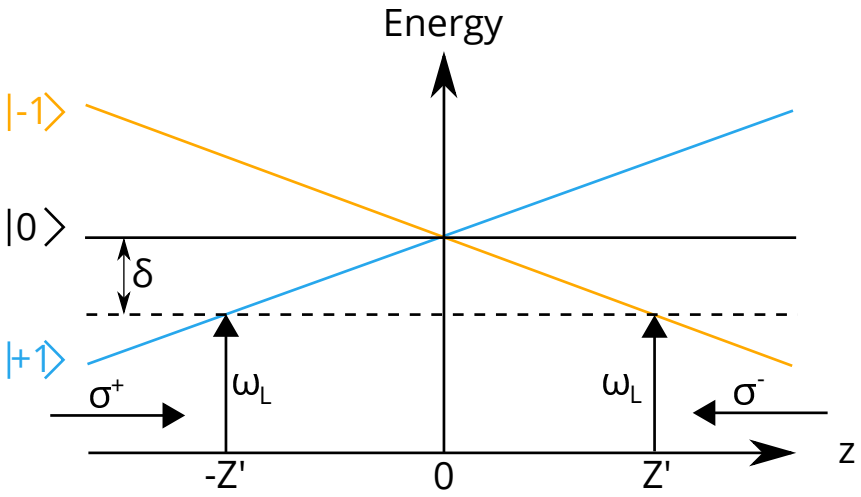

Figure 2.6: Diagram showing the positional dependence of the energy of the three hyperfine states $|m_e\rangle = |-1\rangle, |0\rangle, |1\rangle$. The individual states can then be targeted spatially using beams of the appropriate polarisation and wavelength.

produce a position dependent shift in the hyperfine energy levels, see Fig. 2.6. This shift allows us to target specific transitions depending on the distance from the centre of the quadrupole field. For example, a σ^+ beam propagating in the positive z direction has an on-resonance condition for atoms located at a position of $-Z'$ but is largely off resonance for positions much greater or lower than this. This allows for excitation from the $|m_g\rangle = 0$ state to $|m_e\rangle = 1$ state, and atoms are thereby pushed towards the centre of the trap. Similarly a beam with polarisation σ^- travelling in the negative z direction is on-resonance with atoms located at Z'. This, combined with the velocity-dependent force present due to the Doppler shift, provides us with an adequate cooling and trapping scheme for neutral atoms. This cooling mechanism is further enhanced by the addition of Sisyphus cooling to produce sub-Doppler cooling through the use of polarisation gradients. The laser cooling and trapping of ^{85}Rb is presented in Chapter 4, while ^{87}Rb is used in Chapter 5.

2.4 Plasmonic Enhancement

Another approach to produce optical traps for particles below the Rayleigh limit is that of plasmonics. As discussed in the Introduction, plasmons can be broadly categorised into two types: surface plasmon polaritons (SPP) and localised surface plasmon resonances (LSPR). The description of the plasmon varies largely due to the geometry of the system in question. Here, we shall only discuss LSPRs, since they are an appropriate choice for integration with an ultrathin fibre. There are a number of theoretical approaches to LSPRs. For simplicity, the case of a spherical metallic object will be discussed here. As we shall see the problem is directly related to the scattering problem discussed in Section 2.2 with regards to spheres of different sizes and when it is appropriate to use a dipole approximation. There are two approaches to the problem; a simpler quasi-static approach that we shall discuss here, and the more involved Mie scattering problem for a metallic sphere.

2.4.1 Quasi-static Approximation

In the quasi-static approximation, we look at the interaction of particles with dimensions much smaller than the wavelength of light in the surrounding medium. In this regime we can treat the phase as being approximately constant over the particle volume and merely add the harmonic time dependence later. For a homogeneous, isotropic sphere of radius, a, in a uniform electric field, $\vec{E} = E_0\hat{z}$, we can approach the system as a simple electrostatics problem, see Fig. 2.7 . For a charge free system we know that the solution to the problem must be a solution of the Laplace equation, $\nabla^2\Phi = 0$.

Due to the azimuthal symmetry of the problem, the solutions are expansions of the well-known Legendre polynomials. The general solution is given as:

$$\Phi(r,\theta) = \sum_{l=0}^{\infty}[A_l r^l + B_l r^{-l+1}]P_l(cos(\theta)) \tag{2.24}$$

where P_l are the Legendre polynomials of order l and θ is the angle between the line OP

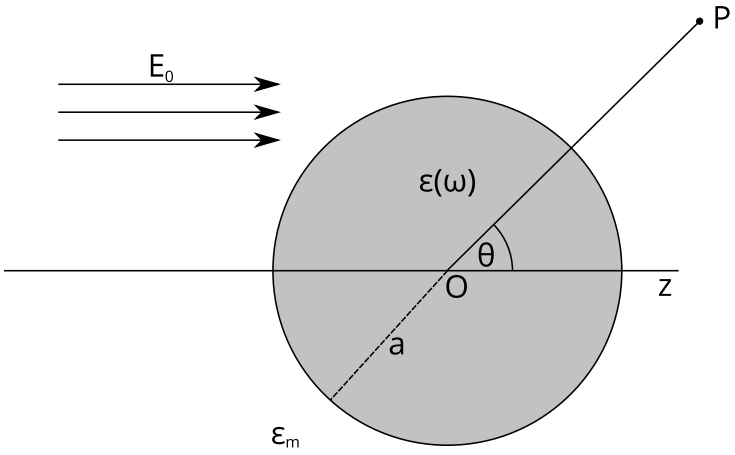

Figure 2.7: Homogeneous sphere of radius a and dielectric constant $\epsilon(\omega)$ in an electrostatic field. The surrounding medium has a dielectric constant of ϵ_m. The origin is at O.

and the z-axis in Fig. 2.7. The internal and external fields have different forms due to the requirement of finite potentials at the origin. Using boundary conditions of the tangential and normal components of the field allows us to come to the following solutions for the internal, Φ_{int}, and external, Φ_{ext}, potentials [146]

$$\begin{aligned}\Phi_{int} &= -\frac{3\epsilon_m}{\epsilon + 2\epsilon_m} E_0 r cos(\theta), \\ \Phi_{ext} &= -E_0 r cos(\theta) + \frac{\epsilon - \epsilon_m}{\epsilon + 2\epsilon_m} E_0 a^3 \frac{cos(\theta)}{r^2}.\end{aligned} \tag{2.25}$$

In the external field we see the appearance of a term, $(\epsilon - \epsilon_m)/(\epsilon + 2\epsilon_m)$, which is related to the polarisability, α, of the particle if we rewrite Φ_{ext} from Eqn. 2.25 as

$$\Phi_{ext} = -E_0 r cos(\theta) + \frac{\vec{p}.\vec{r}}{4\pi\epsilon_0\epsilon_r r^3}, \tag{2.26}$$

with $\vec{p} = 4\pi\epsilon_0\epsilon_m a^3[\epsilon - \epsilon_m/\epsilon + 2\epsilon_m]E_0 = \alpha E_0$. Importantly, for particles with a function of $Re[\epsilon(\omega)]$ that crosses zero for some frequency, ω, it is possible to introduce a resonant enhancement. This condition is known as the Frölich condition where $Re[\epsilon(\omega)] = -2\epsilon_m$ [146]. This may seem like a singularity, but there is always a non-vanishing imaginary

component to balance the field. Both the external and internal fields experience a resonant enhancement for this condition. For extremely small particles, the quasi-static approximation is indeed valid. Further analysis of the dipole as an oscillating dipole can improve the model. However, for larger particles it should be obvious that the static solution cannot be true. In this situation a more complete solution must be found. The problem as laid out is little more than a scattering problem. Hence, it can be approached in exactly the same fashion as for the scattering problem in Section 2.2.3 for intermediate sized particles. In this thesis work we do not deal with large plasmonic devices and a description of this approach is, therefore, not required.

2.4.2 The Dipole Hybridization Model

The resonances of localised plasmons can be shifted by altering the shape and size of the particle, and through the electromagnetic interactions of the localised modes of multiple plasmonic particles. This can only occur when the particles are close enough to each other to interact. To help simplify this interaction and provide a working "intuitive" model the dipole hybridization model was created [147]. The authors showed how a simple dimer consisting of two plasmonic spheres could be easily modelled in such a way, with the plasmon energies decreasing with decreasing values of the separation between the spheres. By modelling the electrons as a charged incompressible liquid sitting on the surface of a sphere, they were able to determine a surface charge for the system and by including the dipole approximation an expression for the interaction energy was found.

This result can be simplified in light of other known systems. When dipoles are placed side-by-side they interact and shifts in their energy levels are observed depending on how the dipoles are oriented [148]. If we accept that, for particular situations LSPRs behave like dipoles, this model is valid. At extremely close distances this approximation breaks down, and the shifts become stronger and vary faster than the $1/D^3$ change in the interaction energy predicted by classical theory would account for, where D is the separation distance of dimer pair. This change is well-described in the full hybridization

model outlined by Nordlander et al. [147]. The additional changes at small distances were contributed to anti-symmetric splitting of the plasmons attributed to interactions of the lower and higher order plasmon modes between the two structures, which have an interaction involving higher orders of $1/D$. When particles are closely spaced the near-field interactions strongly affect the resonance wavelength. This is only significant for spacings much less than the wavelength. Other analogies can be drawn between the dipole hybridization model and molecular orbit theory [147]. This model is important in virtually all dimer systems since the spacing for plasmonic dimers is typically chosen to be of the scale of a few tens of nm, providing enhancements in the form of gap plasmons. The exact details of this interaction are not hugely important for the work presented in this thesis, but their existence needed to be addressed since we discuss a gold dimer system in Chapter 6.

2.5 Conclusions

Here, we have outlined the theory required to understand the optical near-fields of ultrathin fibres and plasmonic devices, as well as discussing the problems of atom and particle trapping. It is important to cover the basics of how the modes propagate in an ultrathin fibre as an understanding of this helps one to visualise how an ultrathin fibre could be used in an experimental setting as an active and passive probe, as well as allowing us to understand how one could modify a fibre to enhance the fields. We also discuss two types of trapping, namely atom and particle trapping. Although we do not discuss it explicitly here, there are many similarities between these two types of trapping. If we approach atom trapping using the simple two-level atom model, we can treat the perturbation to the Hamiltonian as the energy of a dipole in an electric field, which is the same approximation used in particle trapping, provided the particle is sufficiently small. Further parallels can be drawn if one considers small metallic particles, such as silver nanoparticles, where their narrow surface plasmon resonances allows one to tune the real

part of their polarizibilities between positive and negative values thus changing the sign of the optical force. This is somehow analogous to how the sign of the force on an atom can be altered by changing the wavelength of the incident light due to the Stark effect. Finally, we introduced the concept of plasmonic enhancement in the form of a localised surface plasmon resonance. It can be easily understood in the quasi-static approximation, and from there it is not too much of a stretch to imagine the process as a Mie scattering process, very similar to that outlined in Section 2.2.3.

Chapter 3 will draw heavily on the theory outlined in Sections 2.1 and 2.3 while also introducing a few core concepts of atom cooling that are also required to understand the experiment in that chapter.

Chapter 3

Forced Oscillation Temperature Measurement Using an Ultrathin Fibre [1]

An early topic studied in this PhD work was that of a laser cooling-experiment which incorporated an ultrathin optical fibre into a cloud of cold ^{85}Rb atoms. For any experiment in cold atoms, temperature is an essential parameter which must be measured. Thermodynamically, we see the effects of temperature most commonly through the use of partition functions, which quickly allow us to see the relationship between temperature and energy. Since the first magneto-optical trap (MOT) was reported by Raab et al. [149] there have been many proposals for experimentally measuring the average temperature of an atom cloud, although the description of temperature in an atomic ensemble can be somewhat tricky to define. Here, we shall consider the temperature of a cold atom cloud to be related to the average kinetic energy of the atomic system, invoking the idea that

[1] This work led to a publication: Russell, L., Deasy, K., Daly, M. J., Morrissey, M. J. & Nic Chormaic, S. Sub-doppler temperature measurements of laser-cooled atoms using optical nano-fibres. Measurement Science and Technology 23, 015201 (2012). M. Daly contributed throughout the experiment and some of the data analysis. The development of the timing scheme described in this chapter was the sole work of M. Daly. The work was conducted in UCC-Tyndall National Institute, Ireland.

temperature and energy are related, through the standard formalism

$$\frac{1}{2}k_{\mathrm{B}}T = \langle E_k \rangle \,, \tag{3.1}$$

where k_{B} is the Boltzmann constant, T is the temperature in Kelvin, and $\langle E_k \rangle$ is the ensemble-averaged kinetic energy. This may be recognised as an application of the equipartition theorem. To apply this theorem to a cloud of cold atoms, we need only demand that our velocity distribution is well-defined and we assume a Maxwell-Boltzmann distribution.

If we consider the natural linewidth of the atomic transition in question, we can equate the associated energy to the thermal energy and arrive at the Doppler-limited temperature, T_D,

$$T_D = \frac{\hbar\gamma}{2k_{\mathrm{B}}} \tag{3.2}$$

where γ is the natural linewidth of the excited state under consideration and k_{B} is the Boltzmann constant. For ^{85}Rb atoms with γ=2 $\pi\times$ 6.0666(18) MHz, this corresponds to a temperature of approximately 143 μK.

One of the earlier techniques used to measure the average temperature of decelerated atoms was based on the velocity distribution using a thin probe beam propagating at a small angle to the atomic beam [150]. The frequency of the probe beam was slowly scanned over the atomic transitions and the absorption is directly related to the velocity distribution of the atoms. Hence, the average temperature of the atoms in the atomic beam could be measured. This is a precursor to what would later be called the time-of-flight technique, outlined in the following section. This method is limited by the natural linewidth of the excited state, so alternative methods were sought to improve the resolution.

3.1 Alternative Measurement Techniques

Many temperature measurement techniques have been proposed for cold atomic systems to overcome the limits of the time-of-flight measurement. Their merits and demerits are briefly discussed here. Ideally, a temperature measurement should be high resolution, low error, non-destructive, and minimally invasive. However, an ideal method with all of these requirements is difficult to obtain.

3.1.1 Time-of-Flight

The time-of-flight measurement (TOF) was first introduced in the context of measuring sub-Doppler temperatures once it was realised that a simple two-level approach to the problem of laser cooling was insufficient to fully describe the system. When one compares the light-induced energy shifts ($\approx$ GHz) to the Zeeman induced energy shifts ($\approx$ 100 MHz), it is clear that the light shifts can be significantly larger, unless one adheres strictly to the low intensity limit which leads us to the conclusion that a sub-Doppler theory relying wholly on the Zeeman shifts is an inappropriate approach. To investigate this effect, the temperature of the cloud which can be related to its effective spring constant, should be measured with higher resolution. The TOF measurement, simply put, is a ballistic measurement where a probe beam is placed at different distances from the cloud centre and the absorption of the beam is measured over time once the MOT cloud is switched off. This is somewhat different to the initial measurements made by Molenaar et al. [151] where an alkali-metal atom beam was investigated, but the principle is the same. The measurement can be done under gravity, where atoms simply "fall" from the trap, or in a fountain-type setup where the probe is placed above the atom cloud and the maximum height that the atoms are able to achieve, given their initial velocity distribution, is measured. In either case, the measurement is destructive, leading to a loss of the initial atom cloud.

3.1.2 Release and Recapture

The release-and-recapture method was first used by Chu et al. in their study of Doppler cooling in an optical molasses setup [152]. The technique itself is conceptually simple. Once a fully formed atom cloud has been achieved, both the quadrupole magnetic field and the cooling lasers are switched off momentarily to allow the cloud to ballistically expand. After a predetermined period of time, typically of the order of a few milliseconds, the magnetic fields and lasers are switched back on. By monitoring the atomic fluorescence, which is an indication of the atom number, the change in atomic density and number can be determined and, hence, used to estimate the temperature of the cloud. Once again, it is the Maxwellian nature of the atoms' velocity distributions which makes this measurement possible. Like all atomic measurements, the timing of the experiment is crucial. The termination of the quadrupole field is also nontrivial due to the inductive currents in the coils as the fields are shut off. The release-and-recapture method has also been performed using an optical nanofibre to provide a sensitive measurement of the temperature gradient of the cloud as well as providing information about the alignment of the system [153].

3.1.3 Forced Oscillation Method

In the work reported in this thesis, we used a variant of the forced oscillation method introduced by Steane and Foot in 1991 [154]. To understand this method we must consider the forces present on an individual atom. For a single atom in the presence of a laser beam, the optical Bloch equations can be solved to give a scattering rate, γ_p, using a Rabi two-level system. This is reasonable representation of a ^{85}Rb atom for our purposes [151]. Here, we have

$$\gamma_p = \frac{s_0\gamma/2}{1 + s_0 + (2\delta/\gamma)^2}, \tag{3.3}$$

where γ is the decay rate of the excited state and $s_0 = I/I_s$ is the saturation parameter,

i.e. the ratio of the cooling beam's intensity to the saturation intensity. The saturation intensity is the intensity of light at which the population of atoms in the ground state is three times the number in the excited state. Exceeding this value by a few times the saturation intensity would saturate the transition quickly and only result in power broadening. It is interesting to note that, at higher values of the saturation parameter, $\gamma_p \gg 1 + [2\delta/\gamma]^2$, the scattering rate becomes equal to $\gamma/2$, therefore it is prudent to keep this in mind when performing experiments to prevent saturation. Well above saturation we can expect the system to reach an equilibrium where the ground and excited states have the same population since the scattering interactions would dominate. Since the excited state has a decay rate equal to $\gamma/2$, it only makes sense that the scattering rate would have to be equal to this value at high intensities.

We can include the Zeeman and Doppler effects into the detuning term, δ. Note that we are still excluding effects from the optical light shifts. In this case, the detuning can now be written as $\delta_\pm$, depending on the orientation of the incident beam, and it is given by

$$\delta_\pm = \delta \pm \vec{k} \cdot \vec{v} \pm \frac{\mu' B}{\hbar}. \tag{3.4}$$

Here, δ is the physical detuning of the beam, $\vec{k}.\vec{v}$ is the Doppler shift term, and $\mu' B/\hbar$ is the Zeeman shift term. Here, μ is the magnetic moment of the atom and B is the magnetic field strength. Since the force on an atom is related to how it scatters a photon, Eqn. 3.4 can be combined with Eqn. 3.3 to produce a new expression for the optical forces in the low-intensity regime. Here, we simply multiply the scattering rate by the momentum of a single photon to give a force expression, $\vec{F}_\pm$, of

$$\begin{aligned} \vec{F_\pm} &= \pm \frac{\hbar \vec{k} \gamma}{2} \frac{s_0}{1 + s_0 + [2(\delta \pm \vec{k} \cdot \vec{v} \pm \mu' B/\hbar)/\gamma]^2}, \\ \vec{F}_{om} &\approx \frac{8\hbar k^2 \delta s_0 \vec{v}}{\delta(1 + s_0 + [2\delta/\gamma]^2)} \equiv -\beta \vec{v} \end{aligned}, \tag{3.5}$$

where $\vec{F}_{om}$ is the sum of the forces from the counter-propagating optical beams, $\vec{F}_+$ and $\vec{F}_-$, corresponding to light travelling in the positive and negative directions respectively. We have neglected terms of the order $(kv/\gamma)^4$ in the expansion which leads to a velocity-dependent damping force. This velocity dependent force can be combined with the spatially varying force due to the linearly varying magnetic field near the trap centre, introduced by the anti-Helmholtz coils to be discussed in Section 3.2, to produce the familiar damped harmonic oscillator equation (in one dimension). The magnitude of the total force, F, can be then written as

$$F = -\kappa x - \beta v_x, \tag{3.6}$$

with $\kappa = \frac{\mu' A}{\hbar k \beta}$, where A is the gradient of the magnetic field which we assumed to be linear within the confines of the magneto-optical trap. There are, of course, stochastic heating effects present which contribute additional forces to our system but time-averaging effectively removes them; hence, we will ignore stochastic effects throughout our calculations. κ can be viewed as the spring constant of the system.

Steane and Foot [154] showed how a laser beam can be used to temporarily shift the trap centre. By measuring the time it takes for such an overdamped system to return to equilibrium, they were able to determine the spring constant and compare the values to the theoretically determined values in the absence of any correction terms. For lower detunings the effect is not appreciable, but, at large detunings, there is an order of magnitude difference between the measured and expected values, proving that light-shifts play a large role in the trapping behaviour. Despite these issues, we chose to use this theory as the foundation of our temperature method since it, at worst, underestimates the stiffness of the optical trap and provides us with a suitable framework with which to perform an experiment.

3.2 Sub-Doppler Temperature Measurements using an Ultrathin Fibre

In our work, we spatially translate an atom cloud across an MNF and use the time variation of the collected fluorescence signal coupled into the nanofibre to determine the temperature of the cold atoms. The signal is detected using a single photon counting module (SPCM) to monitor the atom cloud's motion with high signal contrast and nanosecond time resolution, limited only by its response. By reworking Eqn. 3.6 in the presence of an external force, we can solve the problem by determining the phase difference between the measured oscillating fluorescence signal and the oscillation of the trap centre.

To theoretically determine the temperature, we must transform the damped harmonic oscillator into a forced, damped harmonic oscillator. This can be realised by superimposing an oscillating magnetic field on top of the quadrupole trapping field in the MOT setup. In our case, we superimposed a sinusoidally varying current on top of the DC current supplied to the anti-Helmholtz coils by using a frequency generator. With this applied current, the trap centre periodically oscillates in 1-D according to the following equation, $\Delta x(t) = \epsilon_0 cos(\omega t)$. Here, ϵ_0 is the amplitude of the motion and ω is the frequency of the oscillation. This will cause the force on the atoms, F_{forced}, to vary (in 1-D) by

$$F_{forced} = -\kappa(x + \Delta x) - \beta v_x = -\kappa x + F_{osc} - \beta v_x. \tag{3.7}$$

This applies to the atoms in the trap, but the concept can be extended to the motion of the centre of an atom cloud. It is also important to note that the axis used is defined relative to the orientation of the anti-Helmholtz coils in the MOT setup, as the slope of the gradient depends on the axis chosen. The presence of the oscillating term in Eqn. 3.7, $F_{osc} = \kappa\epsilon_0 cos(\omega t)$, allows us to treat the system as a forced, damped harmonic oscillator. Two important equations can be obtained when solving this ordinary differential equation:

the amplitude of the motion, $A(\omega)$, and the tangent of the phase of the system, $\phi(\omega)$, such that

$$\begin{aligned} A(\omega) &= \frac{\kappa\epsilon_0}{\sqrt{((\kappa - m\omega^2)^2 + (\beta\omega)^2)}}, \\ \text{and} \quad tan(\phi(\omega)) &= \frac{\beta\omega}{\kappa - m\omega^2}, \end{aligned} \tag{3.8}$$

where m is the mass of a single ^{85}Rb atom. At a phase difference of $\phi = \pi/2$ the tangent is undefined; this corresponds to the denominator equalling zero, or $\kappa = m\omega^2$. Therefore, a measurement of the phase difference at different oscillation frequencies, ω, can help us determine our trap frequency, which is related to the average atom cloud temperature through the equipartition theorem $\kappa \langle x^2 \rangle = k_{\mathrm{B}} T$, where $\langle x^2 \rangle$ can be interpreted as the mean square radius of the atom cloud. The definition of the cloud radius is discussed later in the results section of this chapter.

3.2.1 Ultrathin Optical Fibres in a Vacuum Chamber

In these experiments, we used a tapered optical fibre with a waist diameter of $\approx$ 700 nm, which qualifies it as an optical nanofibre (ONF) as opposed to the microfibres which are used elsewhere in this thesis. This nanofibre was produced using a standard heat-and-pull rig with an oxygen-butane flame. This earlier iteration of the heat-and-pull rig produced relatively low quality fibres and the ONF transmission was found to be $\approx 60\%$. Despite this, the coupling efficiency of the atom fluorescence into the fibre was more than adequate to allow accurate measurements. The 'low' transmission quoted is only in light of the more recent advances in ONF fabrication and was quite an acceptable value for atom-ONF systems during the early days.

Mounting optical nanofibres in vacuum chambers is a very delicate task. Not only are nanofibres inherently fragile, their exposure time to air between fabrication and mounting must be minimised to prevent contamination. Thus, we have a sensitive process that needs

to be accomplished in a very short time frame. We use a U-shaped aluminium mount to support the nanofibre after fabrication. Thorlabs UV cureable glue (NOA 61) is used to affix the nanofibre to this mount; this glue has excellent adhesion between metal and glass and is safe for use in ultra high vacuum systems due to its low-outgassing property. Often, some extra tension is applied to the nanofibre through the translation stages of the heat-and-pull rig to reduce the amount of slack at the fibre waist after the heat-and-pull process. The U-mount is then attached to a CF flange with two fibre throughput holes, which allow the nanofibre pigtails to enter and exit the vacuum chamber. Teflon ferrules are used to seal the holes in the CF flange while still allowing the fibre pigtails to enter the chamber. The increased pressure during pumpdown of the vacuum chamber forms a very tight seal between the Teflon and silica pigtails. The pumpdown process is a three-stage process involving the initial use of a roughing pump before transferring to a turbomolecular pump, and finally switching to an ion pump to achieve ultra high vacuum conditions. To reduce any effects of gravity on the shape of the fibre waist, the fibre is mounted vertically in the vacuum chamber.

3.2.2 Experimental Setup

Magneto-optical traps (MOTs) use a quadrupole magnetic field which is generated from two coils of current carrying wires in the anti-Helmholtz configuration, as indicated in Fig. 3.1. The MOT used in this chapter was built and developed over many years with contributions from many team members[2]. By definition, the coils should be separated by a distance equal to their radii, though, in practice, this separation is typically different as it is dictated by the size of the vacuum chamber. By passing currents with opposite handedness through the coils, a field with an approximately linear magnetic field at the centre of the two-coil system is generated. In the temperature measurement reported here, this quadrupolar field, shown in Fig. 3.2, can be perturbed by superimposing an oscillating current on top of the DC current to provide the necessary oscillation of the

[2]S. Nic Chormaic, K. Deasy, M. Morrissey, S. Yarovitskiy, S. Chakraborty, and L. Russell

trap centre, as described by Eqn. 3.7.

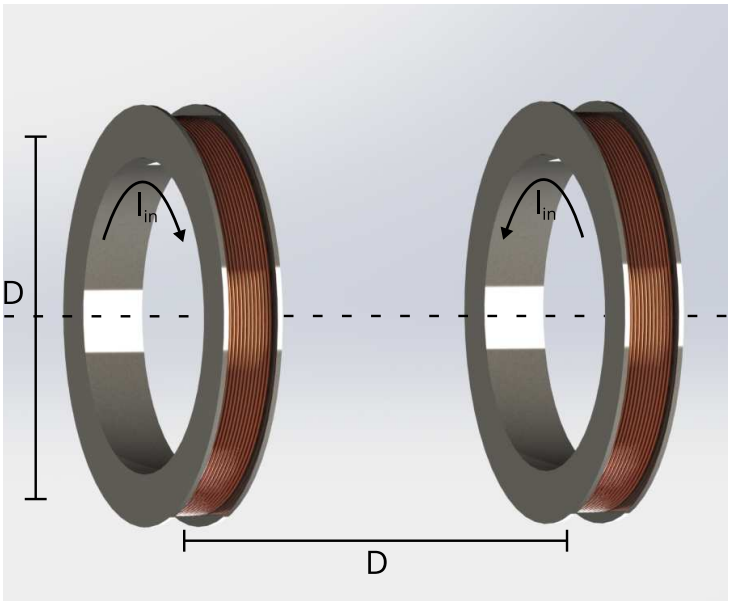

Figure 3.1: Orientation of anti-Helmholtz coils. By definition the separation should be the same as the coil diameter and the current, I_{in}, should be propagating in a different direction in each coil.

Rather than applying the AC current to the primary trapping coils, we instead applied this oscillation to secondary coils, which were used to control the lateral positions of the atom cloud. When the AC current was applied, the trap centre oscillated across the ONF and the emitted fluorescence, which coupled into the guided modes of the fibre, was detected using an SPCM. To enhance the signal, we offset the position of the atom cloud such that its centre never fully crossed the fibre. The diameter of the fibre was 700 nm, which is much smaller than the macroscopic, millimetre size of the atom cloud. We controlled the oscillation so that at one apex of the oscillation the atom cloud was almost completely removed from the fibre surface and at the other apex of its motion the centre was directly over the fibre waist. This gave us high contrast in our detected signal, see Fig 3.3.

We made some minor assumptions about the atom cloud in order to perform this experiment. Firstly, we assumed that the cloud had a Gaussian density profile, thence we assume that the number of atoms which fluoresced into the guided mode at any given time

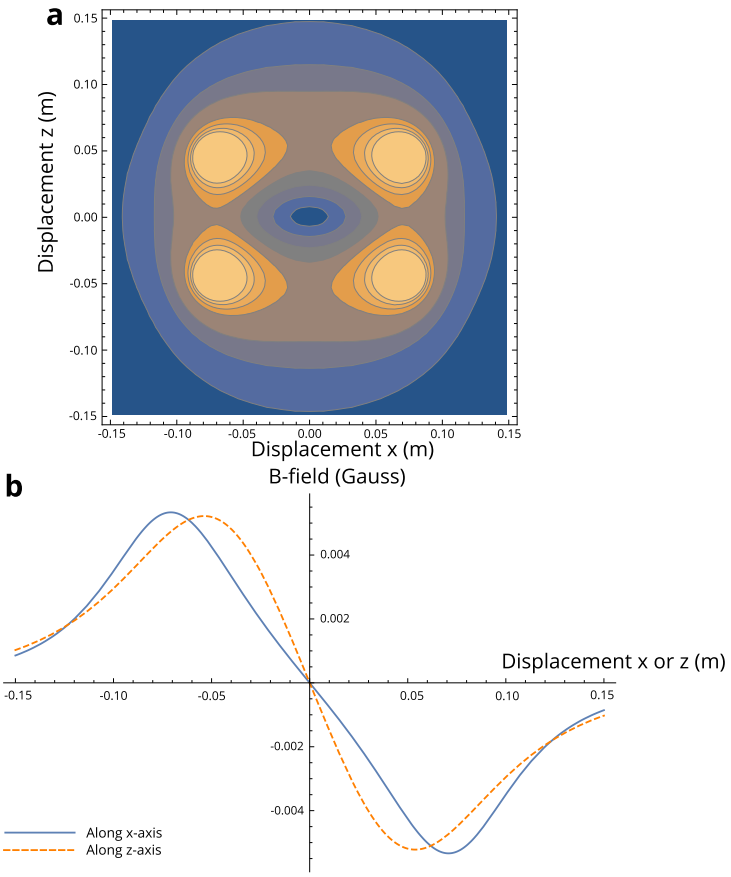

Figure 3.2: (a) Contour plot showing the B-field distribution along the xz-axis of a pair of anti-Helmholtz coils where z is the longitudinal axis with respect to the coils. (b) B-field gradient along the x-axis (blue) and z-axis (dashed orange).

was proportional to the atom density at any point in the cloud. Observation of the atom cloud fluorescence using CCDs supported the argument that the atom cloud distribution remained Gaussian throughout the experiment. The second assumption was that, for small amplitude oscillations of the atom cloud position, we could take the variation in the atom density to be approximately linear. This results in the atom cloud's oscillation being transferred directly to the monitored SPCM signal. Both of these assumptions are minor, and even without these assumptions, the experiment could proceed in a similar fashion.

For this experiment we used the ^{85}Rb isotope due to its naturally higher abundance (72.2%). The cooling laser was locked to the crossover peak [156], $5^2S_{1/2}F_g = 3 \rightarrow 5^2P_{3/2}F_e = (2,4)_{co}$ and then detuned from this frequency using an acousto-optical mod-

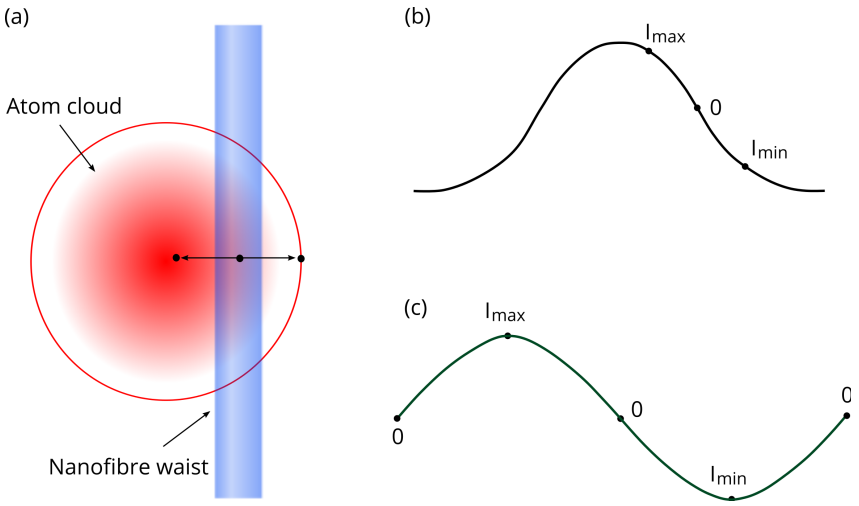

Figure 3.3: As the atom cloud oscillates over the fibre the maximum flourescence intensity, as measured by an SPCM, occurs at different displacements of the cloud. (a) Location of the cloud relative to the fibre surface. The centre of the cloud moves across the fibre. (b) Intensity of the cloud as measured by the SPCM if one were to fully translate over the fibre. (c) Output of the SPCM as we oscillate between I_{min} and I_{max}. Fibre and cloud size not to scale. The fibre and cloud diameters are approximately 700 nm and 2 mm, respectively. Figure adapted from Fig. 2 in [155].

ulator (AOM). The crossover peak is an 'artifical' peak generated due to the saturated absorption spectroscopy (SAS) technique used to lock the cooling and repump lasers. SAS is a spectral hole burning process, which can cause crossover peaks when the frequency difference between two ground to excited state transitions is lower than that of the Doppler shifted frequency. Due to the Maxwellian nature of the velocity distribution, two velocity classes of atoms can be in resonance at the same time causing an artificial peak to appear which can often be larger than the real peaks.

The detuning of the cooling laser was initially chosen to be 12.4 MHz, but later we changed this detuning to observe the temperature dependence. The cooling laser was then split into three beams which were employed in the standard magneto-optical trap (MOT) configuration. A repump laser was locked to a different crossover peak, $5^2S_{1/2}F_g = 2 \rightarrow 5^2P_{3/2}F_e = (1,3)_{co}$, and then shifted towards the repumping frequency as appropriate. The magnetic field gradient of the primary anti-Helmholtz coils was

measured to be $\approx$ 15 Gcm^{-1} using a digital hall probe. The number of atoms in the cloud was found to vary between 10^4 and 10^6 during this experiment due to changes in the detuning, rubidium supply current, etc.

There was a noticeable lag time between changing the centre position of the optical molasses setup and the motion of the atom cloud. This puts an upper bound on the frequency of oscillation for the trap centre. We performed the experiment in the range of 5-50 Hz in intervals of 1 Hz. We also required that the frequency sweep produced a phase difference sweep that covered a $0 - \pi$ interval since the experiment relied on measuring the frequency of the trap at a phase difference of $\pi/2$.

3.2.3 Timing and Triggering

Timing and triggering of the various components of the experiment were crucial. A TTL signal from a function generator, which produced the AC current for the anti-Helmholtz coils, was used as a timing cue to synchronise all data acquisition, while a simple transistor switch was used to manually trigger the data acquisition. The timing scheme was made difficult due to the limitations of the Stanford Research Systems (SRS) SR400 Gated Photon Counter that was used. The counter itself could only store 2000 data points before the buffer needed to be read and cleared. Additionally, the counter had a minimum dwell time between consecutive count periods of 2 ms, which limited our acquisition rate. To overcome this limitation, a timing scheme which could be reliably triggered without causing an overflow error on the SR400 photon counter needed to be created. A sample timing diagram for the various signals used in the experiment is given in Fig. 3.4, while a flow diagram showing how the equipment was daisy-chained together is given in Fig. 3.5.

Once the transistor switch was activated, a controlled burst of 1000 TTL pulses, which had been programmed into a second function generator, was initialised and waited for the next rising TTL edge of the first function generator. The TTL trigger output of this function generator was split in two to allow it to simultaneously trigger both the SRS SR400 photon counter and the National Instrument data acquisition (DAQ) card. The

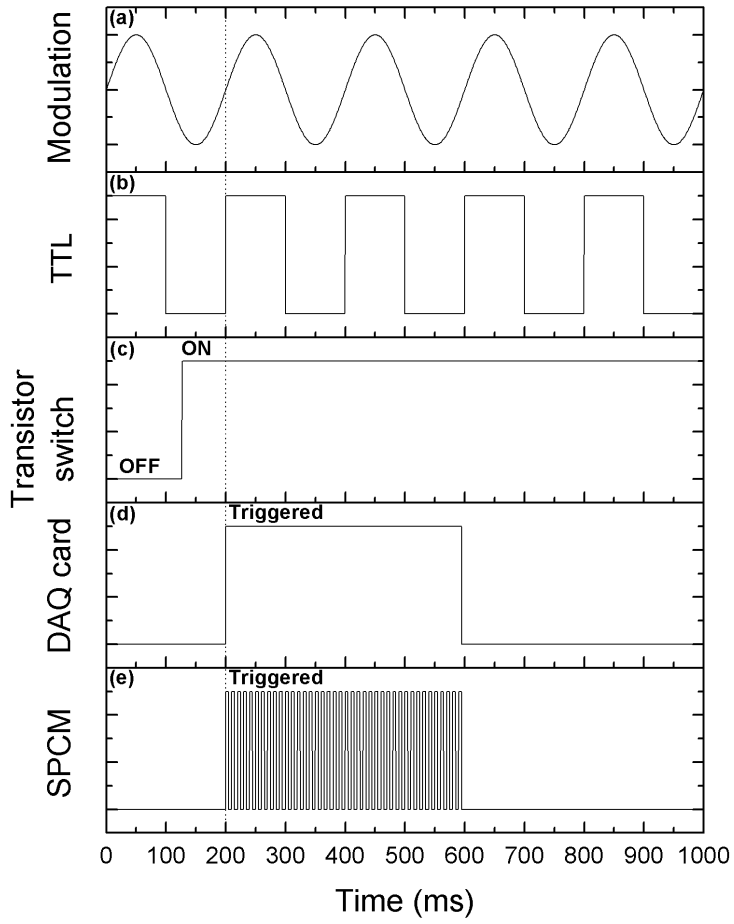

Figure 3.4: (a-e)Timing scheme to perform the forced oscillation temperature measurement. Figure taken from [155].

DAQ card recorded the time stamp of the triggering as well as the TTL output signal from function generator A. Once the burst was complete the DAQ card extracted the data from the SRS SR400 buffer, stored the data with the current time stamp, and cleared the buffer in preparation for the next trial. The duration of the controlled burst could be varied to allow different acquisition time bins for the SPCM.

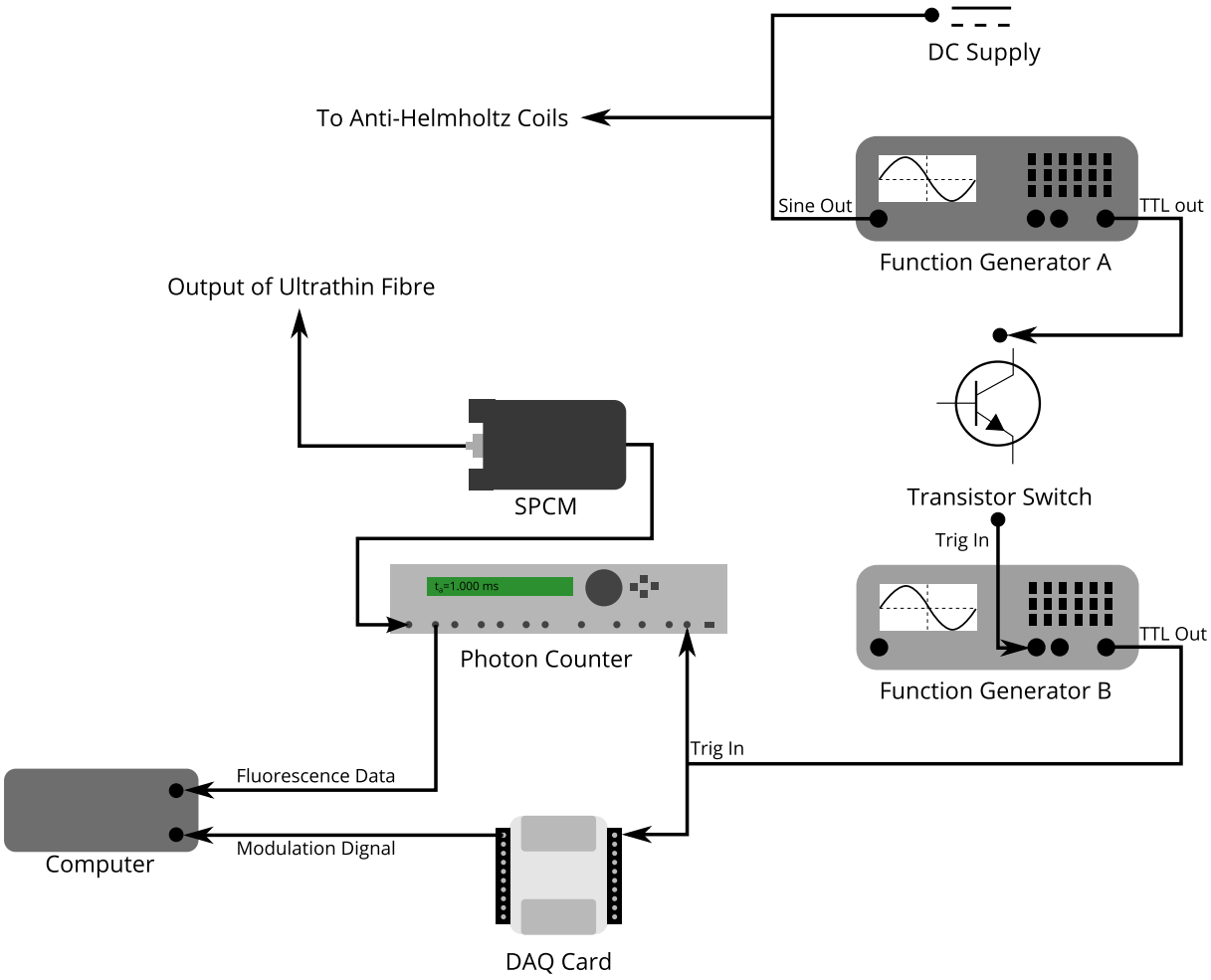

Figure 3.5: Flow diagram of the timing scheme used in the temperature measurement resulting in the simultaneous data collection of the TTL reference signal corresponding to the modulation of the atom trap centre and the collection of the fluorescence data.

3.2.4 Results

To measure the phase difference between the sinusoidally varying current used to move the trap and the fluorescence signal measured using an SPCM, first we had to extract and fit the SPCM data. Using a 1000 burst cycle with a bin time of 1 ms the total measurement time per trial was 1 second. This was repeated a large number of times to reduce error. The output of the SPCM gave a clearly sinusoidal signal which was fitted to a sine wave using a Matlab script. Sample fits are given in Fig. 3.6.

As the oscillation frequency increased, the phase difference of the fluorescence signal with respect to the oscillation signal was seen to increase. A graph of the oscillation

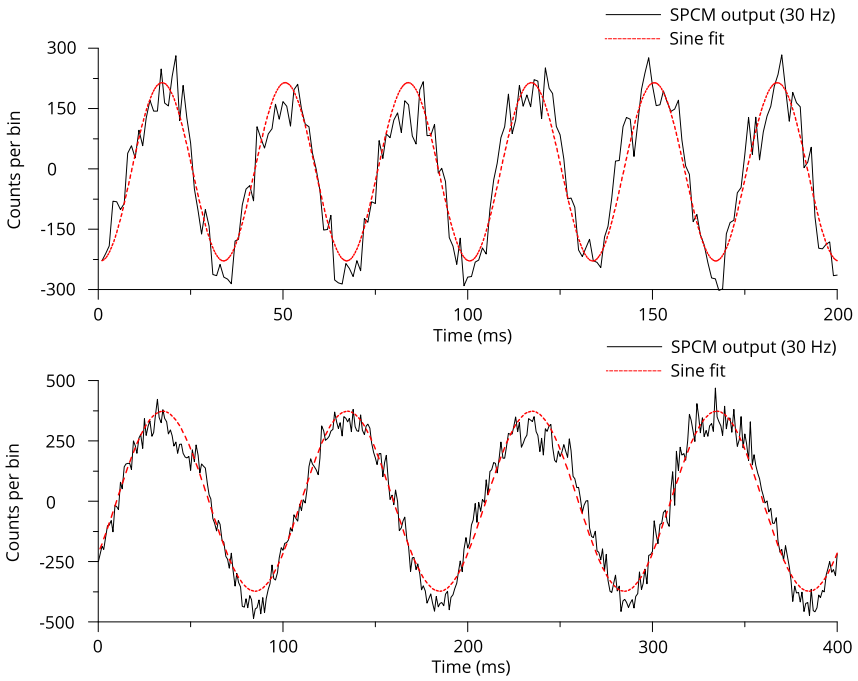

Figure 3.6: Sinusoidal fits to 30 Hz and 10 Hz SPCM signals.

frequency versus phase difference at a fixed value of the detuning is given in Fig. 3.7, where a photodiode was used to provide a comparison between the more conventional measurement approach and the nanofibre approach. To use a PD, we first had to obstruct the PD aperture so that only half of the atom cloud's fluorescence could reach the sensor. A razor edge was used for this purpose and was carefully positioned so that the plane of the cloud's oscillation passed perpendicular to the razor's edge. When the trap centre began to oscillate, the amount of fluorescence which was able to reach the detector changed, resulting in a clear signal at the PD output.

At equilibrium, if we treat an atom as a semiclassical object, we can show that the equation of motion is directly analogous to that of a damped spring system, see Eqn. 3.7. We can equate the energy of the system as: $\frac{1}{2}k\langle x^2\rangle = \frac{1}{2}k_{\mathrm{B}}T = \frac{1}{2}m\langle v^2\rangle$. Therefore, to measure the kinetic energy and corresponding temperature of the atoms, we need only know the effective spring constant, k, and the mean-squared amplitude of its oscillation, $\langle x^2\rangle$. Since we cannot track a single atom and determine its mean-squared amplitude we instead measured the size of the atom cloud using a CCD camera, and this can be

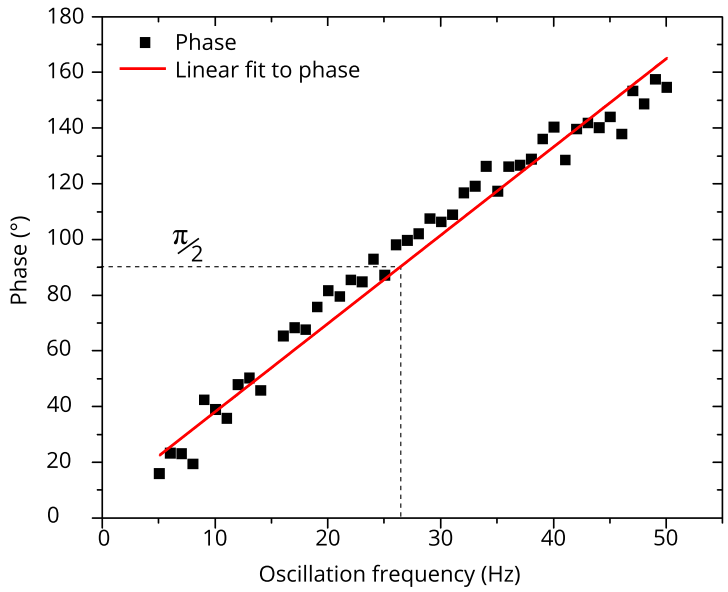

Figure 3.7: Plot showing the linear relationship between the frequency of the trap centre oscillation versus the phase difference accrued between the oscillation signal and the SPCM output.

interpreted as the maximum amplitude of an atom's motion in the harmonic potential. Since we knew the calibration factor of the CCD image from prior investigations, we could, therefore, translate the size of the atom cloud in pixels to a real value. A sample atom cloud profile is given in Fig. 3.8. The exact size of the cloud can be hard to determine since the density of the cloud is Gaussian. We assume the radius of the cloud to be equal to the $1/e$ value, but other values were also investigated since there exists some ambiguity in the literature regarding this definition.

As we increased the pump beam detuning, we saw that the phase difference between the SPCM and the oscillation signal increased, see Fig. 3.9. In the low-intensity limit, we have shown that the spring constant is proportional to $1/\beta$. The expression for β can be determined from Eqn. 3.5 to be

$$\beta = \frac{8\hbar k^2 \delta s_0}{\gamma(1 + s_0 + [2\delta/\gamma]^2)^2}. \tag{3.9}$$

An increase in δ results in the value of β decreasing which, in turn, increases the

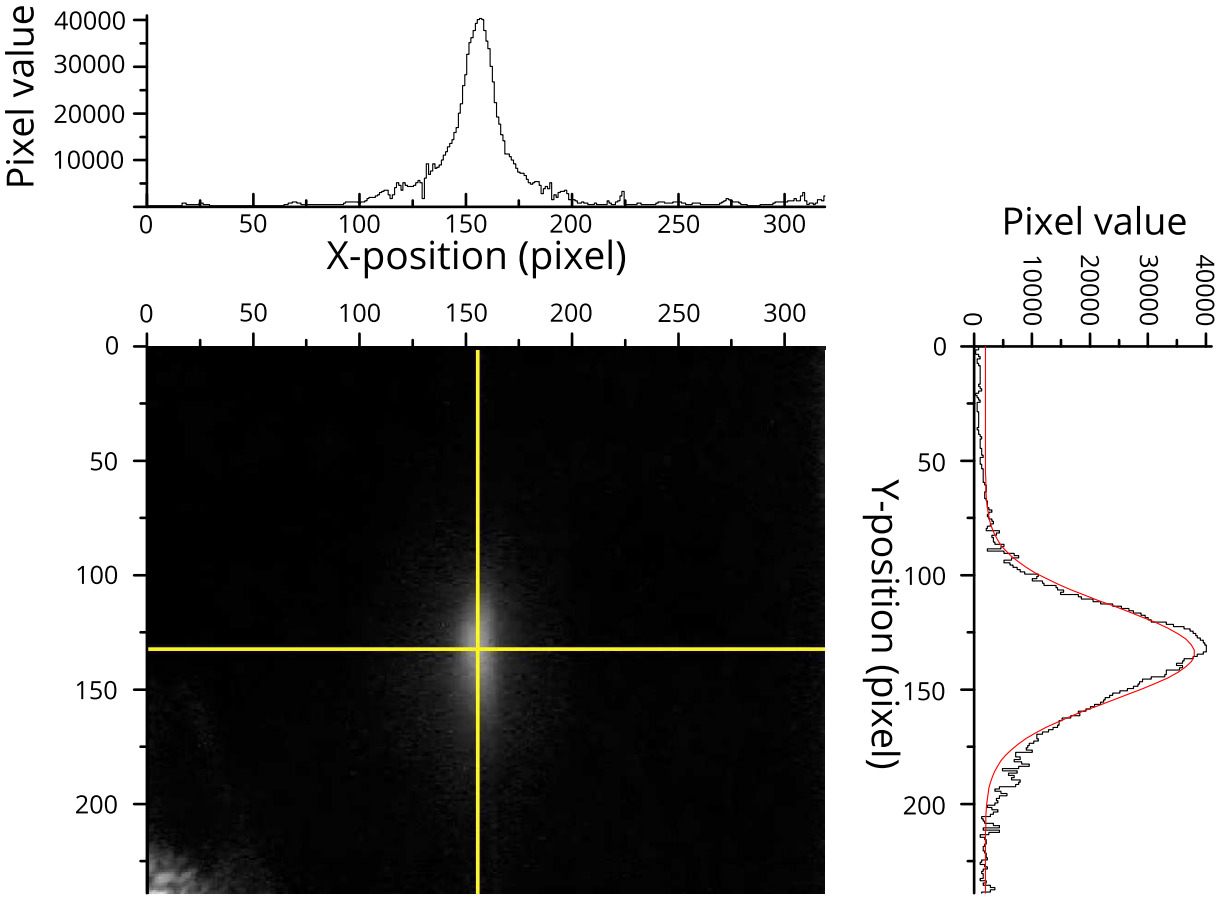

Figure 3.8: CCD image of an atom cloud used to measure the horizontal and vertical profiles, the profiles along the yellow lines are given above and to the right of the image.

effective trap stiffness, resulting in lower atom cloud temperatures. Our experiment was, of course, not in the low-intensity limit, since our pump beams were close to saturation, but we were able to assume a similar trend which was confirmed by this measurement.

The error in measurement was calculated using the standard empirical formulation

$$Error = \Delta T = \left(2\frac{\Delta\omega_n}{\omega_n} + 2\frac{\Delta\left\langle r_x \right\rangle}{\left\langle r_x \right\rangle} \right) T, \tag{3.10}$$

where $\Delta\left\langle r_x \right\rangle$ is the chosen definition for the radius of the cloud, as will be discussed in this section. In general, the error is represented as the square root of the sum of the squares of the fractional errors, but this can be shown to be always less than or equal to the error ΔT [157]. The error in measuring the size of the atom cloud using the CCD camera is taken as 0.5 pixels, equivalent to 0.023 mm, and $\Delta\omega_n$ is the error associated with

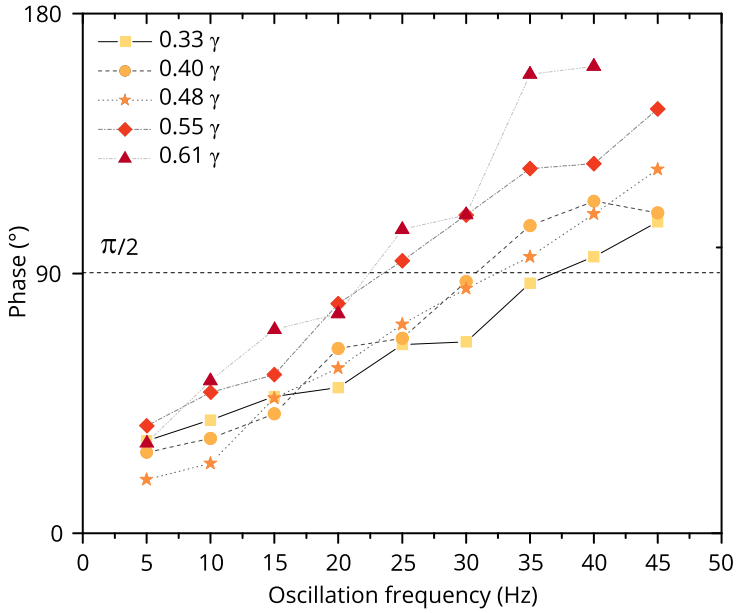

Figure 3.9: Larger pump beam detunings result in lower atom cloud temperature as can be seen by the increase in the natural trap frequency as the detuning is increased. Detunings given in units of the natural line width γ.

determining the natural frequency of the system. Using the values of the trap frequency as determined by finding the oscillation frequency at a phase difference of $\pi/2$ allowed us to determine the trap stiffnesses, which was combined with the atom cloud radius to find the atom cloud temperature. Due to the ambiguity in the definition of the atom cloud radius, as discussed earlier, we also use the $1/e^2$ value and full-width-at-half maximum (FWHM). The choice of the atom cloud radius is important as it drastically affects the measured temperature. The temperature versus pump detuning is given in Fig. 3.10. We can see large discrepancies in the determined temperature values using different metrics for the cloud size.

3.3 Conclusions

Using large enough detunings, we observed sub-Doppler cooling regardless of our definition of the atom cloud radius. This seemed to agree with the fluorescence based-measurements performed externally to the fibre. High signal-to-noise ratios could be obtained with care-

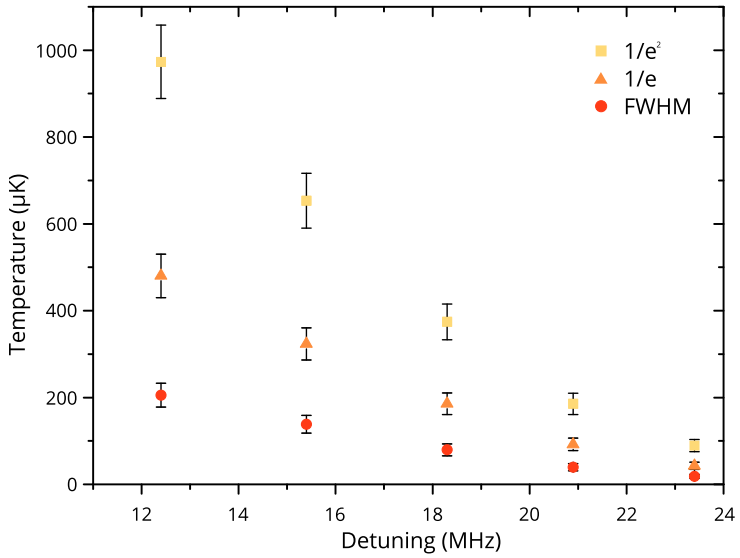

Figure 3.10: Atom cloud temperature versus pump probe detuning using different estimates for $\langle r_x^2 \rangle$ as determined from fits to CCD images.

ful alignment of the MOT with respect to the CCDs and the ultrathin fibre. Though not explicitly shown here, we demonstrated that the ultrathin fibre is especially sensitive to misalignments in the system. Small misalignments of the trapping beams result in large amounts of coupling into the guided mode of the fibre resulting in reduced signal-to-noise ratios. This can be sensitively detected using the ultrathin optical fibre output as measured using an SPCM. The presence of sub-Doppler temperatures is a reassuring measurement in our MOT system, proving that we are indeed working with a Sisyphus cooling mechanism. When we compared the ultrathin fibre measurement to the measurement obtained using the CCD camera we obtained marginally higher temperatures. This could be attributed to interactions with the "hot" fibre surface, perhaps through collision events or other forms of radiative energy transfer. Additionally, the fibre acts as a scatterer, causing the cooling beams to be scattered at the fibre. Indeed, even the presence of the fibre alone may change the mode structure of the surrounding electromagnetic fields which could cause small, but noticeable, shifts in the resonant frequencies of the nearby atom, potentially decreasing the efficiency with which they are cooled. Unlike the fluorescence measurement taken using the CCD, the ultrathin fibre only interacts with atoms

that are near the fibre surface. This may slightly increase the temperature of the atoms locally, and influence the measured temperature. These may account for the increased temperatures reported, though further investigation is required on the subject.

Chapter 4

Slotted Tapered Optical Fibre for Atom Trapping[1]

In Chapter 3 we discussed —and demonstrated —one of the advantages of using an ultrathin fibre in a cold atom system, namely the ability to non-invasively collect fluorescence from an atom cloud. There are many other advantages, including the increased coupling to the guided modes of the fibre being one of the most important factors, and as we shall discuss shortly, their ability to also trap atoms near their surface. The work presented in this thesis is primarily concerned with enhancing the overall effectiveness of ultrathin optical fibres. In this section, we shall discuss how we can modify an ultrathin fibre to improve the local electric fields with a focus on trapping atoms, ^{87}Rb. This work represents the first foray into this idea.

Evanescent wave devices have been commonly used with atomic systems for the past few decades [158, 159]. More recently, the integration of optical nanofibres, i.e. optical fibres with dimensions smaller than the wavelength of the guided light [160–162] into cold atomic systems [59, 153, 163], as discussed in Chapter 3, has been the focus of increasing research interest and a comprehensive review of progress is contained within

[1]This section was largely adapted from Daly, M., Truong, V. G., Phelan, C., Deasy, K. & Nic Chormaic, S. Nanostructured optical nanofibres for atom trapping. New Journal of Physics 16, 053052(2014). M. Daly performed all the calculations except for the initial work relying on the eigenmode expansion method.

[59]. In particular, it has been shown that optical nanofibres can be used for trapping and manipulating cold atoms. Surface traps, such as those presented by Ovchinnikov *et al.* [164], adapted for use on curved optical nanofibre surfaces, make use of the evanescent field present when light is guided through thin optical fibres. The induced potential from a red-detuned field produces an attractive potential, while the atom-surface interaction potential is balanced using a blue-detuned potential barrier that prevents atoms from migrating to the fibre surface. In particular, trapping of alkali atoms in the evanescent field surrounding an optical nanofibre using a combination of red- and blue-detuned optical fields, the so-called *two-colour trap*, has been proposed [17, 165–167] and demonstrated [60, 168], thereby proving the effectiveness of the technique. In these experiments, the trapped atoms are coupled to a mode that is on resonance with the atom transition, and exhibit strong coupling and a large optical depth. These features are desirable for quantum information applications and have led to much research on similar nanophotonic systems for trapping and probing atoms [169, 170]. Red-detuned light traps in hollow fibres have also been used to guide atoms [171]. Alternative methods for guiding and trapping atoms outside optical nanofibres have been proposed by several groups, but practical implementation is still quite limited. Single colour traps that make use of higher order modes above slab waveguides [172], non-Gaussian beam shapes [173], or mode interference [174] to create stable traps have been proposed. Alternative fibre trapping schemes, such as helical trapping potentials around the nanofibre [175], an induced fictitious magnetic field around the fibre [176], or diffracted laser light off the fibre [177], also exist. All of these recently proposed methods have a common feature: the atoms are trapped outside the nanofibre, thereby limiting the efficiency of interaction with any light guided by the fibre.

The fabrication of optical nanofibres with very high transmission (>99%) for the fundamental mode has become a relatively standard technique [178] and alteration of either the chemical or physical properties of optical fibre surfaces is becoming commonplace. For example, the generation of a Bragg grating on an optical nanofibre by selective milling

of the surface using a focussed ion beam [179] and the fabrication of a humidity detector using subwavelength fibres via the application of 80 nm gelatin layers [180] have been reported. More recently, optical nanofibres that permit relatively high transmission of higher order modes have also been fabricated [75, 162] and this opens up the possibility of experimentally investigating a number of heretofore theoretical fibre-based atom trapping schemes.

In this work, we propose a method to trap and probe atoms inside a rectangular slot cut through the waist region of a silica optical nanofibre. The design of this device is analogous to that of a slot waveguide [81]. In a slot waveguide, the slot width is chosen so that it is smaller than the decay length of the evanescent fields. For such structures, a high mode confinement between the two waveguides is possible. Mirroring this structure in an optical nanofibre could allow us to trap atoms in the slot area, thereby resulting in several advantages over systems where the atoms are trapped outside the fibre. The simplicity of the design also opens up many possibilities for atom trapping, whether through single colour, higher mode trapping, or the addition of more rectangular slots allowing for the creation of spatially localised trapping regions. Here, we focussed on a two-colour setup for producing trapping potentials both at the fibre surface and within the slot. With a suitable choice of slot size, deep potentials with substantial trap lifetimes are predicted, with local minima located at positions of 140 nm - 200 nm from the inner surfaces of the slot.

4.1 Guided Modes of the System

4.1.1 Optical Mode Distributions

The system under study, shown schematically in Fig. 4.1, consists of an ultrathin, vacuum clad, silica MNF with a rectangular shaped slot removed from the centre of the fibre. We assumed that fibre diameters were of the order of the wavelength of the guided light. We

defined the axes such that the z-direction corresponded to the fibre axis, the direction parallel to the slot and orthogonal to the z-axis was the x-direction, and the remaining axis perpendicular to the slot was the y-direction.

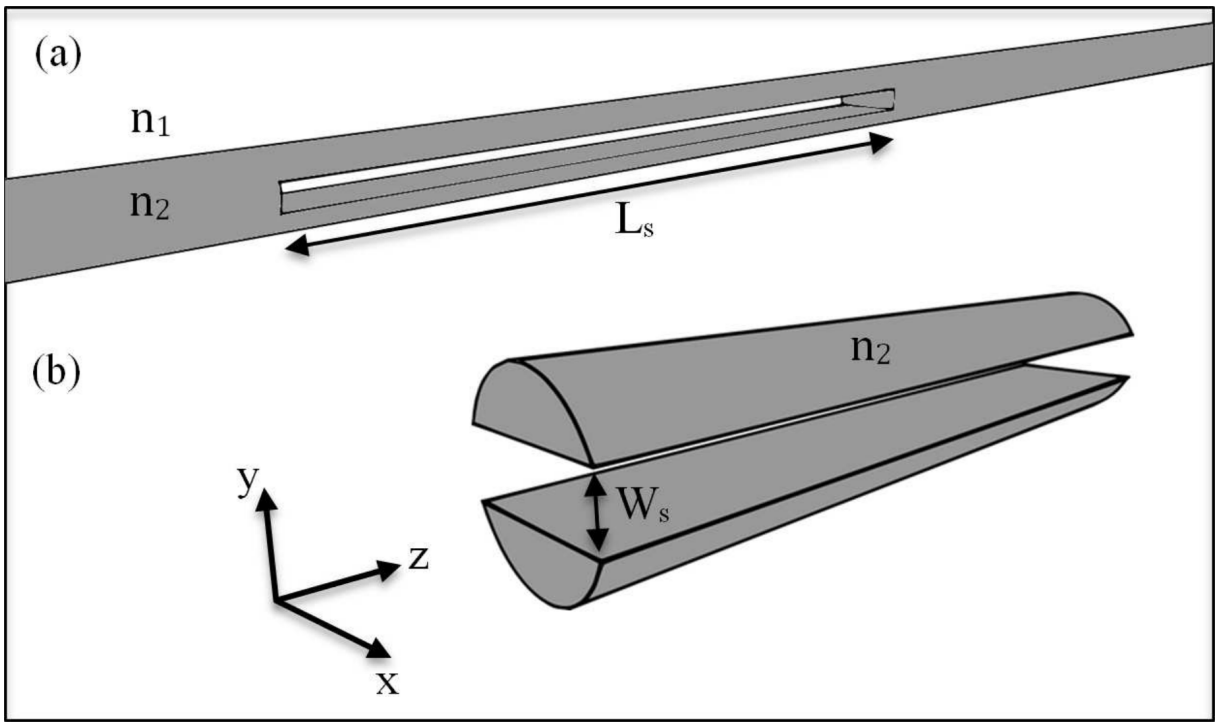

Figure 4.1: Schematic of the slotted fibre for a vacuum-fibre system $n_1 = 1$ and $n_2 = 1.45991$. (a) Tapered region with slot present, (b) slot region only.

For wavelengths of 1064 nm and 720 nm, chosen for their red- and blue-detunings from the 780 nm Rb cooling transition, respectively, and nanofibre diameters ranging from 0.6-1.2 μm, four distinct guided optical modes were identified. Using an approach similar to that developed by Anderson et al. [81], the modes were viewed as being either symmetric or anti-symmetric. The symmetry we refer to here is related to the supermode created by the superposition of the modes in either side of the slotted fibre. For different phase differences between the two modes that make up the supermode a distinct anti-symmetric or symmetric pattern can be seen in the electric fields. Furthermore, each mode can propagate with two orthogonal polarisations, giving rise to the four distinct modes.

The supported optical modes of the slotted fibre were determined from Maxwell's wave

equation, Eqn. 4.1. Using commercially-available finite element (COMSOL Multiphysics), finite difference method (CrystalWAVE), and eigenmode expansion (FIMMWAVE and FIMMPROP) software packages, the spatial variation of the electric field along a waveguide of any geometry could be calculated. For a waveguide as shown in Fig. 4.1, there is symmetry along the z-direction, hence the electric field is translationally invariant in this direction resulting in the following form of the wave equation

$$[\nabla^2 + n^2k^2]\vec{E}_t(x,y) = \beta^2\vec{E}_t(x,y). \tag{4.1}$$

Here, $\vec{E}_t(x,y)$ is the transverse component of the electric field, n is the refractive index, k is the wavenumber and β is the propagation constant. In the slot region, light propagates as two separate modes, one travelling in the fibre section at the top of the slot region and the other in the lower portion of fibre. The total field is written as

$$\begin{aligned}\vec{E}(x,y) &= \vec{E}_{1t}(x,y)\exp^{-\iota\beta_1 z} + \vec{E}_{2t}(x,y)\exp^{-\iota\beta_2 z} \\ &= [\vec{E}_{1t}(x,y) + \vec{E}_{2t}(x,y)\exp^{-\iota(\beta_2-\beta_1)z}]\exp^{-\iota\beta_1 z}\,.\end{aligned} \tag{4.2}$$

For cases where the two propagating modes have the same, or almost the same, effective index Eqn. 4.2 can be greatly simplified and this also allows us to neglect any mode beating effects since the mode beat length, $L_B = 2\pi/(\beta_2 - \beta_1)$, becomes much longer than the length of the slot cavity, L_s. For a slot waveguide, the value of L_s will always be much lower than the beat length. In the following, we shall treat the solutions as supermodes, travelling with a single propagation constant, β, which has a value higher than either of the initial constants, β_1 and β_2, for symmetric modes. Moreover, we assume the two modes to be degenerate, which is true for a symmetric structure of this type. We can also consider the two modes given in Figs. 4.2(a) and (b) as being analogous to the two polarisation states of the HE_{11} modes in a standard tapered optical fibre, albeit with larger differences between their propagation constants.

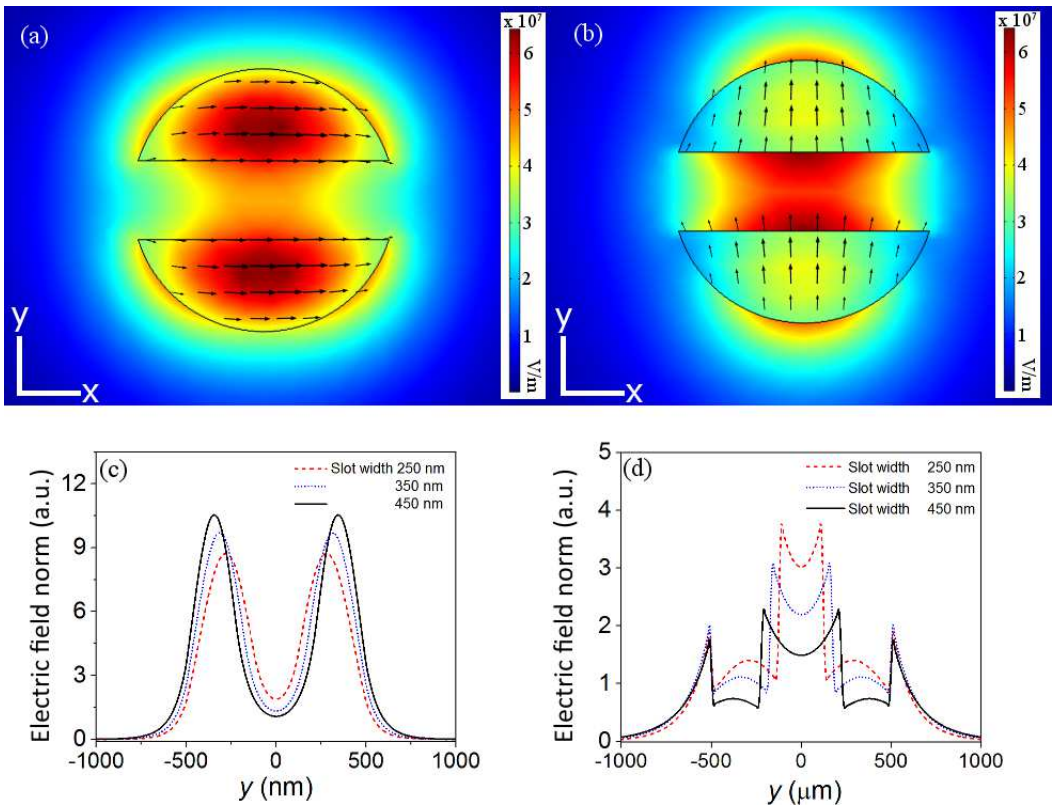

Figure 4.2: Electric field normal of modes generated in a 1 μm diameter fibre using (a) 720 nm light with parallel polarised light and (b) 1064 nm light with perpendicularly polarised light. The arrow fields in both pictures refer to the orientation of the polarisation at those points. (c) and (d) are the normalised electric fields along the y-direction for (a) and (b), respectively, for different slot widths.

When the waveguide dimensions are comparable to the wavelength of light, the polarisations of the modes have greater influence over the intensity distributions. This is most noticeable within the slotted region. Figures 4.2(a) and (b) show two extreme cases where the electric field is polarised parallel and perpendicular to the slot walls. Figures 4.2(c) and (d) give the electric field norms for parallel and perpendicular polarisations, respectively, and for slot widths, W_s, varying from 250-450 nm. In the case of perpendicular polarisation, high intensities can be realised in the vacuum region between the slot walls since the component of the electric field normal to the boundary has no continuity requirement. Figure 4.3 shows the transverse field distributions corresponding to two modes for one polarisation at 1064 nm in a 1 μm diameter fibre with a 350 nm wide slot.

Figure 4.3(a) shows a symmetric mode, while Fig. 4.3(b) shows an anti-symmetric mode. All calculations throughout this section were performed using the total electric field.

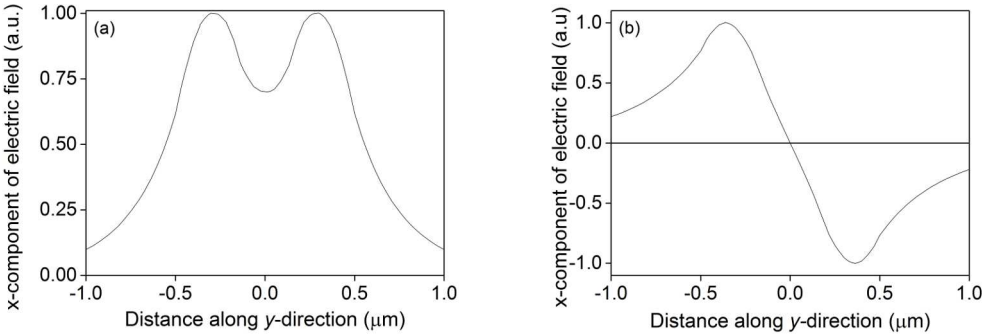

Figure 4.3: Symmetric and anti-symmetric modes for a single polarisation. The plots show the normalised x-component of the electric field across the slotted fibre centre in the y-direction.

4.1.2 Mode Definition

It has been shown that, in waveguides with a circular sector cross-section (i.e. a section of a circle which is enclosed by two radii and an arc) the mode numbers are non-integer, i.e. $m = (p\pi)/\phi_0$, where p is an integer and ϕ_0 is the sectoral angle [181]. This non-integer mode number serves merely to indicate that full circular symmetry has been lost. Here, we are dealing with circular segments, as opposed to sectors (Fig. 4.4). Hence, it is clear that the modes for this system will differ slightly, but one can assume that, in general, they will have similar behaviour.

It is important to distinguish between what can be considered as *single-mode* or *multi-mode* in this system. In the absence of full analytical solutions, we define the single-mode regime as being the region where the only modes propagating are those which have intensity profiles with a single intensity maximum in each fibre segment as given in Fig. 4.2(a). Figure 4.5 indicates the defined single and multimode regions for different fibre radii and slot widths as obtained from numerical models.

Higher-order modes can give rise to interesting intensity distributions within the slot

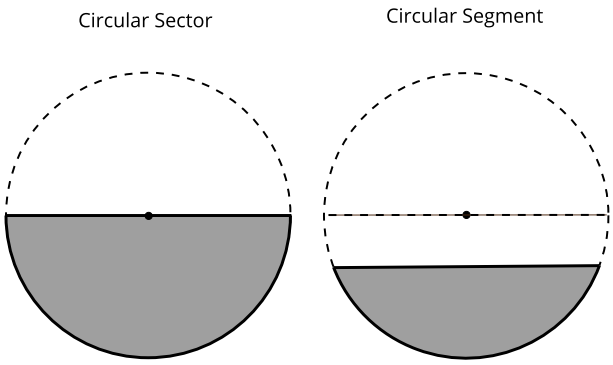

Figure 4.4: Left: A circular segment. Right: A circular sector. Segments of a circle do not necessarily have a portion which cuts through the centre of the circle making analytical solutions more difficult.

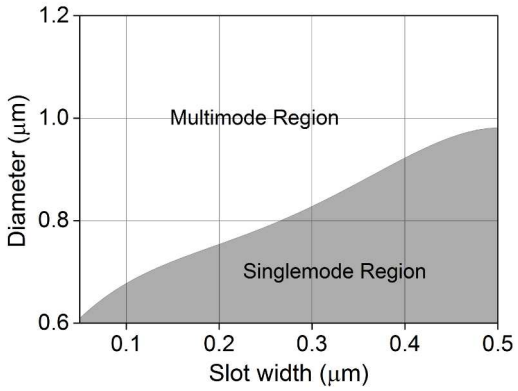

Figure 4.5: Graph of the regions of single-mode and multimode operation for 720 nm wavelength. 720 nm was chosen as the blue-detuned wavelength, used later in this chapter.

and these could also be used for atom trapping. However, in this initial work we focussed on the fundamental mode. To this end, we only considered parameters that were in, or near, the single-mode region, where contributions from the higher modes were either non-existent or small enough to be neglected. It has been shown by Jung *et al.* that modes can be effectively filtered out via selective excitation of the fundamental mode using a tapered fibre [182]. Only symmetric fibre modes were considered as they are excited with much greater efficiency by the HE_{11} mode. Anti-symmetric modes should not be excited by an approximately uniform phase front. It can be seen from Fig. 4.2(a) that the parallel-polarised modes rapidly decay exponentially away from the slot walls. Therefore, these modes are better suited for blue-detuning so as to attract the atom to

the intensity minimum at the centre of the slot. In contrast, the orthogonally polarised modes have a higher intensity than that of the parallel-polarised modes in the centre of the slot, see Fig. 4.2(b), which causes atoms to be attracted towards the walls near the centre of the trap. As we shall see later in Section 4.2.3.2, it is possible to combine these two field distributions with a combination of red- and blue-detuned light to draw atoms towards the centre of the slotted nanofibre.

Analytical solutions to the circular segments are difficult to obtain. Despite the refractive index remaining homogeneous, we lose the isotropy due to the non-symmetric structure. If we begin from Eqn. 2.5, reproduced here for clarity

$$(\nabla^2 + n^2k^2)\vec{E} = -\nabla(\vec{E}.\nabla \ln(n^2)) \tag{4.3}$$

we can see that the wave equation in the absence of isotropy is more difficult to solve. It would be theoretically possible to solve this equation by treating the right-hand side term as a perturbation, but even solving the unperturbed system for the geometry at hand is quite challenging, due to its lack of cylindrical symmetry and there is no guarantee that we can even solve the resulting equation for such a perturbation.

4.2 Trap Design

4.2.1 Surface Interaction Potential

A common issue in atom trapping near dielectric surfaces arises from the contribution to the total potential from the atom-surface interactions. Atoms near dielectric surfaces, such as the inner walls of the slot waveguide, are strongly affected by the attractive van der Waals (vdW) potential [183–185]. To quantify this effect the Lennard-Jones (L-J) potential [186] is often used as an approximation, such that the van der Waals potential,

V_{vdW}, is given as

$$V_{vdW} = -\frac{C_3}{d^3}, \tag{4.4}$$

where d is the distance from the fibre surface to the atom and C_3 has the value of 3.362×10^{-23} mK m^3 for ^{87}Rb. Assumptions that the major contribution to the atomic polarisability come from the first six lowest $P_{1/2}$ and $P_{3/2}$ levels of rubidium and that the wall is a perfect conductor have been made in this calculation [187]. It has been shown [188], that instead of a full QED calculation of this potential, a simple interpolation formula can be used. This formula agrees with the QED calculation to within 0.6%. In a similar process we compare the L-J potential to this interpolation formula in an attempt to justify it, as it is used extensively throughout the literature as an approximation. We find that it agrees to within 1.3% at distances of less than 3 μm from the fibre surface, see Fig. 4.6. Therefore, we use the L-J approximation throughout this paper.

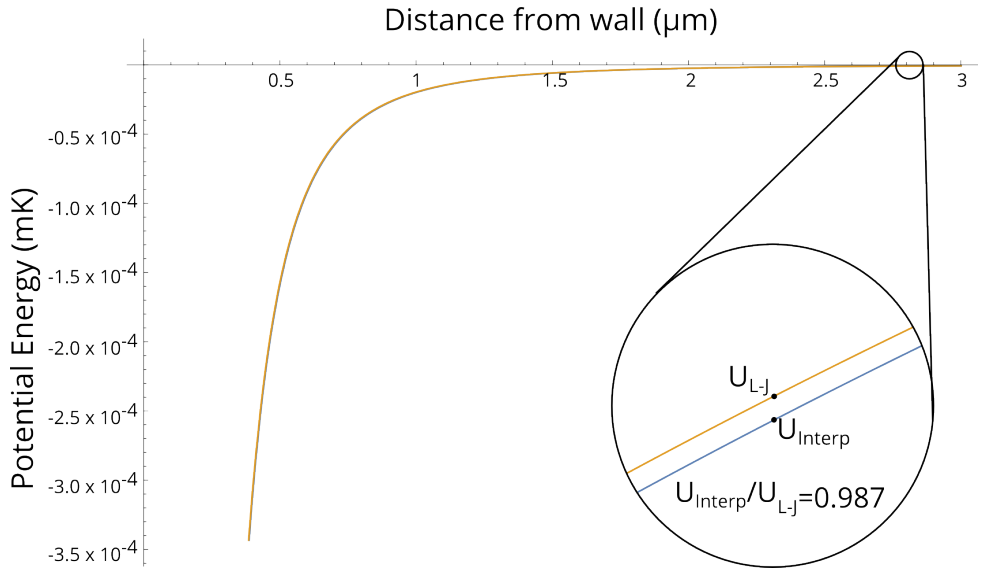

Figure 4.6: Comparison of the simple L-J potential to the interpolation function of the QED calculation.

The effect of the van der Waals potential on neutral atoms located within the slot results in them being pulled towards the surface. Figure 4.7(a) indicates how the vdW potentials from either wall add to produce the total vdW potential seen by an atom in the

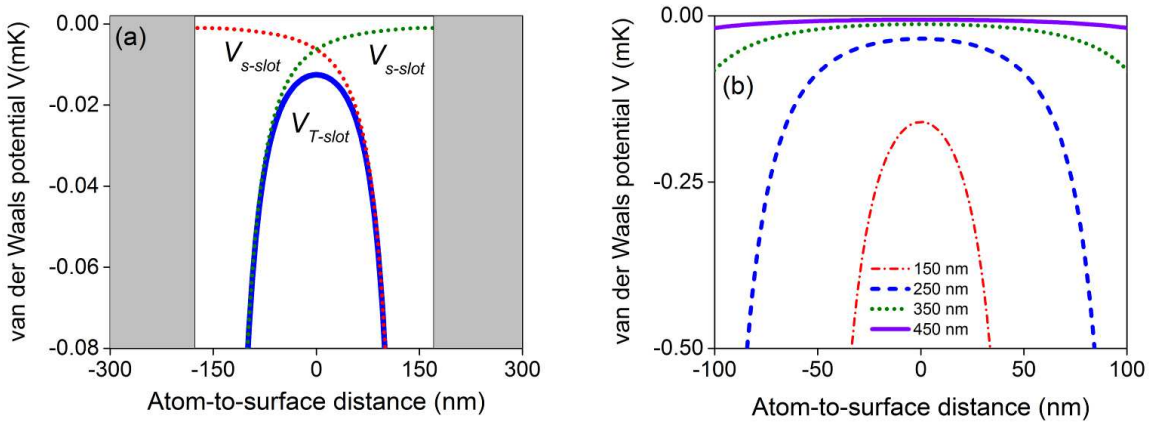

Figure 4.7: The van der Waals potential for an atom located in the fibre slot. (a) The total potential, V_{T-slot}, is created by adding the contributions from each of the two walls, V_{s-slot} for a 1 μm fibre with a 350 nm slot width. The fibre walls are indicated by the grey regions. (b) The total van der Waals potential as a function of atom-to-surface distance for W_s values of 150 nm (dot-dash), 250 nm (dash), 350 nm (dot), and 450 nm (solid).

slot. Figure 4.7(b) explores how changing the slot width affects the total vdW potential. As atoms approach the slot walls, it is clear that the effect of the vdW potential becomes more prominent; also, as the slot width, W_s, becomes smaller, atoms at the trap centre are affected more. The addition of a blue-detuned light field with respect to the atom transition frequencies alters this potential and creates a region in the centre with a stable equilibrium position.

4.2.2 Optically Produced Potential and Atom Trapping

A neutral atom interacting with an electric field, $\vec{E}$, experiences a dipole potential given by [144]

$$U = -\frac{1}{4}\alpha(\omega)\vec{E}^{*}\vec{E}, \tag{4.5}$$

where $\alpha(\omega) = \Sigma_n f_n[(e^2/m)/(\omega_n^2 - \omega^2 - \imath\omega\gamma_n)]$ and α is the atom polarisability as determined using Lorentz's model for a classical oscillator, e is the electron charge, m is the mass, ω_n is the natural frequency of the nth oscillator, γ_n is the damping coefficient of

the nth oscillator and f_n is the oscillator strength [189]. This is a classical approach to the problem. Semi-classical approaches can be performed by summing over the reduced electric-dipole matrix elements for the states of interest in ^{87}Rb. Such measurements have been performed over the ultraviolet to infra-red regions [190]. The exact values of the polarisability are important as they affect the strength of the interaction, which, in turn, affects the distance of the potential minima from the fibre surface.

It can be seen from Eqn. 4.5 that the sign of the polarisability and, hence, the trapping potential, is determined from the detuning of the laser fields involved. In the presence of an intensity gradient, the atom will experience a force along the gradient towards the intensity maximum in the case of red-detuned light and towards the intensity minimum in the case of blue-detuned light, see Eqn. 3.5. In order to trap atoms in the slot region we can choose symmetric modes that are polarised parallel or perpendicular to the slot walls and detuned to the red or blue of the transition frequency.

Neutral atoms in the presence of a laser field of frequency ω, which is close to an atomic resonance, experience a force which can be used to trap and even cool the atoms as discussed in Section 2.3. As the laser frequency is detuned further and further from resonance, either red- or blue-detuned, only the heating due to spontaneous scattering of this far-detuned laser field need be considered as the dominant mechanism for atom loss from the atom trap. The atoms undergo a momentum recoil due to photon scattering. To quantify the usefulness of an atom trap the scattering rates should be determined and, hence, the trap lifetimes for atoms located near the centre of the trap. The scattering rate, Γ_{sc} , for an atom in a dipole trap is given by [187]

$$\Gamma_{sc} = \frac{3\pi c^2}{2\hbar\omega_0^3}\left(\frac{\Gamma}{\Delta}\right)^2 I(r). \tag{4.6}$$

Here, c is the speed of light in vacuum, ω_0 is the frequency at resonance, $\hbar$ is the reduced Planck's constant, Γ is the dipole transition matrix element between the ground, $|g\rangle$, and excited, $|e\rangle$, states and *I(r)* is the intensity. Generally, one would have to solve

for Γ_{sc} by taking every atomic transition including the hyperfine structure into account. For the case of ^{87}Rb in the $D_{1/2}$ ground state, we can assume that the major contributions to this scattering rate are from the dipole transition rates from $5S_{1/2}$ to the $5P_{1/2}$ and $5P_{3/2}$ excited states. With these simplifications Eqn. 4.6 becomes

$$\Gamma_{sc} = \frac{3\pi c^2}{2\hbar\omega_0^3}\left(\frac{\Gamma_{1/2}}{3\Delta_{1/2}} + \frac{2\Gamma_{3/2}}{3\Delta_{3/2}}\right)^2 I(r), \tag{4.7}$$

where $\Gamma_{1/2}$ and $\Gamma_{3/2}$ are the dipole transition matrix elements from $5S_{1/2}$ to $5P_{1/2}$ and $5P_{3/2}$, respectively. The scattering rate will become more important later when we consider recoil heating losses due to atom scattering from the atom trap.

4.2.3 Trapping Potential

While the proposed configuration has the capability of trapping rubidium, it should be clear that the methods laid out here, with the appropriate choice of dimensions and detunings, are transferable to the trapping of other neutral atom species. Table 4.1 lists the values chosen for the models used in this paper. Throughout this chapter we refer to the blue-detuned power as P_b and the red-detuned power as P_r.

Table 4.1: Parameters used in trapping potential models.

Parameter	Value
Blue-detuned wavelength λ_b	720 nm
Red-detuned wavelength λ_r	1064 nm
C_3 for ^{87}Rb	3.362 mK m^3

Single Colour Slot Trapping Potential

Combining a blue-detuned light field with the vdW potentials arising from interactions of the atoms with both inner dielectric walls of the slotted fibre, a stable position in the y-direction can be obtained. Unlike the usual fibre-based atom traps which have potentials largely defined by the fibre radius, the proposed trap, in its most basic form,

has two parameters, radius and slot width, both of which can be varied and are shown to have a large effect on the shape and efficiency of the atom potential, thereby giving more degrees of freedom in the design and increasing the flexibility of the system. Figure 4.8 illustrates how the potential can be altered by varying either of these two parameters. In the following sections the blue-detuned light was always chosen to be polarised parallel to the slot, i.e. along the x-direction.

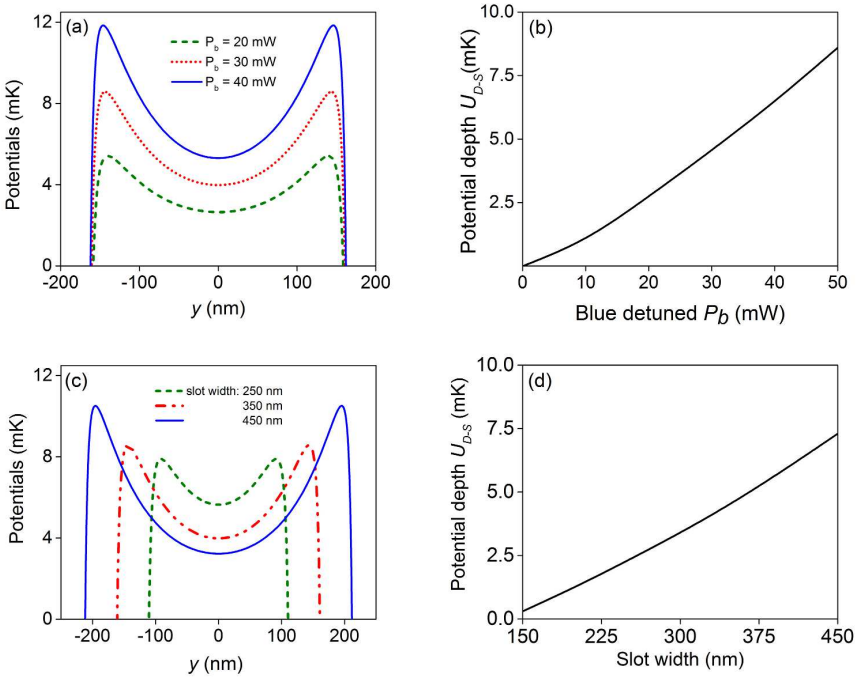

Figure 4.8: (a) Combination of the blue-detuned potential and the van der Waals potential for a slot width of 350 nm. (b) Power, P_b, of the blue-detuned light versus potential depth, U_{total}, for a slot width of 350 nm. (c) Combination of the blue-detuned potential and the van der Waals potential for various slot widths and (d) dependence of trapping potentials on slot width. P_b is fixed at 30 mW.

Figures 4.8(a) and (c) show the effect of changing blue-detuned powers and slot widths, respectively. By changing the power from 0-50 mW, or changing the slot width from 150-450 nm, see Figs. 4.8(b) and (d), trap depths up to 7.5 mK are obtainable. Unfortunately, this single colour trap provides no confinement along the x-direction. To extend this idea to a stable trap in the xy-plane, a red-detuned beam must be included, thereby creating a two-colour trapping scheme within the slot.

Two-colour Slot and Fibre Surface Traps

When a second electric field with sufficiently different frequency is added, mode beating effects between the red- and blue-detuned modes can be neglected. Here, we assumed that the mode beating period between the two fields, E_r and E_b, was much lower than the reaction time of atomic scale motion. Thus, we could assume that the two potentials add linearly such that the total potential was given by $U_T = U_b + U_r$. The addition of an attractive, red-detuned light field, polarised perpendicularly to the slot, created a stable equilibrium position at the centre of the potential in both the x- and y-directions.

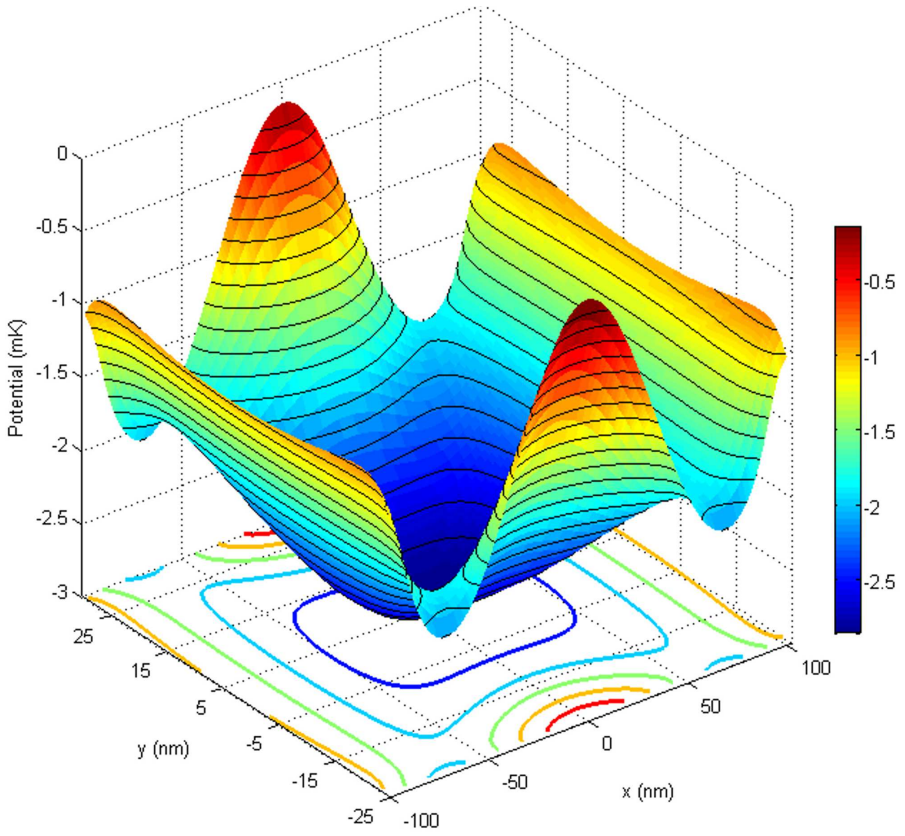

Figure 4.9: Combined surface and contour plot of a trapping potential in the xy-plane for a 1 µm diameter fibre with a 350 nm slot width. P_r=30 mW and P_b=30 mW.

By adding the fields linearly, it can clearly be seen that a trapping well is formed in the xy-plane Fig. 4.9. The shape of this well varies dramatically in shape and depth with different choices of P_b, P_r, slot width, and fibre diameter.

The trap depth in the centre of the slot in the x-direction is largely determined by

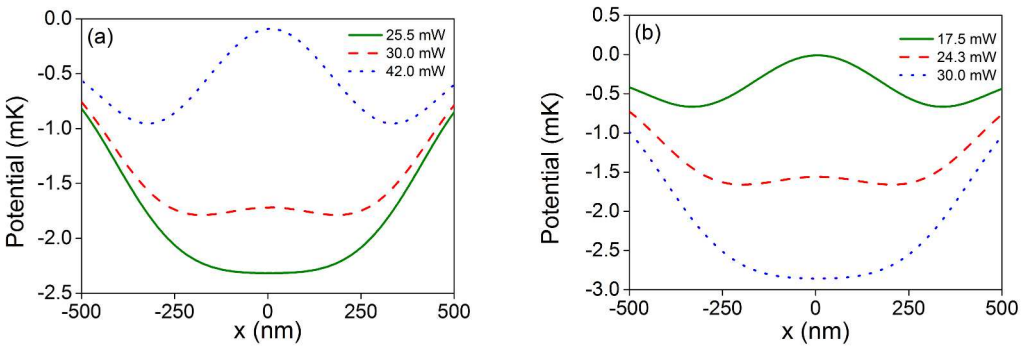

Figure 4.10: Two colour trapping potential for a 1 μm fibre with a 350 nm slot width in the x-direction. (a) P_r is kept at 25 mW while P_b is varied. (b) P_b is fixed at 30 mW while P_r is varied.

the red-detuned power, P_r. At the trap centre, the contribution from the vdW force was found to be negligible, and the contributions from the blue-detuned field were also low since the polarisation of the blue-detuned light was chosen to be parallel to the slot, thereby causing the power to decay away from the walls (see Figs. 4.8(a) and (c)). From Figs. 4.10(a) and (b) we see that a change in the red-detuned power caused the potential depth to change more rapidly than an equivalent change in power of the blue-detuned field (b). When the blue-detuned light field was sufficiently large compared to the red-detuned field the shape of the potential in the x-direction veered away from being harmonic. To avoid complications, such a trap geometry is not considered when we determined the trapping efficiencies.

Varying the power ratio between the red- and blue-detuned fields not only affected the form of the trapping potential inside the slot, Fig. 4.11(b), but also at the outer fibre surface, Fig. 4.11(a). The traps at the fibre surface resembled those proposed by Le Kien *et al.* [165]. An optimal trapping potential configuration for trapping atoms in the slot would maintain a deep trapping potential within the slot while keeping the trapping potential at the outer fibre surface at a local minimum, thereby preventing atoms from accumulating at the outer fibre surface due to the strongly attractive vdW potential.

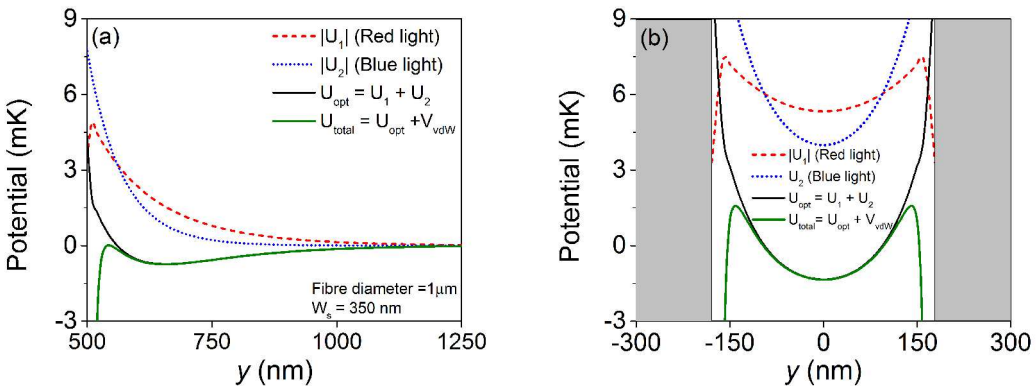

Figure 4.11: Contributions to the two-colour trap at (a) the outer fibre surface, and (b) the slot surfaces to the total trapping potential, U_{total}. Both plots are taken in the y-direction. The configurations are the same for (a) and (b), with P_b= 25 mW and P_r = 30 mW. The grey areas in (b) represent the slot walls.

Trap Optimisation

To optimise the trapping conditions we considered four important parameters: slot width; fibre diameter; and the blue- and red-detuned intensities resulting from the powers P_b and P_r, respectively. Previously, we considered the confinement in the x-and y-direction. Here, only the field in the y-direction was investigated for trap optimisation. This allowed us to compare the fields both inside the slot region and at the outer fibre surface, whilst ensuring the vdW potential was correctly balanced within the slot region. It is known that the x-direction potential forms a stable equilibrium point at the trap centre provided that one avoids the extreme situations such as those given in Fig. 4.10; therefore, only the y-direction trapping potential need be used for determining an optimum configuration. The extreme points we refer to here are the corners of the potential, which we can see visually in Fig. 4.10.

By varying the input powers of the blue- and red-detuned beams, it was possible to choose an appropriate pair of values for use as default powers when considering the other parameters, such as slot width and fibre radius. The values were chosen in order to provide a deep potential inside the slot, with a minimum value below zero to facilitate the entry of rubidium atoms. For example, in Figures 4.12(a) and (b), we can see that, within the

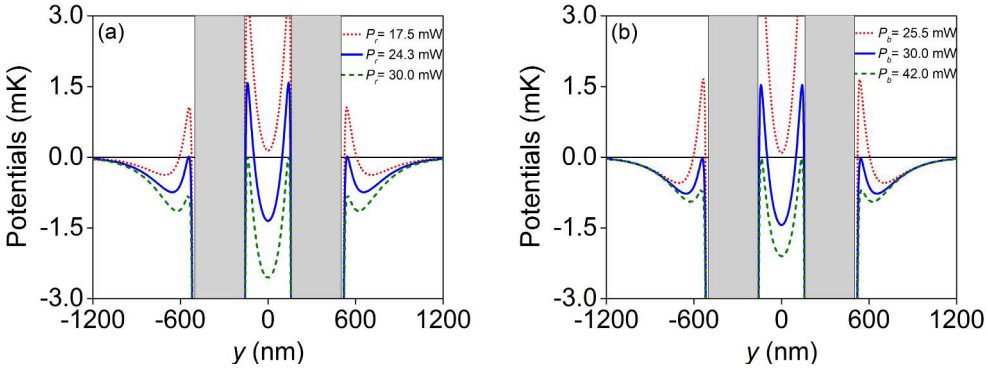

Figure 4.12: (a) Effect of the power, P_r, of the red-detuned light on total potential, U_{total}, while the power of the blue-detuned light, P_b, is fixed at 30 mW; (b) Effect of the power P_b of blue-detuned light while P_r is fixed at 25 mW. All fibre parameters are the same as for Fig. 4.11.

slot region, the minimum value of the potential was only below zero for certain power configurations.

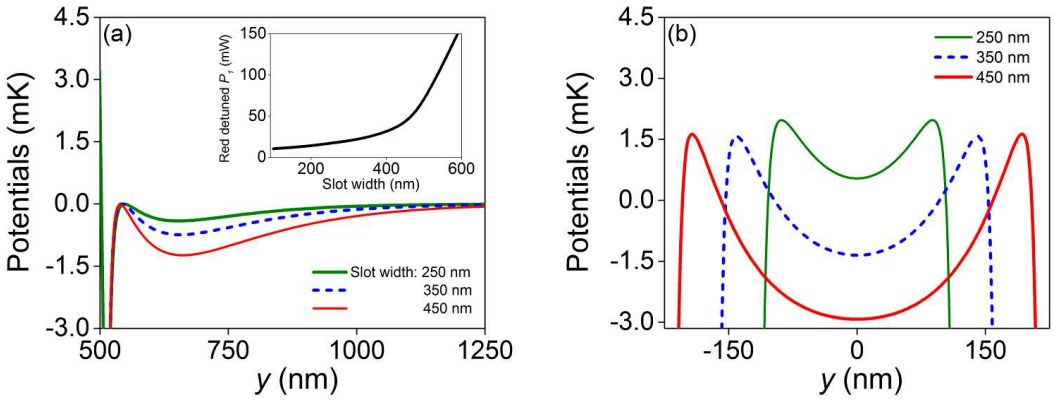

Figure 4.13: (a) Trap depth U_{D-F} at fibre surface and (b) trap depth U_{D-S} at slot fibre centre for different slot width values. The inset in (a) indicates the power P_r of red-detuned light required to keep the net optical potential depth U_{D-F} at a local minimum value for varying slot widths. The power of the blue-detuned light P_b is fixed at 30 mW and the fibre diameter is 1 µm.

The power required to keep the outer surface trap depth at a local minimum as a function of slot width and P_r was important in the choice of a suitable input beam power, leading to values in the 30 mW range. Motivation for this was two-fold: firstly, we

could see from Fig. 4.13(a) that the power required to maintain the fibre surface trap at a minimum became unmanageable beyond a slot width of 400 nm; secondly, we must constrain ourselves in some respect because there is no well-defined upper limit in a trap of this type. Higher powers lead to deeper traps, higher scattering rates and, eventually, fibre performance decay. A power of approximately 30 mW is reasonable for use with an optical nanofibre in ultrahigh vacuum for slot widths in the 250 nm to 450 nm range [17, 167].

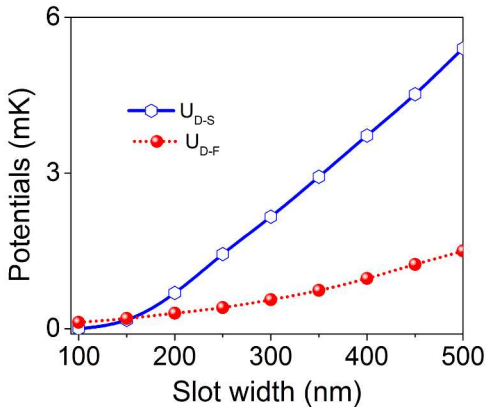

Figure 4.14: Trap depths, U_{D-F}, at fibre surface (dotted line) and U_{D-S} at slot fibre centre (solid line) versus slot width. The power of blue-detuned light, P_b, is fixed at 30 mW while the red-detuned light power, P_r, is varied to place the net optical potential depth, P_{D-F}, at a local minimum value, see the inset in Fig. 4.13(a).

Figure 4.14 demonstrates how this choice of blue-detuned power can produce a trap with a large difference between the trap depths inside and outside the fibre. This also provided some motivation for the choice of a slot width of 350 nm. This value allowed for a significant difference in the outer and inner potentials (U_{D-F} and U_{D-S}, respectively) and this size was approximately one third of the diameter of the fibre, thereby alleviating most issues regarding the fibre's structural stability following etching.

In an *ad hoc* attempt to, at least locally, optimise the trapping conditions we began by using a blue-detuned power, $P_b = 30$ mW, while varying the other parameters independently to see their effect on the potential. Figure 4.15(b) gives a range of values where it is possible to obtain a suitable minimum potential value. Fibres of about 1 µm are located

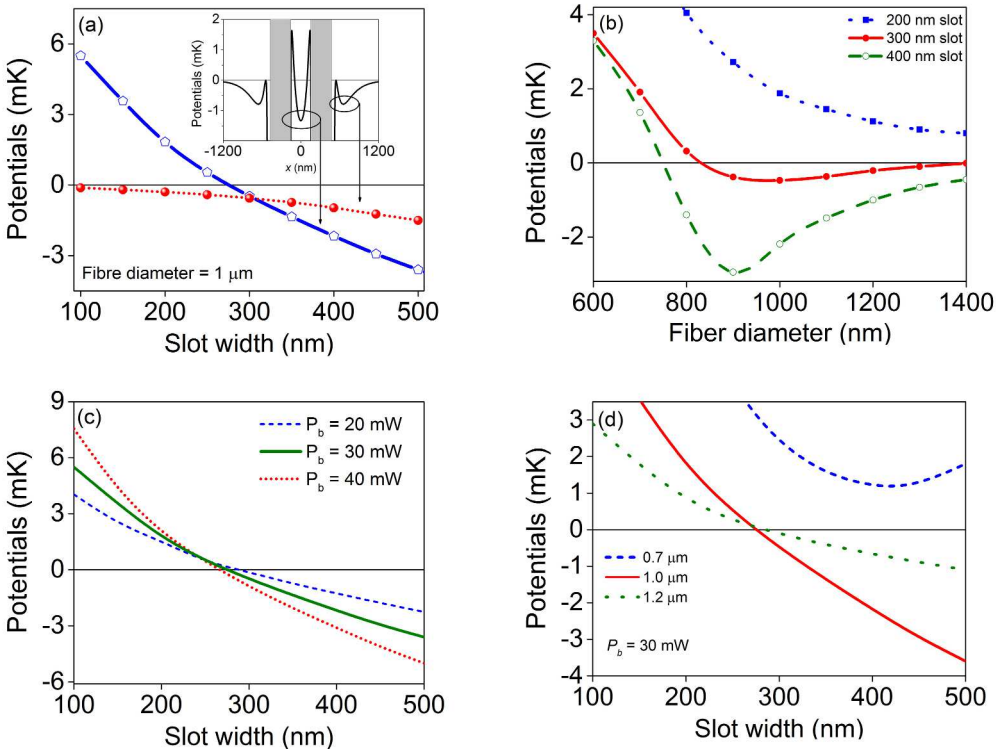

Figure 4.15: (a) Local minimum value of the trap depths at fibre surface, U_{D-F}, and at slot fibre centre, U_{D-S} versus slot width. For all figures the powers of the red- and blue-detuned light, P_r and P_b, are chosen to create an outer fibre surface trap depth at a local minimum value as Fig. 4.14. (b) Minimum trap potential U_{D-S} versus fibre diameter for different slot widths, (c) minimum trap potential versus slot width for varying P_b powers, and (d) minimum trap potential versus slot width for various fibre diameters.

near the minimum of this curve for a 300 nm slot width. In Fig. 4.15(d) we showed that the potential created using 30 mW of both red-detuned and blue-detuned power for both 1 μm and 1.2 μm fibres yielded potentials that are below zero for slot widths greater than 275 nm. For a 0.7 μm fibre it is clear from Fig. 4.15(b) that this condition was never met regardless of the chosen slot width. A 0.7 μm fibre still created a strong trap with an adequate potential depth, but it lacked the capability of allowing atoms to easily enter the trap since those coming from infinity would need to overcome a net positive potential before entering the trap centre. As the fibre diameter was increased further, the mode became well-confined to the larger segment sizes, provided that the slot widths were also in the same range, given in Fig. 4.15(d). This discussion does not preclude the use of

smaller fibre diameters; it merely requires that the wavelengths of light chosen be tailored to the particular fibre size. A 0.7 µm diameter fibre, for instance, could be used provided a blue-detuned wavelength shorter than 720 nm is used.

Data in Figs. 4.15(b) and (d) indicate that larger slot widths produce better trap depths, but this comes at the cost of requiring higher red-detuned powers as is demonstrated by the inset of Fig. 4.13(a). Changing the blue detuned power has relatively little effect on the potential as can be seen in Fig. 4.15(c). Fibre slot sizes much larger than 350 nm require very large red-detuned powers to compensate for the blue-detuned potential at the outer fibre surface. Our final choice of fibre was a 1 µm diameter fibre with a 350 nm slot width. The diameter and slot size were chosen by inspection of Fig. 4.15(b). Here, we see that a low potential minimum occurs at this value. Larger slot sizes were investigated, but the power required to create a viable x-direction trap began to exceed 40 mW once $W_s > 350$ nm slot widths were chosen.

4.2.4 Atom Trap Viability

In a two-colour trap the total scattering rate, Γ_{total}, is the sum of the scattering rates from the blue- and red-detuned fields, i.e. $\Gamma_{total} = \Gamma_{red} + \Gamma_{blue}$. From this value, a characteristic coherence time, $\tau_c = 1/\Gamma_{total}$, can be determined [189]. Each scattered photon from either field contributes some recoil energy to the atom. This will lead to a loss of atoms from the dipole trap. For a trap of depth U_D, a trap lifetime, τ_c, which only takes recoil heating into account for the chosen trap configuration is given as

$$\tau_c = \frac{U_D}{2(E^r_{blue}\Gamma_{blue} + E^r_{red}\Gamma_{red})}, \tag{4.8}$$

where E^r_{blue} and E^r_{red} are the recoil energies associated with a blue and red photon, respectively. Along the x-axis the contribution from the blue-detuned field is at its minimum value, hence the potential here reached a maximum near or below zero. In contrast, the y-axis potential will have the same minimum value at the centre, but due to increasing

blue-detuned intensity. As an atom approaches the walls the maximum value will be above zero due to the field's repulsive property. When determining the trap lifetimes, we only considered the 1-D trap along the x-direction as it has a lower maximum depth than the y-direction.

Table 4.2: Trap parameters found by varying P_r with respect to P_b, which was fixed at 30 mW. Values were obtained for a fibre width of 1 μm and a slot width of 350 nm

P_r (mW)	Trap Depth U_D (mK)	Scattering rate (s^{-1})	Coherence time (ms)	Trap lifetime (s)
24.3	1.5	98.78	10.1	42
30	2.8	105.72	9.46	75
35	4	111.81	8.94	104

4.3 Slot Endface Geometry

Early in our investigations [191], we limited our model to a pseudo-infinite geometry where the transition between the ultrathin optical fibre and the slotted region did not exist. This choice was made due to a number of factors and our inexperience with many of the modelling software packages was chief amongst them. We later revisited the problem to see how the interface between the two regions affected the fields. A simple, yet effective, method for modelling how various modes propagate through a nanostructured ultrathin fibre is to use the eigenmode expansion (EME) method. In this method, one can decompose the electromagnetic fields present in a given structure into a basis set of local eigenmodes. The eigenmodes are found by solving Maxwell's equations in each local cross-section. This can be done at some finite number of locations along the length of a waveguide, hence determining the coupling from one section to the next. For a given ultrathin fibre, all of the modes which can be excited at the input can be determined. The first four modes are shown in Fig. 4.16. These modes can be excited individually at the entrance port of our fibre. As the initial mode propagates through the system it redistributes itself amongst the available modes. Finally the amount of power in each of

the output modes can be measured and a scattering matrix for the modes of the nanostructured ultrathin fibre can subsequently be constructed.

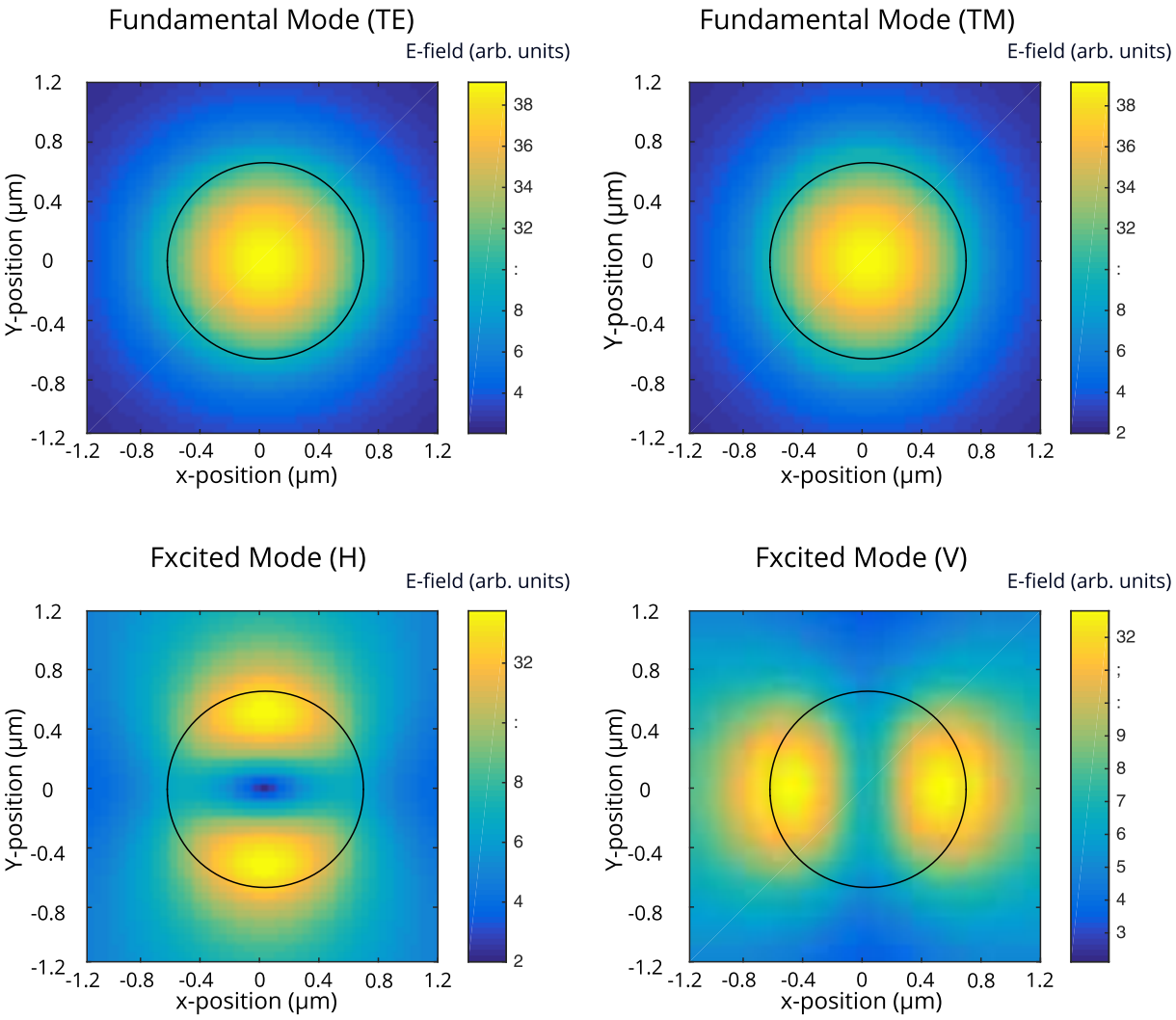

Figure 4.16: The first four modes of a nanostructured ultathin optical fibre with a waist diameter of 1.4 μm and a slot width of 300 nm.

The major drawback to this technique is that it does not consider radiation modes. The model can only account for modes which redistribute themselves amongst the available modes of the system at any given distance along the z-axis. Here, as before, we assume that the fibre's longitudinal axis is coincident with the z-axis. However, as we will discuss in Chapter 5, we know that the transmission of the nanostructured ultrathin fibres is very close to that of the modelled fibres, so we can assume that coupling to radiation modes is negligible.

The simplest geometry for such a nanostructured ultrathin fibre is that shown in Fig. 4.1. The ultrathin section is simply attached directly to the structured region. However, as one might expect, this is not the optimal geometry to allow the adiabatic transfer of the modes from one segment to the next. Instead one might opt for a different geometry where the slot is slowly tapered to the desired slot size, see Fig. 4.17.

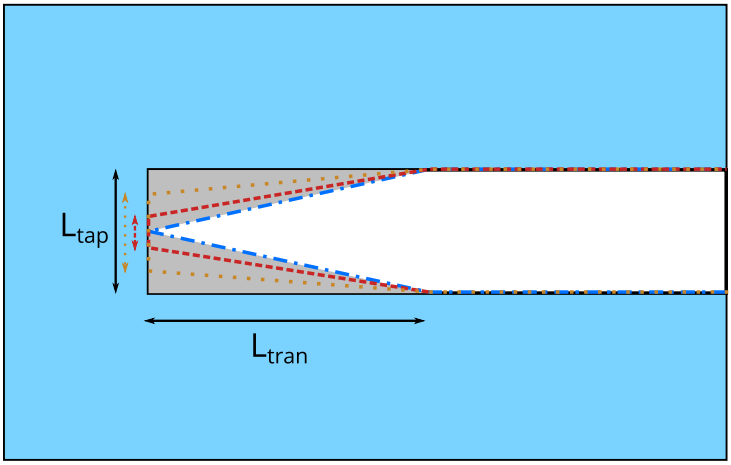

Figure 4.17: Different slot geometries where there exists a transition region for the slot opening with varying starting lengths, L_{tap}. L_{tap} varies from zero to the full length of the opening and L_{tran} denotes the length of the transition region.

For this model we chose a fibre with a waist diameter of 1.4 µm and a slot width of 300 nm. These values are different from those already used in this chapter, but they were chosen to agree with the experimental dimensions in Chapter 5. While a relatively large waist diameter supports a few modes, the nanostructured region can only support the fundamental mode in both TE and TM configurations. Figure 4.18 shows how well these modes of the slotted tapered optical fibre propagate from left to right along the full length of the taper region. The transition length, L_{tran}, was chosen as 1 µm. As may be expected, such high transmissions are not reported when the higher order modes are considered. If we consider the first excited modes, both H and V, given in Fig. 4.16, we can see significant losses. For the V excited mode, the losses can be as high as 30%. This is due to the fact that the lobes of this mode distribution cut across the slot. The H mode retains a high transmission as its mode distribution more closely matches that of

the fundamental mode of the nanostructured region.

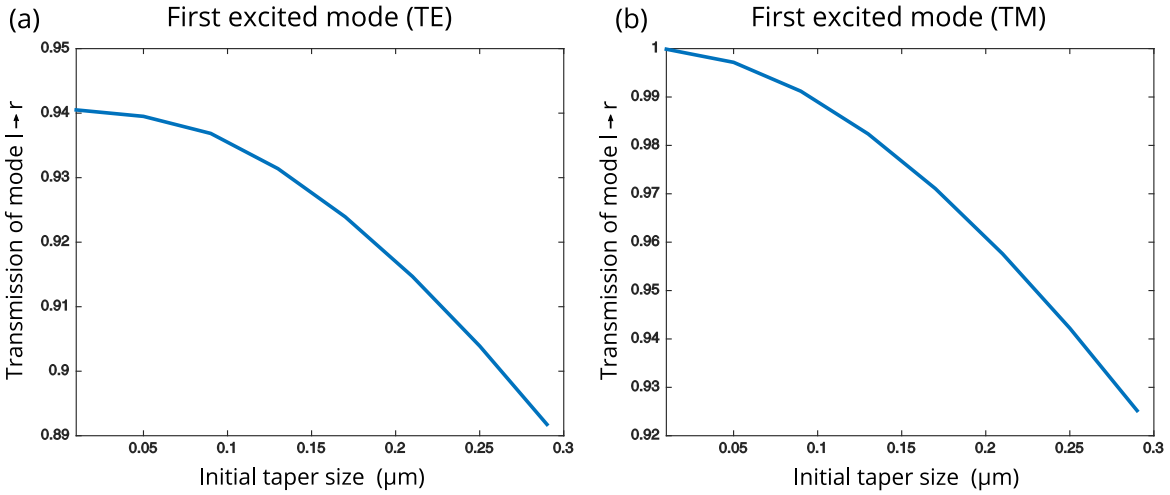

Figure 4.18: Propagation of first two excited modes for a tapered slot geometry. (a) First excited mode in the TE configuration. (b) First excited mode in the TM configuration.

We can see that the TM mode propagates with less loss than the TE mode, but even for an untapered slot region the transmission remains quite high at $\geq 89\%$. With a starting taper opening length, L_{tap}, of zero, we can see that the TM mode propagates with no loss, while the TE mode remains lossy. This result can be understood if one considers that when the TE modes meet the discontinuity there is always some component of the E-field which meets the discontinuity at a 90^o angle, thereby maximising the loss, whereas for the TM mode the E-field travels at some angle with respect to the the fibre axis allowing it to couple more homogeneously to the new modes in the taper region. An image of the E_x fields of a tapered and untapered slot are given in Fig. 4.19. Here we can see a difference in the fields given twodifferent slot geometries. The E_x component was shown as it contributes the most to the field, and is perpendicular to the slot face. While it is difficult to see, there are significantly fewer reflections for the tapered geometry.

Due to the low loss of the nanostructured fibres, both predicted here and measured experimentally, such a geometry was not created. For future work involving atom trapping it would be prudent to use such a geometry. The particle trapping work presented in Chapter 5 was less sensitive to stray light escaping the fibre at the nanostructured region,

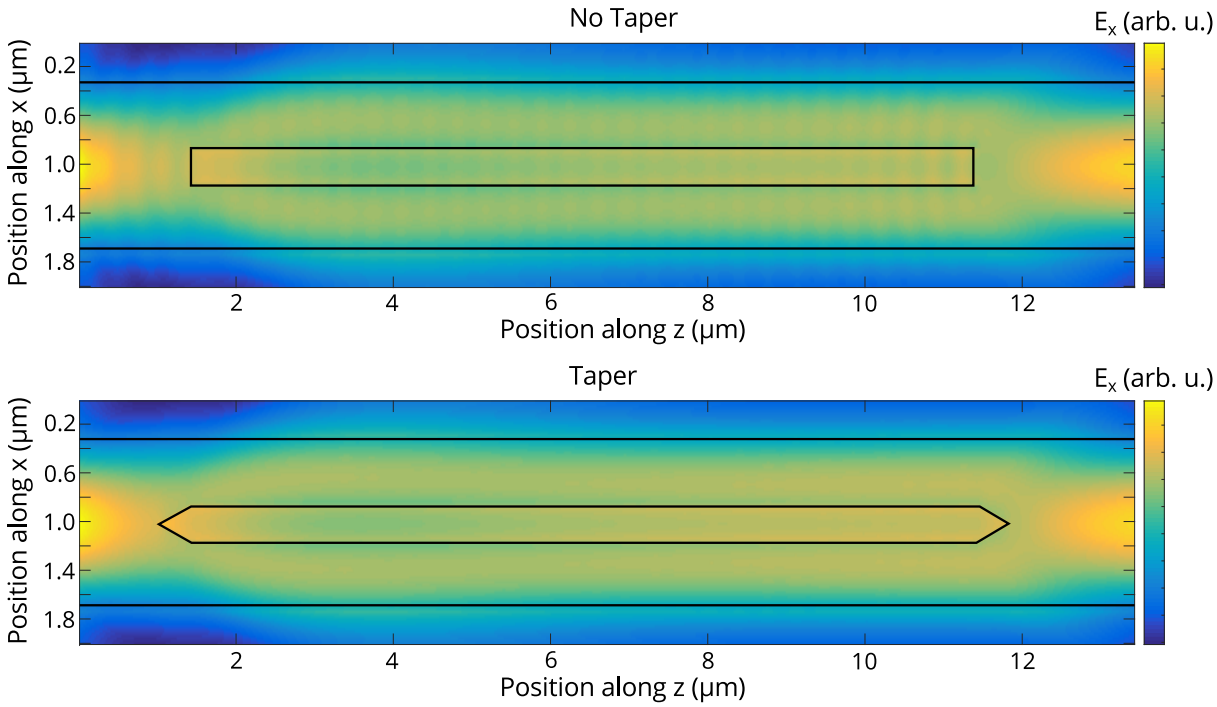

Figure 4.19: Propagation of the fundamental fibre mode, polarized in the x-direction, along an untapered (top) and tapered (bottom) slot. The length of the taper region is 0.4 μm.

hence the fabrication of a tapered slot region was not considered essential.

4.4 Conclusion

Optical micro and nanofibres have already been shown to be an invaluable tool in trapping and probing atomic systems. We proposed that a nanostructured optical nanofibre is capable of trapping atoms inside the slot region, rather than at the surface, via the use of blue- and red-detuned beams. We investigated the use of the slotted waveguide structure over a broad range of configurations. By carefully choosing fibre diameters and slot widths and by using tapered fibres with exponential taper profiles we can ensure that any contributions from higher order modes is negligible [74]. We have also shown that the polarisation of the light plays a crucial role in the realisation of such a trap. With the chosen electric field configuration, atoms should be trapped in a line along the longitudinal axis of the structured fibre with potential minima located at distances of 140

- 200 nm from the slot walls. Using fundamental modes in the slotted region we have shown that a two-colour scheme is a viable method of producing adequate atom traps. For ^{87}Rb, trap depths of 4 mK, coherence times of the order of 10 ms and trap lifetimes of approximately 100 s should be accessible using modest input powers. Using an estimate for the optical depth per atom, namely the ratio of the on resonance scattering cross-section to the effective mode area, i.e. $OD = \sigma_0/A_{eff}$, we obtain a value of 0.33 for the final configuration given in Table 2. We deal exclusively with a slot that is assumed to have an infinite length, but in practice this slot would have a finite length and would be connected to an optical fibre pigtail at each end. Preliminary modelling work shows that $> 70\%$ of the input mode can be transmitted beyond the end face of the slotted region. Flat end surfaces are the simplest case, but by tapering the slot ends we can significantly increase transmission into and out of the slot if required. Further analysis of this would require an in-depth study of how the modes couple from the slot region back into the fibre modes and is beyond the scope of this work.

This preliminary study opens up many other avenues for atom trapping, such as standing waves, two-colour traps, single-colour traps using higher order modes, magic wavelength traps, and the introduction of additional slots. We believe that, with this geometry, a stronger coupling of atom emissions into the guided modes of the waveguide should be achievable, as should more efficient interactions between the atoms and any other light fields present in the nanofibre due to the atom's close proximity to the slot walls. The scalability of this design, along with its long coherence times, high optical depth, and direct integration to optical networks make it an excellent candidate for quantum communication schemes. Experimentally, creating a slotted nanofibre is possible using a combination of existing techniques. Nanostructuring of an optical nanofibre using focussed ion beam (FIB) techniques has been reported [192]. Misalignment of the slot position along the fibre axis would lead to asymmetric potentials. A cursory investigation indicates that it would be possible to create a trapping potential for misalignments of the slot position from the fibre centre of the order of 10 nm, which coincides with the accuracy of

an FEI Helios Nanolab 650 Dualbeam FIB/SEM. Alternatively, processing of the optical fibre using tightly focussed *fs* laser pulses could be considered [193].

In Chapter 5, we shall discuss the fabrication of a nanostructured ultrathin optical fibre, or structured tapered optical fibre (STOF), as well as some experimental evidence for the trapping of 100-200 nm polystyrene and silica beads. This chapter shows how the device can, at least theoretically, be extremely useful in the field of atomic physics. Ideally, an experimental verification of this device in a cold atom system would be the next step but experiments in cold atoms often take a very long time from their inception to their experimental realisation. Instead, it is interesting to look towards the field of optical trapping using dielectric particles as a testbed for such a device since, as discussed in Chapter 2, there are many similarities between the physics behind such systems. This serves as a motivation for the work in the following chapter.

Chapter 5

Particle Trapping using Ultrathin Optical Fibres[1]

Particle trapping and atom trapping are in many ways sister fields, both historically and in their implementation. The development of new tools to probe atomic systems can often be a long, difficult process which requires rigorous experiments to test their viability before they can be fully implemented in an experimental setup. Ideally, one would work with these devices under ultrahigh vacuum in the same conditions as the proposed environment for the cold atomic system, but since cold atom experiments require a lot of resources and personnel it is often not possible to simultaneously test a new device while performing other experiments. In this chapter we shall describe the fabrication process of a STOF, as theoretically discussed in Chapter 4, and then go on to show how it can be combined with a colloidal particle solution for the purpose of particle trapping. In this way, we can test the device in a different setting to a cold atomic system, but still show its viability.

The previous chapters have discussed ultrathin optical fibres in the context of atom trapping. However, the trapping methods which are suitable for atoms are, quite often, also suitable for trapping microscopic particles, provided a few conditions are met; the background to these problems has been briefly discussed in Chapter 2. Typically, a trap

[1]Sections of this chapter have been adapted from published papers. All work presented here is the sole work of M. Daly under guidance from V. G. Truong and S. Nic Cormaic.

can be considered stable if the depth of its trapping potential is $\geq 10k_{\mathrm{B}}T$. This condition comes directly from thermodynamic considerations related to the Boltzmann energy distribution. A stable trap must allow for variations from the mean energy which we can define as requiring that the Boltzman factor be much less than one, i.e. $exp(-U/k_{\mathrm{B}}T) \ll 1$. Particle trapping, the focus of this chapter, can be performed in a variety of different configurations. Free-space beams with Gaussian or more exotic profiles are often used to trap particles. For Gaussian beams it is easy to understand that the Rayleigh diffraction limit fundamentally restricts the electric field gradient across a particle, resulting in difficulty when trapping submicron particles without providing high-intensity fields which can easily destroy the trapped objects.

Today, nano-optical techniques, such as near-field optics and plasmonics, provide primary solutions to this problem [1, 194]. Photonic crystal cavities [85, 195], plasmonic double nano-holes [128, 130], slot waveguides [196, 197], and micro-nanofibres [160, 198] are just some of the devices which can confine light locally to regions smaller than achievable using diffraction-limited systems. Aside from modifying how the trapping fields are generated, it is also possible to change the material of the particles to be trapped, thereby reducing the difficulties associated with trapping submicron particles. For example, higher index particles, such as gold nanoparticles [73, 199] or nanodiamonds [200], are excellent candidates for nanoscale trapping. However, biologically-relevant materials typically have low refractive indices, thereby negating the trapping advantages associated with higher index particles.

In this chapter, we discuss a nanostructured, evanescent optical trapping device based on the combination of a slot waveguide with an ultrathin fibre [191] which has been described in great detail in Chapter 4. Ultrathin fibres are extremely versatile due to their compact size, enabling them to be integrated noninvasively into many systems, such as optical tweezers [78, 201, 202] and cold atom clouds [203]. When light propagates through an ultrathin fibre, a significant portion of the electric field exists outside the waveguide as an evanescent component, allowing for easy interaction between the guided light field

and the surrounding medium. Previously, unmodified ultrathin fibres have been used for various experimental configurations such as (i) optical trapping of dielectric particles [65, 66, 204–206], (ii) cavity quantum electrodynamics (cQED) using single quantum emitters [207], (iii) light coupling in and out of whispering gallery resonators [208], and (iv) trapping and probing cold atomic systems [209–212] or atomic vapours [213, 214]. More recently, ultrathin fibres have been modified to increase their versatility across a range of fields, through, for example, the incorporation of SNOM tips [215] or extraordinary transmission apertures [136]. Evanescent field trapping has also been realised using what is known as a slot waveguide, as first demonstrated by Yang et al. [83] who trapped 75 nm dielectric nanoparticles. Laser powers of 250-300 mW provided stable trapping against a constant fluid flow. The high refractive index contrast between the Si slot and the surrounding water, along with the small slot separation (<100 nm), produced a quasi-TE mode with a large field discontinuity across the boundary that was used for trapping.

While other trapping techniques, such as self-induced back action [115] (SIBA), can confine particles in three dimensions with low optical powers, they lack adequate control over the particle's position. For optical fibres, dynamic three dimensional control over the position of trapped particles becomes difficult, but recent developments using orbital angular momentum carrying beams for particle trapping [24] may soon allow for the spatial translation of particles, whilst still maintaining strong trap stiffnesses.

The slotted tapered optical fibre (STOF) used in this work is a device which exploits the overlapping evanescent fields of a slot waveguide-like structure to further enhance its trapping ability, both for atoms [191] and submicron particle trapping [216]. We sought to create an entirely fibre-based trapping device using evanescent fields to localise particles with a high degree of control in regimes inaccessible to standard ultrathin fibres. A nanoscale slot is introduced at the waist of an ultrathin fibre using focussed ion beam (FIB) milling, thereby creating a slot waveguide-like region where the optical forces are greatly enhanced. This provides three dimensional confinement within a small trapping volume, while also providing the potential for one dimensional position control of the

trapped particles along the slot through the use of a sliding standing wave, i.e. a particle conveyor belt. Here, we demonstrate trapping of 200 nm silica particles using a STOF. We also show how light transmitted through the fibre pigtails either side of the STOF can be analysed to determine the trap characteristics. Finite element method (FEM) and frequency domain time domain (FDTD) simulations are used to simulate the STOF modes and these are subsequently used to model the forces acting on the particles using perturbative and energy density methods.

The confined geometry of the STOF, as discussed in Chapter 4, produces electric fields within the slot which can induce optical forces in dielectric particles which are more than sufficient to trap them. While there are many similarities between cold atom and particle trapping, it should be clear that the orders of magnitude are very different. A relatively small trap depth may be sufficient to trap cold atoms, but, due to the increased Brownian motion of the large, hotter dielectric particles, a deeper potential is required. Optically induced forces are typically the dominant force in such traps, though in some cases the thermophoretic force, i.e. the force induced due to temperature gradients in the system, can also be appreciable. It is typically easy to distinguish between these two types of trapping, as we shall discuss later.

To prove the concept of the STOF we needed to be able to trap low refractive index contrast particles with diameters below 500 nm. A demonstration of such trapping would be irrefutable evidence of the trapping capability of the device. In this section we will introduce the experimental setup as well as the necessary analytical techniques necessary to interpret the resulting data and, hence, show the trapping of submicron particles.

Here, optical trapping is discussed exclusively for situations where there is a low refractive index contrast between the trapped object and the surrounding medium, i.e. metallic particles and high-index materials, such as gold, silver, diamond, etc. are excluded. This choice was made since we focus on systems with optical properties comparable to biological systems. Ultrathin optical fibres have previously been used, in our group and other groups [64–66, 78], to trap micron-sized particles (with low refractive index contrast with

respect to their surroundings) near the surface using the gradient forces exerted by their evanescent fields. However, their application in submicron regimes is limited, with particle sizes much smaller than 500 nm becoming quite diffcult to trap unless other materials, such as diamond or metallic particles, are used [65, 217].

5.1 STOF Fabrication[2]

The fabrication procedure for a STOF, as summarised graphically in Fig. 5.1, is a three step process consisting of (i) optical fibre tapering and mounting, (ii) coating, and (iii) FIB milling. Each step is discussed in detail in the following sections.

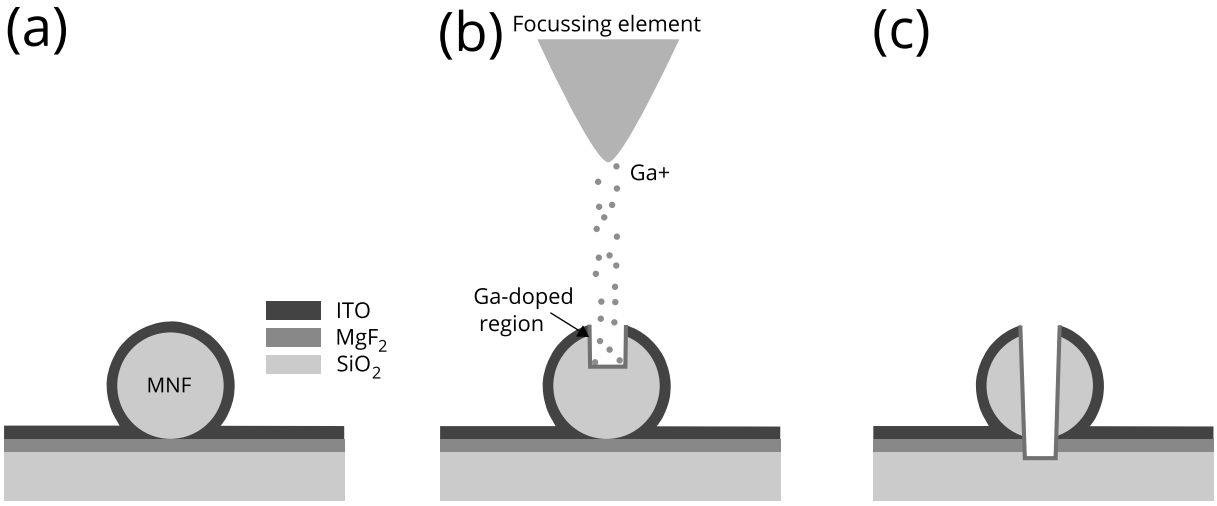

Figure 5.1: Outline of the fabrication process. (a) An ultrathin fibre is placed on a microscope slide that has been pre-coated with a thin layer of MgF_2 which is then sputter coated with a 30 nm layer of ITO. (b) Using a focussed ion beam, the structure is etched into the ultrathin fibre. (c) The finished STOF after etching; typically the etch depth is overestimated to ensure complete milling of the cavity.

[2]Parts of this section were adapted from Daly, M., Truong, V. G., & Nic Chormaic, S. Nanostructured tapered optical fibers for particle trapping Proc. SPIE 9507, Micro-structured and Specialty Optical Fibres IV, 95070E (May 7, 2015)

5.1.1 Tapering Process

The first step of the process is tapering. This has been discussed in Section 2.1.3 so the finer details will be excluded. Here, optical tapers were produced from standard, telecommunications-grade optical fibre. All the STOFs shown in this section, and in almost all the cases shown in this thesis, were produced using Thorlabs 1060XP single mode fibre. For our purposes, adiabatically tapered fibres with an exponential taper profile were used. Tapering was performed using a heat-and-pull rig; we used either a static, microheater based rig, or a hydrogen/oxygen flame-brushed rig, as described in Ward et al. [62]. Experimentally, little difference was observed between STOFs produced using either heat-and-pull system although higher transmission fibres were more consistently obtained using the hydrogen/oxygen rig.

Ultrathin fibres with diameters between 1 and 2 µm were produced and SEM images, which were taken during the STOF fabrication process, show that the ultrathin fibres were uniform in diameter over a large ($\gg 2$ mm) distance. A crucial element which led to the success of this project is cleanliness. Cleanliness is essential for all ultrathin optical fibre processes. The fabricated ultrathin fibres were immediately mounted and transferred to clean containers and either stored in a vacuum desiccator until they were needed, or immediately transferred to the vacuum chamber of the sputter deposition system for the next step in the process. Isopropyl alcohol (IPA) was used to clean the containers used for transferrals, as well as cleaning the work surfaces near the heat-and-pull rigs. Acetone was also used on non-plastic surfaces since acetone is corrosive when used with certain plastics. Between any two steps great efforts were made to keep the environment clean and minimise contamination.

5.1.2 Coating Process

The microfibres must be mounted on a suitable substrate prior to coating because of requirements in the ion beam processing stage; MgF_2 was chosen due to its low refractive

index relative to that of the optical fibre's cladding/core indices. This serves to prevent light loss through coupling between the fibre and the higher refractive index soda-glass microscope slides that are typically used to mount the fibres for optical manipulation experiments. Initially, it was thought that during the transfer of the ultrathin fibre from the heat-and-pull rig to the coated slides care must be taken to ensure that the fibre is in contact with the slide at the waist region (as shown in the process diagram in Fig. 5.1), to allow the coating process to form a semi-continuous layer between the MgF_2 and the ultrathin fibre fiber. Later it was discovered that this was not necessary, the reasons for which will be discussed in the following section. In practice, a freely floating ultrathin fibre coated with a thin conductive material is sufficient for high resolution FIB milling.

To minimise charging effects induced in the dielectric ultrathin fibres by the intense incident beam of Ga+ ions from the FIB, a thin layer of conductive ITO (Indium Tin Oxide) must be placed over the ultrathin fibre + MgF_2 system. ITO was chosen due to its high conductivity and high transparency in the 700-1100 nm regime. The layer thickness of ITO is kept extremely thin. Initially, layers of 30 nm were used, but, through subsequent testing, layers as thin as 5 nm were sufficient to mitigate any charging effects. Thinner layers may have also been successful, but it was difficult to accurately measure these using simple techniques. Thinner layers also serve to prevent light from propagating in this new, higher refractive index material and their presence in FDTD and FEM calculations can be effectively ignored. An ULVAC vacuum sputter deposition system was used to coat the fibres with ITO. The recipe for the ITO layer is given in Table 5.1.

Table 5.1: Parameters for ITO sputter process

Parameter	Value
Power Supply	100 W
Deposition Time	180 s
Shutter Time	20 s
Temperature	100°C
Mass Flow Controller	20 sccm
Rotation Speed	5 rpm

5.1.3 Etching Process

After coating, the samples were quickly transferred to the vacuum chamber of the Helios FIB systems. Two different FIB systems were used to create the STOFs. The system with which we worked initially (Helios Nanolab^{TM}Dualbeam 650) was heavily used by the biological sciences community and, despite having relatively high resolution, its stability was not ideal. Later, a new FIB system (FIB-SEM Helios G3 UC) was bought primarily for the use of the physical and chemical sciences.

The stated operational vacuum for both FIB-SEM systems is between 10^{-2}-10^{-5} Pa. However, to achieve high resolution milling of the samples, they were often left in the vacuum chamber overnight, if possible, or for a minimum of two hours, to achieve a vacuum pressure at the lower limit of the operational value of approximately 2×10^{-4} Pa. Once an adequate vacuum pressure was reached, the etching process could begin. Despite the preventative measures, some small amount of drift may remain in the system. This can be attributed to either dielectric charging, poor adhesion of the ultrathin fibre to the MgF_2 surface, or drift in the piezo stages used to translate the samples within the vacuum chamber. The older Helios Nanolab^{TM}650 was found to have substantial stage drift. To counteract this, the etching process was broken down into short etching periods of a few seconds each. Using a beam voltage of 30 kV, a current of 33 pA, and a dosage of 0.27 m^3/nC, the etch rate of the ultrathin fibre was found to be approximately 3.5 nm/s. Between samples, the operational current was found to vary somewhat. The software used for the Helios Nanolab DualBeam 650 reflects changes in the operational current in its calculations, so the exact etch rate was altered on a sample-to-sample basis. Fibres with slot widths of 300 nm were fabricated in this way and are shown in figure 5.2.

The second FIB system, namely the FIB-SEM Helios G3 UC, was found to have much higher stability. With this system, etching could be performed continuously which removed the need to realign the structure periodically. Again, a beam voltage of 30 kV and a beam current of 33 pA were used. However, a dosage of 0.29 m^3/nC was used

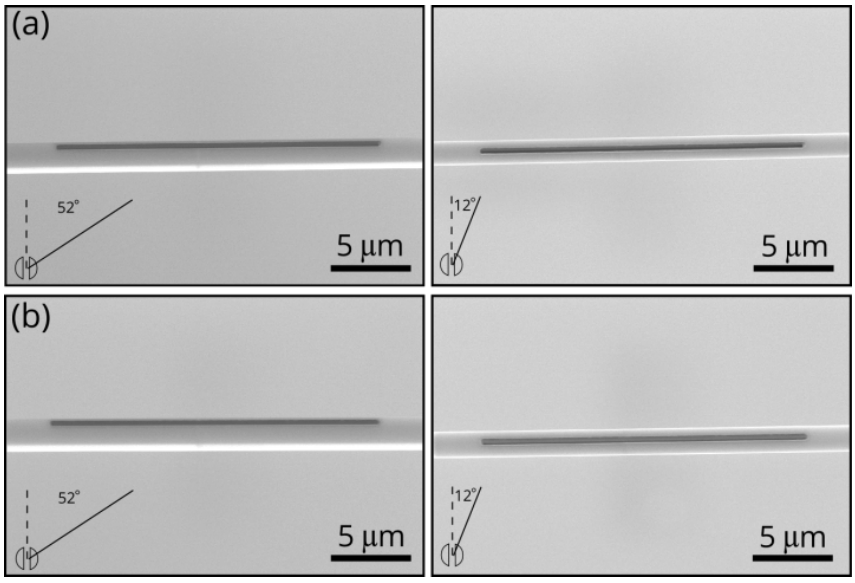

Figure 5.2: SEM images of two fibres (a) and (b) from two different viewing angles (viewing angles shown on images, solid black line indicates line of sight). Fibre diameters are 1.56 µm and 1.4 µm for (a) and (b), respectively.

as the depth of the etch could be more reliably tracked at these settings. Etching times varied from 3-5 minutes depending on the thickness of the ultrathin fibre. SEM images of STOFs fabricated using this system are given in Fig. 5.3. In Fig. 5.3(b) we can clearly see the 'shadow' cast below the etched STOF. This 'shadow' indicates that the milling has been performed directly through the fibre which confirms our fabrication process. Initially concerns were raised that the slot was not being milled directly through the fibre as it was very difficult to observe using conventional imaging techniques. The image also shows that the fibre does not need to be located on the surface of a substrate to be successfully etched. This is of particular interest when cold atoms are considered as the fibre can be left on a U-mount and still be etched successfully. This reduces the number of steps required, thereby reducing the exposure of the device to contaminants.

STOFs fabricated in the older FIB system were produced less reliably and took a considerable amount of time to make due to the hands-on approach required to control the etching parameters. There exist other means of automatically controlling the etch which were not explored, for example the use of a marker on the substrate which could

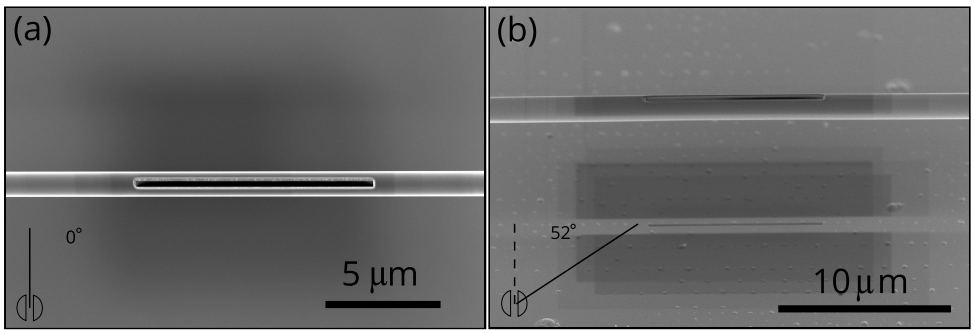

Figure 5.3: SEM images of two fibres (a) and (b) from two different viewing angles (viewing angles shown on images, solid black line indicates line of sight). Both fibres have a diameter of 1.4 µm, a slot width of 300 nm, and a slot length of 10 µm.

be used to automatically align the system between etchs. The Helios GC U3 system has such an operational mode since it can be used to automate the cutting and sectioning of large samples. We did not pursue this technique since the marker would have to be in the same focal plane as the raised ultrathin fibre. This is not easy to do since, in general, the height of the ultrathin fibre above the MgF_2 substrate was not held constant between samples.

5.1.4 Alternative Approaches

Aside from the three-step process outlined above, numerous other approaches were attempted. Initially, we tackled the problem using one of the more successful approaches which involved partially embedding an ultrathin fibre in a polymer and subsequently coating the embedded ultrathin fibre with a metallic layer [218]. This was a successful method previously, but since we did not wish to embed our fibre in a polymer we attempted to do so without this step. We experimented with a number of different coatings: carbon, silver, gold, and titanium. Carbon coatings proved to be entirely unsuccessful, probably due to the lack of uniformity in the evaporative coating process which made it difficult to electrically connect the coating on the fibre to the FIB stage. The coating process was also performed using an older instrument with poor calibration. Drift dominated in these samples and every fibre was destroyed in the etching process. Titanium was used briefly,

but we achieved better results when titanium was merely used as a thin seed layer to improve the adhesion of gold and silver to the surface of the SiO_2 fibre. The first successfully etched sample was produced using gold as the conductive layer. Despite the etch being successful, the gold layer produced far too much absorption, which destroyed the fibre's transmission. A commercially available etching fluid known as Pirahna, a mixture of sulfuric acid (H2SO4) and hydrogen peroxide (H2O2), was used to selectively etch the metallic coating from the ultrathin fibre surface. This eventually produced some positive results, but overall the process was very unclean and typically ruined the sample. A technique using the controlled flow of Pirahna etching solutions followed by ultrapure water was proposed, but ultimately was not followed up since the cleaner MgF_2 approach was discovered.

5.2 Transmission Characteristics of STOFs

The transmission characteristics of STOFs are quite variable. The initial analysis in Chapter 4 shows how the fields should be strongly affected by a number of parameters and the transmission of a STOF is also strongly affected by these processes. Many methods can be used to model the transmission of a STOF. Once again we rely on a combination of three numerical techniques to analyse the STOFs: FEM, FDTD, and EME. Initial work was done with a rather heavy-handed FEM approach using COMSOL's RF package, which required copious amounts of memory to solve for STOFs with length dimensions of tens of microns. COMSOL's more recent wave optics package has since significantly reduced the computational requirements. Later we focussed on a combination of EME and FDTD methods since they were more suitable for desktop calculations; the FEM calculations were often performed on OIST's SANGO computing cluster. The codes used for the calculation are included in **Appendix.**

The STOF study from Chapter 4 showed how sensitive the fields are to small changes in both the diameter of the fibre and to changes to the slot geometry. Since performing

an analysis of the transmission for such a large parameter space would be excessively time consuming, we restricted the scope to the parameters of the devices we fabricated. Here we will show transmission data for a STOF with a diameter of 1.4 µm and a slot width of 300 nm. Unlike in Chapter 4, where much of the modelling was performed for an infinite STOF with no transition region from the ultrathin fibre to the STOF region, here all of the calculations were performed including the transition region to produce more accurate models.

5.3 Experimental Setup[3]

5.3.1 Ultrathin Optical Fibres and Slotted Tapered Optical Fibres

The ultrathin fibres used in these experiment were fabricated from optical fibres which act as single-mode in the 980–1600 nm regime. The slotted tapered optical fibres were created using the previously mentioned three step process (Section 5.1) while exclusively using the hydrogen/oxygen flame-brush rig. A representation of the STOF in a trapping experiment as well as the STOF's geometry is given in Fig. 5.4.

5.3.2 Field Distribution

We have discussed, in Chapter 4, how the electric fields of a STOF differ greatly from those of a typical tapered fibre. The physical asymmetry introduced to the ultrathin fibre at the slot region and the polarisation of the guided light plays a larger role in the field distribution than for standard ultrathin fibres. To maximise the field at the slot for the trapping of dielectric particles with a refractive index contrast greater than 1 ($n_{particle}/n_{media} > 1$), the polarisation must be chosen to be perpendicular to the walls of the slotted region. This removes the continuity requirement of the perpendicular com-

[3]This section is adapted from Daly, M., Truong, V. G., & Nic Chormaic, S. Evanescent field trapping of nanoparticles using nanostructured ultrathin optical fibers. Optics Express **24**, 14470-14482 (2016).

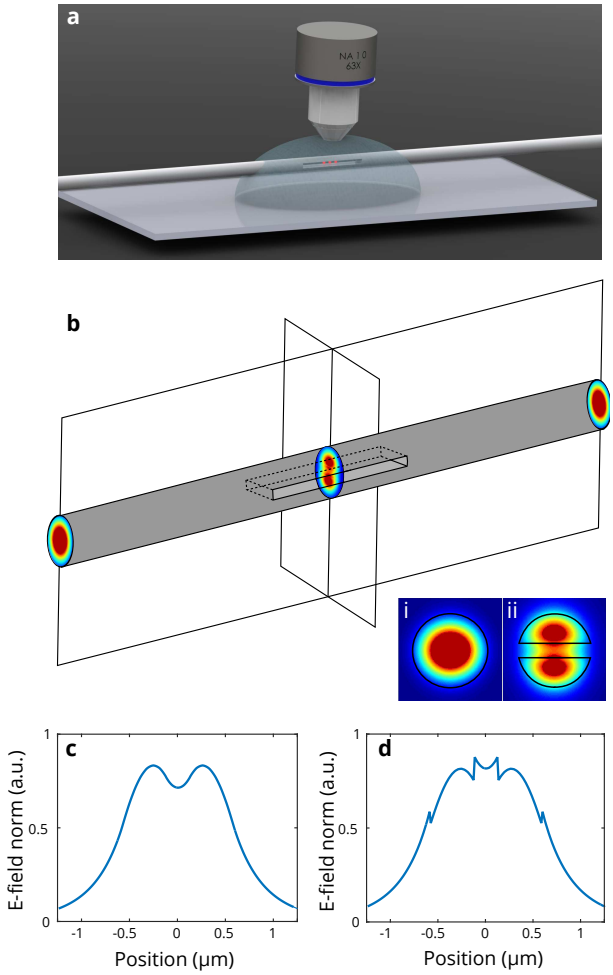

Figure 5.4: (a): Representation of the slotted tapered optical fibre (STOF) in a solution of red fluorescent silica nanoparticles. A 63x immersion lens is used to image the system. (b): A schematic showing the STOF section of the optical fibre with the fundamental fibre mode (i) seen at either side of the cavity region and the fundamental STOF mode (ii) at the centre. (c) and (d) show the electric field norm along a line cutting through the centre of the fibre perpendicularly to the slot walls for polarisations parallel to and perpendicular to the slot wall, respectively. The field within the slot is up to 1.7 times higher than the field at the outer fibre surfaces.

ponents of the electric field at the dielectric boundary, thereby allowing a large portion of the field to exist outside of the waveguide, see Fig. 5.4(d). Once again, the strength of the field at the slotted region depends on a number of parameters: the diameter, the slot width, the polarisation and the wavelength of the guided light. We chose a 1.4 μm fibre waist with a slot width of 300 nm. In general, the field strength increases with

decreasing slot size, but, since we have an additional requirement that the STOF opening must be large enough to facilitate the entry of submicron particles, the slot width used was the minimal possible, while still being practical for particle trapping. Slot widths much smaller than 300 nm would cause particles to become occluded in the slot region effectively destroying any optical measurement.

When the slot region is excited by the fundamental mode of an ultrathin fibre, as illustrated in Fig. 5.4(b) inset (i), a 'fundamental' type mode is excited in either section, see Fig. 5.4(b) inset (ii). Slot waveguides can exhibit symmetric or anti-symmetric modes depending on the phase difference between the upper and lower sections. The fundamental mode of an ultrathin fibre has an approximately uniform phase front, so we neglect the possibility of anti-symmetric modes in the following discussion.

Theoretically, one can predict the fraction of the field that exists outside an ultrathin fibre. However, this theory is somewhat unreliable since it predicts that the fundamental mode of an ultrathin fibre continues to propagate with an increasing fraction of the field as the diameter of the fibre tends towards zero. A comparison of the fraction of the field travelling in the core or cladding of a waveguide is given in Fig. 5.5 for a standard ultrathin fibre and a waveguide with a cross-section equivalent to the segment of a circle. We can see that the amount of the field outside of the core increases more rapidly for a circular segment. For a real system, however, the surface roughness of the waveguide is not perfect as one reduces the size of the fibre. As discussed in [219], this surface roughness prevents the transmission of the fundamental modes below a certain diameter dictated by the wavelength of the guided light. To optimise our process, a balance between maximising the external field while maintaining high transmission was required. Experimentally, a value for the diameter of 1.4 µm was found to be the most appropriate.

5.3.3 Experimental Outline

Optical trapping forces are typically divided into two categories in experiments. As discussed in Section 2.2.2, in the dipole approximation, where the particle size is smaller

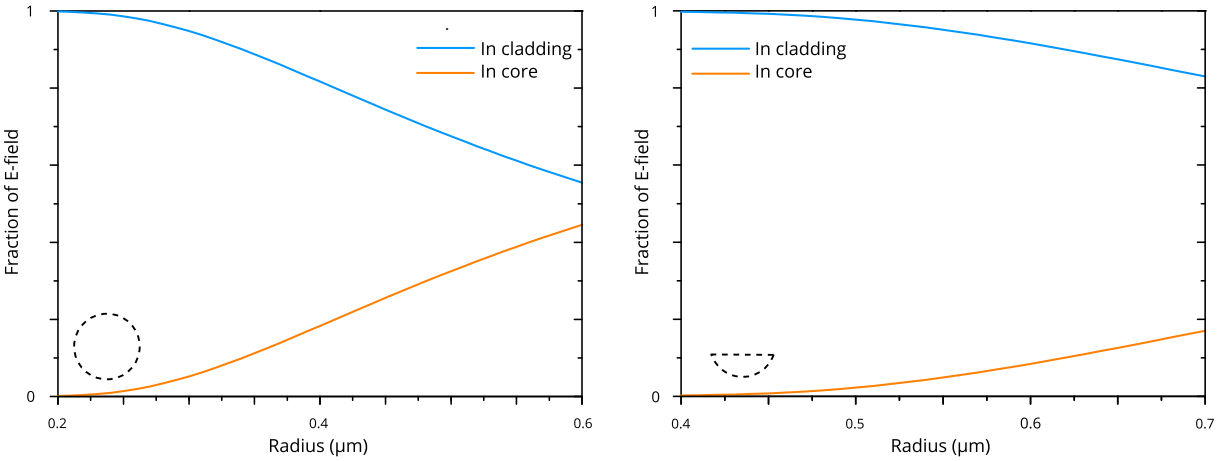

Figure 5.5: Fraction of the field travelling in the core and cladding portions of an ultrathin fibre (left) and a segment of circle (right). The lower left corner of each graph shows the waveguide cross-section. The radius of the segment refers the the radius of a full fibr minus the slot section. Hence, a segment with a radius of 0.4 µm corresponds to a segment with a 'height' of only 0.25 µm.

than the wavelength of the trapping laser light, the force can be decomposed into the gradient and scattering force components [24]. This formalism is not necessarily accurate for very small particles, such as the ones we use in this section, but gives a qualitative and intuitive picture of how the local electric fields affect particles placed within them. We chose not to use the dipole approximation in our calculations here as we were working with 100 nm and 200 nm particles and, hence, are working close to the limit of applicability $[n_{particle}/n_{media}]ka \ll 1$.

Previously, in the context of atom trapping (Chapter 4), a two-colour optical trap which was to be used to balance the van der Waals (vdW) forces near the slot walls was discussed. However, 100 and 200 nm particles are significantly larger than single atoms and we can, in general, ignore the effects of the vdW force in such cases. When the particles are in contact with the slot walls, there is seldom a molecular-scale interaction between the two surfaces; rather, asperities on the 'smooth' surface of the spheres can interact with the surface in such a way as to drastically reduce the effect of the vdW force on the particle as a whole [220]. Of course, interactions between molecularly smooth surfaces may exhibit non-negligible vdW forces, but we do not consider this to be the case

in this study. Separation distances of < 10 nm are needed to even begin considering the vdW force [220].

For the case of unidirectional excitation of a STOF waveguide, the gradient force, which seeks to pull particles towards regions of high intensity, draws particles towards the walls at the centre of the slot, while the scattering force propels particles in the direction of propagation of the trapping laser field. To produce a trap with longitudinal confinement, a standing wave is necessary. This provides an extra degree of confinement for the particles, as well as increasing the overall trap efficiency due to the cancellation of the scattering force components, thereby improving the axial trapping strength. A more in-depth analysis of the trap is made using a combination of FDTD/FEM models and various optical trapping models.

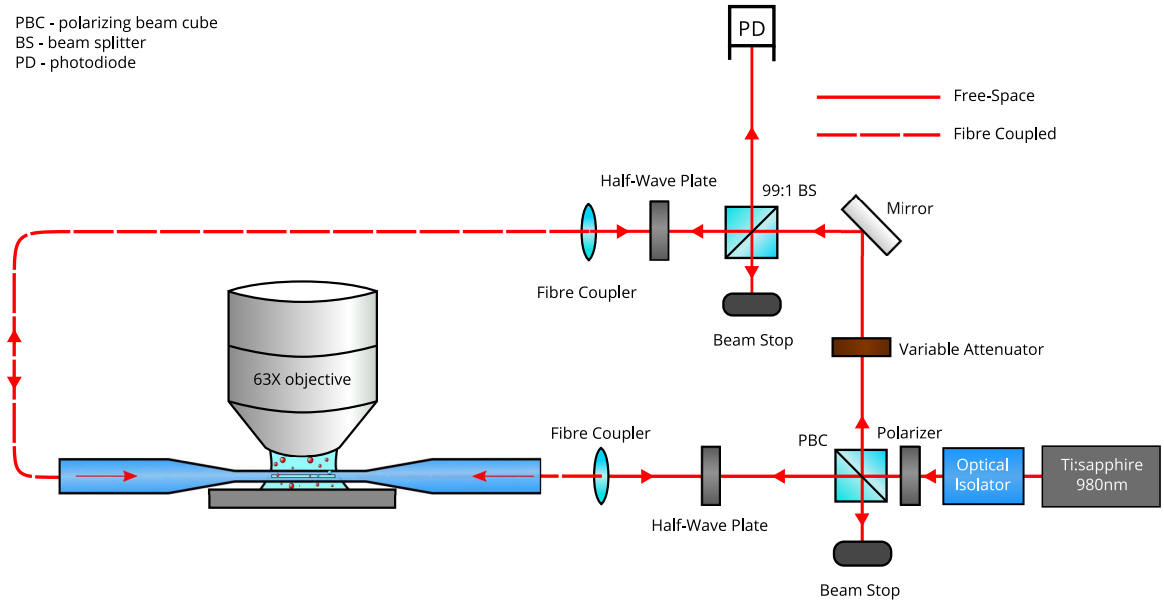

Figure 5.6: Optical setup used to trap nanoparticles. 980 nm light from a Ti:Sapphire laser is passed through a polarising beam splitter to split the beam while providing some initial control over the power balance. From here the beams are passed through polarisation control optics and finally fibre-coupled to the STOF. Transmission data is collected via a photodiode.

We introduced a low density nanoparticle solution between the water immersion 63x

lens and the STOF, shown in Fig. 5.6. The low density solution was used to prevent large numbers of particles occluding the slot. We used a particle solution of approximately 10^9 particles ml^{-1}, equivalent to an average particle occupancy of < 1 over the volume of the slot when no light is present. Fluorescent nanoparticles (200 nm polystyrene Sicastar®-redF. Excitation wavelength: 569 nm. Emission wavelength: 585 nm) were used to increase visibility of the system and we collected data visually, using a high sensitivity, fluorescence camera (Zeiss AxioCam MRc). Transmission and fluorescence data were also collected through the fibre using either a photodiode, for transmission, or a single photon counting module (Perkin Elmer), for fluorescence.

5.3.4 Polarisation Preparation

Polarisation preparation of light in an ultrathin fibre is often a source of contention as temperature and pressure variations (i.e. stresses and strains) along the fibre can cause the polarisation to rotate, leading to little correlation between the input and output polarisation states. Because of this behaviour, polarisation measurement methods, such as the observation of Rayleigh scattering along the fibre waist, need to be used [221]. In our experiment, we counter-propagated 980 nm light from a Ti:Sapphire laser through the STOF to provide a 3-dimensional trapping potential. The standing wave pattern that was set up within the wave guiding structure extended to the evanescent field, which then interacted with nearby particles to produce a periodic potential within the cavity section of the STOF. Two half-wave plates placed in the path of the two beams gave us fine control over the input polarisation states. By monitoring the output at opposite ends of the STOF, we obtained an estimate for the polarisation at the slot. However, by directly monitoring the slot region using a 63x water immersion objective lens, we were better able to determine the polarisation state via the intensity of the scattered light. When the light was polarised perpendicular to the plane of the slot, scattering was further enhanced due to the increased fraction of light contained within the small region. The slot is viewed at an angle perpendicular to both the fibre and the plane of the slot face to ensure that

maximum scattering is observed at the correct polarisation state.

5.4 Numerical Analysis

A thorough calculation of the electric fields, using both FDTD and FEM methods, provides us with reliable estimates for the optical forces in the STOF system. The optical fields of the device were calculated both in the presence of and without the particles to be trapped. Optical forces on small particles are often described using the dipole approximation, as discussed in Section 2.2.2, where the size of the particle must be much less than the wavelength of the trapping beams. For 200 nm particles and 980 nm light this criterion is not quite satisfied. To this end, we sought to make a comparison between the dipole gradient and scattering forces, and the more standard methods of force calculation for medium-sized particles. The total optical force in mid-sized optical trapping systems, $\vec{F}_{MST}$, is often calculated through use of the Maxwell stress tensor, a concept discussed in detail in Section 2.2. The force calculation in this method is calculated through the following integral

$$\vec{F}_{MST} = \oint_S (\vec{T}.\vec{n})da. \tag{5.1}$$

While this is an accurate method, it can be somewhat difficult to implement when the boundary of the system is ill-defined due to the mesh shape and/or the step size of the FEM/FDTD method used. As an alternative, we used an equivalent form derived from the Minkowski formalism for calculating the force; this method relies on the gradient of the electric permittivity, a value which can be easily extracted from the optical force calculation [222], such that the force, $\vec{F}_{min}$, is given by

$$\vec{F}_{min} = -\frac{1}{4}\epsilon_0 \iiint_V \vec{E}.\vec{E}\nabla\epsilon_r dV, \tag{5.2}$$

where ϵ_0 is the permittivity of free space, ϵ_r is the relative permittivity, $\vec{E}$ is the electric field and dV is the unit volume element. Accepted values of the refractive indices of

silica and polystyrene at a wavelength of 980 nm (1.4507 and 1.5731 respectively) were used in all calculations. The effect of the 5 nm layer of ITO was ignored due to its negligible influence on the ultrathin fibre modes. Force measurements using data from the FDTD and FEM methods give almost identical results for the trapping forces within the slot except near the slot walls where a maximum discrepancy of 7.6% was found. The dipole approximation for the force calculation proved unreliable in regions where the local gradient was insignificant, but became more accurate as this gradient increased. This method could be improved by considering the particle as a distributed dipole, but this treatment is beyond the scope of this work. FDTD images of the optical fields of the STOF are given in Fig. 5.7 and a comparison of the trapping forces for different particle locations inside the slot are given in Fig. 5.8.

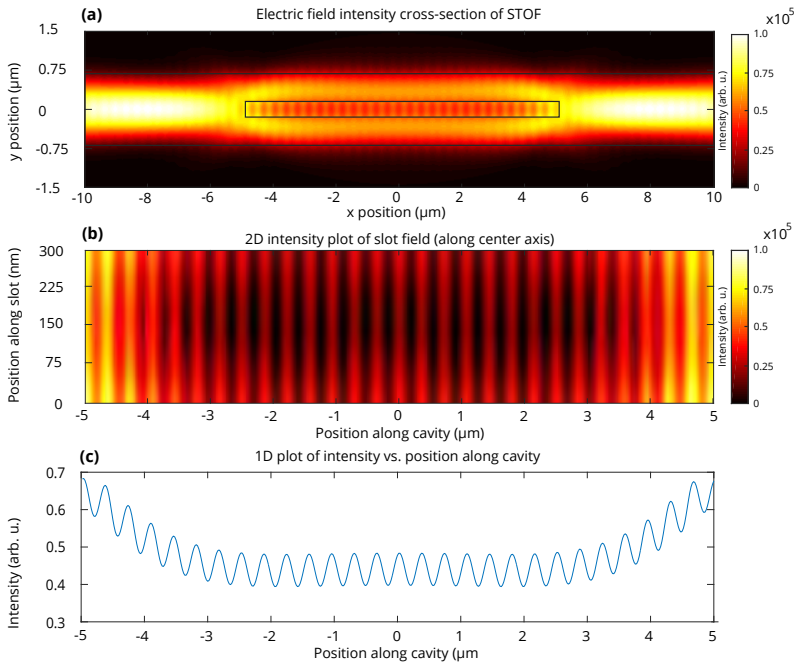

Figure 5.7: (a): Results of FDTD analysis showing a cross-section of the STOF. The mode evolves from the fundamental mode of the ultrathin fibre to the fundamental mode of the STOF at the centre and back to the fundamental mode of the ultrathin fibre with little loss. (b): Electric field intensity within the 10 μm × 300 nm slot in a 1.4 μm diameter ultrathin fibre. The field increases in strength near the slot walls. (c): 1D plot of the electric field across the centre of the STOF to show the variation in the field as a function of the distance along the cavity. The field stabilises at the centre of the cavity.

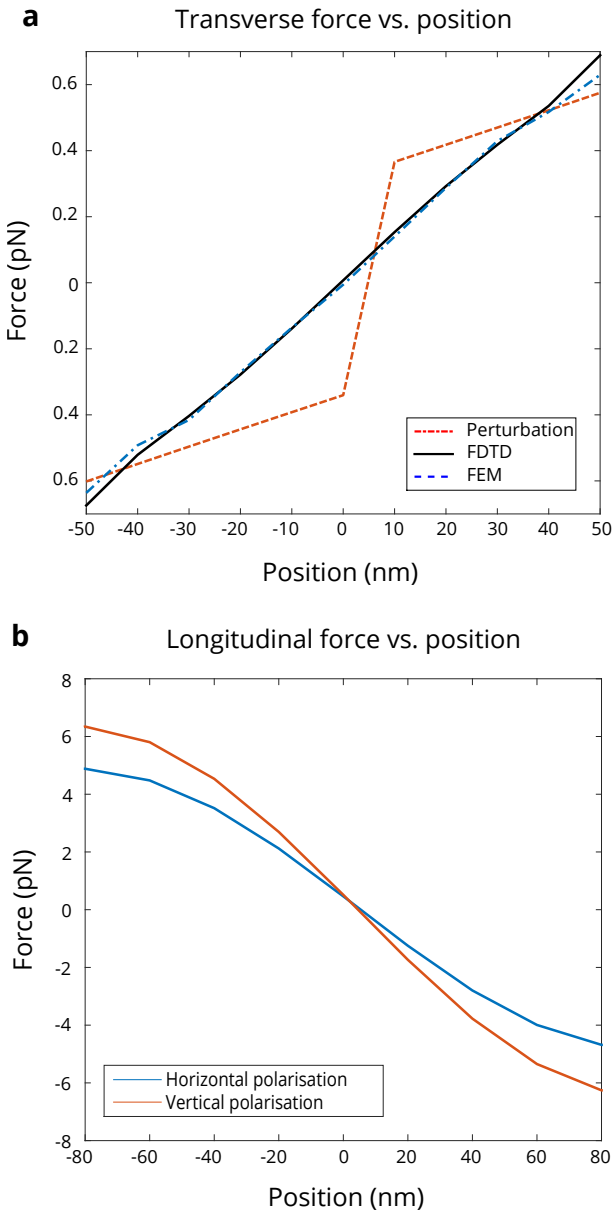

Figure 5.8: (a): Forces on a 200 nm particle moving perpendicularly between the upper and lower walls of a STOF as determined using optical fields from FDTD and FEM calculations and Eqn. 2.20, compared to a perturbative approach using the optical fields of the cavity in the absence of a particle as modelled using the FEM. 1 W of power was used in all simulations. (b): Longitudinal trapping force for two orthogonal polarisation states showing the increased trapping forces for the vertical polarisation state.

Considering the close agreement between the FDTD and FEM simulations, we chose to largely model the system using the FDTD method due to the reduced memory require-

ments and regular grid pattern. The dipole approximation for the force, $\vec{F}_{dipole}$,

$$\vec{F}_{dipole} = \frac{1}{2}\alpha\nabla\vec{E}^2, \tag{5.3}$$

was also used to provide a contrast to the force calculation using the Minkowski formalism. The nature of Mie scattering requires smaller particle dimensions before one can neglect the higher order poles in the multipole expansion, hence the discrepancy between the two methods.

At the ends of the slot, the local electric fields were found to increase due to reflections off the walls. Proposed solutions to this problem involve the introduction of a slot with tapered ends to allow the modes to evolve adiabatically between the ultrathin fibre and STOF modes. After a distance of ≈ 2 µm from the walls, the strength of the electric field within the cavity reaches a constant value, see Fig. 5.7(c). The trapping forces along the directions which run parallel to the STOF wall are considered to have normal restoring forces, but the trap which runs perpendicularly between the upper and lower walls of the STOF does not experience a standard restoring force. Here, the optical forces seek to pull particles towards the wall, at which point any restoring character is lost. Nevertheless, we determined a trap strength for this direction, indicated by k_{eff} in Table 5.2.

An FDTD mesh size of 20 nm was used throughout the calculations. We began with models that ran with much smaller mesh sizes and gradually increased the mesh size while calculating the force. At a value of 20 nm there was little deviation in the calculated forces, but for larger mesh sizes the force estimation was found to become unreliable. A 20 nm mesh size considerably increased the time-performance of our modelling as it depends on the number of mesh elements, which has a cubic scaling law. An image plot of the fields for a 200 nm particle near the centre of the STOF with a 20 nm mesh size is given in Fig. 5.9. The simulations were performed for counter-propagating fields.

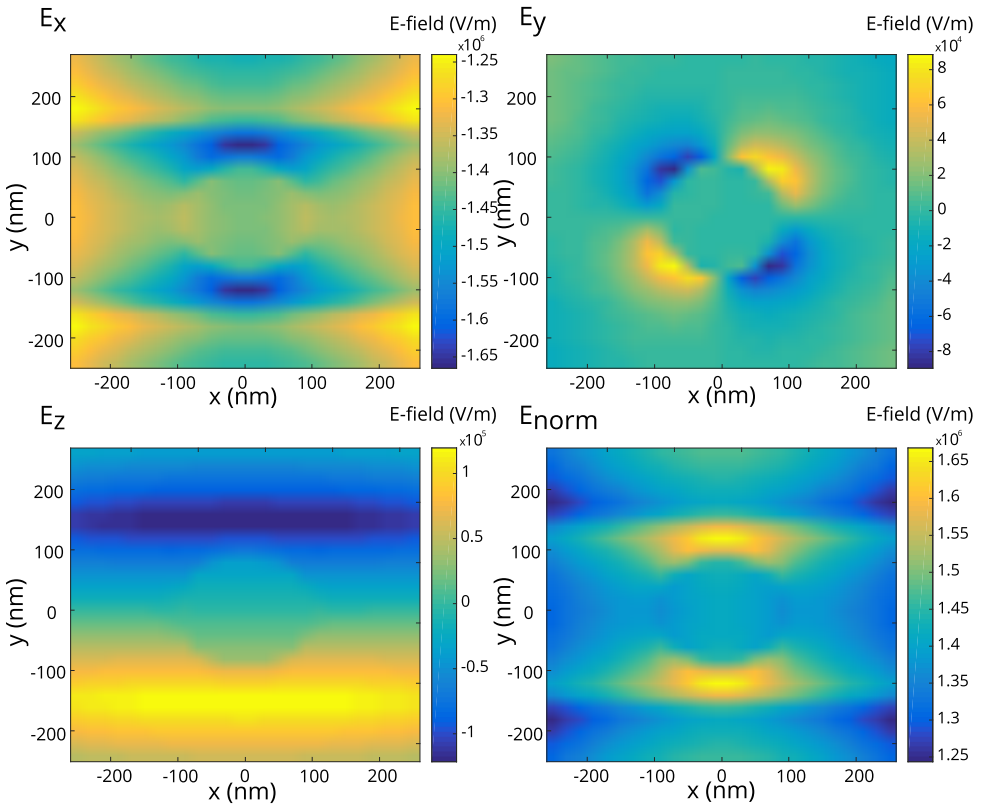

Figure 5.9: FDTD simulations for the E_x, E_y, E_z, and E_{norm} field components for a 200 nm particle at the centre of a STOF.

5.5 Additional Considerations

5.5.1 Multiple Particle Scattering

As is often the case for optical trapping experiments, the influence of multiple scatterers can make analysis more difficult. Light-mediated interactions between particles induce what is known in the field of optical trapping as optical binding effects. In the discussion on Mie scattering in Chapter 2, a plane wave illuminating a spherical object results in a scattered electric field of non-negligible amplitude. Similarly, superpositions of plane waves induce scattered fields. For particles situated near each other, the scattered fields' interaction with nearby particles induces forces on the particles as well as producing secondary scattered fields. This multiple scattering regime is extremely difficult to determine in three-dimensional systems though some work has been done to quantify the

effects of such interactions in 1-D by modelling each scatterer as a type of beam splitter with reflected and transmitted components [223].

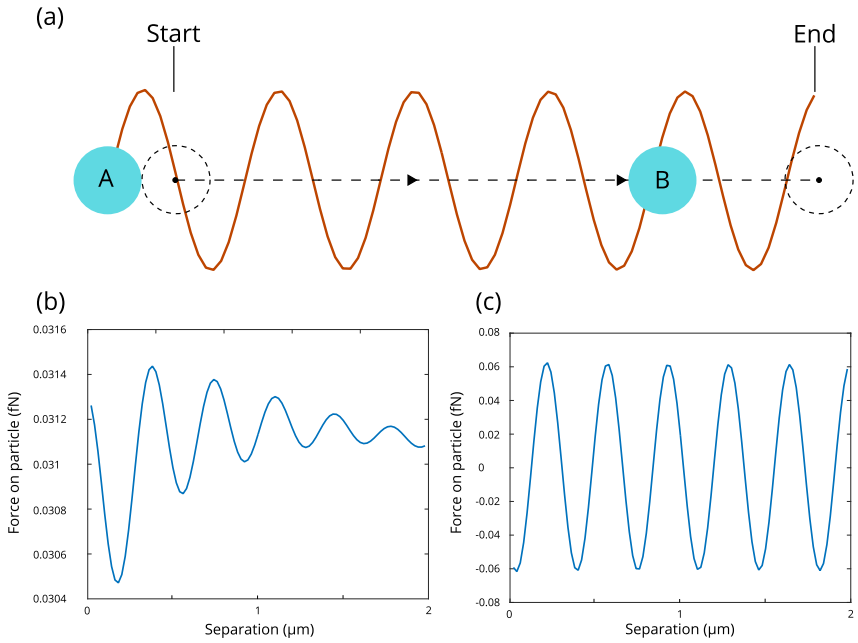

Figure 5.10: (a) Particle A is kept fixed at a certain position of the standing wave while particle B is moved away along the z-axis of the trap. (b) Force on particle A as a function of the separation. (c) Force on particle B as a function of the separation.

Using FDTD analysis it is possible to see how the interactions between particles behave. However, the difficulty of such calculations dramatically increases with the number of particles as the parameter space of every possible combination of particle position within the field increases as $\binom{N_m}{N_p}$ where N_m is the number of available particle positions and N_p is the number of particles. Here, we perform the calculation for two particles to quantify their effect on the system.

To simplify the problem, we fix the position of one particle while translating the other particle along the z-axis of the trap away from the first particle. The particles are placed at the centre of the STOF to keep them away from the walls. From Fig. 5.10 we can see how the force on each particle varies. The particle which is moving primarily sees the force of the trap since it is crossing over large changes in the potential landscape. However, since particle A has its position fixed, it is more susceptible to the small changes induced

by the re-scattered light. The change in the force felt by particle A can vary by as much as 4% due to the re-scattered light from particle B. Such binding effects are more visible in larger particle systems and tend to reduce as the particle size reduces. For 200 nm particles, we are in an interesting regime where the forces are still present, but their influence is reduced. These small changes in the force should be noted since, for multiple particle trapping, their influences on the measured trap stiffness can be non-negligible.

5.5.2 Thermophoretic Forces

Under certain conditions, it was possible to see the effects of thermally-induced forces using the slotted ultrathin fibre. Typically, the experiments were performed with low optical powers and the slot area of the fibre was free from contamination. However, on occasion the slot region could be either poorly formed during the milling process, or otherwise obstructed with dust particles. In this case a large amount of heat was generated at the slot region, thereby introducing a thermal gradient in the surrounding water. When particles are in the presence of a thermal gradient, they can display a steady drift velocity on top of their Brownian motion [224]. The magnitude of the drift velocity, v_T ,is characterised as

$$v_T = -D_T \nabla T, \tag{5.4}$$

where v_T is the thermal drift velocity, ∇T is the thermal gradient, and $-D_T$ is a thermal diffusion coefficient. It is the thermal diffusion coefficient which is important in optical trapping experiments as it is the deciding factor on whether particles move with or against thermal gradients. A parameter known as the Soret coefficient, $S_T = D_T/D$ where D is the diffusion coefficient, determines the sign of the particle drift velocity. This parameter is well known for many materials. For silica particles this parameter is negative, causing them to congregate at sources of heat.

During our experiments we observed this effect in devices with imperfections at the

slotted region. The presence of the defect caused heating due to the absorption of the laser light which propagated through the device. At optical powers greater than 40 mW, large scale assembly of particles near the slot could be seen. A time series of micrographs is shown in Fig. 5.11.

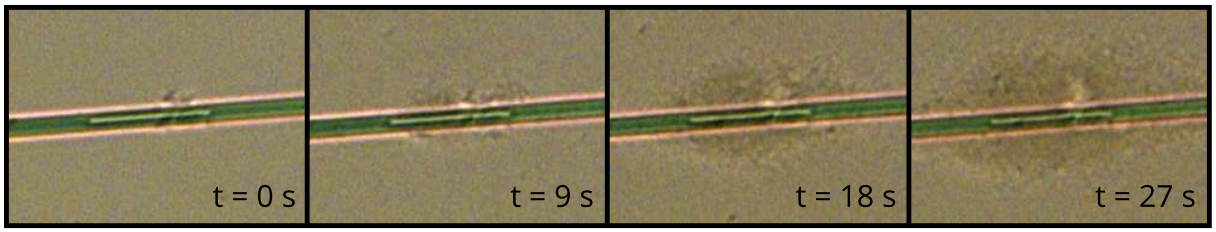

Figure 5.11: Time series of images showing the effect of thermophoresis. A unidirectional beam with 40 mW of power was used.

At time $t = 0$, we can see that the slot is somewhat obstructed by an unknown contaminant. Additionally, the shape of the slot seems somewhat imperfect near the right slot edge, though this aberration may be an optical artefact due to the presence of the contaminant. Greatly increased scattering can be observed in the dark field when contaminants are present. Since we know the optical fields to be well confined within the fibre and slotted regions, we can assume that such a large scale assembly of particles cannot be due to purely optical forces. Rescattered light from the contaminant would also produce insuffucient optical forces to trap 200 nm silica particles. The type of particle assembly shown in Fig. 5.11 is indicative of thermophoretic trapping [225]. It is important to know that this effect is only present in our device when there is an imperfection and high optical powers are used. For well-fabricated devices this effect is not present, even at high optical powers. This helps to alleviate any fears that the observed trapping might be due to thermal effects rather than purely optical effects. This is often a source of contention in optical trapping experiments. We also observed the trapping of polystyrene particles, which have a positive Soret coefficient causing them to seek equilibrium at regions of low temperature. This also helps to confirm that the observed trapping was indeed an optical one.

The investigation of thermophoretic forces, while a very interesting topic, was not the focus of this thesis so the effect was not pursued further. It may be worth investigating in more detail at a later date.

5.6 Results and Trap Analysis

The small dimensions of the STOF make it hard to image the slot adequately without resorting to SEM imaging, see Fig. 5.12(a). This problem also applies to the much smaller dimensions of the particles we wish to trap. Fluorescence imaging, see Fig. 5.12(b), however, allows us to capture live video of the particles' motion; due to the low-light levels, exposure times of $\approx$ 70 ms are required to actually image the particles. This limits our ability to perform Fourier analyses of the visual data since the trap operates at relatively low trap frequencies, requiring prohibitively long data collection times [226]. We can, however, track the particles and bin their positions to observe interesting behaviour in their motion, as shown in Figs. 5.12(e) and (f). With an imaging resolution of 13.3 pixels per micron we were able to track the particles' positions to a high degree of accuracy. Gaussian fitting of the positions showed trapping occurs at regular intervals along the central axis of the STOF. After performing the experiment further SEM images were taken of the fibres, see Figs. 5.12(c) and (d). Here, we can see that the slotted region remains intact, allaying any fears that the slot may have collapsed during the experiment, as well showing that particles were able to enter the slot.

In the bright-field, it was difficult to distinguish single particle trapping events from multiple particle trapping, but fluorescent imaging indicates that typically more than one particle is trapped. The dynamics of multiple particle trapping may shed some light on the larger spacing between "stable" trapping positions. Simulations show that two particles in the trap have non-negligible interactions over distances of $\approx$ 1 µm and this may explain the observation of stable trapping positions which are multiples of the approximately 350 nm standing wave separation, $\lambda/2n_{eff}$, where n_{eff} is the effective refractive index, as

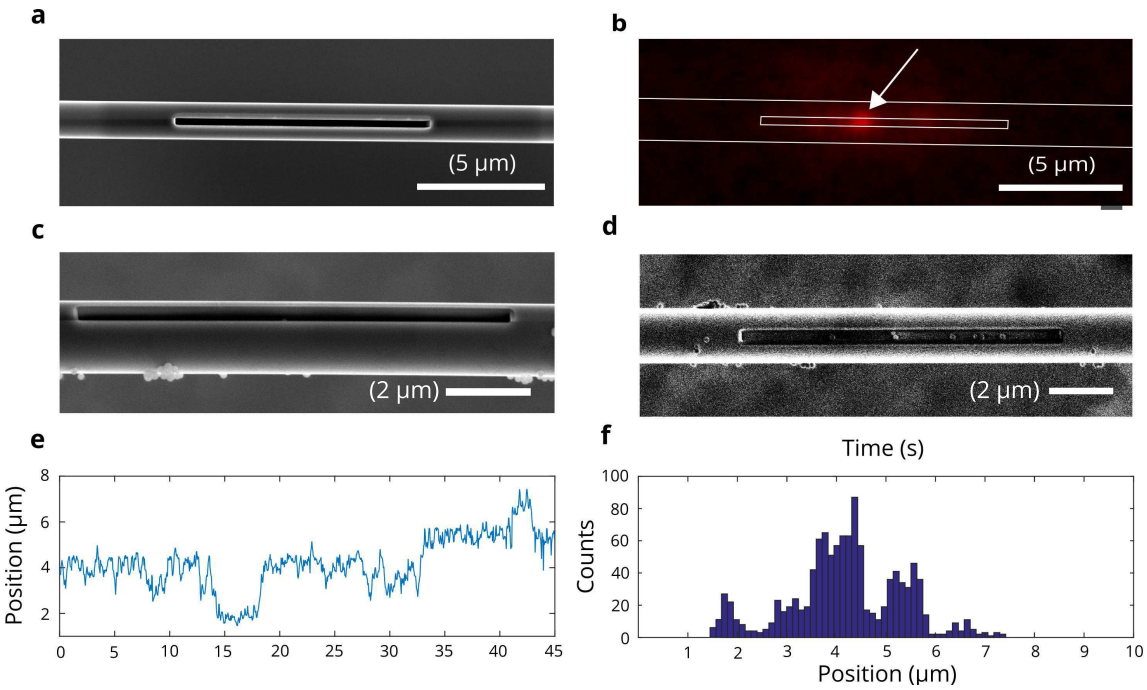

Figure 5.12: (a) SEM image of a STOF. (b) Microscope image of a trapped fluorescent particle with an outline of the STOF for clarity. (c) and (d) show SEM images of the fibre after the experiment was performed. Particles can be seen inside the slot was well as on the surface. (e) Particle position versus time along the z-axis of the STOF. The particle is seen to spend most of its time near the slot centre. Each pixel was found to correspond to a 100 nm $\times$ 100 nm area and Gaussian fits to the particle centre enable high resolution tracking. (f): Histogram of the particle positions given in (e) showing bunching at regular intervals.

evident from the histogram in Fig. 5.12(f).

The unrestricted motion of Brownian particles leads to a characteristic $1/f^2$ noise spectrum. In contrast, for a trapped particle, the power spectral density (PSD) follows a Lorentzian distribution, $A/[f^2 + f_c^2]$, which is derived from the Langevin equations of motion [39]. Log-log plots of these data allow one to visually interpret this Lorenztian lineshape as the combination of two regimes, which overlap at the corner frequency, f_c. All frequencies higher than f_c can be viewed as the unbound motion of free Brownian particles, which behaves as $1/f^2$, while everything below this value represents the restricted motion of the trapped particles.

Throughout our experiments we recorded the transmission through the STOF during

Table 5.2: Trap stiffnesses for varying input powers

Trap Stiffness	2 mW	5mW	10 mW
k_x	28 fN μm^{-1}	69 fN μm^{-1}	138 fN μm^{-1}
k_y	102 fN μm^{-1}	255 fN μm^{-1}	510 fN μm^{-1}
k_z	202 fN μm^{-1}	510 fN μm^{-1}	1020 fN μm^{-1}
k_{eff}	78 fN μm^{-1}	124 fN μm^{-1}	176 fN μm^{-1}

trapping and non-trapping events. Analysing the power spectral density of this signal can be difficult when low trap frequencies are considered (Fig. 5.13). Additionally, our detected signal is coupled to the three non-degenerate trap stiffnesses and it is difficult to distinguish between single-particle and multiple-particle trapping; this adds more noise to the detected signal. To overcome some of these issues, we opted for autocorrelation measurements which are analogous to the PSD, but do not suffer from some of the associated measurement problems. Data was taken in 50 s intervals at a sample rate of 2 kHz. The autocorellation data, given in Fig. 5.13(b), exhibits a not quite exponential decay rate, as would be expected for a clean optical trap.

The introduction of "random" forces, can alter the lineshape [227]. We expect the interactions of multiple particles, as well as the motions of the slot walls in the particle solution, to be sources of these 'random' forces. Despite these random contributions, the trap stiffnesses are seen to increase proportionally to the input powers, as determined by closest exponential fits to the data. The increase is directly proportional to the input laser power, see Fig. 5.13(c), and the experiment yielded results which were of the same magnitude as the expected theoretical values, given in Table 5.2. If we instead take the root mean square value for the power to adjust for the losses along the fibre and use this power to calculate k_x, k_y, and k_z and then average these contributions we arrive at an effective spring constant, k_{eff},

$$k_{eff} = \frac{\sqrt{2}}{P}\frac{(k_x + k_y + k_z)}{3}, \tag{5.5}$$

where P is the power at the input of the STOF. Consideration of multiple particle in-

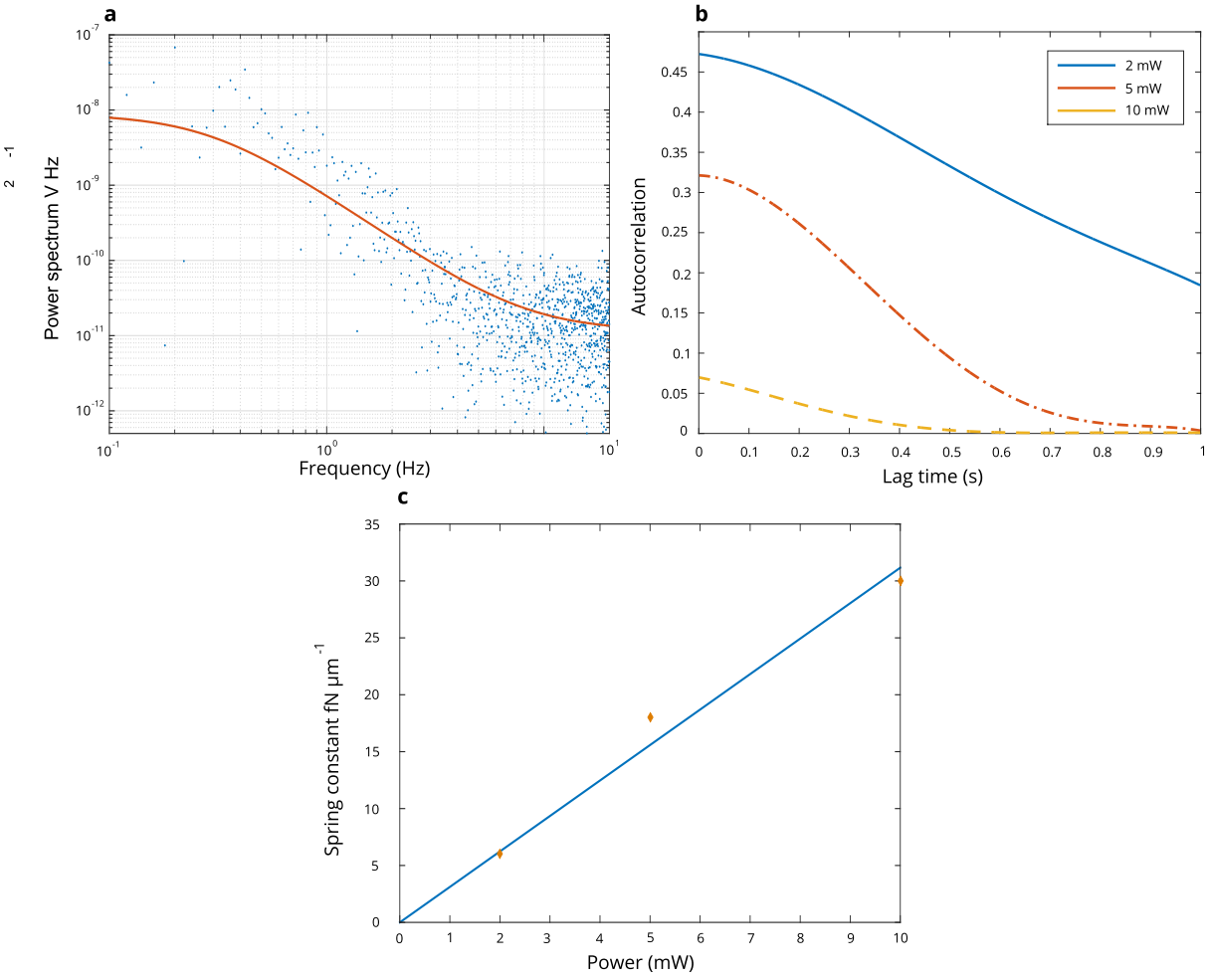

Figure 5.13: (a) Power spectrum density of the transmitted signal for 5 mW of trapping power. A corner frequency of 0.6 Hz is measured.(b) Autocorrelation signals at 2 mW, 5 mW and 10 mW. The observed decrease in the slope of the autocorrelation signal at different powers indicates a linear increase in trap strength with power as is expected. (c) Plot of the spring constant as determined using the autocorrelation measurement vs. the power in the trapping beams. The subsequent plot is linear with respect to power as predicted.

teractions and surface-particle interactions such as the Faxen corrections would reduce this value further. We assume that the longitudinal trap stiffness, k_z, may have a smaller contribution to the effective trap strength and we note that removing this value from our average significantly bridges the gap between the experimental and theoretical values.

Following the experiment SEM images of the device were taken as well as allowing us confirm that particles could diffuse into the slot region of the STOF it also allowed us to

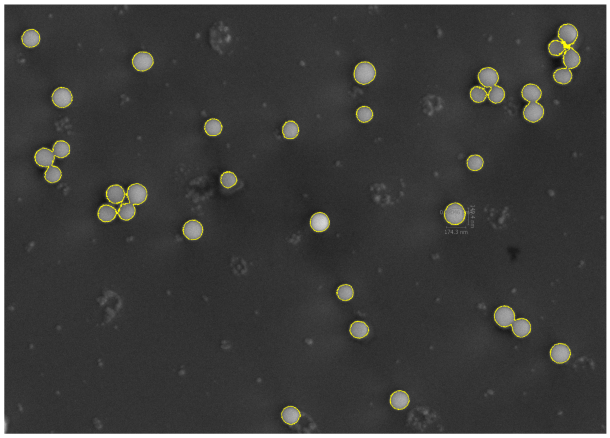

Figure 5.14: SEM image of fluorescent particles with a stated diameter of 200 nm on an MgF_2 substrate combined with an overlay showing the particle boundaries in yellow.

check the size distribution of the fluorescent particles. Using imaging software we were able to determine the sizes of the particles. A mean diameter of 161±11 nm was found 5.14. This is much smaller than the stated diameters of 200 nm[4]. The polydisperity index for the particle solution was given as 0.2. This is a measure of the square of the width of the Gaussian describing the diameter distribution to the square of the mean of the Gaussian (PDI = $[width/mean]^2$). This discrepancy in the diameter was not included in the simulations as all the simulation work had been done before the experiment though we may expect this to lower the expected trap stiffnesses helping to bring the experimental and theoretical values closer together. Since the force has an r^3 dependence we can expect the total force to trap as a cube of the ratio between the stated and measured diameters ($\approx 50\%$).

5.7 Conclusion

The previous chapter discussed how one could theoretically design an ultrathin fibre with a slot to trap atoms. While an interesting topic in and of itself, without any method of fabrication any discussion about the device would be pointless. Here we have shown that we can not only fabricate nanostructured ultrathin fibres but that we could do so with

[4] `http://www.micromod.de/pdf/aktuell/40-00-202_tds_en.pdf`

a high degree of precision and still maintain a high transmission. This is a vital step towards the realisation of an atom trap using such a device. The creation of the device is an important part of this chapter, but, the creation of the technique to reliably fabricate such structures in ultrathin fibres is a much more important achievement. The literature outlines a number of similar techniques to create structures in ultrathin fibres [92, 218]. However, these techniques are dirty and generally irreproducible without a large investment in time and manpower. Our addition of an ITO coating to the fabrication process allowed us to produce nanostructured ultrathin fibres with a high success rate. Of course, much of this success comes with experience in the field, but we believe the technique can be easily adopted by many groups worldwide provided they have the equipment at hand.

Here, we have shown definitively that a nanostructured ultrathin fibre can be used to trap 100 and 200 nm dielectric particles. In some ways it is more challenging to trap colloidal dielectric particles than cold atomic gases. The environment is much noisier, scattering plays a larger role, larger potential depths are required, and it is more difficult to isolate the system from external contaminants. The unique trapping geometry we have shown here which confines particles, and perhaps atoms in the future, within the slot leads us to believe that spectroscopic measurements are also possible by passing probe beams of different wavelengths through the ultrathin fibre while simultaneously recording the transmission or captured fluorescence at the output fibre pigtail. A substantial improvement to earlier work, such as the self-organisation of atoms along nanophotonic waveguides [228], should also be possible since light coupling into the STOF is increased compared to for standard optical nanofibres.

Chapter 6

Plasmon Enhanced Ultrathin Fibres

Plasmonic devices have been extensively used in the trapping and manipulation of particles with submicron dimensions. This topic has been thoroughly discussed in the introduction of this thesis. Combining plasmonic structures with an ultrathin optical fibre would provide large local field enhancements over a bare ultrathin fibre alone, either as an $\mid E^2 \mid$ increase in the field when dealing with surface plasmon polaritons or an increase which is proportional to the figure-of-merit (FOM), i.e. $(Re(n_m^2)/Im(n_m^2).)$, for the case of localised surface plasmons. The process of combining these two techniques is a difficult task. Conventional lithographic techniques are difficult to work with on glass substrates, let alone the curved surface of an ultrathin fibre. The problems previously associated with etching structures on dielectric materials also arise here, but with additional factors. Electron beam lithography is often done 'blind', where no direct imaging of the surface is performed other than using a laser to determine the height from the surface. This makes it exceedingly difficult to locate the waist region of an ultrathin fibre, effectively ruling out a lithographic technique requiring the use of a photoresist. Alternative approaches that allow imaging during structuring have been investigated. For example, a plasmonic bowtie-aperture has been etched at the end-face of an ultrathin optical fibre half taper. Since this was on the end-face, rather than the surface of a fibre, some of the advantages that come with using an optical fibre are lost, primarily the ability to collect the

light which has propagated through the fibre which can be used to monitor the state of the system. Groups have worked on this by scattering plasmonically active objects over an ultrathin fibre [123, 124], and then investigating the absorption spectra using various techniques. Unfortunately, this is a highly non-deterministic process, which results in gold nanorods with random alignments and orientations on the fibre surface.

In this chapter, we show how plasmonic devices can be written directly onto the surface of an ultrathin fibre with a high degree of control and accuracy using a technique called electron beam induced deposition (EBID). Using EBID, a small array of elongated gold nanodisk dimers at the central waist region of a 5 µm fibre were created. Rather than bulk modification of the fibre waist itself, the inclusion of plasmonic structures to the surface allows for hotspots with submicron dimensions at very precise locations along the fibre waist. This could be used to trap particles and also has potential uses in surface enhanced Raman spectroscopy due to the plasmonic nature.

6.1 Design and Fabrication

The design of the plasmonic structure was chosen with the consideration of a few constraints. Firstly, the plasmonic peak of the structure should be accessible using a Ti:Sapphire laser. This limited the scope to 700 nm–1000 nm. We decided on a gold nanodisk-like structure with a 3:1 aspect ratio and a large plasmonic peak at 800 nm in water, as illustrated later in simulation work. To increase the active area of the device, and to also prove the concept of designing custom plasmonic structures on a fibre, an array of such structures, with a small gap between the rods along their long axis, and a larger gap along the shorter axis, was considered. Such an array is depicted in Fig. 6.1.

The larger gap distance was chosen to be approximately equal to the Bragg spacing of 800 nm light in water. The shorter gap between the elongated gold nanodisks causes the resonance to shift slightly due to the dipole-dipole interaction between them and also results in a more significant hot spot. The larger array size also makes it easier to locate

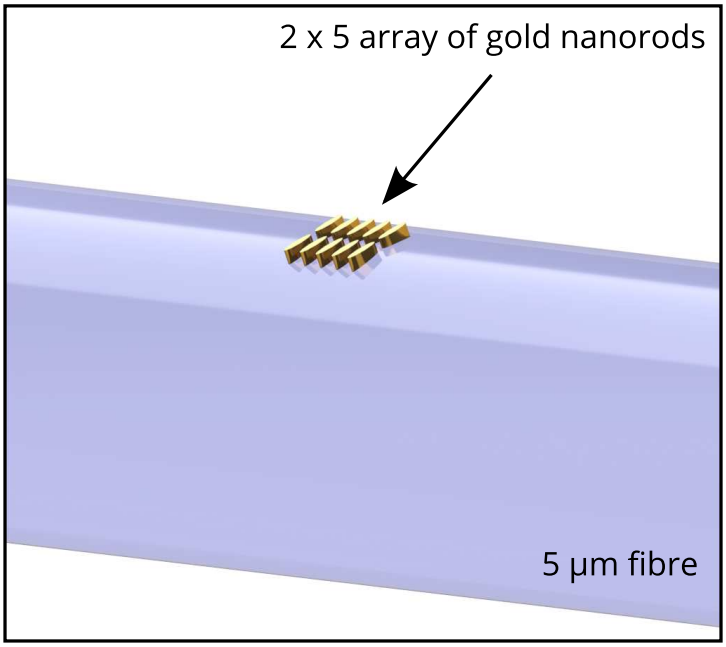

Figure 6.1: Elongated gold nano disk dimers patterned on the surface of an MNF. Fibre diameter 5 µm/

the structure using conventional microscopy techniques and, hence, perform measurements on the array. The exact dimensions of the gold dimer array are given in Fig. 6.2. We chose a major axis size of 210 nm and a minor axis size of 60 nm. Post fabrication, we found the minor axis length to be closer to 70 nm.

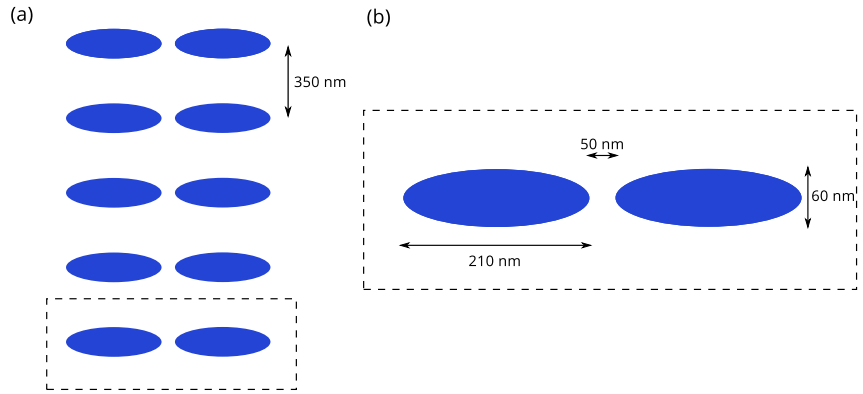

Figure 6.2: Layout used to create the elongated gold nanodisk dimer.

6.1.1 Electron Beam Induced Deposition

To deposit a gold structure on a dielectric fibre the EBID method was used. In EBID, or focussed-electron-beam-induced deposition (FEBID), as it is sometimes referred to, is a direct-write technique which can produced precise structures on a substrate. EBID or FEBID is performed by using a focussed electron beam to decompose precursor molecules adsorbed on a surface. The precursors used for gold are often organic in nature and this can be a problem. The abundance of organic material results in structures with poor conductivity. However, it was shown by a number of groups [229, 230] that, if one uses a common precursor gas, in our case dimethylgold-acetylacetonate ($C_7H_{13}AuO_2$), post-processing treatments can dramatically increase the quality of the deposited gold. This can be done via annealing the sample at high temperatures or through oxygen plasma cleaning. Either treatment can result in exceptionally high Au fractions (>70%) [229, 230] as measured by energy-dispersive X-ray spectroscopy (EDS). We opted for oxygen plasma cleaning since we had access to such a system in our university and it was the recommended option from our collaborators at FEI. Typically, the gas precursor is brought near the sample surface via a capillary tube and, in the focus of the electron beam, the adsorbed precursor molecules are dissociated followed by a desorption process. A more in-depth review of the field can be found here [231]. After deposition and post-processing the

remaining gold forms a polycrystalline structure.

The fabrication of the device was performed by the group of Dr. Hans Mulder of FEI. While the technique has been around for some time now, the application to plasmonic structures is still a relatively unexplored field, hence the interest of FEI in working with us.

6.1.2 FEM Simulations

We modelled the structure at a planar glass-air interface as shown in Fig. 6.3. This was used to determine the approximate wavelengths of the plasmon resonances in air. The ultimate goal would be to excite the devices in a water environment, but, due to the limited quantity of manufactured devices by FEI (quantity:2) we were hesitant to introduce them into a water environment which could contaminate the devices over a much shorter time frame. Future plans do involve investigating the trapping ability of these devices. We chose to finally model the structures using the FEM rather than the FDTD method for two reasons. Firstly, a rather fine mesh is needed to accurately model plasmonic nanostructures and the dynamic meshing ability of COMSOL proved to be more memory efficient. Secondly, COMSOL permits the empirical values of the permittivity of gold to be used in the simulation while CrystalWave, the FDTD software, required the use of approximating models such as the Lorentz-Drude or Debye models. Given the relatively low mesh around the gold nanostructure, we were often left with best approximation functions to the permittivity which varied as much as 15% from the true value. COMSOL also has a well-developed system for analysing data post-simulation, allowing us to easily extract it. In the model, given in Fig. 6.3, a plane wave„ propagating in the positive z-direction, was used to excite the structure from below. A polarisation value of 0^o corresponded to polarisation along the x-direction, while 90^o corresponded to a polarisation along the y-direction. This polarisation convention is used in all of the following figures.

The FEM simulations show peaks in the transmission spectra; these can be shifted

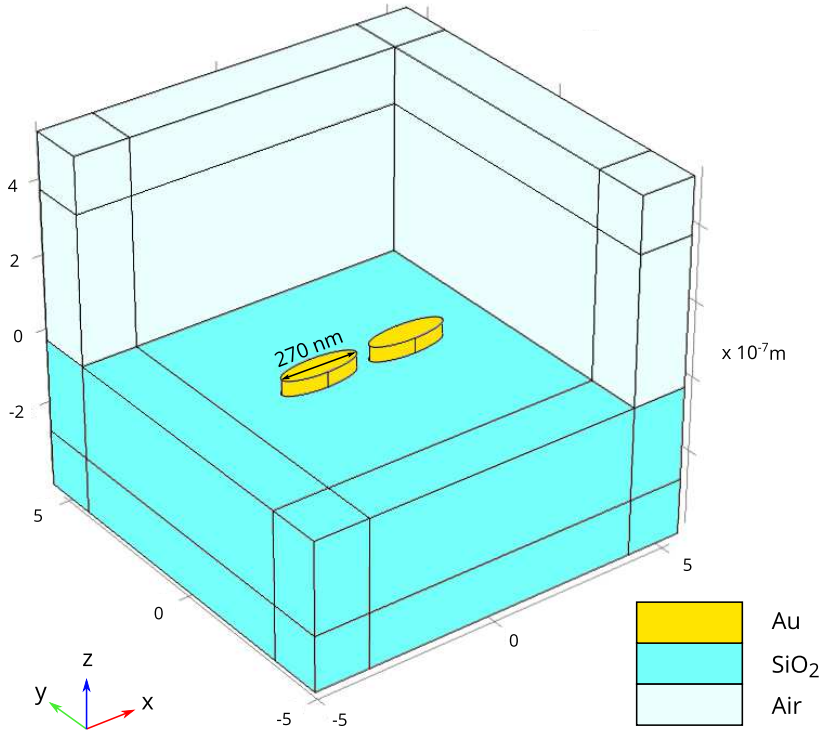

Figure 6.3: Layout used in the FEM simulation using COMSOL. The 3D image shows the three different materials used in the simulation. We ignore the effects of the < 5 nm ITO layer. The entire structure was surrounded by a perfectly matching layer to remove reflections at the boundaries.

slightly by adjusting the distance between adjacent gold nanodisks due to the effect previously discussed in Section 2.4.3. A further shift can be achieved by changing the ratio between the major and minor axes of the elliptical structures. The results of the simulations are given in Section 6.2.3. The important peaks in the transmission spectra of the device can be attributed to the two modes shown in Fig. 6.4, corresponding, to the longitudinal and transverse modes of the gold dimers.

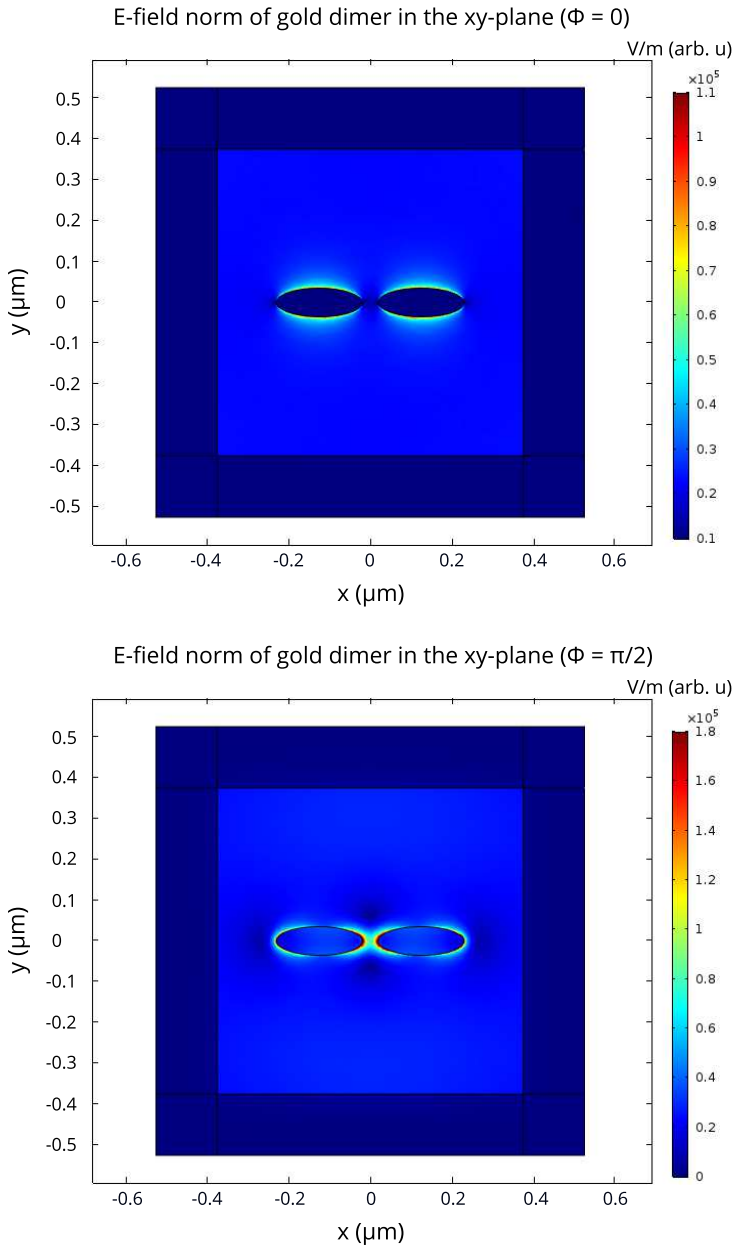

Figure 6.4: COMSOL simulation of a gold dimer on silica substrate for two orthogonal polarisations. A plane wave was used to illuminate the structures from below.

6.2 Characterisation

6.2.1 SEM Imaging

A test sample was prepared on a flat silicon substrate to determine the deposition parameters. An SEM image of this is given in Fig. 6.5(a), showing a deposition with good

resolution, agreeing well with the proposed design. Figure 6.5(b) shows the same pattern deposited on a 5 µm microfibre and post treated with the oxygen plasma cleaning technique mentioned early. In this image, we can see that the structure is somewhat less defined, though some of the discrepancy can be linked to the poor imaging conditions. Significant charging-like effects can be seen in the image as bright white spots. Deposition on glass is difficult for the very same reasons outlined in Chapter 5 with regards to the focussed ion beam milling of silica fibres, namely the excessive charge build-up in the dielectric material.

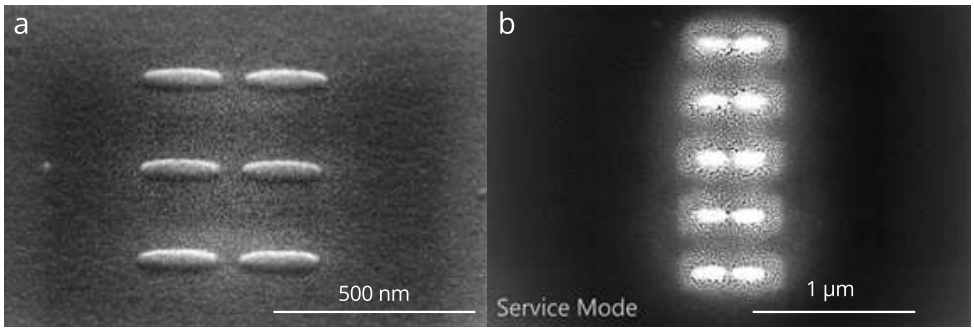

Figure 6.5: SEM images from FEI of the gold nanodisk structures.

Upon receipt of the devices from FEI, we performed SEM analyses at OIST. Unfortunately, of the two samples received only one was of a good quality. Sample 1 is shown in Fig. 6.6. Here, we can see a uniform structure which is well aligned with the axis of the fibre. This sample was not oxygen plasma cleaned.

The second sample can be seen in Fig. 6.7. In Fig. 6.7(a) we see that the fibre waist is not uniform near the plasmonic structure and a slight bend in the fibre is visible. Such fibre defects were observed when high electron beam voltages and currents were used, typically for voltages in excess of 10 kV. We believe this to be the source of the strange depression on the fibre surface, shown in more detail in Fig. 6.7(b) where the structure was imaged at an acute angle with respect to the plane of the device.

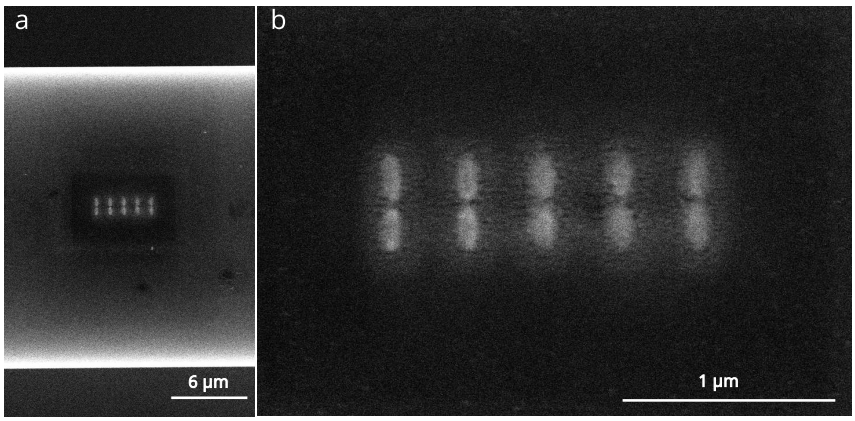

Figure 6.6: SEM images of the gold nanorod structures. Images were taken after extensive use, hence the presence of small dust particles. A higher resolution image was not possible due to significant charge build-up during the SEM imaging.

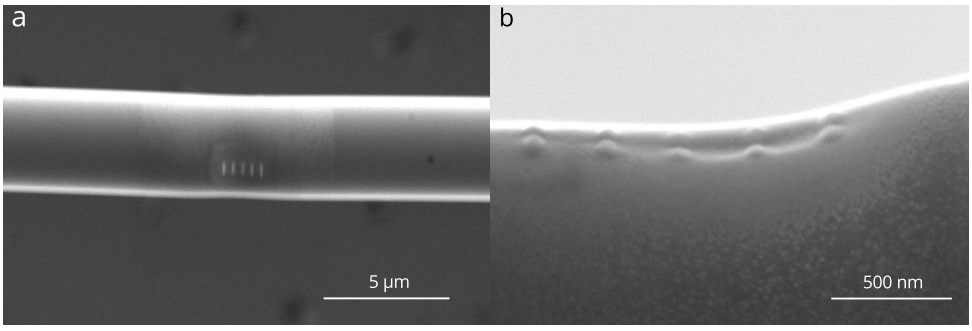

Figure 6.7: SEM images of the gold nanorod structures. (a) A slight bend in the fibre can be seen with a small indentation visible near the structured region; (b) The large depression formed during fabrication.

6.2.2 Energy-Dispersive X-ray Spectroscopy and Oxygen Plasma Treatment

To characterise the fabricated device, we needed to know the relative ratio of carbon to gold in it. This can help us to understand how well the post deposition oxygen treatment purified the gold precursor. For this, we performed energy-dispersive X-ray spectroscopy (EDS). EDS measurements rely on the detection of X-rays emitted from atoms when electrons from higher energy shells move to lower energy shells. These "hole" states are generated either through bombardment with X-rays or high energy electrons. We used a beam of electrons to liberate the inner shell electrons as the EDS sensor is integrated

in a Quanta SEM. Individual atom isotopes have characteristic X-ray lines which can be used to identify them. This technique can often be problematic, since some atoms have overlapping lines. However, our devices are relatively clean systems with known elements present. The most abundant elements are silicon, oxygen, carbon, and gold. Trace amounts of other elements are present.

We performed the EDS measurement on a fibre which had been oxygen plasma treated and spectra are given in Fig. 6.8. The spectrum with the black line is for the ITO coated ultrathin fibre alone. Here, we can see the presence of indium from the ITO coating at approximately 3.35 keV, indicating that the EDS process can detect even a 5 nm layer of ITO. Gold is difficult to measure using EDS since it has many X-ray lines. This is evident in the broadness of the Au peak. Because of this, it is difficult to quantitatively compare the ratio of carbon to oxygen directly. Instead, we hoped to compare the spectra before and after oxygen treatment to see the relative change in the carbon peak. Figure 6.8 shows the the EDS spectrum of the second sample, which had already been oxygen plasma treated. We compared the EDS spectrum of just the ITO-coated silica fibre to that of the section of fibre containing the gold structures. We can see a rather large, broad peak at $\approx$ 2.2 keV corresponding to gold. Unfortunately, further imaging with the EDS process resulted in destruction of the fibre. A beam voltage of 20 kV proved to be too intense and cleaved the fibre at the imaging spot. Because of this we were hesitant to analyse the remaining sample with this technique.

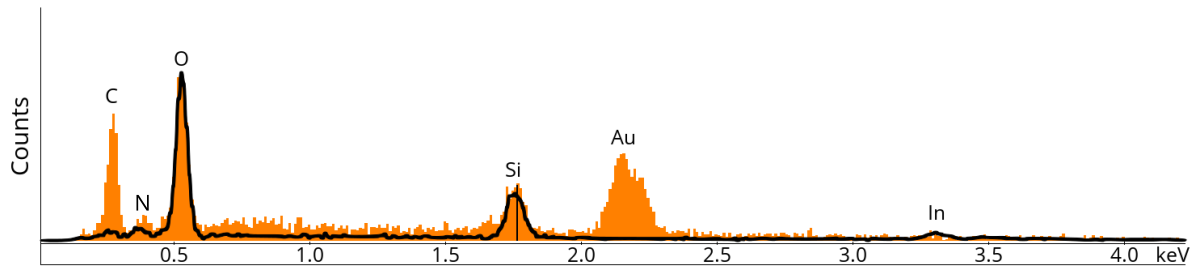

Figure 6.8: Energy-dispersive X-ray spectroscopy measurement on an ultrathin fibre plasmonic structure. The black line shows the EDS spectrum of the gold structures while the orange histogram shows the spectrum on the gold structures.

Despite this, we were able to glean some important facts from the EDS spectra. We see that there is a large amount of gold present and this level of purity should allow for plasmonic activity. We can use this spectrum as a benchmark for future studies. We can also see that the presence of the structure does not seem to influence the silica and oxygen ratios of the plain fibre itself.

Sample 1 was oxygen treated in a Plasma Prep III Plasma Asher for 5 minutes at 100 W. A significant change in the spectra before and after treatment was observed.

6.2.3 Absorption Measurements

To detect the presence of the gold nanorod array on the surface of the optical fibre a microspectrophotometer (CRAIC 20/30 PV) was used. This piece of equipment combines a microscope, broadband light sources, and high resolution spectrometers to allow the transmission and reflectance spectra of a sample to be accurately recorded. This is further enhanced by the use of pinhole apertures, which can collect light from precise locations in the sample. Using a 100x objective we were able to pinpoint the location of the structure on the waist region of the ultrathin fibre and determine the transmission and reflection spectra for the nanorod array. The sample shown in Fig. 6.6 was analysed twice; once before plasma treatment and once following the plasma treatment. The absorption spectra are given in Figs. 6.9 and 6.10

We can see a major change in the absorption spectrum of the device after the plasma treatment. This change can be attributed to an increase in the purity level of the gold nanostructures. The pre-treated structure exhibits some scattering behaviour with little polarisation dependence, whereas the post-treated structure exhibits a large polarisation dependence typical of plasmonic structures. The CRAIC system uses both Si and InGaAs detectors to measure light levels in the visible and NIR, respectively. The region over which the detectors switch is at 850 nm, leading to slight discontinuity in the spectrum at that region so it was best avoided.

The simulations agree qualitatively with the obtained data, see Fig. 6.11, though

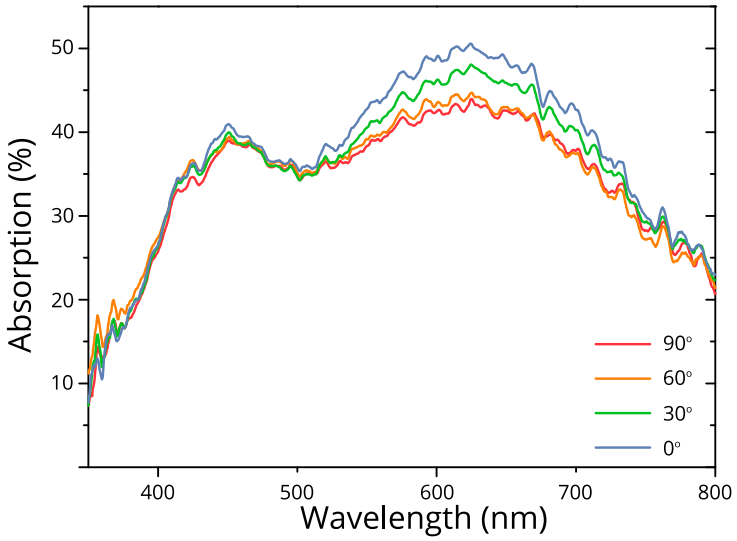

Figure 6.9: Absorption spectra for the gold nanodisk array on the surface of an ultrathin fibre prior to oxygen plasma cleaning, taken using a microphotospectrometer with a 0.8 µm by 0.8 µm aperture size.

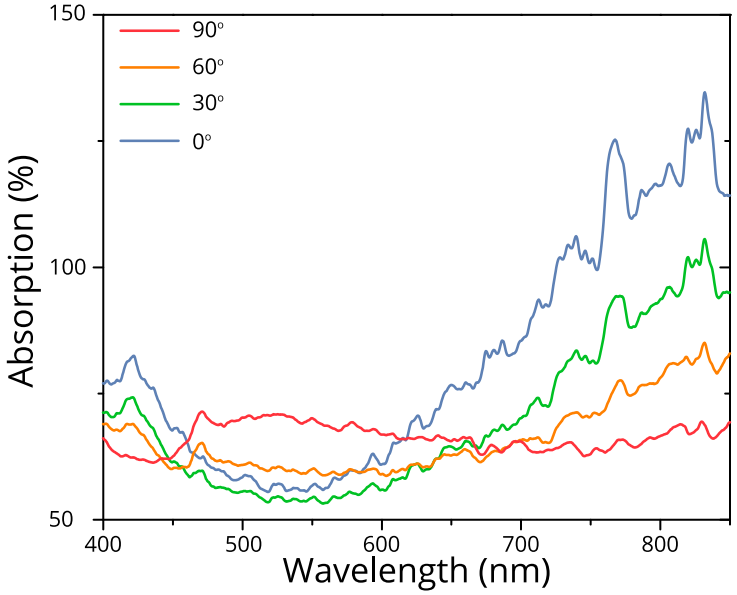

Figure 6.10: Absorption spectra for the gold nanodisk array on the surface of an ultrathin fibre after oxygen plasma cleaning, taken using a microphotospectrometer with a 0.8 µm by 0.8 µm aperture size.

the positions of the peaks are red-shifted. Deviations from theory are expected for a number of reasons. The position of the peaks is largely dependent on the aspect ratio of the ellipses, which can be hard to determine from the SEM images, see Fig. 6.6. Additionally, the exact purity of the gold film is hard to determine, meaning that the

values for the permittivity of gold used in the simulations may not agree well with the actual values of the material. There is also the possibility of a thin, continuous gold film remaining on the surface which may introduce surface plasmon polaritons. In Fig. 6.7(b) one can easily see the residual gold forming a halo around the plasmonic gold dimer array. One would assume the effect of this layer to be negligible, but it should not be removed from consideration. The simulations, shown in Fig. 6.11, predict a large peak at $\approx$ 1000 nm for polarisation parallel to the long axis of the elliptical structures, corresponding to the longitudinal mode shown in the top image of Fig. 6.4, while, for light perpendicular to the long axis of the elliptical structures, we see a peak at 600 nm, and a smaller peak at 400 nm. The 400 nm peak may correspond to the gap plasmon formed between the two components of the gold dimer. As with all plasmonic simulations, the wavelengths can be shifted and toyed with by varying parameters such as the thickness, shape, and separation of the disks. However, the benefit of altering the model to fit obtained data is questionable. We believe that the model used closely matches the parameters we determined from SEM imaging, although the thickness of the gold layer is difficult to estimate. The greatest deviations probably arise from the values used as the permittivity of gold in the models. We used the values given by Rakíc et al. [232], but, due to the questionable gold purity, one could expect large deviations from the permittivity of a pure gold structure.

6.3 Conclusions

Accurately producing plasmonic structures on glass substrates is a difficult task and here we showed how one could write a plasmonic structure directly on the surface of a micron-sized optical fibre. This is an important step forward. Unlike the work in Chapter 5, which sought to push the boundaries of ultrathin optical fibres through increasing the evanescent field alone, in this chapter, we sought to sidestep the problem by adding elements directly to the surface of the fibre. Many groups have sought to plasmonically modify ultrathin fibres as was discussed earlier, but, to-date, no group has been able to

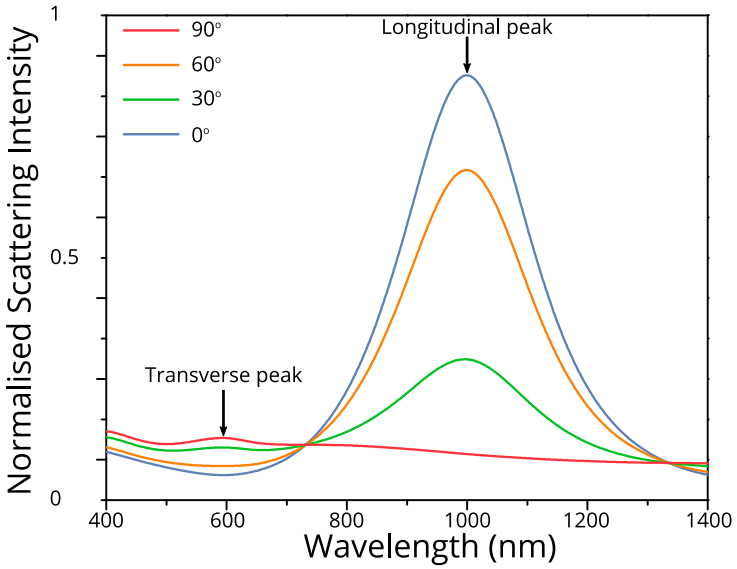

Figure 6.11: The spectra for light scattered from a single gold dimer for various polarisations. Two polarisation dependent peaks are located at approximately 600 and 1000 nm, corresponding to the transverse and longitudinal plasmonic modes, respectively.

write, in a controlled manner, plasmonic structures onto the curved face of an ultrathin fibre to our knowledge.

Perhaps the most exciting outcome of this chapter was that the fabrication process was successful. We can foresee many applications of this technique, such as the production of plasmonic structures with chiral scattering properties, as well as creating more traditional trapping structures on the ultrathin fibre, such as bowtie nano apertures. Unlike the previous modifications, plasmonic modifications provide an E^2 enhancement of the field. This is a much more efficient process for increasing the local electric field which would allow for particle trapping with very low input powers. Some future work would involve reducing the fibre diameter to allow more light in the evanescent field thereby providing a stronger interaction with the gold dimer array.

Chapter 7

Fresnel Microlens Array for Atom Trapping

Aside from fibre-based work, our group had previously proposed trapping neutral atoms using Fresnel diffraction at a thin aperture [233]. During the early stages of my PhD work (conducted as a student of the University College Cork and at the Tyndall National Institute, Cork, Ireland), fabrication methods to combine the Fresnel microlens with an atom chip were explored [233]. Atom trapping is an area of interest in the physics community, something we have discussed at length throughout this thesis. In the early stages of cold atom experiments, attention was paid to ensure that atoms would stay within a certain region of the vacuum chamber, but, as techniques advanced, novel methods of trapping atoms emerged. Trapping atoms in a cloud via the use of a MOT, useful when large numbers of cold atoms are required, has become a straightforward process. By now, there are numerous trapping configurations e.g. 2-D lattices using counter propagating beams, mirror MOTs [234], pyramidal mirror MOTs [235] and atom chips [236, 237], to mention but a few.

Our atom chip design aimed to combine existing techniques, namely mirror MOTs, U-chips and Z-chips, with a Fresnel atom microlens. The purpose of the atom chip is to trap atoms extremely close to a surface (< 2 µm) to investigate surface effects. This atom

trap proposal has generated some interest from the quantum information community due to its potential for large arrays of single occupancy trapping sites [238, 239].

Note that this work does not involve the use of ultrathin optical fibres as it was undertaken at an early stage while still in Ireland.

7.1 Fresnel Atom Microlens

In summary, the Fresnel atom microlens [240] uses the electric field generated by the diffraction of laser light through micron-sized apertures, which have been patterned into a gold layer on the surface of a borosilicate wafer to create an optical trap for cold neutral atoms, see Fig. 7.1. The Fresnel atom microlens operates on the basis of diffraction optics as described in the following.

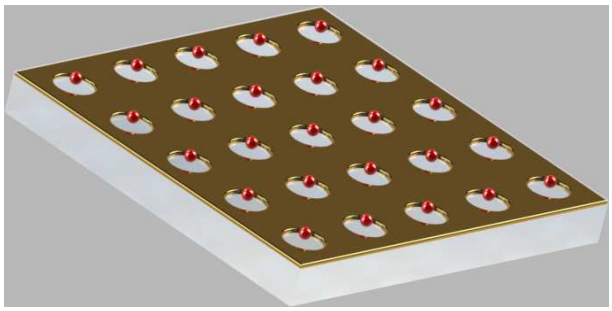

Figure 7.1: Representation of a Fresnel microlens array with individual trapping sites.

7.1.1 Wave Diffraction Optics

Wave diffraction optics has been studied quite rigorously since the 17th century and although huge advances have been made in optics, the basic laws that govern how classical light propagates have essentially remained unchanged since Christiaan Huygens and Augustin-Jean Fresnel proposed their theory of light as a wave.

There are many different theories that can be used to solve problems in diffraction, but the applicability of these theories depends on the situation in which they are to be used. Kirchhoff's diffraction theory is often used to solve such problems, but it becomes

inaccurate as we approach the plane of the aperture. To determine the electric field closer to the plane of an aperture the Rayleigh-Sommerfeld (R-S) integrals can be used, although it should be noted that neither theory is appropriate for solving the field at the plane of the aperture. For planes far from the aperture the Kirchhoff and R-S theories are equal, leading to the commonly held belief that the R-S theory is somewhat superior since it is "manifestly consistent" over a wider range of distances from the aperture surface than the standard Kirchhoff theory. The R-S theory requires an aperture which only varies in two dimensions to be valid. The R-S integral, $E(\rho, z)$, is given as

$$E(\rho, z) = \frac{E_0}{2\pi} \int\int \left(\frac{1}{R} - ik\right) \frac{z}{R} \frac{exp(ikR)}{R} dx'dy', \tag{7.1}$$

where R is the distance from the aperture plane to a point P at some distance from the aperture and E_0 is the input field. For a circular aperture, it is simpler to change the integral in Eqn. 7.1 to polar coordinates over the area of the aperture, such that

$$E(\rho, z) = \frac{E_0}{2\pi} \int_0^a \int_0^{2\pi} \left(\frac{1}{R} - ik\right) \frac{z}{R} \frac{exp(ikR)}{R} d\varphi\rho' d\rho', \tag{7.2}$$

where $R = \sqrt{z^2 - \rho^2 + \rho'^2 + 2\rho\rho' cos(\varphi)}$, $\varphi = \phi - \phi'$ is the relative angular coordinate and ρ is the radial coordinate.

7.1.2 Atom Potential

We have already discussed the trapping of atoms in an electric field in Chapter 2, so we need not discuss the theory deeply here. Instead, we shift our focus to the specific problem at hand, namely the Fresnel aperture atom trap. This theory was originally developed by other group members [233]. The atom trapping effect is only significant if the apertures have a radius, a, comparable to that of the wavelength of light used, λ, as determined by the Fresnel Number, $N_f = a^2/(\lambda z_m) \approx 1$. z_m is a characteristic vertical distance from the aperture to the maximum of the electric field intensity. Using this, we can estimate an

appropriate aperture radius of $a = 1.5\lambda$. For values of $N_F \ll 1$ Fraunhofer or Kirchhoff diffraction can be applied.

The atom trap discussed here is a one-colour, red-detuned trap. For a single Fresnel microtrap, a single atom will see a potential, U, given as

$$U = -U_0 \frac{|E|}{E_0^2}, \tag{7.3}$$

where $U_0 = (-3\gamma E_0^2)/(8\,|\delta|\,k^3)$. The solution of this equation is typically non-analytical, but if only the on-axis solutions are required they can be determined. The expansion of the integrand in Eqn. 7.2 for $\rho \ll a$ is quite cumbersome so we omit the details here. The full derivation can be found in [240]. In summary, the integrand is broken down appropriately since only on-axis terms are required and the higher order terms in the resulting expansion are omitted. The final result for the potential, $U(\rho, z)$, is

$$\begin{aligned} U(\rho,z) = &- U_0\Bigg(1 + \frac{z^2}{R_a^2} - \frac{2z}{R_a}\cos[k(R_a - z)] \\ &- \frac{k^2a^2z\rho^2}{2R_a^3}[\Big(1 - \frac{3}{k^2R_a^2}\Big)\Big(\frac{z}{R_a} - \cos[k(R_a - z)]\Big) + \frac{3}{kR_a}\sin[k(R_a - z)]\Bigg), \end{aligned} \tag{7.4}$$

where $R_a = \sqrt{a^2 + z^2}$. This potential has a minimum at $z = z_m \approx 1.46a$ defined by the transcendental equation

$$cos[k(R_a - z) - \chi] = \frac{a^2z^2}{(a^2 + z^2)^{3/2}} \frac{1}{(A + B)^{1/2}}, \tag{7.5}$$

which allows us to pick a suitable aperture radius of 1.5λ.

To get a clearer picture of what is happening, and to allow us to fully characterise the trap, a numerical solution of Eqn. 7.2 was sought using Mathematica's Monte Carlo NIntegrate method. To determine the minimum potential depth value along z, i.e. above the aperture, for a fixed aperture size, a surface plot of the potential for varying values of ρ and z was created, see Fig. 7.2.

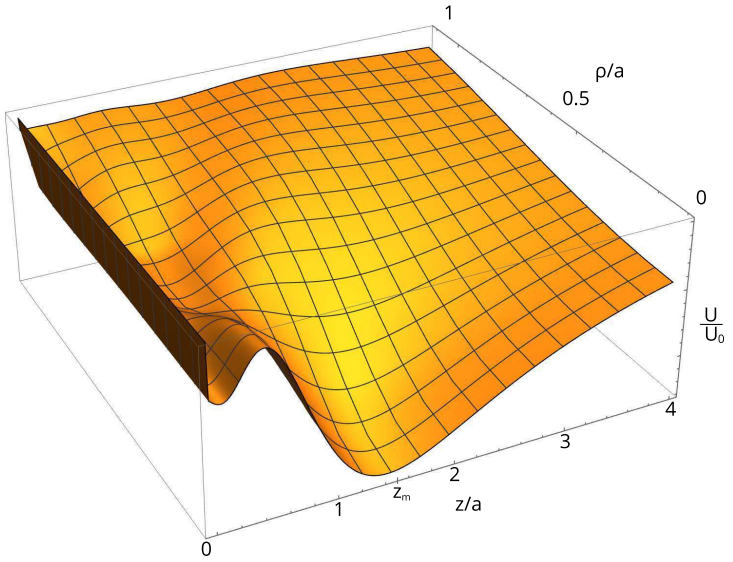

Figure 7.2: Fresnel atom trap potential along central axis. A clear minimum can be seen at $z = 1.46a$.

By inspection of Fig. 7.3, we can see how the potential evolves as we move further away from the surface of the chip. For a value of $z = 1.5a$, Fig. 7.3(b), a rather sharp, deep potential is produced. Closer to the surface the potential is shallower, due to the value of ρ-independent terms in Eqn. 7.4 (the first three terms) increasing in value towards z=0. As we move further from the surface, a roughly harmonic potential is maintained, but the depth gradually decreases due to the increasing ratio of the z/R_a terms in Eqn. 7.4. The trap depth near the surface is adequate to trap atoms, but, since the potential rapidly drops off as we move away from the surface, the loading of the trap may be problematic. In order to rectify this problem, a combination atom chip using U- and Z-chips is required.

7.1.3 U- & Z-chips

In order to draw atoms gradually closer to the atom chip surface, we propose a combination of U- and Z-chips. U- and Z-chips are current carrying wires in different configurations which resemble the shapes of the letters U and Z (Fig. 7.4).

A single Fresnel atom lens creates a stable potential at a height of approximately 1.5 µm above the aperture. U- and Z-chips can produce stable traps as far as a few millimetres

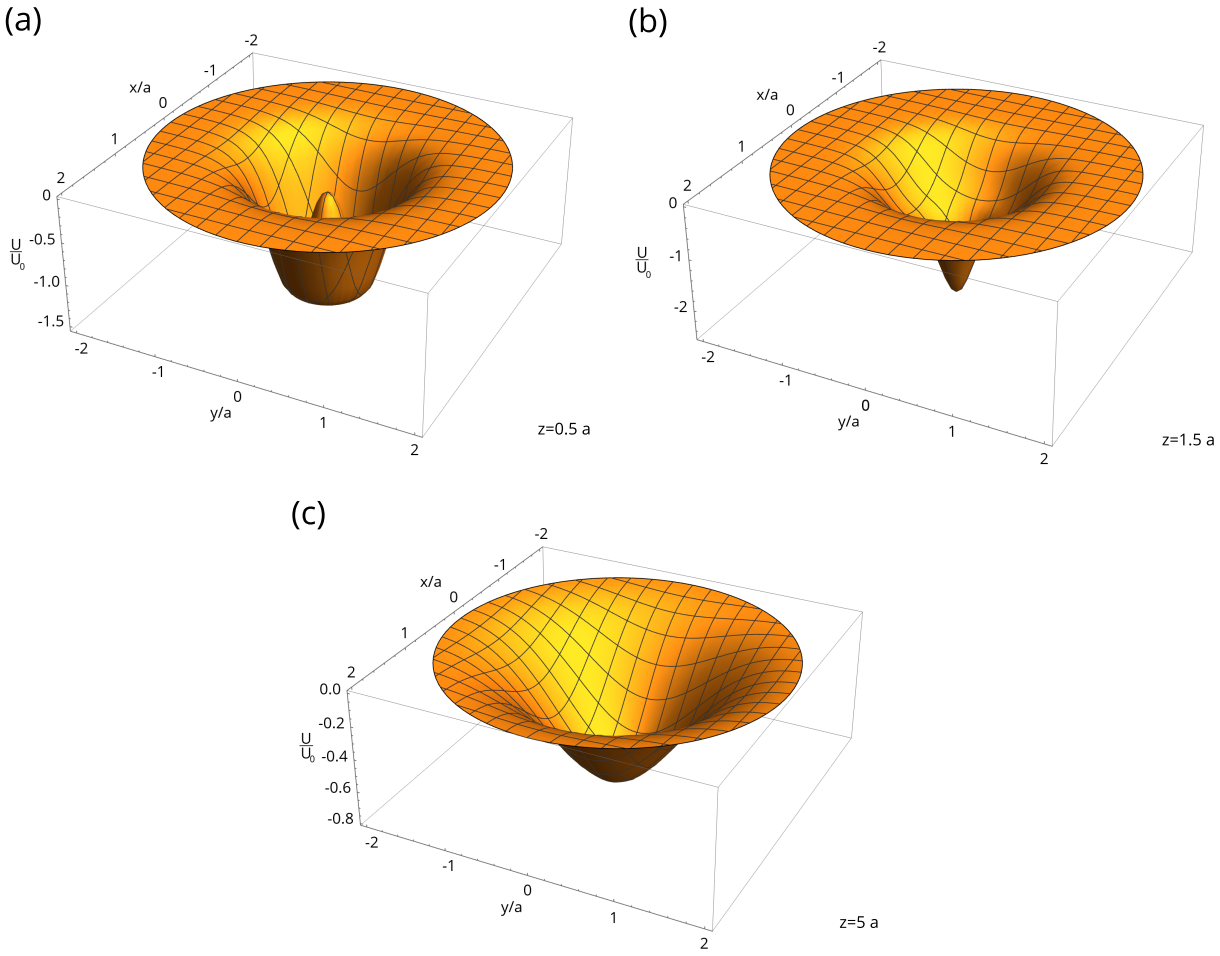

Figure 7.3: Fresnel atom trap potential for three different z-planes. (a) $z = 0.5a$, (b) $z = 1.5a$, and (c) $z = 5a$. The depth of the potential is much deeper at $z = 1.5a$, agreeing with earlier data.

from the surface of the wires [236]. The trap is formed by combining the magnetic field generated from the current carrying wires, as determined using the Biot-Savart law, with a bias field. This combination produces a magnetic field with a well-defined minimum. U-shaped wires and Z-shaped wires have similar magnetic field magnitudes, but a very different field distribution; this is not apparent when the total B-field is viewed. If we instead look at the three components of the fields we find some important differences, see Fig. 7.5, even at large distances. These differences carry over to the types of trapping potentials which can be obtained. For U-chips, due to the wire geometry, when an appropriate bias-field is applied, a quadrupole trap with a minimum B-field norm of zero is

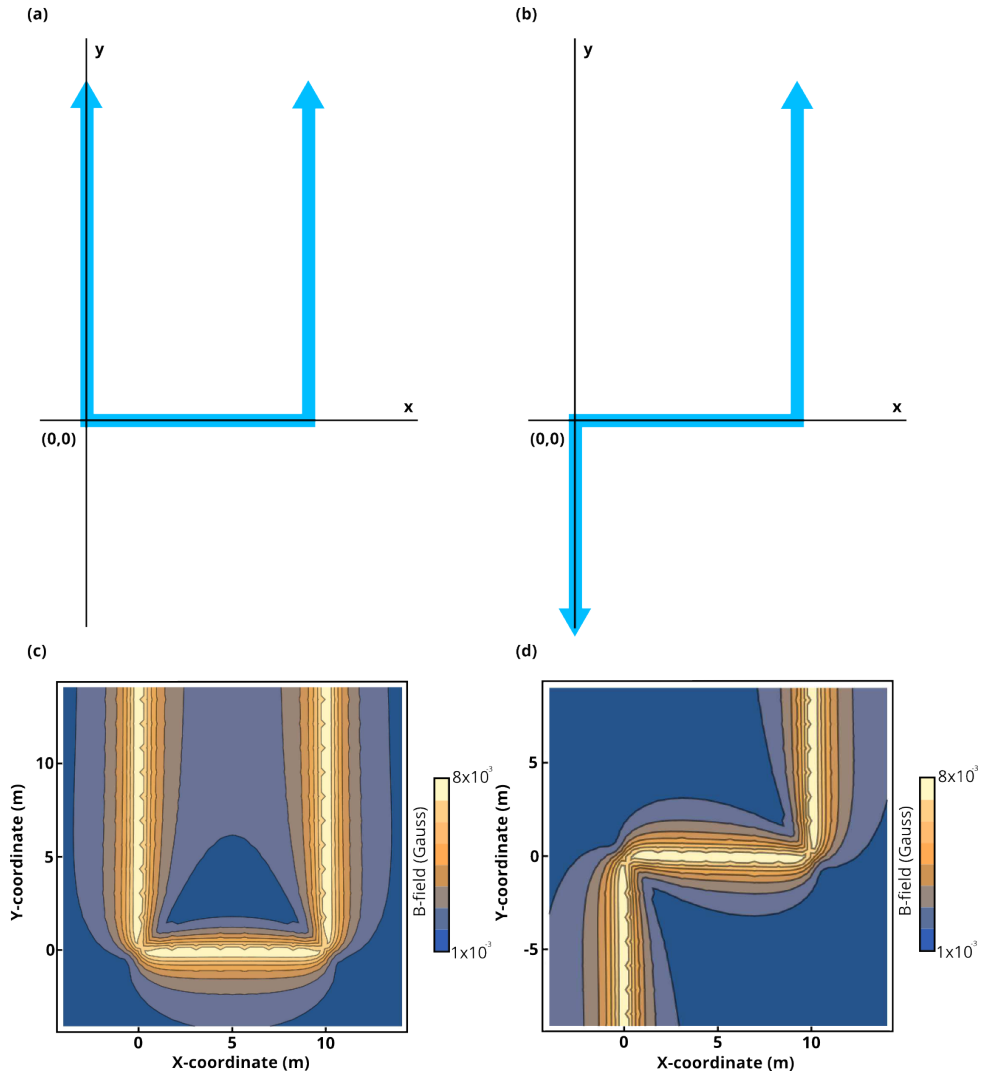

Figure 7.4: (a) and (b) U- and Z-wire trap designs respectively. (c) and (d) example fields generated from U- and Z-wires at a height of 0.5 m above the wires. Large values for the distances were chosen to give better visual representations of the fields.

produced. Z-chips, however, can have potentials which do not have a minimum of zero. These traps are more commonly referred to as Ioffe-Pritchard traps and are preferred for ultracold atoms in Bose-Einstein condensates (BECs) since they help to reduce the losses due to Majorana spin flips. For U-chips, the literature often represents the total field, $B_{tot} = B_{Uchip} + B_{bias}$, without the additional fields from the two 'arms' of the chip. Instead, only the central bar of the U-chip is modelled. This is not an adequate approximation for chips with mm-scale dimensions. A comparison of the simple model versus the complete model is given in Fig. 7.6.

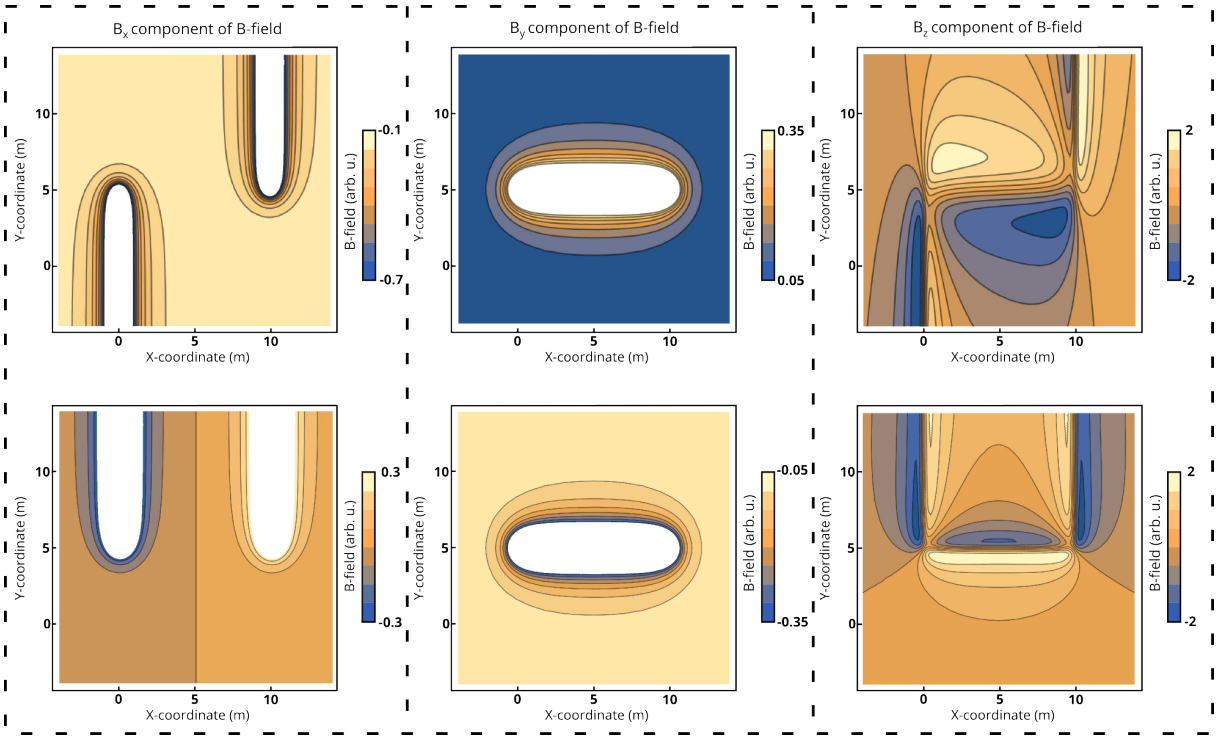

Figure 7.5: Top: The field for a Z-shaped wire. Bottom: The field of a U-shaped wire. Simulations were performed for the same conditions as Fig. 7.4.

Z-chips are typically modelled in full so this does not pose a problem. This slight displacement in the y-direction is important in this application since it may affect the atom loading of the Fresnel lenses since the trap will be formed preferentially above the Frensel microlens array rather than directly above the U- or Z-shaped wire of the atom-chip.

7.1.4 Fabrication

As the name atom-chip might imply, they are fabricated using a lithography technique on a wafer substrate. This design and fabrication work was conducted in Tyndall National Institute with the assistance of the microfabrication engineering staff. Initially, a quartz material was chosen as the substrate for the device due to its high transmission in the NIR range. However, a 200 mm diameter quartz wafer was difficult to obtain so we had to opt for a borosilicate wafer. Borosilicate, more commonly known by its commercial name

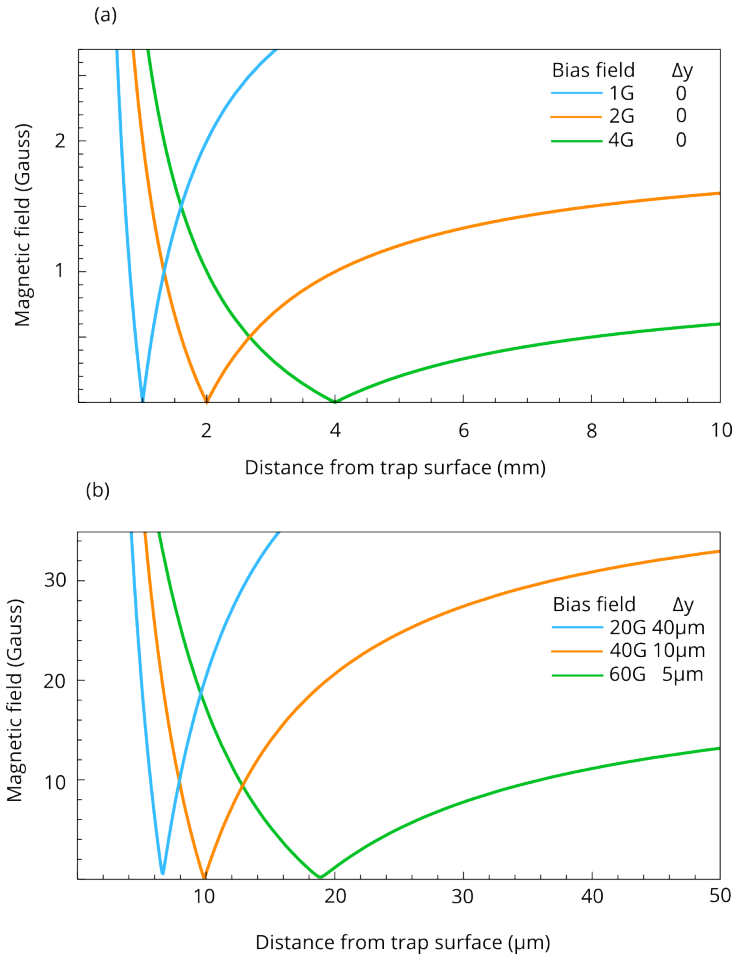

Figure 7.6: (a) Magnetic field versus the distance from the trap surface when the chip is approximated as a straight wire. Here, the minimum is located directly above the central bar of the U-chip. (b) Model of a full chip. The required bias fields are different and the trap minimum is displaced in the y-direction by as much as 40 μm depending on the bias field.

of Pyrex, also has a high transmission value for the region of interest. Gold was chosen as the material for the Fresnel apertures, as well as the U- and Z-shaped wires. This choice was decided upon after considering a few factors: (1) Gold is relatively easy to work with in lithographic device fabrication, (2) gold is highly reflective, which is necessary since we intend to also use the device as a reflective surface for the creation of a mirror-MOT, and (3) gold is highly conductive allowing us to print wires directly in the gold layer. The AutoCAD layout for the wafer, along with a single element is given in Fig. 7.7.

Any single device is symmetric under 180° rotations. On either side of the cental

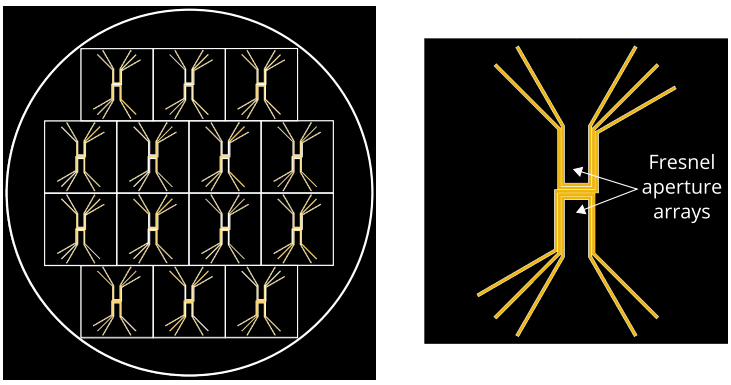

Figure 7.7: Left: Atom-chip layout for full wafer. Right: Single element of the wafer. Apertures not shown due to the large number of elements ($>$ 100,000). The final device also had large bond-pads at the ends of each of the wires to allow electrical connectivity. Here, only the wires are highlighted in gold. In reality the entire device is covered in gold with the obvious exceptions of the apertures and the insulating gaps between the U- and Z-shaped wires.

bar of the Z-wire, there are two U-shaped wires and a large array of Fresnel microlenses. Sixteen different Fresnel microlens array configurations were created with varying pitches between the Fresnel microlens arrays as well as different radii. Each chip was labelled uniquely in the bottom right-hand corner.

Table 7.1: Device parameters

Device number	Array size	Radius (µm)	Pitch (µm)	Distance from edge (µm)
1	500x323	1.20	4.80	11.20
2	500x431	1.20	3.60	10.00
3	400x259	1.20	6.00	10.00
4	350x216	1.20	7.20	10.00
5	500x369	1.40	4.20	11.20
6	400x277	1.40	5.60	11.20
7	400x222	1.40	7.00	10.50
8	350x158	1.40	8.40	11.20
9	500x323	1.60	4.80	11.20
10	400x243	1.60	6.40	9.60
11	300x195	1.60	8.00	12.00
12	250x162	1.60	9.60	11.20
13	350x216	1.80	7.20	10.00
14	300x195	2.00	8.00	8.00
15	300x173	1.80	9.00	10.00
16	250x156	2.00	10.00	9.00

The devices were fabricated using electron beam lithography, gold sputtering, and gold lift-off techniques[1]. First, the wafer was coated with a photoresist (SPR220). Next, the pattern, given in Fig. 7.7, was lithographically etched using an electron-beam. The untreated resist was then removed and a sputter deposition process created a 200 nm layer of gold across the entire device. A lift-off process was subsequently used to remove the unwanted gold leaving the patterned device behind. Since current carrying wires are prone to large heating effects, wires of 200 nm thickness would not survive the relatively high currents required, often as large as 1A, hence, electroplating was used in the final step to raise the thickness of the U- and Z-shaped wires.

After fabrication, the atom chips were mounted on a specifically fabricated printed circuit board (PCB), see Fig. 7.8. The mount was created to allow direct handling of the devices as well as providing ease-of-access to the U- and Z-shaped wires through the use of larger bond-pads. A photograph of the finished device is given in Fig. 7.9.

SEM imaging shows that the apertures were well formed using the lift-off process, see Fig. 7.10. The separation of the wires after the electroplating process was very close to the expected gap of 16 µm. The initial gap was much larger since the electroplating process raises the thickness of the wires in both the vertical and horizontal directions. The wire thickness was estimated to be 4 µm, which seems to agree with the SEM imaging results shown in Fig. 7.10(d).

7.2 Reflection Spectra

To ensure that the device could transmit light and that the lift-off process was successful a measure of the devices reflection spectrum was performed. We again used the CRAIC Microphotspectrometer system at OIST. The reflection spectrum of a device is given in Fig. 7.11. This was performed for device number 7 as given in Table 7.1. A section of the

[1]The fabrication work itself was performed by Richard Murphy, Thomas Healy and Dan O'Connell of the Tyndall National Institute. They contributed in some way to the chip design either through converting the original CAD design to the appropriate format or with the actual fabrication process.

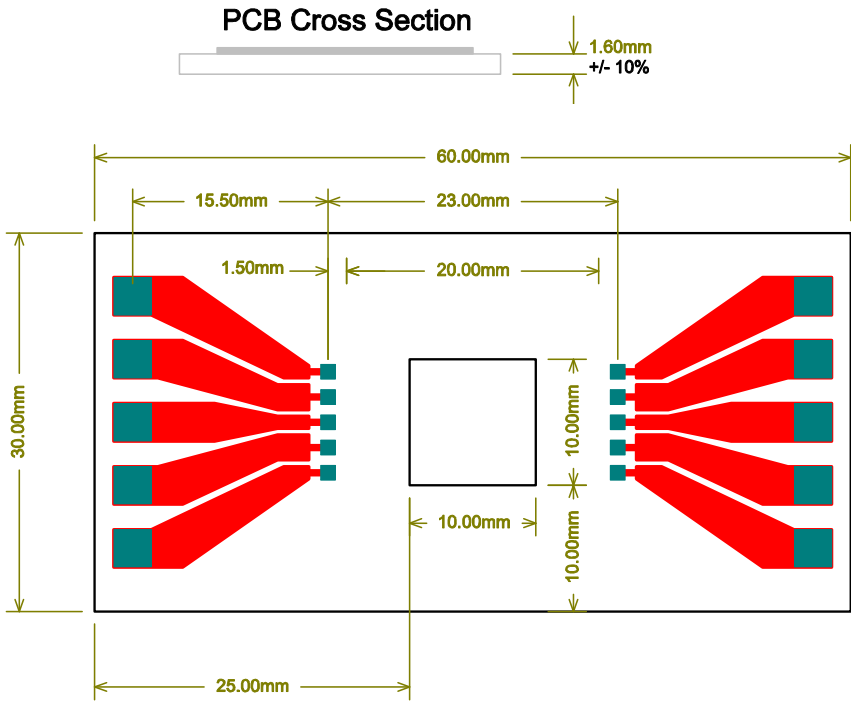

Figure 7.8: Diagram of the printed circuit board for use with atomchips. The central section contains a small 'window' to allow light to pass through the Fresnel microlenses. The red wires serve as a connection between the small bond pads on the atom chip and the larger green bond pads on the PCB. PCBs were manufactured by Shipco Circuits Ltd., Ireland.

gold surface without any Fresnel apertures was used as the reference for this measurement. A 10x objective lens was used so that a large number of the apertures could be included in the measurement. A peak in the transmission was observed at approximately 1050 nm. Device 7 had an aperture radius of 1.4 µm, allowing light to pass through it over a large range of wavelengths. As one approaches smaller aperture radii, a consideration of the plasmonic nature of the gold coating becomes important.

7.3 Conclusion

Balykin and Minogin's early proposal [240] of how a Fresnel atom microlens would operate in a cold atom system led to the development of the Frensel lens array atom-chip. Unfortunately, as this project was part of early work before moving to OIST, we never truly

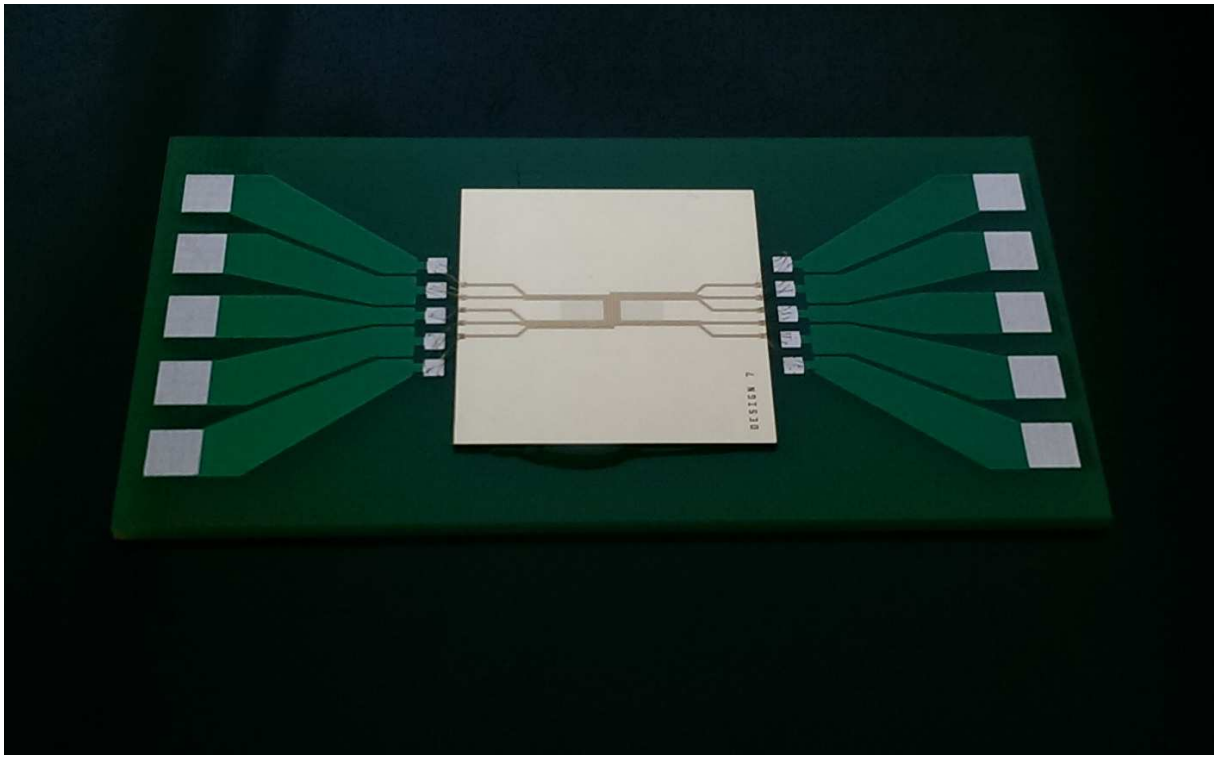

Figure 7.9: Packaged Fresnel microlens atom trap with U- and Z-wires. The U- and Z-shaped wires can clearly be seen, the Fresnel microlens array is more difficult to distinguish, but the slight discolourations of the gold to the left and right of the centre of the chip indicates their position.

had time to investigate the device's operation in a cold atom system. We did, however, manage to create a promising device with a high degree of accuracy in its production. The SEM imaging of the device after the lift-off and electroplating processes show that all of our goal dimensions were well met. The electrical contacts were tested at low currents and were found to be in working order. A reflection spectrum in the visible-NIR range shows that the apertures do transmit light, though it would be preferable to map out the optical near field. Perhaps a near-field scanning optical microscope would be up to such a task as very low surface-to-sensor distances are required.

The future of this device is quite uncertain as the direction of the cold atom section of this unit has moved towards higher-order mode trapping and the use of the STOF in the vacuum chamber, but the device may still be tested. The finished atom chip, as planned, is a self-contained device. The 'atom chip' aspect means that it could be

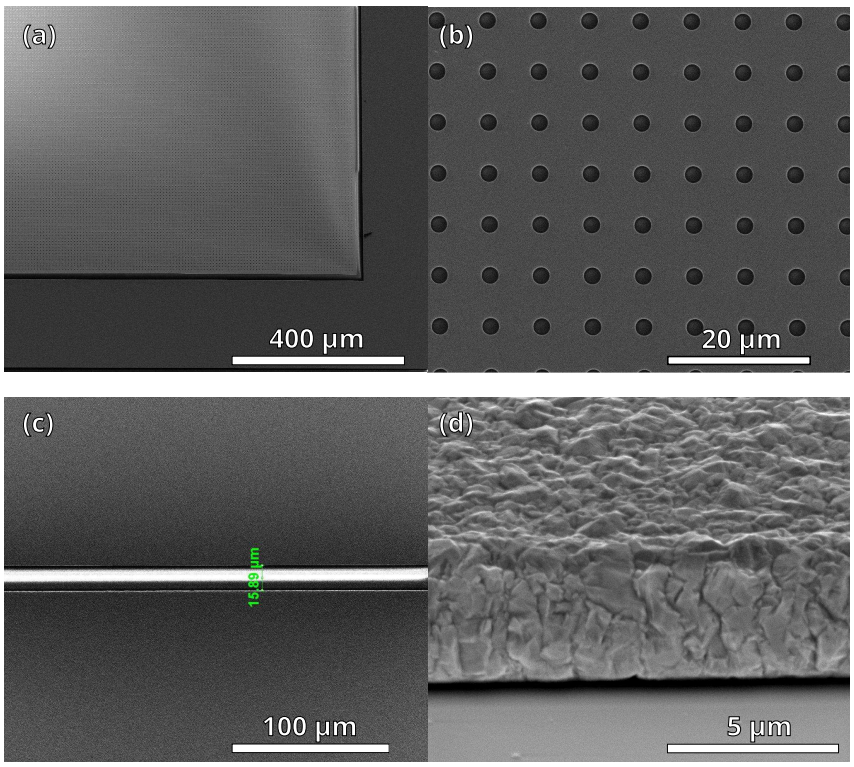

Figure 7.10: (a) Low-magnification image showing the corner of an array of Fresnel microlenses. (b) Close-up of a small number of Frensel microlenses. (c) Gap between two closely spaced wires. (d) Angled view showing the thickness of the wires.

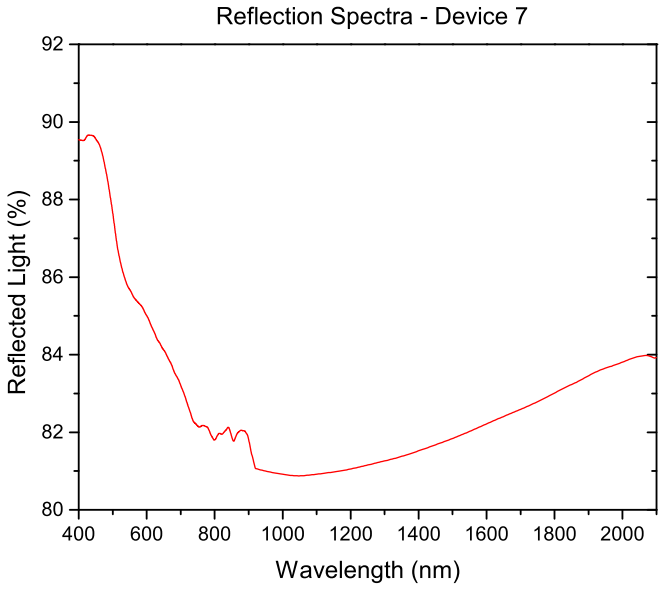

Figure 7.11: Reflection spectrum of Device 7.

implemented with few problems since it can be installed as a single device with few requirements. Problems only arise when the geometry of the cold atom chamber prevents the operation of the device as a mirror-MOT. There are, of course, technical problems, but none should be insurmountable. The ability to control the atom-surface distance using three separate techniques —Z-chip, U-chip, and Fresnel atom microlens array —would allow one to investigate the lineshape of the atom species at many different heights. This could potentially be used to measure the interaction effects of the atoms with the surface.

Chapter 8

Conclusion

Optical near-fields are an excellent way to probe and control matter at length-scales smaller than the wavelength of light. In the work presented in this thesis, we show how optical near-fields, in various forms, can be used to interact with atoms and submicron particles both theoretically and experimentally. Optical near-fields can be formed in a plethora of different ways, for example, through the total internal reflection of light at the face of a prism, or the passage of light through subwavelength apertures. We investigated a number of these techniques and in some cases applied them to physical systems to gauge their effectiveness. Ultrathin optical fibres play a central role in this thesis work, primarily due to the significant evanescent field present at their surfaces, as well as their small dimensions which allow them to be placed minimally invasively into many systems.

8.1 Thesis Summary

We have discussed a number of techniques for generating optical near-fields, while focussing on their application to physical systems. In cold atom systems — Chapter 3 — we used the evanescent field generated at the surface of an ultrathin optical fibre to probe a gas of ^{85}Rb. In Chapter 4 we showed, theoretically, how one could modify an ultrathin fibre through the addition of a slot at the fibre waist to further increase the strength of

the local evanescent field. This could allow for the enhanced emission of the atoms' fluorescence into the guided modes of the ultrathin optical fibre, provided that atoms were trapped in the slotted region of the nanostructured ultrathin optical fibre, which we also showed to be possible with relatively low trapping powers. Both of these chapters deal with the problem of atom trapping.

Moving to applications in dielectric particle trapping in Chapter 5, we exploited the increased evanescent field of such a nanostructured ultrathin optical fibre to trap 100 and 200 nm dielectric particles, as well as discussing the fabrication process. The trapping of dielectric particles of this size with low refractive index contrasts around ultrathin fibres had yet to be demonstrated in the community and this paper showed how it could be done provided some modifications were made. While we have initially demonstrated only the trapping ability of this device, in the future we would like to show how the device could be used to passively and actively probe the trapped particles through various spectroscopic techniques such as fluorescence correlation spectroscopy.

In Chapter 6, we demonstrated how localised surface plasmons can produce optical near-fields and, hence, produced a device which combines ultrathin optical fibres with gold dimer arrays. The creation of the device was successful and while further investigation into this device needs to be performed, we have shown solid evidence for the presence of plasmonic peaks in the transmission spectrum of the device.

Finally, in Chapter 7, we outlined how a Frensel microlens [233] in an array configuration could be used to trap ^{85}Rb atoms, and created an atom chip device which incorporated U- and Z- wires, Fresnel microlens arrays and a mirror-MOT which could be used to trap atoms with extremely low atom-surface distances.

8.2 Impact and Future Work

For the nanostructured ultrathin optical fibre, the ultimate goal was to trap cold atoms; namely ^{85}Rb. As mentioned in the conclusions of Chapter 4, the device could have a

significant impact due to its ability to capture an increased fraction of the light emitted from trapped atoms as well as providing a cavity like structure which can further enhance this signal. We also commented on how the geometric nature of the atom trap would necessitate small atom-surface distances, potentially leading to the investigation of interaction forces. However, undertaking experiments under ultra high vacuum is both time consuming and resource consuming so it was important to prove that the device could trap in a different environment before it could be brought to the cold atomic subgroup. These problems led us to the field of colloidal particle trapping where one could test the device in a different, but somehow analogous system.

The success of the device in particle trapping proved that the fabrication of a low loss nanostructured ultarthin optical fibre was possible, and served as a step towards the realisation of more complex applications involving the incorporation of different slot geometries as well as custom ultrathin fibres Bragg gratings [211] to further increase the fields of the nanostructured ultrathin fibre. We have shown that multiple slots can be written on the fibres while maintaining high transmission, but the work has yet to be followed up. Whether as a platform for studying optical binding effects, as an analytical tool, or as a trap for cold, neutral atoms, nanostructured ultrathin fibres have many exciting applications which remain to be investigated.

Chapter 6 showed how gold structures with strong localised surface plasmons can be combined with an ultrathin optical fibre. Here, we showed a direct-write solution allowing us to deterministically place a gold dimer array on a fibre. This technique could prove quite valuable as it allows one to accurately design a structure to be used in an experiment which could potentially combine many ideas. For example a fibre Bragg grating could be combined with a plasmonic device on an ultrathin fibre to produce an enhanced cavity region for particle or atom trapping. Work has also been performed on "controlling the flow of light with nanoparticles" [241] using gold nanoparticles on ultrathin fibres, and the technique outlined in Chapter 6 could be extremely useful in this application. While we were able to show the plasmonic nature of the device, further work needs to be performed.

Ideally we would seek to detect the transmission spectra through the optical fibre in a fashion similar to one of the works of Tong et al. [160] by detecting the scattered light along through the guided fibre modes. However, we have a very small number of gold structures on the fibre surface meaning the amount of light scattered into the guided modes of the fibre would be exceptionally small. This can potentially be overcome using a combination of highly sensitive detectors with lock-in amplification techniques. This is an experiment we would like to conduct immediately.

In Chapter 7 we successfully fabricated a composite device which included Fresnel microlens arrays, U- and Z-chips, and a Mirror-MOT. Through SEM imaging and transmission measurements we verified that the device was well-fabricated, but we did not manage to experimentally test the device in a cold atom system. This represents an area of future work which could be pursued.

8.3 Final remarks

Ultrathin optical fibres have come to be used in multiple areas of physics [59]. This thesis focusses, in part, on methods to push the boundaries of ultrathin fibres in experimental settings. Without venturing into areas involving the higher order modes of ultrathin optical fibres, the use of ultrathin optical fibres is limited by the finite extent of the evanescent field. For simple applications, such as the trapping of larger, micro-sized particles or atoms around a fibre, ultrathin optical fibres in their current state are more than adequate, but if we want to continue using them in an experimental setting it is necessary to seek ways to enhance the fields even further. Currently it is possible to create high transmission optical fibres for both the fundamental and higher order modes [78], which indicates that little can be improved in the initial fibre fabrication process to improve their versatility.

With this in mind modifications involving the addition of cavities or plasmonic structures are very important to the field. By correctly developing the techniques to modify

ultrathin fibres we can make perfect the process of creating such devices and allow them to become widely used throughout the field. In the case of the nanostructured ultrathin fibres presented in Chapters 4 and 5, the FIB etching technique has been perfected and can be used not only to created slots, but also FBGs, and perhaps other as of yet undiscovered modifications. The work demonstrated in Chapter 6 needs to be perfected, but it paves the way for combining ultrathin fibres and plasmonic structures with arbitrary geometries.

In summary, the techniques outlined in the work of this thesis can be relatively easily adopted by many groups and potentially allow the investigation of interesting physical phenomena through the enhanced near-field interactions that they facilitate.

Appendix A

Solutions to the Scalar Helmholtz Equation — Mie Scattering

In Section 2.2.3 we briefly discuss the scattering solutions for a sphere. Here I will outline how one could obtain the solutions to the scalar Helmholtz equation.

Let us start with the scalar Helmholtz equation given in-text in Section 2.2.3

$$\nabla^2\psi_{l,m} + k_m^2\psi_{l,m} = 0. \tag{A.1}$$

To solve this we must first make the assumption that the function $\psi_{l,m}$ is separable. Hence, we have $\psi_{l,m} = R(r)\Theta(\theta)\Phi(\phi)$. Here, r, θ, and ϕ represent the three coordinates in spherical coordinates. Remaining in a spherical coordinate system the scalar Helmholtz equation can be expanded as

$$\frac{1}{R}\frac{d}{dr}\left[r^2\frac{dR}{dr}\right] + k^2r^2 + \frac{1}{\Theta\sin\theta}\frac{d}{d\theta}\left[\sin\theta\frac{d\Theta}{d\theta}\right] + \frac{1}{\Phi\sin^2\theta}\frac{d^2\Phi}{d\phi^2} = 0. \tag{A.2}$$

When solving for a similar equation for step-index optical fibres we use cylindrical coordinates since we have the liberty of assuming a form of the solution for the infinitely long cylinder along the z-axis. However, here we do not have the same freedom, instead we must solve for each part of the function. On inspection of this equation we see that

the last term depends only of ϕ, provided we multiply the entire equation by $\sin^2\theta$. This allows us to write

$$\frac{1}{\Phi}\frac{d^2\Phi}{d\phi^2} = -m^2 \tag{A.3}$$

where m is some integer chosen so that the boundary condition, $\Phi(\phi + 2\pi) = \Phi(\phi)$, is satisfied. The form of the right-hand side of this equation is chosen since we have some prior knowledge of how the solutions to such equations behave and this will simplify the problem later. This is easily solved with the function $\Phi(\phi) = e^{im\phi}$. We can then substitute this solution into Eqn. A.3 to obtain

$$\frac{1}{R}\frac{d}{dr}\left[r^2\frac{dR}{dr}\right] + k^2r^2 + \frac{1}{\Theta\sin\theta}\frac{d}{d\theta}\left[\sin\theta\frac{d\Theta}{d\theta}\right] - \frac{m^2}{\sin^2\theta} = 0. \tag{A.4}$$

We can now repeat this process as we now see that the last two terms in this equation depend only on the θ variable. We set these terms equal to $-l(l+1)$, where l is a non-negative integer, and letting $z = \cos\theta$. After rearranging we obtain

$$\frac{d}{dz}\left[(1-z^2)\frac{d\Theta(z)}{dz}\right] + \left[l(l+1) - \frac{m^2}{1-z^2}\right]\Theta(z) = 0. \tag{A.5}$$

This is another well known class of problems which can be solved directly using the associate Legendre functions, $P_{lm}(z)$. This leaves us with the remaining radial function to solve for. Let us substitute this solution into Eqn. A.4 to obtain

$$r^2\frac{d^2R(r)}{dr^2} + 2r\frac{dR(r)}{dr} + \left[k^2r^2 - l(l+1)\right]R(r) = 0, \tag{A.6}$$

where we have also multiplied the equation by $R(r)$. If use the substitution $z = kr$ we obtain the more familiar form of

$$z^2\frac{d^2R(z)}{dz^2} + 2r\frac{dR(z)}{dz} + \left[z^2 - l(l+1)\right]R(z) = 0, \tag{A.7}$$

which has solutions known as the spherical Bessel and Neumann functions, $j_l(z)$ and $y_l(z)$,

respectively.

These are the solutions to the scalar Helmholtz equation, and a general solution consists of a summation of these solutions over the allowed values of l and m, where m is bounded by $\pm l$. The Spherical Bessel and Neumann functions behave similarly to the cylindrical Bessel and Neumann functions in so much as that they are non-zero or zero at the origin, respectively. Hence, we have conditions restricting their use inside and outside of the spherical scatterer. For the complete Mie scattering solutions we must adapt the scalar solutions using Eqn 2.21. This leads to the use of the multipole expansions mentioned in Section 2.2.3. Though we do not explicitly make use of the Mie solutions in this thesis, a knowledge of how the scattering is caused is crucial to understanding the problems of the field.

Appendix B

Relevant Code and Model Files

Many programs were used to create the plots and data shown in this thesis. Rather than include the code and model files here, which would be impossible in some cases, we instead include a link to a public GitHub account which contains the most pertinent models used.

The programs required to run the models are COMSOL MultiPhysics 5.2+, FIMMWAVE, FIMMPROP, CrystalWave, and Matlab.

Please follow the following link to gain access to this models: `https://github.com/MarkJDaly/Appendix`.

Bibliography

[1] Daly, M., Sergides, M. & Nic Chormaic, S. Optical trapping and manipulation of micrometer and submicrometer particles. *Laser & Photonics Review* **9**, 309–329 (2015).

[2] Kepler, J. *De cometis libelli tres : I. Astronomicvs, theoremata continens de motu cometarum ubi demonstratio apparentiarum & altitudinis cometarum qui annis 1607. & 1618. conspecti sunt, ... : II. Physicvs, continens physiologiam comentarum nouam ... : III. Astrologicvs, de significationibus cometarum annorum 1607. & 1618* (typis Andreae Apergeri, sumptibus Sebastiani Mylii bibliopolæ augustani, Avgvstae Vindelicorum, 1619).

[3] Poynting, J. H. Some astronomical consequences of the pressure of light. *Nature* **75**, 90 (1906).

[4] Maiman, T. H. Stimulated optical radiation in ruby. *Nature* **187**, 493–494 (1960).

[5] Ashkin, A., Dziedzic, J. M., Bjorkholm, J. E. & Chu, S. Observation of a single-beam gradient force optical trap for dielectric particles. *Optics Letters* **11**, 288–290 (1986).

[6] Ashkin, A. Acceleration and trapping of particles by radiation pressure. *Physical Review Letters* **24**, 156–159 (1970).

[7] Pendry, J. B. Negative refraction makes a perfect lens. *Physical Review Letters* **85**, 3966–3969 (2000).

[8] Juan, M. L., Righini, M. & Quidant, R. Plasmon nano-optical tweezers. *Nature Photonics* **5**, 349–356 (2011).

[9] Quidant, R. & Girard, C. Surface-plasmon-based optical manipulation. *Laser & Photonics Reviews* **2**, 47–57 (2008).

[10] Ashok, P. C. & Dholakia, K. Optical trapping for analytical biotechnology. *Current Opinion in Biotechnology* **23**, 16–21 (2012).

[11] Fazal, F. M. & Block, S. M. Optical tweezers study life under tension. *Nature Photonics* **5**, 318–321 (2011).

[12] Lee, M. P. & Padgett, M. J. Optical tweezers: a light touch. *Journal of Microscopy* **248**, 219–222 (2012).

[13] Waleed, M., Hwang, S.-U., Kim, J.-D., Shabbir, I., Shin, S.-M. & Lee, Y.-G. Single-cell optoporation and transfection using femtosecond laser and optical tweezers. *Biomedical Optics Express* **4**, 1533–1547 (2013).

[14] Svoboda, K., Schmidt, C. F., Schnapp, B. J. & Block, S. M. Direct observation of kinesin stepping by optical trapping interferometry. *Nature* **365**, 721–727 (1993).

[15] Abbondanzieri, E. A., Greenleaf, W. J., Shaevitz, J. W., Landick, R. & Block, S. M. Direct observation of base-pair stepping by RNA polymerase. *Nature* **438**, 460–465 (2005).

[16] Mortezaei, N., Singh, B., Bullitt, E., Uhlin, B. E. & Andersson, M. P-fimbriae in the presence of anti-papa antibodies: new insight of antibodies action against pathogens. *Scientific Reports* **3**, 3393 (2013).

[17] Lee, S. & Hohng, S. An optical trap combined with three-color FRET. *Journal of the American Chemical Society* **135**, 18260–18263 (2013).

[18] Heller, I., Sitters, G., Broekmans, O. D., Farge, G., Menges, C., Wende, W., Hell, S. W., Peterman, E. J. G. & Wuite, G. J. L. STED nanoscopy combined with optical tweezers reveals protein dynamics on densely covered DNA. *Nature Methods* **10**, 910–916 (2013).

[19] Dasgupta, R., Ahlawat, S., Verma, R. S. & Gupta, P. K. Optical orientation and rotation of trapped red blood cells with Laguerre-Gaussian mode. *Optics Express* **19**, 7680–7688 (2011).

[20] Petrov, D. V. Raman spectroscopy of optically trapped particles. *Journal of Optics A: Pure and Applied Optics* **9**, S139 (2007).

[21] Amato, I. Nanotechnologists seek biological niches. *Cell* **123**, 967 – 970 (2005).

[22] Maruyama, H., Kotani, K., Honda, A., Takahata, T. & Arai, F. Nanomanipulation of single influenza virus using optical tweezers and dielectrophoretic force on a microfluidic chip. In *Nanotechnology (IEEE-NANO), 2010 10th IEEE Conference on*, 879–884 (2010).

[23] Ashkin, A. Trapping of atoms by resonance radiation pressure. *Physical Review Letters* **40**, 729–732 (1978).

[24] Jones, P., Maragó, O. & Volpe, G. *Optical Tweezers: Principles and Applications* (Cambridge University Press, 2015).

[25] Gahagan, K. T. & Swartzlander, G. A. Trapping of low-index microparticles in an optical vortex. *Journal of the Optical Society of America B* **15**, 524–534 (1998).

[26] Hulst., H. C. v. d. Light scattering by small particles. *Quarterly Journal of the Royal Meteorological Society* **84**, 198–199 (1958).

[27] Liou, K.-N. A complementary theory of light scattering by homogeneous spheres. *Applied Mathematics & Computation* **3**, 331–358 (1977).

[28] Stilgoe, A. B., Nieminen, T. A., Knöner, G., Heckenberg, N. R. & Rubinsztein-Dunlop, H. The effect of Mie resonances on trapping in optical tweezers. *Optics Express* **16**, 15039–15051 (2008).

[29] Albaladejo, S., Marqués, M. I., Laroche, M. & Sáenz, J. J. Scattering forces from the curl of the spin angular momentum of a light field. *Physical Review Letters* **102**, 113602 (2009).

[30] Visscher, K., Brakenhoff, G. & Krol, J. Micromanipulation by "multiple" optical traps created by a single fast scanning trap integrated with the bilateral confocal scanning laser microscope. *Cytometry* **14**, 105–114 (1993).

[31] Lee, M. P. & Padgett, M. J. Optical tweezers: a light touch. *Journal of Microscopy* **248**, 219–222 (2012).

[32] Padgett, M. & Di Leonardo, R. Holographic optical tweezers and their relevance to lab on chip devices. *Lab on a Chip* **11**, 1196–1205 (2011).

[33] Bowman, R. W., Gibson, G. M., Linnenberger, A., Phillips, D. B., Grieve, J. A., Carberry, D. M., Serati, S., Miles, M. J. & Padgett, M. J. "Red tweezers": Fast, customisable hologram generation for optical tweezers. *Computer Physics Communications* **185**, 268–273 (2014).

[34] Agate, B., Brown, C., Sibbett, W. & Dholakia, K. Femtosecond optical tweezers for in-situ control of two-photon fluorescence. *Optics Express* **12**, 3011–3017 (2004).

[35] Svoboda, K. & Block, S. M. Biological applications of optical forces. *Annual Review of Biophysics and Biomolecular Structure* **23**, 247–285 (1994).

[36] Fazal, F. M. & Block, S. M. Optical tweezers study life under tension. *Nature Photonics* **5**, 318–321 (2011).

[37] Deng, Y., Bechhoefer, J. & Forde, N. R. Brownian motion in a modulated optical trap. *Journal of Optics A: Pure and Applied Optics* **9**, S256 (2007).

[38] Lukić, B., Jeney, S., Tischer, C., Kulik, A. J., Forró, L. & Florin, E. L. Direct observation of nondiffusive motion of a Brownian particle. *Physical Review Letters* **95**, 160601 (2005).

[39] Berg-Sørensen, K. & Flyvbjerg, H. Power spectrum analysis for optical tweezers. *Review of Scientific Instruments* **75**, 594–612 (2004).

[40] Balijepalli, A., Gorman, J. J., Gupta, S. K. & LeBrun, T. W. Significantly improved trapping lifetime of nanoparticles in an optical trap using feedback control. *Nano Letters* **12**, 2347–2351 (2012).

[41] Arita, Y., Mazilu, M. & Dholakia, K. Laser-induced rotation and cooling of a trapped microgyroscope in vacuum. *Nature Communications* **4**, 2374 (2013).

[42] Garces-Chavez, V., McGloin, D., Melville, H., Sibbett, W. & Dholakia, K. Simultaneous micromanipulation in multiple planes using a self-reconstructing light beam. *Nature* **419**, 145–147 (2002).

[43] Melville, H., Milne, G., Spalding, G., Sibbett, W., Dholakia, K. & McGloin, D. Optical trapping of three-dimensional structures using dynamic holograms. *Optics Express* **11**, 3562–3567 (2003).

[44] Visscher, K., Gross, S. P. & Block, S. M. Construction of multiple-beam optical traps with nanometer-resolution position sensing. *IEEE Journal of Selected Topics in Quantum Electronics* **2**, 1066–1076 (1996).

[45] Moffitt, J. R., Chemla, Y. R., Izhaky, D. & Bustamante, C. Differential detection of dual traps improves the spatial resolution of optical tweezers. *Proceedings of the National Academy of Sciences* **103**, 9006–9011 (2006).

[46] Sahoo, H. Forster resonance energy transfer - a spectroscopic nanoruler: Principle and applications. *Journal of Photochemistry and Photobiology C-Photochemistry Reviews* **12**, 20–30 (2011).

[47] Kawata, S. & Tani, T. Optically driven Mie particles in an evanescent field along a channeled waveguide. *Optics Letters* **21**, 1768–1770 (1996).

[48] Snyder, A. W. & Love, J. *Optical waveguide theory* (Kluwer Academic Publishing, Boston, 1983).

[49] Kretschmann, E. Decay of non radiative surface plasmons into light on rough silver films. comparison of experimental and theoretical results. *Optics Communications* **6**, 185 – 187 (1972).

[50] Schmidt, B. S., Yang, A. H., Erickson, D. & Lipson, M. Optofluidic trapping and transport on solid core waveguides within a microfluidic device. *Optics Express* **15**, 14322–14334 (2007).

[51] Yang, A. H. J. & Erickson, D. Stability analysis of optofluidic transport on solid-core waveguiding structures. *Nanotechnology* **19**, 045704 (2008).

[52] Ng, L. N., Luff, B. J., Zervas, M. N. & Wilkinson, J. S. Propulsion of gold nanoparticles on optical waveguides. *Optics Communications* **208**, 117–124 (2002).

[53] Grujic, K., Hellesø e, O. G., Hole, J. P. & Wilkinson, J. S. Sorting of polystyrene microspheres using a Y-branched optical waveguide. *Optics Express* **13**, 1–7 (2005).

[54] Marchington, R. F., Mazilu, M., Kuriakose, S., Garcés-Chávez, V., Reece, P. J., Krauss, T. F., Gu, M. & Dholakia, K. Optical deflection and sorting of microparticles in a near-field optical geometry. *Optics Express* **16**, 3712–3726 (2008).

[55] Lin, S., Schonbrun, E. & Crozier, K. Optical manipulation with planar silicon microring resonators. *Nano Letters* **10**, 2408–2411 (2010).

[56] Erickson, D., Serey, X., Chen, Y. F. & Mandal, S. Nanomanipulation using near field photonics. *Lab on a Chip* **11**, 995–1009 (2011).

[57] Sheu, F.-W. & Huang, Y.-S. Trapping and propelling microparticles at long range by using an entirely stripped and slightly tapered no-core optical fiber. *Sensors* **13**, 2884–2894 (2013).

[58] Xu, C., Lei, H., Zhang, Y. & Li, B. Backward transport of nanoparticles in fluidic flow. *Optics Express* **20**, 1930–1938 (2012).

[59] Morrissey, M., Deasy, K., Frawley, M., Kumar, R., Prel, E., Russell, L., Truong, V. & Nic Chormaic, S. Spectroscopy, manipulation and trapping of neutral atoms, molecules, and other particles using optical nanofibers: A review. *Sensors* **13**, 10449–10481 (2013).

[60] Goban, A., Choi, K. S., Alton, D. J., Ding, D., Lacroûte, C., Pototschnig, M., Thiele, T., Stern, N. P. & Kimble, H. J. Demonstration of a state-insensitive, compensated nanofiber trap. *Physical Review Letters* **109**, 033603 (2012).

[61] Birks, T. A. & Li, Y. W. The shape of fiber tapers. *Journal of Lightwave Technology* **10**, 4 (1992).

[62] Ward, J. M., Maimaiti, A., Le, V. H. & Nic Chormaic, S. Contributed review: Optical micro- and nanofiber pulling rig. *Review of Scientific Instruments* **85**, 111501 (2014).

[63] Pastrana, E. Optogenetics: controlling cell function with light. *Nature Methods* **8**, 24–25 (2011).

[64] Brambilla, G., Murugan, G. S., Wilkinson, J. S. & Richardson, D. J. Optical manipulation of microspheres along a subwavelength optical wire. *Optics Letters* **32**, 3041–3043 (2007).

[65] Skelton, S., Sergides, M., Patel, R., Karczewska, E., Maragó, O. & Jones, P. Evanescent wave optical trapping and transport of micro-and nanoparticles on tapered

optical fibers. *Journal of Quantitative Spectroscopy and Radiative Transfer* **113**, 2512–2520 (2012).

[66] Frawley, M. C., Gusachenko, I., Truong, V. G., Sergides, M. & Nic Chormaic, S. Selective particle trapping and optical binding in the evanescent field of an optical nanofiber. *Optics Express* **22**, 16322–16334 (2014).

[67] Xin, H., Xu, R. & Li, B. Optical trapping, driving, and arrangement of particles using a tapered fibre probe. *Scientific Reports* **2**, 2045–2322 (2012).

[68] Mellor, C. D. & Bain, C. D. Array formation in evanescent waves. *ChemPhysChem* **7**, 329–332 (2006).

[69] Lekner, J. Forces on scatterers in particle beams. *Journal of Physics B: Atomic, Molecular and Optical Physics* **38**, 3849 (2005).

[70] Grujic, K. & Hellesø, O. G. Dielectric microsphere manipulation and chain assembly by counter-propagating waves in a channel waveguide. *Optics Express* **15**, 6470–6477 (2007).

[71] Lei, H., Xu, C., Zhang, Y. & Li, B. Bidirectional optical transportation and controllable positioning of nanoparticles using an optical nanofiber. *Nanoscale* **4**, 6707–9 (2012).

[72] Zhang, Y. & Li, B. Particle sorting using a subwavelength optical fiber. *Laser & Photonics Reviews* **7**, 289–296 (2013).

[73] Ploschner, M., Čižmár, T., Mazilu, M., Di Falco, A. & Dholakia, K. Bidirectional optical sorting of gold nanoparticles. *Nano Letters* **12**, 1923–1927 (2012).

[74] Petcu-Colan, A., Frawley, M. & Nic Chormaic, S. Tapered few-mode fibers: mode evolution during fabrication and adiabaticity. *Journal of Nonlinear Optical Physics and Materials* **20**, 293–307 (2011).

[75] Frawley, M. C., Petcu-Colan, A., Truong, V. G. & Nic Chormaic, S. Higher order mode propagation in an optical nanofiber. *Optics Communications* **285**, 4648–4654 (2012).

[76] Čižmár, T., Garces-Chavez, V., Dholakia, K. & Zemanek, P. Optical trapping in counter-propagating Bessel beams. *Proc. SPIE* **5514**, 643–651 (2004).

[77] Tanaka, T. & Yamamoto, S. Optically induced propulsion of small particles in an evenescent field of higher propagation mode in a multimode, channeled waveguide. *Applied Physics Letters* **77**, 3131–3133 (2000).

[78] Maimaiti, A., Truong, V. G., Sergides, M., Gusachenko, I. & Nic Chormaic, S. Higher order microfibre modes for dielectric particle trapping and propulsion. *Scientific Reports* **5**, 9077 (2015).

[79] Fu, J., Yin, X., Li, N. & Tong, L. Atom waveguide and 1D optical lattice using a two-color evanescent light field around an optical micro/nano-fiber. *Chinese Optics Letters* **6**, 112–115 (2008).

[80] Kumar, R., Gokhroo, V., Deasy, K., Maimaiti, A., Frawley, M. C., Phelan, C. & Chormaic, S. N. Interaction of laser-cooled 87 Rb atoms with higher order modes of an optical nanofibre. *New Journal of Physics* **17**, 013026 (2015).

[81] Anderson, P. A., Schmidt, B. S. & Lipson, M. High confinement in silicon slot waveguides with sharp bends. *Optics Express* **14**, 9197–9202 (2006).

[82] Yang, A. H. J., Lerdsuchatawanich, T. & Erickson, D. Forces and transport velocities for a particle in a slot waveguide. *Nano Letters* **9**, 1182–1188 (2009).

[83] Yang, A. H. J., Moore, S. D., Schmidt, B. S., Klug, M., Lipson, M. & Erickson, D. Optical manipulation of nanoparticles and biomolecules in sub-wavelength slot waveguides. *Nature* **457**, 71–75 (2009).

[84] Lin, S. & Crozier, K. B. An integrated microparticle sorting system based on near-field optical forces and a structural perturbation. *Optics Express* **20**, 3367–3374 (2012).

[85] Song, B.-S., Noda, S., Asano, T. & Akahane, Y. Ultra-high-Q photonic double-heterostructure nanocavity. *Nature Materials* **4**, 207–210 (2005).

[86] Mejia, C. A., Huang, N. & Povinelli, M. L. Optical trapping of metal-dielectric nanoparticle clusters near photonic crystal microcavities. *Optics Letters* **37**, 3690–3692 (2012).

[87] Seidler, P., Lister, K., Drechsler, U., Hofrichter, J. & Stöferle, T. Slotted photonic crystal nanobeam cavity with an ultrahigh quality factor-to-mode volume ratio. *Optics Express* **21**, 32468–32483 (2013).

[88] Robinson, J. T., Manolatou, C., Chen, L. & Lipson, M. Ultrasmall mode volumes in dielectric optical microcavities. *Physical Review Letters* **95**, 143901 (2005).

[89] Barth, M. & Benson, O. Manipulation of dielectric particles using photonic crystal cavities. *Applied Physics Letters* **89** (2006).

[90] Lin, S., Hu, J., Kimerling, L. & Crozier, K. Design of nanoslotted photonic crystal waveguide cavities for single nanoparticle trapping and detection. *Optics Letters* **34**, 3451–3453 (2009).

[91] Lin, P.-T. & Lee, P.-T. All-optical controllable trapping and transport of subwavelength particles on a tapered photonic crystal waveguide. *Optics Letters* **36**, 424–426 (2011).

[92] Nayak, K. P., Zhang, P. & Hakuta, K. Optical nanofiber-based photonic crystal cavity. *Optics Letters* **39**, 232–235 (2014).

[93] Yalla, R., Sadgrove, M., Nayak, K. P. & Hakuta, K. Cavity quantum electrodynamics on a nanofiber using a composite photonic crystal cavity. *Physical Review Letters* **113**, 143601 (2014).

[94] van Leest, T. & Caro, J. Cavity-enhanced optical trapping of bacteria using a silicon photonic crystal. *Lab on a Chip* **13**, 4358–4365 (2013).

[95] Jaquay, E., Martínez, L. J., Mejia, C. A. & Povinelli, M. L. Light-assisted, templated self-assembly using a photonic-crystal slab. *Nano Letters* **13**, 2290–2294 (2013).

[96] Mejia, C. A., Dutt, A. & Povinelli, M. L. Light-assisted templated self assembly using photonic crystal slabs. *Optics Express* **19**, 11422–11428 (2011).

[97] Mirsadeghi, S. H. & Young, J. F. Ultrasensitive diagnostic analysis of au nanoparticles optically trapped in silicon photonic circuits at sub-milliwatt powers. *Nano Letters* **14**, 5004–5009 (2014).

[98] Zhao, X., Sun, Y., Bu, J., Zhu, S. & Yuan, X. C. Microlens-array-enabled on-chip optical trapping and sorting. *Applied Optics* **50**, 318–322 (2011).

[99] Yong, J., Chen, F., Yang, Q., Du, G., Bian, H., Zhang, D., Si, J., Yun, F. & Hou, X. Rapid fabrication of large-area concave microlens arrays on pdms by a femtosecond laser. *ACS Applied Materials & Interfaces* **5**, 9382–9385 (2013).

[100] Quidant, R. Plasmonic tweezers—the strength of surface plasmons. *MRS Bulletin* **37**, 739–744 (2012).

[101] Tsai, W.-Y., Huang, J.-S. & Huang, C.-B. Selective trapping or rotation of isotropic dielectric microparticles by optical near field in a plasmonic Archimedes spiral. *Nano Letters* **14**, 547–552 (2014).

[102] Roxworthy, B. J. & Toussaint Jr., K. C. Femtosecond-pulsed plasmonic nanotweezers. *Scientific Reports* **2**, 2045–2322 (2012).

[103] Zhang, W., Huang, L., Santschi, C. & Martin, O. J. F. Trapping and sensing 10 nm metal nanoparticles using plasmonic dipole antennas. *Nano Letters* **10**, 1006–1011 (2010).

[104] Ploschner, M., Mazilu, M., Krauss, T. F. & Dholakia, K. Optical forces near a nanoantenna. *Journal of Nanophotonics* **4**, 041570 (2010).

[105] Galloway, C. M., Kreuzer, M. P., Aćimović, S. S., Volpe, G., Correia, M., Petersen, S. B., Neves-Petersen, M. T. & Quidant, R. Plasmon-assisted delivery of single nano-objects in an optical hot spot. *Nano Letters* **13**, 4299–4304 (2013).

[106] Donner, J. S., Baffou, G., McCloskey, D. & Quidant, R. Plasmon-assisted optofluidics. *ACS Nano* **5**, 5457–5462 (2011).

[107] Wang, K., Schonbrun, E., Steinvurzel, P. & Crozier, K. B. Trapping and rotating nanoparticles using a plasmonic nano-tweezer with an integrated heat sink. *Nature Communications* **2**, 469 (2011).

[108] Roxworthy, B. J., Bhuiya, A. M., Vanka, S. P. & Toussaint Jr, K. C. Understanding and controlling plasmon-induced convection. *Nature Communications* **5**, 3173 (2014).

[109] Seol, Y., Carpenter, A. E. & Perkins, T. T. Gold nanoparticles: enhanced optical trapping and sensitivity coupled with significant heating. *Optics Letters* **31**, 2429–2431 (2006).

[110] Demergis, V. & Florin, E.-L. Ultrastrong optical binding of metallic nanoparticles. *Nano Letters* **12**, 5756–5760 (2012).

[111] Wong, H. M. K., Righini, M., Gates, J. C., Smith, P. G. R., Pruneri, V. & Quidant, R. On-a-chip surface plasmon tweezers. *Applied Physics Letters* **99** (2011).

[112] Righini, M., Volpe, G., Girard, C., Petrov, D. & Quidant, R. Surface plasmon optical tweezers: Tunable optical manipulation in the femtoNewton range. *Physical Review Letters* **100**, 186804 (2008).

[113] Chen, K. Y., Lee, A. T., Hung, C. C., Huang, J. S. & Yang, Y. T. Transport and trapping in two-dimensional nanoscale plasmonic optical lattice. *Nano Letters* **13**, 4118–4122 (2013).

[114] Tatarkova, S. A., Sibbett, W. & Dholakia, K. Brownian particle in an optical potential of the washboard type. *Physical Review Letters* **91**, 038101 (2003).

[115] Juan, M. L., Gordon, R., Pang, Y., Eftekhari, F. & Quidant, R. Self-induced back-action optical trapping of dielectric nanoparticles. *Nature Physics* **5**, 915–919 (2009).

[116] Tanaka, Y. & Sasaki, K. Optical trapping through the localized surface-plasmon resonance of engineered gold nanoblock pairs. *Optics Express* **19**, 17462–17468 (2011).

[117] Righini, M., Ghenuche, P., Cherukulappurath, S., Myroshnychenko, V., García de Abajo, F. J. & Quidant, R. Nano-optical trapping of Rayleigh particles and escherichia coli bacteria with resonant optical antennas. *Nano Letters* **9**, 3387–3391 (2009).

[118] Scheibe, G., Kandler, L. & Ecker, H. Polymerisation und polymere adsorption als ursache neuartiger absorptionsbanden von organischen farbstoffen. *Naturwissenschaften* **25**, 75–75 (1937).

[119] Jelley, E. E. Molecular, nematic and crystal states of i: I-diethyl-cyanine chloride. *Nature* **139**, 631–632 (1937).

[120] Zamecnik, C. R., Ahmed, A., Walters, C. M., Gordon, R. & Walker, G. C. Surface-enhanced Raman spectroscopy using lipid encapsulated plasmonic nanoparticles and

j-aggregates to create locally enhanced electric fields. *Journal of Physical Chemistry C* **117**, 1879–1886 (2013).

[121] Genevet, P., Dellinger, J., Blanchard, R., She, A., Petit, M., Cluzel, B., Kats, M. A., de Fornel, F. & Capasso, F. Generation of two-dimensional plasmonic bottle beams. *Optics Express* **21**, 10295–10300 (2013).

[122] Pérez-Juste, J., Pastoriza-Santos, I., Liz-Marzán, L. M. & Mulvaney, P. Gold nanorods: Synthesis, characterization and applications. *Coordination Chemistry Reviews* **249**, 1870 – 1901 (2005).

[123] Wang, P., Zhang, L., Xia, Y., Tong, L., Xu, X. & Ying, Y. Polymer nanofibers embedded with aligned gold nanorods: A new platform for plasmonic studies and optical sensing. *Nano Letters* **12**, 3145–3150 (2012).

[124] Wang, P., Wang, Y., Yang, Z., Guo, X., Lin, X., Yu, X.-C., Xiao, Y.-F., Fang, W., Zhang, L., Lu, G., Gong, Q. & Tong, L. Single-band 2-nm-line-width plasmon resonance in a strongly coupled au nanorod. *Nano Letters* **15**, 7581–7586 (2015).

[125] Born, M. & Wolf, E. *Principles of optics: electromagnetic theory of propagation, interference and diffraction of light* (Cambridge University Press, New York, 2000).

[126] Weiner, J. The physics of light transmission through subwavelength apertures and aperture arrays. *Reports on Progress in Physics* **72**, 064401 (2009).

[127] Ebbesen, T. W., Lezec, H. J., Ghaemi, H. F., Thio, T. & Wolff, P. A. Extraordinary optical transmission through sub-wavelength hole arrays. *Nature* **391**, 667–669 (1998).

[128] Zehtabi-Oskuie, A., Bergeron, J. G. & Gordon, R. Flow-dependent double-nanohole optical trapping of 20 nm polystyrene nanospheres. *Scientific Reports* **2**, 966 (2012).

[129] Baida, F. I. & Van Labeke, D. Three-dimensional structures for enhanced transmission through a metallic film: Annular aperture arrays. *Physical Review B* **67**, 155314 (2003).

[130] Kotnala, A. & Gordon, R. Quantification of high-efficiency trapping of nanoparticles in a double nanohole optical tweezer. *Nano Letters* **14**, 853–856 (2014).

[131] Berthelot, J., Acimovic, S. S., Juan, M. L., Kreuzer, M. P., Renger, J. & Quidant, R. Three-dimensional manipulation with scanning near-field optical nanotweezers. *Nature Nano* **9**, 295–299 (2014).

[132] Rodríguez-Fortuño, F. J., García-Meca, C., Ortuño, R., Martí, J. & Martínez, A. Coaxial plasmonic waveguide array as a negative-index metamaterial. *Optics Letters* **34**, 3325–3327 (2009).

[133] Liu, Y. J., Si, G. Y., Leong, E. S. P., Xiang, N., Danner, A. J. & Teng, J. H. Light-driven plasmonic color filters by overlaying photoresponsive liquid crystals on gold annular aperture arrays. *Advanced Materials* **24**, OP131–OP135 (2012).

[134] de Waele, R., Burgos, S. P., Polman, A. & Atwater, H. A. Plasmon dispersion in coaxial waveguides from single-cavity optical transmission measurements. *Nano Letters* **9**, 2832–2837 (2009).

[135] Saleh, A. A. E. & Dionne, J. A. Toward efficient optical trapping of sub-10-nm particles with coaxial plasmonic apertures. *Nano Letters* **12**, 5581–5586 (2012).

[136] Neumann, L., Pang, Y., Houyou, A., Juan, M. L., Gordon, R. & van Hulst, N. F. Extraordinary optical transmission brightens near-field fiber probe. *Nano Letters* **11**, 355–360 (2010).

[137] Gordon, R. Bethe's aperture theory for arrays. *Physical Review A* **76**, 053806 (2007).

[138] Tong, L. & Sumetsky, M. *Subwavelength and Nanometer Diameter Optical Fibers* (Springer, Berlin, 2010).

[139] Draine, B. T. The discrete-dipole approximation and its application to interstellar graphite grains. *Astrophysical Journal* **333**, 848–872 (1988).

[140] Draine, B. T. & Flatau, P. J. Discrete-dipole approximation for scattering calculations. *Journal of the Optical Society of America A* **11**, 1491–1499 (1994).

[141] Allardice, J. R. & Ru, E. C. L. Convergence of Mie theory series: criteria for far-field and near-field properties. *Applied Optics* **53**, 7224–7229 (2014).

[142] Wiscombe, W. J. Improved Mie scattering algorithms. *Applied Optics* **19**, 1505–1509 (1980).

[143] Mansuripur, M. The force law of classical electrodynamics: Lorentz versus Einstein and Laub. In *Frontiers in Optics 2014*, JS1A.3 (Optical Society of America, 2014).

[144] Metcalf, H. J. & Straten, P. *Laser cooling and trapping of neutral atoms* (Sprinер-Verlag, New York, 1999).

[145] Foot, C. J. *Atomic physics* (OUP Oxford, 2004).

[146] Maier, S. A. *Plasmonics: fundamentals and applications* (Springer Science & Business Media, New York, 2007).

[147] Nordlander, P., Oubre, C., Prodan, E., Li, K. & Stockman, M. I. Plasmon hybridization in nanoparticle dimers. *Nano Letters* **4**, 899–903 (2004).

[148] Rechberger, W., Hohenau, A., Leitner, A., Krenn, J., Lamprecht, B. & Aussenegg, F. Optical properties of two interacting gold nanoparticles. *Optics Communications* **220**, 137 – 141 (2003).

[149] Raab, E. L., Prentiss, M., Cable, A., Chu, S. & Pritchard, D. E. Trapping of neutral sodium atoms with radiation pressure. *Physical Review Letters* **59**, 2631–2634 (1987).

[150] Phillips, W. D. & Metcalf, H. Laser deceleration of an atomic beam. *Physical Review Letters* **48**, 596–599 (1982).

[151] Molenaar, P. A., van der Straten, P., Heideman, H. G. M. & Metcalf, H. Diagnostic technique for Zeeman-compensated atomic beam slowing: Technique and results. *Physical Review A* **55**, 605–614 (1997).

[152] Chu, S., Bjorkholm, J. E., Ashkin, A. & Cable, A. Experimental observation of optically trapped atoms. *Physical Review Letters* **57**, 314–317 (1986).

[153] Russell, L., Kumar, R., Tiwari, V. B. & Nic Chormaic, S. Measurements on release–recapture of cold ^{85}Rb atoms using an optical nanofibre in a magneto-optical trap. *Optics Communications* **309**, 313–317 (2013).

[154] Steane, A. M. & Foot, C. J. Laser cooling below the Doppler limit in a magneto-optical trap. *Europhysics Letters* **14**, 231 (1991).

[155] Russell, L., Deasy, K., Daly, M. J., Morrissey, M. J. & Nic Chormaic, S. Sub-Doppler temperature measurements of laser-cooled atoms using optical nanofibres. *Measurement Science and Technology* **23**, 015201 (2012).

[156] Preston, D. W. Doppler-free saturated absorption: Laser spectroscopy. *American Journal of Physics* **64**, 1432–1436 (1996).

[157] Taylor, J. R. *An Introduction to Error Analysis* (University Science Books, New York, 1997).

[158] Feron, S., Reinhardt, J., Le Boiteux, S., Gorceix, O., Baudon, J., Ducloy, M., Robert, J., Miniatura, C., Nic Chormaic, S., Haberland, H. & Lorent, V. Reflection

of metastable neon atoms by a surface plasmon wave. *Optics Communications* **102**, 83–88 (1993).

[159] Dowling, J. P. & Gea-Banacloche, J. *Evanescent Light-Wave Atom Mirrors, Resonators, Waveguides, and Traps* (Academic Press, Boston, 1996).

[160] Tong, L., Gattass, R. R., Ashcom, J. B., He, S., Lou, J., Shen, M., Maxwell, I. & Mazur, E. Subwavelength-diameter silica wires for low-loss optical wave guiding. *Nature* **426**, 816–819 (2003).

[161] Yariv, A. *Optical Electronics 3rd Edition* (Holt, Reinhart and Winston, New York, 1985).

[162] Ravets, S., Hoffman, J. E., Orozco, L. A., Rolston, S. L., Beadie, G. & Fatemi, F. K. A low-loss photonic silica nanofiber for higher-order modes. *Optics Express* **21**, 18325–18335 (2013).

[163] Nayak, K. P., Le Kien, F., Morinaga, M. & Hakuta, K. Antibunching and bunching of photons in resonance fluorescence from a few atoms into guided modes of an optical nanofiber. *Physical Review A* **79**, 021801 (2009).

[164] Ovchinnikov, Y. B., Shul'ga, S. V. & Balykin, V. I. An atomic trap based on evanescent light waves. *Journal of Physics B: Atomic, Molecular and Optical Physics* **24**, 3173 (1991).

[165] Le Kien, F., Balykin, V. I. & Hakuta, K. Atom trap and waveguide using a two-color evanescent light field around a subwavelength-diameter optical fiber. *Physical Review A* **70**, 063403 (2004).

[166] Le Kien, F., I. Balykin, V. & Hakuta, K. State-insensitive trapping and guiding of cesium atoms using a two-color evanescent field around a subwavelength-diameter fiber. *Journal of the Physical Society of Japan* **74**, 910–917 (2005).

[167] Lacroute, C., Choi, K. S., Goban, A., Alton, D. J., Ding, D., Stern, N. P. & Kimble, H. J. A state-insensitive, compensated nanofiber trap. *New Journal of Physics* **14** (2012).

[168] Vetsch, E., Reitz, D., Sagué, G., Schmidt, R., Dawkins, S. T. & Rauschenbeutel, A. Optical interface created by laser-cooled atoms trapped in the evanescent field surrounding an optical nanofiber. *Physical Review Letters* **104**, 203603 (2010).

[169] Hung, C. L., Meenehan, S. M., Chang, D. E., Painter, O. & Kimble, H. J. Trapped atoms in one-dimensional photonic crystals. *New Journal of Physics* **15**, 083026 (2013).

[170] Thompson, J. D., Tiecke, T. G., de Leon, N. P., Feist, J., Akimov, A. V., Gullans, M., Zibrov, A. S., Vuletic, V. & Lukin, M. D. Coupling a single trapped atom to a nanoscale optical cavity. *Science* **340**, 1202–1205 (2013).

[171] Ol'Shanii, M. A., Ovchinnikov, Y. B. & Letokhov, V. S. Laser guiding of atoms in a hollow optical fiber. *Optics Communications* **98**, 77–79 (1993).

[172] Burke, J. P., Chu, S.-T., Bryant, G. W., Williams, C. J. & Julienne, P. S. Designing neutral-atom nanotraps with integrated optical waveguides. *Physical Review A* **65**, 043411 (2002).

[173] Xu, P., He, X., Wang, J. & Zhan, M. Trapping a single atom in a blue detuned optical bottle beam trap. *Optics Letters* **35**, 2164–2166 (2010).

[174] Sagúe, G., Baade, A. & Rauschenbeutel, A. Blue-detuned evanescent field surface traps for neutral atoms based on mode interference in ultrathin optical fibres. *New Journal of Physics* **10**, 113008 (2008).

[175] Phelan, C. F., Hennessy, T. & Busch, T. Shaping the evanescent field of optical nanofibers for cold atom trapping. *Optics Express* **21**, 27093–27101 (2013).

[176] Philipp, S., Fam Le, K. & Arno, R. Nanofiber-based atom trap created by combining fictitious and real magnetic fields. *New Journal of Physics* **16**, 013014 (2014).

[177] Le Kien, F. & Hakuta, K. Microtraps for atoms outside a fiber illuminated perpendicular to its axis: Numerical results. *Physical Review A* **80**, 013415 (2009).

[178] Morrissey, M. J., Deasy, K., Wu, Y., Chakrabarti, S. & Nic Chormaic, S. Tapered optical fibers as tools for probing magneto-optical trap characteristics. *Review of Scientific Instruments* **80**, 053102 (2009).

[179] Nayak, K. P., Le Kien, F., Kawai, Y., Hakuta, K., Nakajima, K., Miyazaki, H. T. & Sugimoto, Y. Cavity formation on an optical nanofiber using focused ion beam milling technique. *Optics Express* **19**, 14040–14050 (2011).

[180] Zhang, L., Lou, J. & Tong, L. Micro/nanofiber optical sensors. *Photonic Sensors* **1**, 31–42 (2010).

[181] Elsherbeni, A., Kajfez, D. & Zeng, S. Circular sectoral waveguides. *IEEE Antennas and Propagation Magazine* **33**, 20–27 (1991).

[182] Jung, Y., Jeong, Y., Brambilla, G. & Richardson, D. J. Adiabatically tapered splice for selective excitation of the fundamental mode in a multimode fiber. *Optics Letters* **34**, 2369–2371 (2009).

[183] Russell, L., Gleeson, D. A., Minogin, V. G. & Nic Chormaic, S. Spectral distribution of atomic fluorescence coupled into an optical nanofibre. *Journal of Physics B: Atomic and Molecular Physics* **42**, 185006 (2009).

[184] Minogin, V. G. & Nic Chormaic, S. Manifestation of the van der Waals surface interaction in the spontaneous emission of atoms into an optical nanofiber. *Laser Physics* **20**, 32–37 (2009).

[185] Frawley, M. C., Nic Chormaic, S. & Minogin, V. G. The van der Waals interaction of an atom with the convex surface of a nanocylinder. *Physica Scripta* **85**, 058103 (2012).

[186] Jones, J. E. On the determination of molecular fields. ii. from the equation of state of a gas. *Proceedings of the Royal Society of London A: Mathematical, Physical and Engineering Sciences* **106**, 463–477 (1924).

[187] Derevianko, A., Johnson, W. R., Safronova, M. S. & Babb, J. F. High-precision calculations of dispersion coefficients, static dipole polarizabilities, and atom-wall interaction constants for alkali-metal atoms. *Physical Review Letters* **82**, 3589–3592 (1999).

[188] Marani, R., Cognet, L., Savalli, V., Westbrook, N., Westbrook, C. I. & Aspect, A. Using atomic interference to probe atom-surface interactions. *Physical Review A* **61**, 053402 (2000).

[189] Grimm, R., Weidemüller, M. & Ovchinnikov, Y. B. *Optical Dipole Traps for Neutral Atoms*, vol. 42 (Academic Press, 2000).

[190] Safronova, M. S., Arora, B. & Clark, C. W. Frequency-dependent polarizabilities of alkali-metal atoms from ultraviolet through infrared spectral regions. *Physical Review A* **73**, 022505 (2006).

[191] Daly, M., Truong, V. G., Phelan, C., Deasy, K. & Nic Chormaic, S. Nanostructured optical nanofibres for atom trapping. *New Journal of Physics* **16**, 053052 (2014).

[192] Daly, M. Near-field trap for submicron particles and cold, neutral atoms using rectangular etched cavities in optical nanofibers. In *Frontiers in Optics 2013*, OSA Technical Digest (online), FTh1D.5 (Optical Society of America, 2013).

[193] Buividas, R., Mikutis, M., Gervinskas, G., Day, D., Slekys, G. & Juodkazis, S. Femtosecond laser drilling of optical fibers for sensing in microfluidic applications.

In *Femtosecond laser drilling of optical fibers for sensing in microfluidic applications*, vol. 8463, 84630T–84630T–10 (2012).

[194] Maragó, O. M., Jones, P. H., Gucciardi, P. G., Volpe, G. & Ferrari, A. C. Optical trapping and manipulation of nanostructures. *Nature Nanotechnology* **8**, 807–819 (2013).

[195] Jing, P., Wu, J., Liu, G. W., Keeler, E. G., Pun, S. H. & Lin, L. Y. Photonic crystal optical tweezers with high efficiency for live biological samples and viability characterization. *Scientific Reports* **6**, 19924 (2016).

[196] Anderson, P. A., Schmidt, B. S. & Lipson, M. High confinement in silicon slot waveguides with sharp bends. *Optics Express* **14**, 9197–9202 (2006).

[197] Soltani, M., Lin, J., Forties, R. A., Inman, J. T., Saraf, S. N., Fulbright, R. M., Lipson, M. & Wang, M. D. Nanophotonic trapping for precise manipulation of biomolecular arrays. *Nature Nanotechnology* **9**, 448–452 (2014).

[198] Hoffman, J., Ravets, S., Grover, J., Solano, P., Kordell, P., Wong-Campos, J., Orozco, L. & Rolston, S. Ultrahigh transmission optical nanofibers. *AIP Advances* **4**, 067124 (2014).

[199] Brzobohatỳ, O., Šiler, M., Trojek, J., Chvátal, L., Karásek, V., Paták, A., Pokorná, Z., Mika, F. & Zemánek, P. Three-dimensional optical trapping of a plasmonic nanoparticle using low numerical aperture optical tweezers. *Scientific Reports* **5**, 8106 (2015).

[200] Geiselmann, M., Juan, M. L., Renger, J., Say, J. M., Brown, L. J., De Abajo, F. J. G., Koppens, F. & Quidant, R. Three-dimensional optical manipulation of a single electron spin. *Nature Nanotechnology* **8**, 175–179 (2013).

[201] Xin, H. & Li, B. Targeted delivery and controllable release of nanoparticles using a defect-decorated optical nanofiber. *Optics Express* **19**, 13285–13290 (2011).

[202] Gusachenko, I., Truong, V. G., Frawley, M. C. & Nic Chormaic, S. Optical nanofiber integrated into optical tweezers for in situ fiber probing and optical binding studies. *Photonics* **2**, 795 (2015).

[203] Nieddu, T., Gokhroo, V. & Nic Chormaic, S. Optical nanofibres and neutral atoms. *Journal of Optics* **18**, 053001 (2016).

[204] Li, Y., Svitelskiy, O. V., Maslov, A. V., Carnegie, D., Rafailov, E. & Astratov, V. N. Giant resonant light forces in microspherical photonics. *Light: Scientific Applications* **2**, 64 (2013).

[205] Murugan, G. S., Belal, M., Grivas, C., Ding, M., Wilkinson, J. S. & Brambilla, G. An optical fiber optofluidic particle aspirator. *Applied Physics Letters* **105**, 101103 (2014).

[206] Cheng, C., Xu, X., Lei, H. & Li, B. Plasmon-assisted trapping of nanoparticles using a silver-nanowire-embedded pmma nanofiber. *Scientific Reports* **6**, 20433 (2016).

[207] Knight, J., Cheung, G., Jacques, F. & Birks, T. Phase-matched excitation of whispering-gallery-mode resonances by a fiber taper. *Optics Letters* **22**, 1129–1131 (1997).

[208] Mitsch, R., Sayrin, C., Albrecht, B., Schneeweiss, P. & Rauschenbeutel, A. Quantum state-controlled directional spontaneous emission of photons into a nanophotonic waveguide. *Nature Communications* **5**, 5713 (2014).

[209] Béguin, J.-B., Bookjans, E., Christensen, S., Sørensen, H., Müller, J., Polzik, E. & Appel, J. Generation and detection of a sub-poissonian atom number distribution in a one-dimensional optical lattice. *Physical Review Letters* **113**, 263603 (2014).

[210] Kato, S. & Aoki, T. Strong coupling between a trapped single atom and an all-fiber cavity. *Physical Review Letters* **115**, 093603 (2015).

[211] Kumar, R., Gokhroo, V., Deasy, K. & Nic Chormaic, S. Autler-Townes splitting via frequency up-conversion at ultralow-power levels in cold Rb 87 atoms using an optical nanofiber. *Physical Review A* **91**, 053842 (2015).

[212] Watkins, A., Tiwari, V. B., Ward, J. M., Deasy, K. & Nic Chormaic, S. Observation of Zeeman shift in the rubidium D2 line using an optical nanofiber in vapor. In *8th Ibero American Optics Meeting/11th Latin American Meeting on Optics, Lasers, and Applications*, 87850S–87850S (International Society for Optics and Photonics, 2013).

[213] Jones, D., Franson, J. & Pittman, T. Ladder-type electromagnetically induced transparency using nanofiber-guided light in a warm atomic vapor. *Physical Review A* **92**, 043806 (2015).

[214] Xin, H., Xu, R. & Li, B. Optical trapping, driving, and arrangement of particles using a tapered fibre probe. *Scientific Reports* **2**, 818 (2012).

[215] Daly, M., Truong, V. G. & Nic Chormaic, S. Evanescent field trapping of nanoparticles using nanostructured ultrathin optical fibers. *Optics Express* **24**, 14470–14482 (2016).

[216] Swaim, J. D., Knittel, J. & Bowen, W. P. Tapered nanofiber trapping of high-refractive-index nanoparticles. *Applied Physics Letters* **103**, 203111 (2013).

[217] Ding, M., Wang, P., Lee, T. & Brambilla, G. A microfiber cavity with minimal-volume confinement. *Applied Physics Letters* **99**, 051105 (2011).

[218] Hartung, A., Wirth, F. & Bartelt, H. Light propagation in tapered optical fibers: Spatial light confinement and generation of plasmonic waves. In *Proceedings to Progress in Electromagnetics Research Symposium*, 255–258 (2011).

[219] Walton, O. R. Review of adhesion fundamentals for micron-scale particles. *KONA Powder and Particle Journal* **26**, 129–141 (2008).

[220] Szczurowski, M., Urbanczyk, W., Napiorkowski, M., Hlubina, P., Hollenbach, U., Sieber, H. & Mohr, J. Differential Rayleigh scattering method for measurement of polarization and intermodal beat length in optical waveguides and fibers. *Applied Optics* **50**, 2594–2600 (2011).

[221] Brevik, I. Experiments in phenomenological electrodynamics and the electromagnetic energy-momentum tensor. *Physics Reports* **52**, 133–201 (1979).

[222] Holzmann, D., Sonnleitner, M. & Ritsch, H. Self-ordering and collective dynamics of transversely illuminated point-scatterers in a 1D trap. *The European Physical Journal D* **68**, 1–11 (2014).

[223] Piazza, R. Thermophoresis: moving particles with thermal gradients. *Soft Matter* **4**, 1740–1744 (2008).

[224] Chao Zhao, A. O., Jinxin Fub & Chenga, X. Measuring the Soret coefficient of nanoparticles in a dilute suspension. *Journal of Nanoparticle Research* **16**, 2625 (2015).

[225] van der Horst, A. & Forde, N. R. Power spectral analysis for optical trap stiffness calibration from high-speed camera position detection with limited bandwidth. *Optics Express* **18**, 7670–7677 (2010).

[226] Roldán, É. *Irreversibility and Dissipation in Microscopic Systems* (Springer, New York, 2014).

[227] Chang, D., Cirac, J. I. & Kimble, H. Self-organization of atoms along a nanophotonic waveguide. *Physical Review Letters* **110**, 113606 (2013).

[228] Botman, A., Mulders, J. J. L., Weemaes, R. & Mentink, S. Purification of platinum and gold structures after electron-beam-induced deposition. *Nanotechnology* **17**, 3779 (2006).

[229] Graells, S., Alcubilla, R., Badenes, G. & Quidant, R. Growth of plasmonic gold nanostructures by electron beam induced deposition. *Applied Physics Letters* **91** (2007).

[230] Huth, M., Porrati, F., Schwalb, C., Winhold, M., Sachser, R., Dukic, M., Adams, J. & Fantner, G. Focused electron beam induced deposition: A perspective. *Beilstein Journal of Nanotechnology* **3**, 597–619 (2012).

[231] Rakić, A. D., Djurišić, A. B., Elazar, J. M. & Majewski, M. L. Optical properties of metallic films for vertical-cavity optoelectronic devices. *Appl. Opt.* **37**, 5271–5283 (1998).

[232] Bandi, T. N., Minogin, V. G. & Nic Chormaic, S. Atom microtraps based on near-field fresnel diffraction. *Physical Review A* **78**, 013410 (2008).

[233] Lewis, G. N., Moktadir, Z., Gollasch, C., Kraft, M., Pollock, S., Ramirez-Martinez, F., Ashmore, J. P., Laliotis, A., Trupke, M. & Hinds, E. A. Fabrication of magnetooptical atom traps on a chip. *Journal of Microelectromechanical Systems* **18**, 347–353 (2009).

[234] Vangeleyn, M., Griffin, P. F., Riis, E. & Arnold, A. S. Single-laser, one beam, tetrahedral magneto-optical trap. *Optics Express* **17**, 13601–13608 (2009).

[235] Hui, Y., Guo-Qing, Y., Jin, W. & Ming-Sheng, Z. Directly trapping atoms in a U-shaped magneto-optical trap using a mini atom chip. *Chinese Physics Letters* **25**, 3219 (2008).

[236] Haase, A., Cassettari, D., Hessmo, B. & Schmiedmayer, J. Trapping neutral atoms with a wire. *Physical Review A* **64**, 043405 (2001).

[237] Banchi, L., Bayat, A., Verrucchi, P. & Bose, S. Nonperturbative entangling gates between distant qubits using uniform cold atom chains. *Physical Review Letters* **106**, 140501 (2011).

[238] Lapasar, E. H., Kasamatsu, K., Nic Chormaic, S., Takui, T., Kondo, Y., Nakahara, M. & Ohmi, T. Two-qubit gate operation on selected nearest-neighbor neutral atom qubits. *Journal of the Physical Society of Japan* **83**, 044005 (2014).

[239] Balykin, V. I. & Minogin, V. G. Focusing of atomic beams by near-field atom microlenses: The Bethe-type and the Fresnel-type microlenses. *Physical Review A* **77**, 013601 (2008).

[240] Petersen, J., Volz, J. & Rauschenbeutel, A. Chiral nanophotonic waveguide interface based on spin-orbit interaction of light. *Science* **346**, 67–71 (2014).

Published articles

New Journal of Physics
The open access journal at the forefront of physics
Deutsche Physikalische Gesellschaft DPG | IOP Institute of Physics

Nanostructured optical nanofibres for atom trapping

M Daly, V G Truong, C F Phelan, K Deasy and S Nic Chormaic
Light-Matter Interactions Unit, OIST Graduate University, 1919-1 Tancha, Onna-son, Okinawa 904-0495, Japan
E-mail: sile.nicchormaic@oist.jp

Received 18 November 2013, revised 31 March 2014
Accepted for publication 22 April 2014
Published 29 May 2014
New Journal of Physics **16** (2014) 053052
doi:10.1088/1367-2630/16/5/053052

Abstract
We propose an optical dipole trap for cold, neutral atoms based on the electric field produced from the evanescent fields in a hollow, rectangular slot cut through an optical nanofibre. In particular, we discuss the trap performance in relation to laser-cooled rubidium atoms and show that a far off-resonance, blue-detuned field combined with the attractive surface-atom interaction potential from the dielectric material forms a stable trapping configuration. With the addition of a red-detuned field, we demonstrate how three dimensional confinement of the atoms at a distance of 140–200 nm from the fibre surface within the slot can be accomplished. This scheme facilitates optical coupling between the atoms and the nanofibre that could be exploited for quantum communication schemes using ensembles of laser-cooled atoms.

Keywords: optical nanofibre, cold atoms, nanostructure, rubidium, nano-optics

1. Introduction

Evanescent wave devices have been commonly used with atomic systems for the past few decades [1, 2], but more recently the integration of optical nanofibres, i.e. optical fibres with dimensions smaller than the wavelength of the guided light [3–5], into cold atomic systems [6–8] has been the focus of increasing research interest and a comprehensive review of progress is contained in [9]. In particular, it has been shown that optical nanofibres can be used for trapping and manipulating cold atoms. Surface traps, such as those presented by Ovchinnikov

et al [10], adapted for use on curved optical nanofibre surfaces, make use of the evanescent field present when light is guided along thin optical fibres. The induced potential from a red-detuned field produces an attractive potential, while the atom-surface interaction potential is balanced using a blue-detuned potential barrier that prevents atoms from migrating to the fibre surface. In particular, trapping of alkali atoms in the evanescent field surrounding an optical nanofibre using a combination of red- and blue-detuned optical fields, the so-called *two-colour trap*, has been proposed [11–14] and demonstrated [15, 16], thereby proving the effectiveness of the technique. In these experiments, the trapped atoms are coupled to a mode which is on resonance with the atom transition and exhibit strong coupling and a large optical depth. These features are desirable for quantum information applications and have led to much research on similar nanophotonic systems for trapping and probing atoms [17, 18]. Red-detuned light traps in hollow fibres have also been used to guide atoms [19]. Alternative methods for guiding and trapping atoms outside optical nanofibres have been proposed by several groups, but practical implementation is still quite limited. Single colour traps which make use of higher order modes above slab waveguides [20], non-Gaussian beam shapes [21], or mode interference [22] to create stable traps have been proposed. Alternative fibre trapping schemes, such as helical trapping potentials around the nanofibre [23], an induced fictitious magnetic field around the fibre [24], or diffracted laser light off the fibre [25], also exist. All of these recently proposed methods have a common feature in that the atoms are trapped outside the nanofibre, thereby limiting the efficiency of interaction with any light guided by the fibre.

The fabrication of optical nanofibres with very high transmission (>99%) for the fundamental mode has become a standard technique [26] and alteration of either the chemical or physical properties of optical fibre surfaces is becoming commonplace. For example, the generation of a Bragg grating on an optical nanofibre by selective milling of the surface using a focused ion beam (FIB) [27] and the fabrication of a humidity detector using subwavelength fibres via the application of 80 nm gelatin layers [28] have been reported. More recently, optical nanofibres that permit relatively high transmission of higher order modes have also been fabricated [5, 29] and this opens up the possibility of experimentally investigating a number of heretofore theoretical fibre-based atom trapping schemes.

In this paper, we propose a method to trap and probe atoms inside a rectangular slot cut through the waist region of a silica optical nanofibre. The design of this device is analogous to that of a slot waveguide [30]. In a slot waveguide, the slot width is chosen so that it is smaller than the decay length of the evanescent fields. For such structures a high mode confinement between the two waveguides is possible. Mirroring this structure in an optical nanofibre allows us to trap atoms in the slot area, thereby resulting in several advantages over systems where the atoms are trapped outside the fibre. The simplicity of the design also opens up many possibilities for atom trapping, whether through single colour, higher mode trapping, or the addition of more rectangular slots allowing for the creation of spatially localized trapping regions. Here, we focus on a two-colour setup for producing trapping potentials both at the fibre surface and within the slot. By a suitable choice of slot size, deep potentials with substantial trap lifetimes are predicted, with local minima located at positions of 140–200 nm from the inner surfaces of the slot.

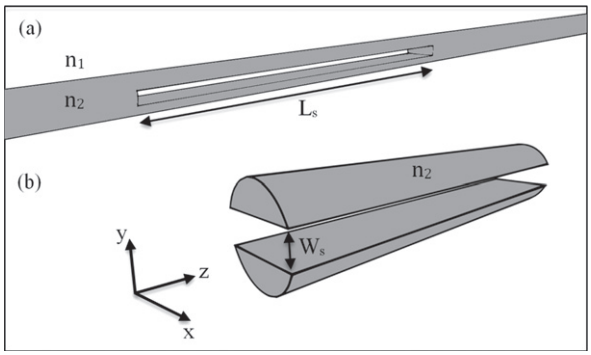

Figure 1. Schematic of the slotted fibre for a vacuum-fibre system $n_1 = 1$ and $n_2 = 1.45991$. (a) Tapered region with slot present, (b) slot region only.

2. Guided modes of the system

2.1. Optical mode distributions

The system under study, shown schematically in figure 1, consists of an ultra-thin, vacuum clad, silica nanofibre with a rectangular shaped slot removed from the centre of the fibre. We assume that fibre diameters are of the order of the wavelength of the guided light. We define the axes such that the z-direction corresponds to the fibre axis, the direction parallel to the slot and orthogonal to the z-axis is the x-direction, and the remaining axis perpendicular to the slot is the y-direction.

For wavelengths of 1064 nm and 720 nm, chosen for their red- and blue-detunings from the 780 nm Rb cooling transition, respectively, and nanofibre diameters ranging from 0.6–1.2 μm, four distinct guided optical modes can be identified. Using an approach similar to that developed by Anderson *et al* [30] the modes are viewed as being either symmetric or anti-symmetric. Furthermore, each mode can propagate with two orthogonal polarizations, giving rise to the four distinct modes.

The supported optical modes of the slotted fibre can be determined from Maxwell's wave equation, equation (1). Using commercially-available finite element (COMSOL Multiphysics) and finite difference method (FIMMWAVE) software packages, the spatial variation of the electric field along a waveguide of any geometry can be calculated. For a waveguide as shown in figure 1, there is symmetry along the z-direction, hence the electric field is translationally invariant in this direction resulting in the following form of the wave equation:

$$\left[\nabla^2 + n^2k^2\right]\vec{E}_t(x, y) = \beta^2\vec{E}_t(x, y). \tag{1}$$

Here, $\vec{E}_t(x, y)$ is the transverse component of the electric field, n is the refractive index, k is the wavenumber and β is the propagation constant. In the slot region, light propagates as two separate modes, one travelling in the fibre section at the top of the slot region and the other in the lower portion of fibre. The total field is written as:

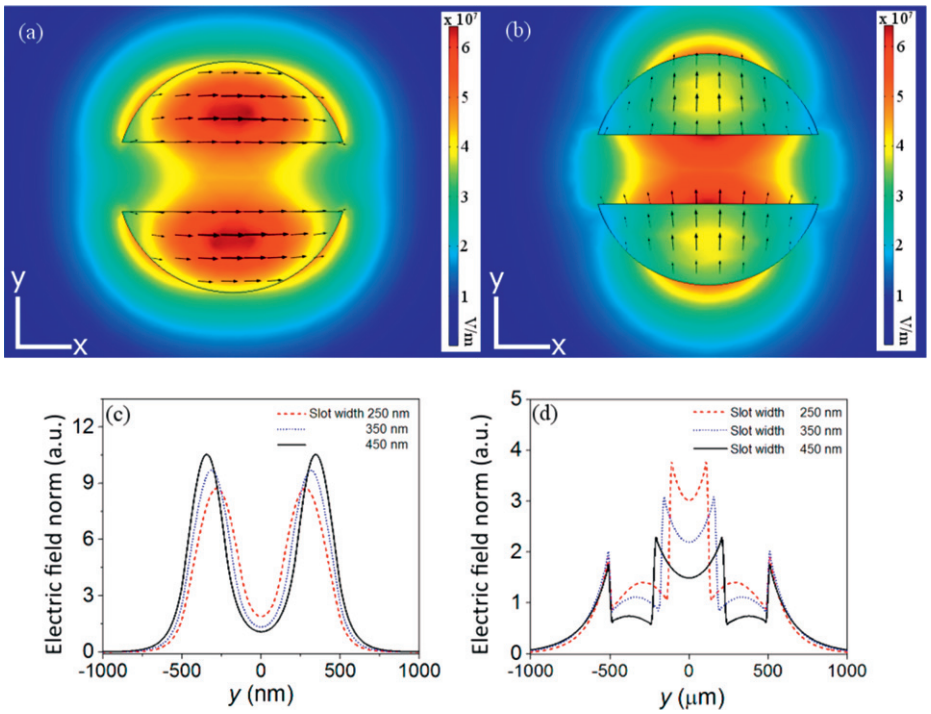

Figure 2. Electric field normal of modes generated in a 1 μm diameter fibre using (a) 720 nm light with parallel polarized light and (b) 1064 nm light with perpendicularly polarized light. (c) and (d) are the potentials along the y-direction for (a) and (b), respectively.

$$\vec{E}(x, y) = \vec{E}_{1t}(x, y)\exp^{-\iota\beta_{1z}} + \vec{E}_{2t}(x, y)\exp^{-\iota\beta_{2z}}$$
$$= \left[\vec{E}_{1t}(x, y) + \vec{E}_{2t}(x, y)\exp^{-\iota(\beta_2-\beta_1)z}\right]\exp^{-\iota\beta_{1z}}. \quad (2)$$

For cases where the two propagating modes have the same, or almost the same, effective index equation (2) can be greatly simplified and this also allows us to neglect any mode beating effects since the mode beat length, $L_B = 2\pi/(\beta_2 - \beta_1)$, becomes much longer than the length of the slot cavity, L_s. For a slot waveguide, the value of L_s will always be much lower than the beat length. In the following, we shall treat the solutions as super-modes, travelling with a single propagation constant, β, which has a value higher than either of the initial constants, β_1 and β_2, for symmetric modes. Moreover, we assume the two modes to be degenerate, which is true for a symmetric structure of this type. We can also consider the two modes given in figures 2(a) and (b) as being analogous to the two polarization states of the HE_{11} modes in a standard tapered optical fibre albeit with larger differences between their propagation constant.

When the waveguide dimensions are comparable to the wavelength of light, the polarizations of the modes have more influence over the intensity distributions. This is most noticeable within the slotted region. Figures 2(a) and (b) show two extreme cases where the electric field is polarized parallel and perpendicular to the slot walls. Figures 2(c) and (d) give the electric field norms for parallel and perpendicular polarizations, respectively, and for slot widths, W_s, varying from 250–450 nm. In the case of perpendicular polarization, high intensities can be realized in the vacuum region between the slot walls since the component of the electric

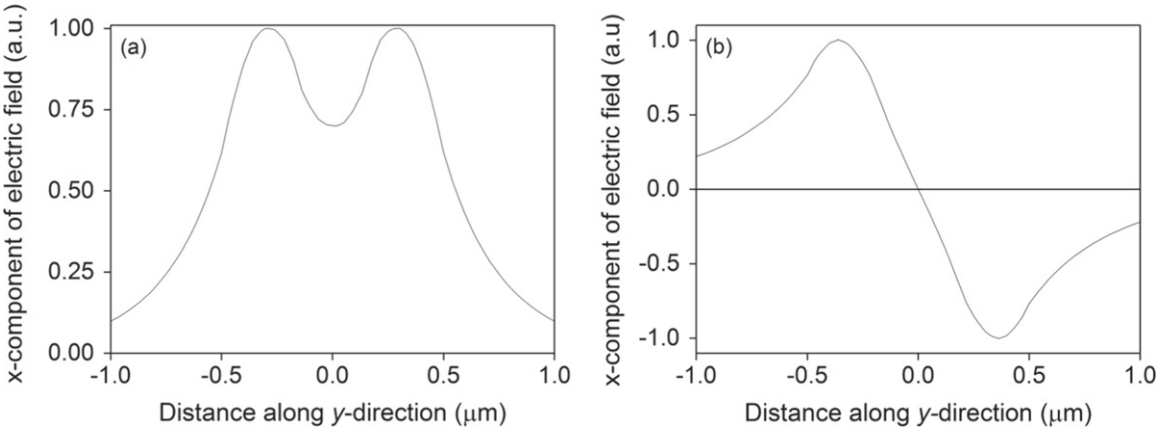

Figure 3. Symmetric and anti-symmetric modes for a single polarization.

field normal to the boundary has no continuity requirement. Figure 3 shows the transverse field distributions corresponding to two modes for one polarization at 1064 nm in a 1 μm diameter fibre with a 350 nm wide slot. Figure 3(a) shows a symmetric mode, while figure 3(b) shows an anti-symmetric mode. All calculations throughout this paper are performed using the total electric field.

2.2. Mode definition

It has been shown that, in waveguides with a circular sector cross-section (i.e. a section of a circle which is enclosed by two radii and an arc) the mode numbers are non-integer, i.e. $m = (p\pi)/\phi_0$, where p is an integer and ϕ_0 is the sectoral angle [31]. This non-integer mode number serves merely to indicate that full circular symmetry has been lost. In this paper we are dealing with circular segments, as opposed to sectors. Hence, it is clear that the modes for this system will differ slightly, but one can assume that, in general, they will have similar behaviour. It is important to distinguish between what can be considered as *single-mode* or *multi-mode* in this system. In the absence of full analytical solutions, we define the single-mode regime as being the region where the only modes propagating are those which have intensity profiles with a single intensity maximum in each fibre segment as given in figure 2(a). Figure 4 indicates the defined single and multimode regions for different fibre radii and slot widths as obtained from numerical models.

Higher-order modes can give rise to interesting intensity distributions within the slot and these could also be used for atom trapping. However, in this initial work we focus on the fundamental mode. To this end, we only consider parameters that are in, or near, the single-mode region, where contributions from the higher modes are either non-existent or small enough to be neglected. It has been shown by Jung *et al* [32] that modes can be effectively filtered out via selective excitation of the fundamental mode using a tapered fibre [32]. Only symmetric fibre modes are considered as they are excited with much greater efficiency by the HE_{11} mode. Anti-symmetric modes should not be excited by an approximately uniform phase front. It can be seen from figure 2(a) that the parallel-polarized modes rapidly decay exponentially away from the slot walls. Therefore, these modes are better suited for blue-detuning so as to attract the atom to the intensity minimum at the centre of the slot. In contrast,

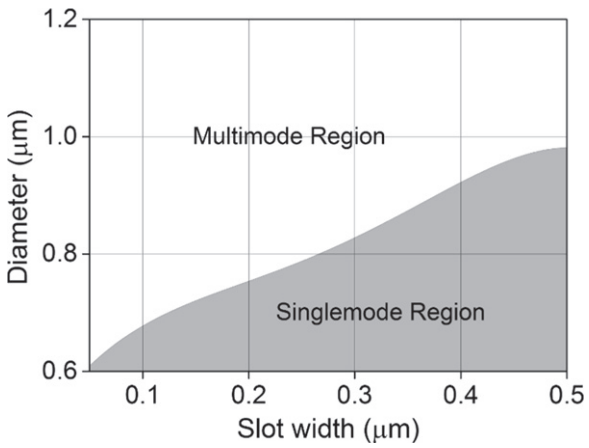

Figure 4. Graph of the regions of single-mode and multimode operation for 720 nm wavelength.

the orthogonally polarized modes have a higher intensity than that of the parallel-polarized modes in the centre of the slot (figure 2(b)) which causes atoms to be attracted towards the walls near the centre of the trap. As we shall see later, it is possible to combine these two field distributions with a combination of red- and blue-detuned light to draw atoms towards the centre of the slotted nanofibre.

3. Trap design

3.1. Surface interaction potential

A common issue in atom trapping near dielectric surfaces arises from the contribution to the total potential from the atom-surface interactions. Atoms near dielectric surfaces, such as the inner walls of the slot waveguide, are strongly affected by the attractive van der Waals (vdW) potential [33–35]. To quantify this effect the Lennard-Jones (L-J) potential [36] is often used as an approximation, such that

$$V_{\mathrm{vdW}} = -\frac{C_3}{d^3}, \tag{3}$$

where d is the distance from the fibre surface to the atom and C_3 has the value of 3.362×10^{-23} mK m^3. Assumptions that the major contribution to the atomic polarizability come from the first six lowest $P_{1/2}$ and $P_{3/2}$ levels of rubidium, and that the wall is a perfect conductor, have been made in this calculation [37]. It has been shown [38] that instead of a full QED calculation of this potential a simple interpolation formula can be used. This formula agrees with the QED calculation to within 0.6%. In a similar process we compare the L-J potential to this interpolation formula in an attempt to justify it, as it is used extensively throughout the literature as an approximation. We find that it agrees to within 1.4% at distances of less than 3 μm from the fibre surface. Therefore, we use the L-J approximation throughout this paper.

The effect of the vdWs potential on neutral atoms located within the slot results in them being pulled towards the surface. Figure 5(a) indicates how the vdW potentials from either wall

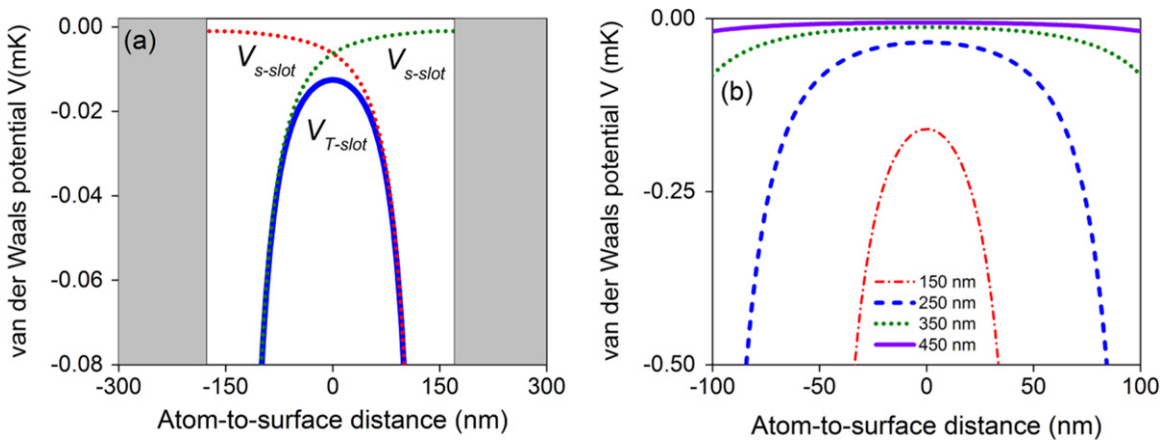

Figure 5. The van der Waals potential for an atom located in the fibre slot. (a) The total potential, $V_{T-\text{slot}}$, is created by adding the contributions from each of the two walls, $V_{s-\text{slot}}$ for a 1 μm fibre with a 350 nm slot width. The fibre walls are indicated by the grey regions. (b) The total van der Waals potential as a function of atom-to-surface distance for W_s values of 150 nm (dot-dash), 250 nm (dash), 350 nm (dot), and 450 nm (solid).

add to produce the total vdW potential seen by an atom in the slot. Figure 5(b) explores how changing the slot width affects the total vdW potential. As atoms approach the slot walls, it is clear that the effect of the vdW potential becomes more prominent; also as W_s becomes smaller atoms at the trap centre are affected more. The addition of a blue-detuned light field with respect to the atom transition frequencies alters this potential and creates a region in the centre with a stable equilibrium position.

3.2. Optically produced potential and atom trapping

A neutral atom interacting with an electric field $\vec{E}$ experiences a dipole potential given by

$$U = -\frac{1}{4}\alpha(\omega)\vec{E}^{*}\cdot\vec{E}, \tag{4}$$

$$\alpha(\omega) = \Sigma_n f_n\left[\frac{e^2/m}{\omega_n^2 - \omega^2 - \imath\omega\gamma_n}\right], \tag{5}$$

where α is the atom polarizability as determined using Lorentz's model for a classical oscillator, e is the electron charge, m is the mass, ω_n is the natural frequency of the nth oscillator, γ_n is the damping coefficient of the nth oscillator and f_n is the oscillator strength [39]. It can be seen from equation (5) that the sign of the polarizability and, hence, the trapping potential is determined from the detuning of the laser fields involved. In the presence of an intensity gradient, the atom will experience a force along the gradient towards the intensity maximum in the case of red-detuned light, and towards the intensity minimum in the case of blue-detuned light. In order to trap atoms in the slot region we can choose symmetric modes that are polarized parallel or perpendicularly to the slot walls and detuned to the red or blue of the transition frequency.

Neutral atoms in the presence of a laser field of frequency ω, which is close to an atomic resonance, experience a force which can be used to trap and even cool the atoms. As the laser

Table 1. Parameters used in trapping potential models.

Parameter	Value
Blue-detuned wavelength λ_b	720 nm
Red-detuned wavelength λ_r	1064 nm
C_3 for ^{87}Rb	3.362 J m^3

frequency is detuned further and further from resonance, only the heating due to spontaneous scattering of this far-detuned laser field need be considered as the dominant mechanism for atom loss from the atom trap. The atoms undergo a momentum recoil due to photon scattering. To quantify the usefulness of an atom trap, the scattering rates should be determined and, hence, the trap lifetimes for atoms located near the centre of the trap. The scattering rate, Γ_{sc}, for an atom in a dipole trap is given as [37]:

$$\Gamma_{sc} = \frac{3\pi c^2}{2\hbar\omega_0^3}\left(\frac{\Gamma}{\Delta}\right)^2 I(r). \tag{6}$$

Here, c is the speed of light in vacuum, ω_0 is the frequency at resonance, $\hbar$ is the reduced Planck's constant, Γ is the dipole transition matrix element between the ground $|g\rangle$ and $|e\rangle$ excited states, and $I(r)$ is the intensity. Generally, one would have to solve for Γ_{sc} by taking every atomic transition including the hyperfine structure into account. For the case of ^{87}Rb in the $D_{1/2}$ ground state, we can assume that the major contributions to this scattering rate are from the dipole transition rates from $S_{1/2}$ to the $P_{1/2}$ and $P_{3/2}$ excited states. With these simplifications equation (6) becomes:

$$\Gamma_{sc} = \frac{3\pi c^2}{2\hbar\omega_0^3}\left(\frac{\Gamma_{1/2}}{3\Delta_{1/2}} + \frac{2\Gamma_{3/2}}{3\Delta_{3/2}}\right)^2 I(r), \tag{7}$$

where $\Gamma_{1/2}$ and $\Gamma_{3/2}$ are the dipole transition matrix elements from the $S_{1/2}$ to the $P_{1/2}$ and $P_{3/2}$ states, respectively. The scattering rate will become more important later when we consider recoil heating losses due to atom scattering from the atom trap.

3.3. Trapping potential

While the proposed configuration has the capability of trapping rubidium, it should be clear that the methods laid out here, with the appropriate choice of dimensions and detunings, are transferable to the trapping of other neutral atom species. Table 1 lists the values chosen for the models used in this paper. Throughout the paper we refer to the blue-detuned power as P_b and the red-detuned power as P_r.

3.3.1. Single colour slot trapping potential. Combining a blue-detuned light field with the vdW potentials arising from interactions of the atoms with both inner dielectric walls of the slotted fibre, a stable position in the y-direction can be obtained. Unlike usual fibre-based atom traps which have potentials largely defined by the fibre radius, the proposed trap, in its most basic form, has two parameters, radius and slot width, both of which can be varied and are shown to have a large effect on the shape and efficiency of the atom potential, thereby giving more degrees of freedom in the design and increasing the flexibility of the system. Figure 6 illustrates

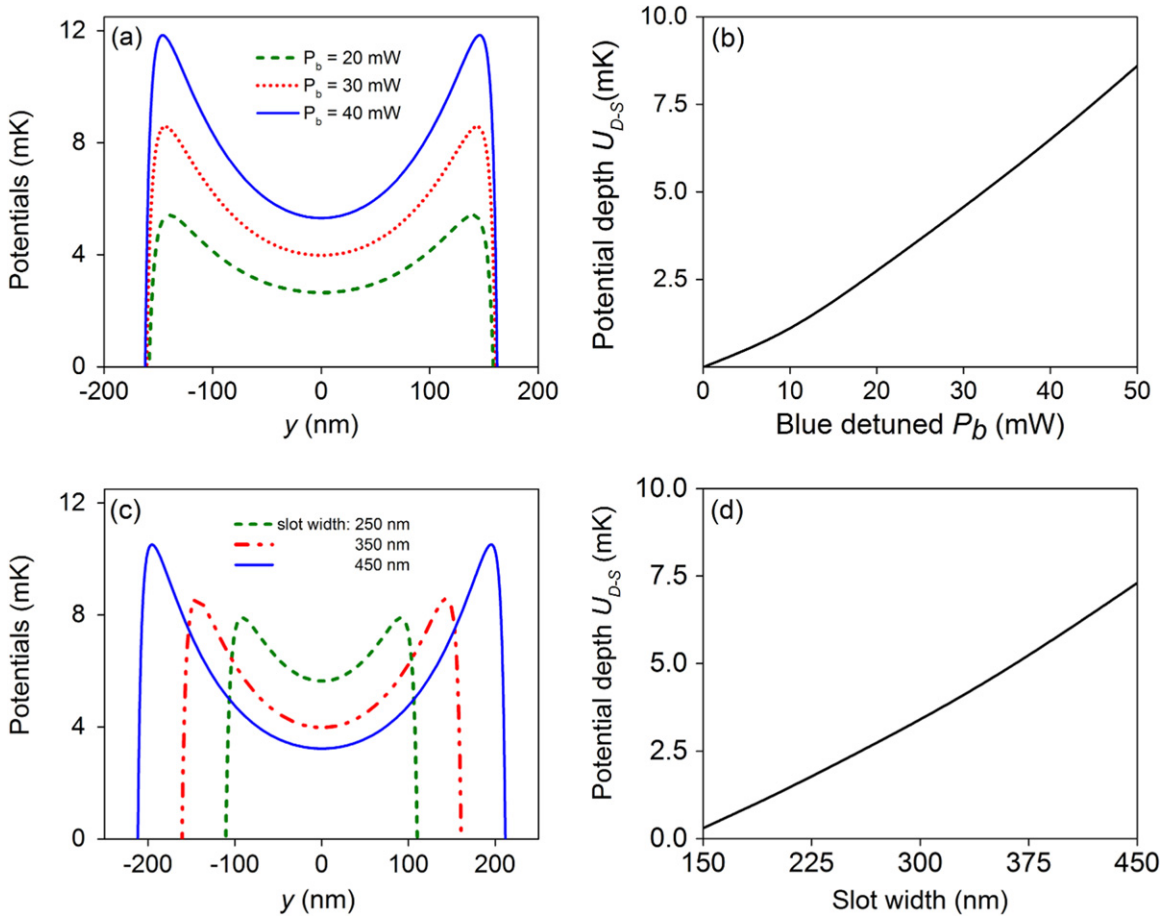

Figure 6. (a) Combination of the blue-detuned potential and the van der Waals potential for a slot width of 350 nm. (b) Power P_b of the blue-detuned light varse potential depth U_{total} for a slot width of 350 nm. (c) Combination of the blue-detuned potential and the van der Waals potential for various slot widths and (d) dependence of trapping potentials on slot width. P_b is fixed at 30 mW.

how the potential can be altered by varying either of these two parameters. In the following sections the blue-detuned light is always chosen to be polarized parallel to the slot, i.e. along the *x*-direction.

Figures 6(a) and (c) show the effect of changing blue-detuned powers and slot widths, respectively. By changing the power from 0–50 mW, or changing the slot width from 150–450 nm (figures 6(b) and (d)) trap depths up to 7.5 mK are obtainable. Unfortunately, this single colour trap provides no confinement along the *x*-direction. To extend this idea into a stable trap in the *xy*-plane, a red-detuned beam must be included, thereby creating a two-colour trapping scheme within the slot.

3.3.2. Two-colour slot and fibre surface traps. When a second electric field, with sufficiently different frequency, is added, mode beating effects between the red- and blue-detuned modes can be neglected. We assume that the mode beating period between the two fields, E_r and E_b, is much lower than the reaction time of atomic scale motion. Thus, we can assume that the two

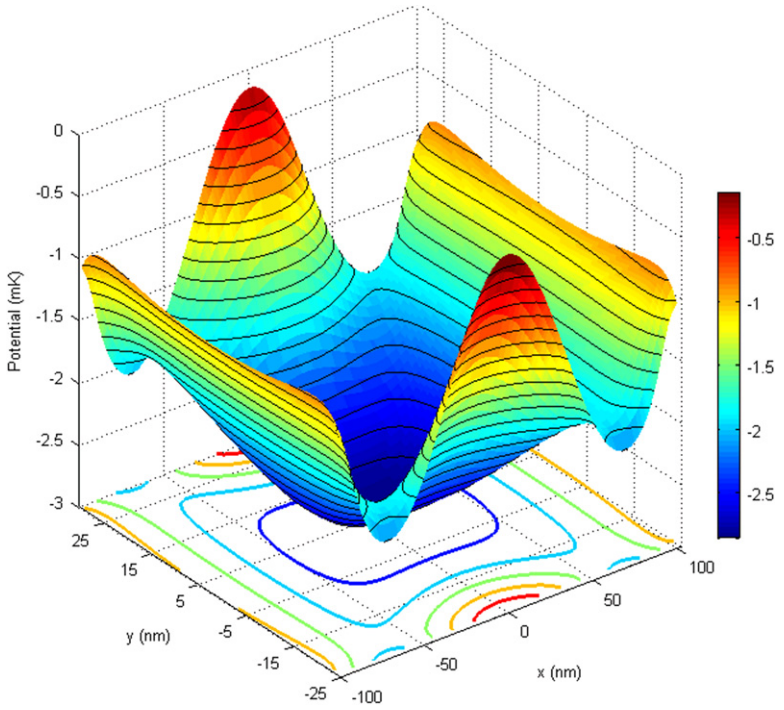

Figure 7. Combined surface and contour plot of a trapping potential in the *xy*-plane for a 1 μm diameter fibre with a 350 nm slot width. P_r = 30 mW and P_b = 30 mW.

potentials add linearly such that the total potential is given by $U_T = U_b + U_r$. The addition of an attractive, red-detuned light field, polarized perpendicularly to the slot, creates a stable equilibrium position at the centre of the potential in both the *x*- and *y*-directions.

By adding the fields linearly, it can clearly be seen that a trapping well is formed in the *xy*-plane (figure 7). The shape of this well varies dramatically in shape and depth with different choices of P_b, P_r, slot width, and fibre diameter.

The trap depth in the centre of the slot in the *x*-direction is largely determined by the red-detuned power, P_r. At the trap centre, the contribution from the vdW force is negligible and the contributions from the blue-detuned field are also low since the polarization of the blue-detuned light is chosen to be parallel to the slot, thereby causing the power to decay away from the walls (see figures 6(a) and (c)). From figure 8 we see that a change in the red-detuned power (a) causes the potential depth to change more rapidly than an equivalent change in power of the blue-detuned field (b). When the blue-detuned light field is sufficiently large compared to the red-detuned field the shape of the potential in the *x*-direction veers away from being harmonic. To avoid complications, such a trap geometry is not considered when we determine trapping efficiencies.

Varying the power ratio between the red and blue-detuned fields not only affects the form of the trapping potential inside the slot, figure 9(b), but also at the outer fibre surface, figure 9(a). The traps at the fibre surface resemble those proposed by Le Kien *et al* [11]. An optimal trapping potential configuration for trapping atoms in the slot would maintain a deep trapping potential within the slot while keeping the trapping potential at the outer fibre surface

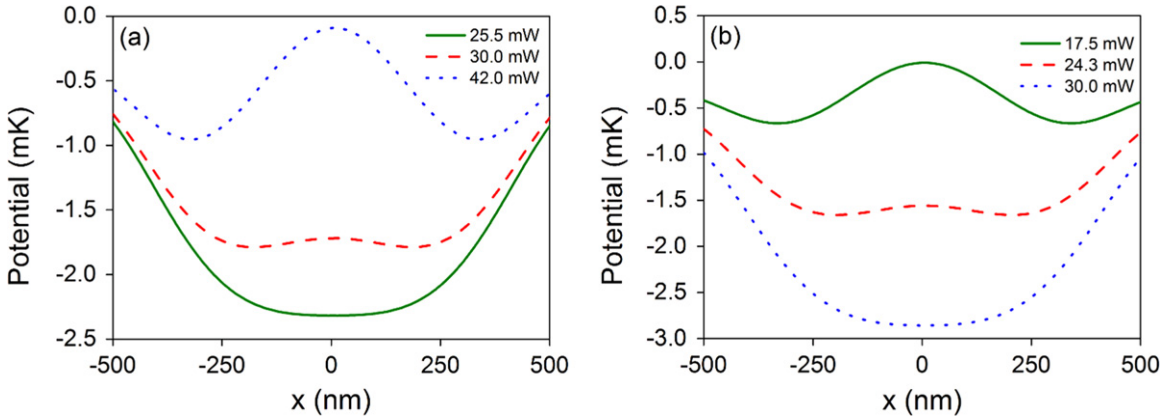

Figure 8. Two colour trapping potential for a 1 μm fibre with a 350 nm slot width in the x-direction. (a) P_r is kept at 25 mW while P_b is varied. (b) P_b is fixed at 30 mW while P_r is varied.

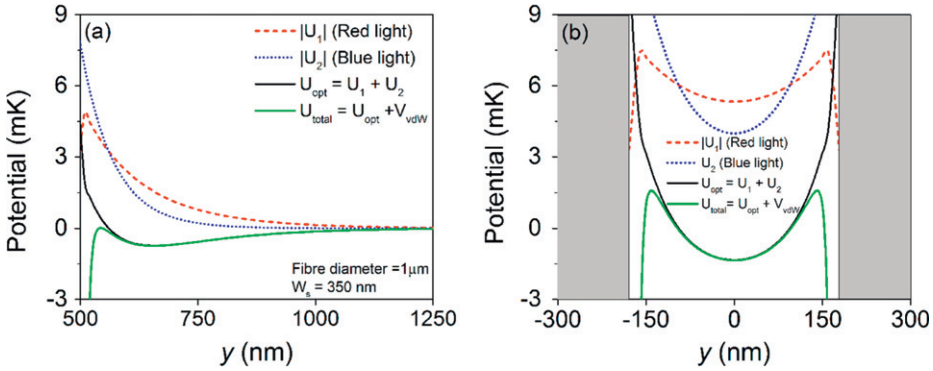

Figure 9. Contributions to the two-colour trap at (a) the outer fibre surface, and (b) the slot surfaces, to the total trapping potential U_{total}. Both plots are taken in the y-direction. The configurations are the same for (a) and (b), with P_b = 25 mW and P_r = 30 mW. The grey areas in (b) represent the slot walls.

at a local minimum, thereby preventing atoms from accumulating at the outer fibre surface due to the strongly attractive vdW potential.

3.3.3. Trap optimization. To optimize the trapping conditions we must consider four important parameters: slot width, fibre diameter, and the blue and red-detuned intensities resulting from the powers P_b and P_r respectively. Previously, we considered the confinement in the x-and y-direction. Here, only the field in the y-direction is investigated for trap optimization. This allows us to compare the fields both inside the slot region and at the outer fibre surface, whilst ensuring the vdW potential is correctly balanced within the slot region. It is known that the x-direction potential forms a stable equilibrium point at the trap centre provided that one avoids the extreme situations such as those given in figure 8; therefore, only the y-direction trapping potential need be used for determining an optimum configuration.

By varying the input powers of the blue- and red-detuned beams, it is possible to choose an appropriate pair of values for use as default beam powers when considering the other

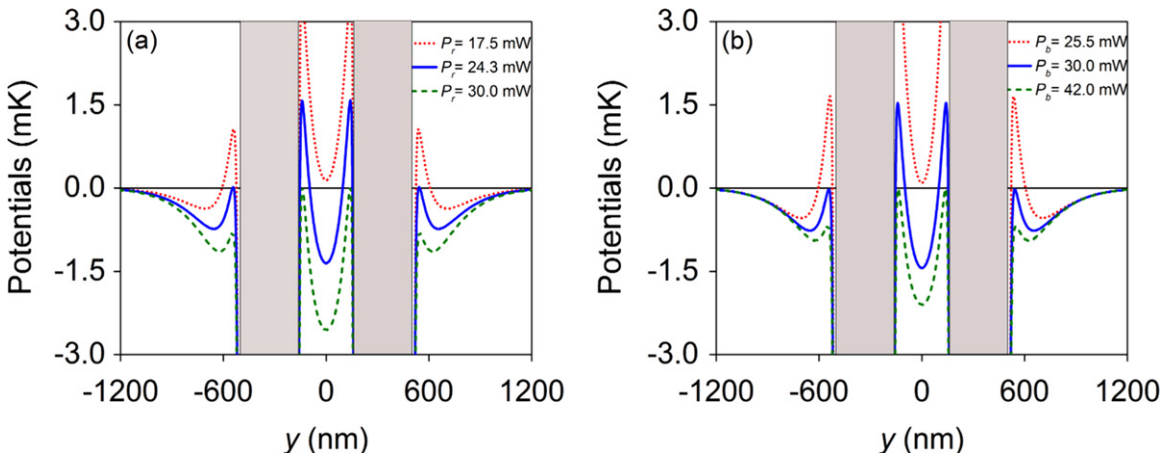

Figure 10. (a) Effect of the power P_r of the red-detuned light on total potential U_{total} while the power of blue-detuned light P_b is fixed at 30 mW; (b) Effect of the power P_b of blue-detuned light while P_r is fixed at 25 mW. All fibre parameters are the same as for figure 9.

parameters, such as slot width and fibre radius. The values are chosen in order to provide a deep potential inside the slot, with a minimum value below zero to facilitate the entry of rubidium atoms. For example, in figures 10(a) and (b), we can see that, within the slot region, the minimum value of the potential is only below zero for certain power configurations.

The power required to keep the outer surface trap depth at a local minimum as a function of slot width and P_r is important in the choice of a suitable input beam power, leading to values in the 30 mW range. Motivation for this comes from two major facts: firstly, we can see from figure 11(a) that the power required to maintain the fibre surface trap at a minimum becomes unmanageable above a slot width of 400 nm and, secondly, we must constrain ourselves in some respect because there is no well-defined upper limit in a trap of this type. Higher powers lead to deeper traps, higher scattering rates and, eventually, fibre performance decay. A power of approximately 30 mW is reasonable for use with an optical nanofibre in ultrahigh vacuum for slot widths in the 250–450 nm range [13, 14].

Figure 12 demonstrates how this choice of blue-detuned power can produce a trap with a large difference between the trap depths inside and outside the fibre. This also provides some motivation for the choice of a slot width of 350 nm. This value allows for a significant difference in the outer and inner potentials (U_{D-F} and U_{D-S}, respectively) and this size is approximately one third of the diameter of the fibre, thereby alleviating most issues regarding the fibre's structural stability following etching.

In an ad hoc attempt to, at least locally, optimize the trapping conditions we begin by using a blue-detuned power, P_b = 30 mW, while varying the other parameters independently to see their effect on the potential. Figure 13(b) gives a range of values where it is possible to obtain a suitable minimum potential value. Fibres of about 1 μm are located near the minimum of this curve for a 300 nm slot width. In figure 13(d) we show that the potential created using 30 mW of both red-detuned and blue-detuned power for both 1 μm and 1.2 μm fibres yield potentials that are below zero for slot widths greater than 275 nm. For a 0.7μm fibre it is clear from figure 13 that this condition is never met regardless of the chosen slot width. A 0.7 μm fibre still

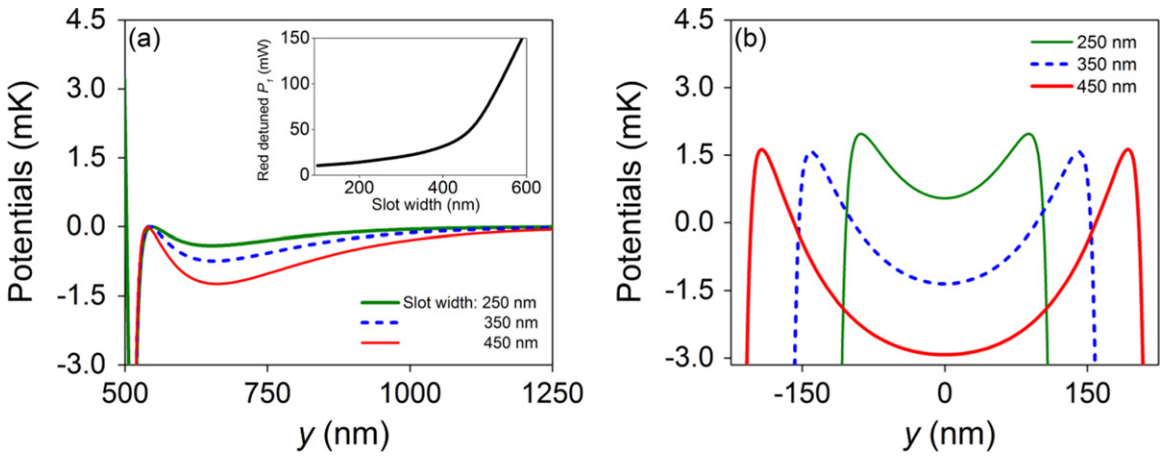

Figure 11. (a) Trap depth U_{D-F} at fibre surface and (b) trap depth U_{D-S} at slot fibre centre for different slot width values. The inset in (a) indicates the power P_r of red-detuned light required to keep the net optical potential depth U_{D-F} at a local minimum value for varying slot widths. The power of the blue-detuned light P_b is fixed at 30 mW and the fibre diameter is 1 μm.

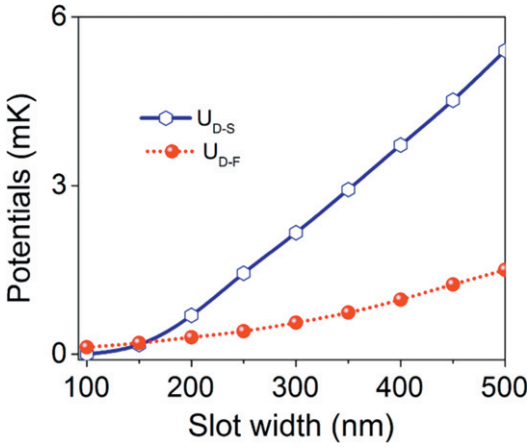

Figure 12. Trap depths U_{D-F} at fibre surface (dotted line) and U_{D-S} at slot fibre centre (solid line) versus slot width. The power of blue-detuned light P_b is fixed at 30 mW while the red-detuned light power P_r is varied to place the net optical potential depth P_{D-F} at a local minimum value (see the inset in figure 11(a)).

creates a strong trap with an adequate potential depth, but it lacks the capability of allowing atoms to easily enter the trap since atoms coming from infinity would need to overcome a net positive potential before entering the trap centre. As the fibre diameter is increased further, the mode will become well-confined to the larger segment sizes provided the slot widths are also in the same range as given in figure 13(d). This discussion does not preclude the use of smaller fibre diameters; it merely requires that the wavelengths of light chosen be tailored to the particular fibre size. A 0.7 μm diameter fibre, for instance, could be used provided a blue-detuned wavelength shorter than 720 nm is used.

Data in figures 13(b) and (d) indicate that higher slot widths produce better trap depths, but this comes at the cost of requiring higher red-detuned powers as is demonstrated by the inset of

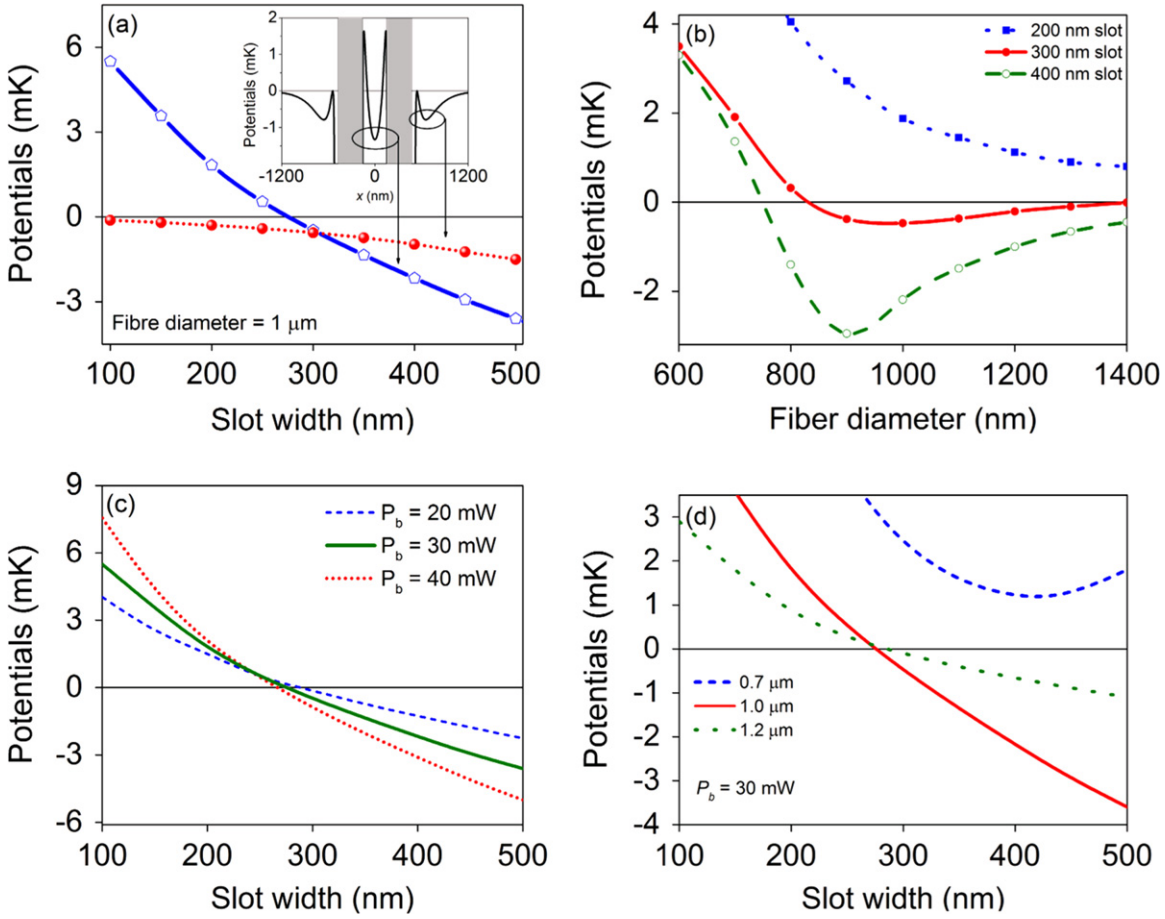

Figure 13. (a) Local minimum value of the trap depths at fibre surface U_{D-F} and at slot fibre center U_{D-S} versus slot width. For all figures the powers of the red- and blue-detuned light, P_r and P_b, are chosen to create an outer fibre surface trap depth at a local minimum value as in figure 12. (b) Minimum trap potential U_{D-S} versus fibre diameter for different slot widths, (c) minimum trap potential versus slot width for varying P_b powers, and (d) minimum trap potential versus slot width for various fibre diameters.

figure 11(a). Changing the blue detuned power has a relatively low effect on the potential as can be seen in figure 13(c). Fibre sizes much larger than 350 nm require very large red-detuned powers to compensate for the blue-detuned potential at the outer fibre surface. Our final choice of fibre is a 1 μm diameter fibre with a 350 nm slot width. The diameter and slot size were chosen by inspection of figure 13(b). Here, we see that a low potential minimum occurs at this value. Larger slot sizes were investigated, but the power required to create a viable x-direction trap began to exceed 40 mW once $W_s > 350$ nm slot widths were chosen.

3.4. Atom trap viability

In a two-colour trap the total scattering rate, Γ_{total}, is the sum of the scattering rates from the blue- and red-detuned fields, i.e. $\Gamma_{\text{total}} = \Gamma_{\text{red}} + \Gamma_{\text{blue}}$. From this value, a characteristic coherence time $\tau_c = 1/\Gamma_{\text{total}}$ can be determined [39]. Each scattered photon from either field contributes

some recoil energy to the atom. This will lead to a loss of atoms from the dipole trap. For a trap of depth U_D a trap lifetime which only takes recoil heating into account for the chosen trap configuration is given as:

$$\tau_c = \frac{U_D}{2\left(E^r_{\text{blue}}\Gamma_{\text{blue}} + E^r_{\text{red}}\Gamma_{\text{red}}\right)}, \tag{8}$$

where E^r_{blue} and E^r_{red} are the recoil energies associated with a blue and red photon, respectively. Along the x-axis the contribution from the blue-detuned field is at its minimum value, hence the potential here reaches a maximum near or below zero. In contrast, the y-axis potential will have the same minimum value at the centre but, due to increasing blue-detuned intensity, as one approaches the walls the maximum value will be above zero due to the field's repulsive property. When determining the trap lifetimes we only consider the 1D trap along the x-direction as it has a lower maximum depth than the y-direction.

4. Conclusions

Optical micro and nanofibres have already been shown to be an invaluable tool in trapping and probing atomic systems. In this paper we propose that a nanostructured optical nanofibre is capable of trapping atoms inside the slot region, rather than at the surface, via the use of blue- and red-detuned beams. We investigated the use of the slotted waveguide structure over a broad range of configurations. By keeping the fibre diameters and slot widths near the curve given in figure 4 and by using exponentially tapered fibres we can ensure that any contributions from the higher order modes is negligible [40]. We have also shown that the polarization of the light plays a crucial role in the realization of such a trap. With the current electric field configuration, atoms will be trapped in a line along the longitudinal axis of the structured fibre with potential minima located at distances of 140–200 nm from the slot walls. Using fundamental modes in the slotted region we have shown that a two-colour scheme is a viable method of producing adequate atom traps. For rubidium, trap depths of 4 mK, coherence times of the order of 10 ms and trap lifetimes of approximately 100 s should be accessible using modest input powers. Using an estimate for the optical depth per atom, namely the ratio of the on resonance scattering cross-section to the effective mode area $OD = \sigma_0/A_{\text{eff}}$, we obtain a value of 0.33 for the final configuration given in table 2. Experimentally values of 0.08 have been measured [13]. We deal exclusively with a slot which is assumed to have an infinite length, but in practice it would have a finite length and would be connected to an optical fibre pigtail at each end. Preliminary modelling work shows that >70% of the input mode can be transmitted beyond the end face of the slotted region. Flat end surfaces are the simplest case, but by tapering the slot ends we can significantly increase transmission into and out of the slot if required. Further analysis of this would require an in depth study of how the modes couple from the slot region back into the fibre modes and is beyond the scope of this paper. This preliminary work opens up many other avenues for atom trapping, such as standing waves, two-colour traps, single-colour traps using higher order modes, magic wavelength traps, and the introduction of additional slots. We believe that, with this geometry, a stronger coupling of atom emissions into the guided modes of the waveguide should be achievable, as should more efficient interactions between the atoms and any other light fields present in the nanofibre due to the atom's close proximity to the slot walls. The scalability of this design, along with its long coherence times, high optical depth, and

Table 2. Trap parameters found by varying P_r with respect to P_b, which was fixed at 30 mW. Values were obtained for a fibre width of 1 μm and a slot width of 350 nm.

Red-detuned power (mW)	Trap depth U_D (mK)	Scattering rate (s^{-1})	Coherence time (s)	Trap lifetime (s)
24.3	1.5	98.78	$1.01E^{-2}$	42
30	2.8	105.72	$9.46E^{-3}$	75
35	4	111.81	$8.94E^{-3}$	104

direct integration to optical systems make it an excellent candidate for quantum communication schemes. Experimentally, creating a slotted nanofibre is possible using a combination of existing techniques. Nanostructuring of an optical nanofiber using FIB techniques has recently been reported [41]. Misalignment of the slot position along the fibre axis would lead to asymmetric potentials. A cursory investigation indicates that it would be possible to create a trapping potential for misalignments of the slot position from the fibre center of the order of 10 nm, which coincides with the accuracy of a FEI Helios Nanolab 650 Dualbeam FIB/SEM. Alternatively, processing of the optical fibre using tightly focussed *fs* laser pulses could be considered [42].

Acknowledgments

This work is supported by OIST Graduate University.

References

[1] Féron S *et al* 1993 Reflection of metastable neon atoms by a surface plasmon wave *Opt. Commun.* **102** 1
[2] Dowling J P and Gea-Banacloche J 1996 Evanescent light-wave atom mirrors, resonators, waveguides, and traps *Adv. At. Mol. Opt. Phys.* **36** 1
[3] Tong L, Gattass R R, Ashcom J B, He S, Lou J, Shen M, Maxwell I and Mazur E 2003 Subwavelength-diameter silica wires for low-loss optical wave guiding *Nature* **426** 816
[4] Yariv A 1985 *Optical Electronics* 3rd edn (New York: CBS College) chapter 3
[5] Ravets S, Hoffman J E, Orozco L A, Rolston S L, Beadie G and Fatemi F K 2013 A low-loss photonic silica nanofiber for higher-order modes *Opt. Express* **21** 18325
[6] Russell L, Kumar R, Tiwari V B and Nic Chormaic S 2013 Measurements on release-recapture of cold Rb-85 atoms using an optical nanofibre *Opt. Commun.* **309** 313
[7] Russell L, Deasy K, Daly M, Morrissey M and Nic Chormaic S 2012 Sub-Doppler temperature measurements of laser-cooled atoms using optical nanofibres *Meas. Sci. Technol.* **23** 015201
[8] Nayak K P, le Kien F, Morinaga M and Hakuta K 2009 Antibunching and bunching of photons in resonance fluorescence from a few atoms into guided modes of an optical nanofiber *Phys. Rev.* A **79** 021801
[9] Morrissey M J, Deasy K, Frawley M, Kumar R, Prel E, Russell L, Truong V G and Nic Chormaic S 2013 Spectroscopy, manipulation and trapping of neutral atoms, molecules, and other particles using optical nanofibers: a review *Sensors* **13** 10449
[10] Ovchinnikov B, Shul'ga S V and Balykin V I 1991 An atomic trap based on evanescent light waves *J. Phys. B: At. Mol. Opt. Phys* **24** 3173

[11] Kien F Le, Balykin V I and Hakuta K 2004 Atom trap and waveguide using a two-color evanescent light field around a subwavelength-diameter optical fiber *Phys. Rev.* A **70** 063403
[12] le Kien F, Balykin V I and Hakuta K 2005 State-insensitive trapping and guiding of cesium atoms using a two-color evanescent field around a subwavelength-diameter fiber *J. Phys. Soc. Japan* **74** 910
[13] Lacroûte C, Choi K S, Goban A, Alton D J, Ding D, Stern N P and Kimble H J 2012 A state-insensitive, compensated nanofiber trap *New. J. Phys.* **14** 023056
[14] Lee J, Park D H, Mittal S, Dagenais M and Rolston S L 2013 Integrated optical dipole trap for cold neutral atoms with an optical waveguide coupler *New. J. Phys.* **15** 043010
[15] Vetsch E, Reitz D, Sageé G, Schmidt R, Dawkins S T and Rauschenbeutel A 2010 Optical interface created by laser-cooled atoms trapped in the evanescent field surrounding an optical nanofiber *Phys. Rev. Lett.* **104** 203603
[16] Goban A, Choi1 K S, Alton D J, Ding D, Lacroûte C, Pototschnig M, Thiele T, Stern N P and Kimble H J 2013 Demonstration of a state-insensitive compensated nanofiber trap *Phys. Rev. Lett.* **109** 033603
[17] Hung C L, Meenehan S M, Chang D E, Painter O and Kimble H J 2013 Trapped atoms in one-dimensional photonic crystals *New. J. Phys.* **15** 083026
[18] Thompson J D, Tiecke T G, de Leon N P, Feist J, Akimov A V, Gullans M, Zibrov A S, Vuletić V and Lukin M D 2013 Coupling a single trapped atom to a nanoscale optical cavity *Science* **340** 6137
[19] Ol'Shanii M A, Ovchinnikov Yu B and Letokhov V S 1993 Laser guiding of atoms in a hollow optical fiber *Opt. Commun.* **98** 77
[20] Burke J P, Chu S, Bryant G W, Williams C J and Julienne P S 2002 Designing neutral-atom nanotraps with integrated optical waveguides *Phys. Rev.* A **65** 043411
[21] Xu P, He X, Wang J and Zhan M 2010 Trapping a single atom in a blue detuned optical bottle beam trap *Opt. Lett.* **35** 2164
[22] Sagué G *et al* 2008 Blue-detuned evanescent field surface traps for neutral atoms based on mode interference in ultrathin optical fibres *New. J. Phys.* **10** 113008
[23] Phelan C F, Hennessy T and Busch T 2013 Shaping the evanescent field of optical nanofibers for cold atom trapping *Opt. Express* **21** 27093
[24] Schneeweiss P, le Kien F and Rauschenbeutel A 2014 Nanofiber-based atom trap created by combining fictitious and real magnetic fields *New J. Phys.* **16** 013014
[25] le Kien F and Hakuta K 2009 Microtraps for atoms outside a fiber illuminated perpendicular to its axis: numerical results *Phys. Rev.* A **80** 013415
[26] Morrissey M J, Deasy K, Wu Y, Chakrabarti S and Nic Chormaic S 2009 Tapered optical fibers as tools for probing magneto-optical trap characteristics *Rev. Sci. Instrum.* **80** 053102
[27] Nayak K P, le Kien F, Kawai Y, Hakuta K, Nakajima K, Miyazaki H T and Sugimoto Y 2011 Cavity formation on an optical nanofiber using focused ion beam milling technique *Opt. Express* **19** 14040
[28] Zhang L, Lou J and Tong L 2011 Micro/nanofiber optical sensors *Photonic Sensors* **1** 31
[29] Frawley M C, Petcu-Colan A, Truong V G and Nic Chormaic S 2012 Higher order mode propagation in an optical nanofiber *Opt. Commun.* **285** 4648
[30] Anderson P A, Schmidt B S and Lipson M 2006 High confinement in silicon slot waveguides with sharp bends *Opt. Express* **14** 20
[31] Elsherbeni A, Kaifez D and Zeng S 1991 Circular Sectoral Waveguides *IEEE Antennas and Propag. Mag.* **33** 6
[32] Jung Y, Jeong Y, Brambilla G and Richardson D J 2009 Adiabatically tapered splice for selective excitation of the fundamental mode in a multimode fiber *Opt. Lett.* **34** 2369
[33] Russell L, Gleeson D A, Minogin V G and Nic Chormaic S 2009 Spectral distribution of atomic fluorescence coupled into an optical nanofibre *J. Phys. B: At. Mol. Opt. Phys.* **42** 185006
[34] Minogin V G and Nic Chormaic S 2010 Manifestation of the van der Waals surface interaction in the spontaneous emission of atoms into an optical nanofiber *Laser Phys.* **20** 2

[35] Frawley M C, Nic Chormaic S and Minogin V G 2012 The van der Waals interaction of an atom with the convex surface of a nanocylinder *Phys. Scr.* **85** 058103
[36] Lennard-Jones J E 1924 On the determination of molecular fields *Proc. R. Soc.* A **106** 463
[37] Derevianko A, Johnson W R, Safronova M S and Babb J F 1999 High-precision calculations of dispersion coefcients, static dipole polarizabilities and atom-wall interaction constants for alkali-metal atoms *Phys. Rev. Lett.* **82** 3859
[38] Marani R, Cognet L, Savalli V, Westbrook N, Westbrook C I and Aspect A 2000 Using atomic interference to probe atom-surface interaction *Phys. Rev.* A **61** 053402
[39] Grimm R, Weidemüller M and Ovchinnikov Yu B 2000 Optical dipole traps for neutral atoms *Adv. At. Mol. Opt. Phys.* **42** 95
[40] Petcu-Colan A, Frawley M C and Nic Chormaic S 2011 Tapered few-mode fibers: mode evolution during fabrication and adiabaticity *JNOPM* **20** 293–307
[41] Daly M, Truong V G, Phelan C and Nic Chormaic S 2013 Near-field trap for submicron particles and cold, neutral atoms using rectangular etched cavities in optical nanofibers *Frontiers in Optics 2013/Laser Science XXIX* FTh1D.5
[42] Buividas R, Mikutis M, Gervinskas G, Day D, Slekys G and Juodkazis S 2012 Femtosecond laser drilling of optical fibers for sensing in microfluidic applications *Proc. SPIE* **8463** 84630T

LASER
& PHOTONICS
REVIEWS

Laser Photonics Rev. **9,** No. 3, 309–329 (2015) / **DOI** 10.1002/lpor.201500006

Abstract Subwavelength features in conjunction with light-guiding structures have gained significant interest in recent decades due to their wide range of applications to particle and atom trapping. Lately, the focus of particle trapping has shifted from the microscale to the nanoscale. This few orders of magnitude change is driven, in part, by the needs of life scientists who wish to better manipulate smaller biological samples. Devices with subwavelength features are excellent platforms for shaping local electric fields for this purpose. A major factor that inhibits the manipulation of submicrometer particles is the diffraction-limited spot size of free-space laser beams. As a result, technologies that can circumvent this limit are highly desirable. This review covers some of the more significant advances in the field, from the earliest attempts at trapping using focused Gaussian beams, to more sophisticated hybrid plasmonic/metamaterial structures. In particular, examples of emerging optical trapping configurations are presented.

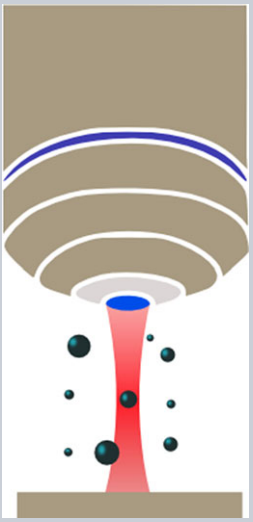

REVIEW ARTICLE

Optical trapping and manipulation of micrometer and submicrometer particles

Mark Daly, Marios Sergides, and Síle Nic Chormaic*

1. Introduction

The idea that particles could be influenced by the radiation pressure from light has existed as a concept for a very long time; almost 400 years ago Johannes Kepler published a treatise entitled "*De cometis libelli tres*" [1], wherein he proposed that solar rays were the cause of the deflection of a comet's tail. However, it was not until much later, when Maxwell formalized his theory of electromagnetism, that this force could be quantified. In 1906, John Henry Poynting, in relation to the force induced by radiation pressure, stated that "*even here, so minute is the force that it only need be taken into account with minute bodies*" [2]. The next major milestone on the road to harnessing radiation pressure came with the discovery and invention of the laser in 1960 [3].

Just over two decades after the first operational laser was created, Ashkin et al. published their seminal paper in which they proposed and demonstrated how a laser could be used to trap and manipulate micrometer- and submicrometer-sized dielectric particles by considering the total conservation of momentum in a light–particle system [4]. The initial design for the "*optical tweezers*", as the design based on Ashkin's seminal work came to be known, required very few optical components, with the laser source being the most costly. While Ashkin pioneered the work [5], other research groups quickly began to improve upon the design to make it more versatile. Modern optical tweezers allow for a high degree of control over several trapping parameters, such as particle location and trap strength. This has been achieved by including components such as acousto-optical deflectors, servo-controlled mirror arrays, etc. to create multiple trapping sites and/or to provide control over the particle's motion in the 2D focal plane of the optical tweezers. Optical tweezers are capable of performing high-resolution measurements when it comes to sensing small displacements of the trapped objects. This property has made the technique of interest in the life sciences where, typically, such small measurements of displacement, or force, were previously very difficult to examine.

In more recent years, the field of optical trapping has benefitted greatly from advances in other optics-related areas. To overcome limitations imposed by the diffraction limit of free-space laser beams, the research direction of many optical manipulation groups has shifted to devices that exploit optical near-fields. Optical near-fields, unlike far-fields, can create subdiffraction-limited spot sizes. Near-field devices range from the superresolution lens as described by Pendry [6] to the use of surface plasmons [7, 8] created by the coherent oscillation of electrons near

Light-Matter Interactions Unit, OIST Graduate University, Onna, Okinawa, 904-0495, Japan
*Corresponding author: e-mail: sile.nicchormaic@oist.jp

Wiley Online Library

the boundary of a metal–dielectric system. Both of these designs are capable of creating electric field 'hotspots' that can greatly enhance the field strength locally.

This review seeks to outline the current state of the field while focusing mainly on methods that can be employed to shift optical trapping into the nanometer regime through the use of methods and techniques that are not overly complex in design. The scope of the field of optical trapping makes a complete review an almost impossible task. This paper touches on many aspects of optical trapping, but for extensive reviews of the biological applications of optical tweezers, or more indepth discussions about how optical tweezers can be improved by algorithms or diffractive elements, the reader's attention is drawn to other reviews [9–11].

Section 2 mentions a few of the important applications that have stemmed from the field of optical trapping in order to provide some motivation for the work as a whole. Section 3 outlines the fundamental theory behind optical trapping along with details about where more rigorous calculations of the trapping forces can be found. Sections 4 through 6 review a subset of the many types of traps used in optical manipulation today, with the order of the sections somewhat governed by the decreasing size of the particles that can be trapped.

2. Applications

The field of optical trapping, as with many scientific fields, is motivated by the potential applications that can stem from it. The high degree of control and precision with which one can trap and localize particles using optical tweezers, or other similar trapping systems based on optical forces, is impressive in and of itself, but it is the ability to then apply these techniques experimentally with incredible resolution that is of interest to scientists, especially those in the life sciences.

One of the most common applications of optical tweezers is the strong confinement and manipulation of small objects. For example, Waleed et al. used optical tweezers to spatially localize plasmid-coated microparticles that were then optically inserted into MCF-7 cells. The cells were optically perforated using a femtosecond laser to guarantee transfection [12]. In this work the versatility of the optical tweezers is shown since, not only were the optical tweezers used to manipulate the particle's position, but they were also used to experimentally determine the focal length of various laser sources.

Other work has been done using optical tweezers to measure exceptionally minute position changes with high resolution. Examples include measuring the step sizes of kinesin proteins along microtubules [13], the distance between adjacent basepairs via determination of the step sizes of DNA polymerase [14], and, more recently, unwinding–rewinding dynamics in P-fimbriae [15]. Some of these applications will be discussed in more detail in Section 4.2.

Application of force to trapped particles can also be achieved using optical tweezers system, and this has been exploited to analyse biological systems. By incorporating optical tweezers with Förster resolved energy transfer (FRET) [16], conformational dynamics of Holliday junctions and the folding dynamics of DNA hairpins have been measured. Integrating optical tweezers with other spectroscopic and microscopic techniques is a vital step in the furthering of their applications in the life sciences. This has led to the integration of optical tweezers with techniques such as Raman spectroscopy (see Section 4.3) and stimulated emission depletion (STED) fluorescence microscopy [17–19]. All of these modifications have served to further increase the effectiveness of optical tweezing techniques in many fields.

Moving from manipulating 'large', i.e. micrometer-sized, particles to smaller nanoscale particles opens up a vast array of applications. The previous examples, which certainly involved the investigation of nanoscale objects such as DNA, were only able to do so via the use of micrometer-sized spheres. A lot of research in the field is, therefore, focused on overcoming this size limitation. Eventually, we can expect that trapping small particles, such as bacteria and viruses, will become routine. This would be an excellent achievement for the nanobiology world [20] and some progress in this direction has already been made. For example, influenza viruses, of about 100 nm size, have been individually manipulated using optical forces alone [21]. Within this review we aim to discuss some of the progress made in these applications, commencing with the introduction of the more well-established techniques in the field.

3. Optical trapping regimes

The first applications of light to trap particles utilized a technique that came to be known as optical tweezing. By employing a tightly focused Gaussian beam, particles can be trapped near the focus due to the gradient force induced by the momentum exchange of photons with the dielectric particles. Ashkin proposed the application of focused Gaussian beams for both particle [5] and atom trapping [22] using radiation pressure, albeit almost a decade apart. The description of how a particle behaves in a light field can be described using different models that depend on the particle's size in relation to the wavelength of the light used for trapping. For example, if the particle is large in comparison to the wavelength, a ray-optics approach can be used. Since this review focuses on the transition between the micro- and nanoworlds of optical trapping, the details of the ray-optics approach will not be discussed. However, the simple ray-optics explanation does provide a somewhat intuitive model for how trapping occurs, and should not be discarded as an invalid approach to describing the optical forces on particles.

3.1. Rayleigh regime

For particles with sizes equal to, or smaller than, the wavelength of light, an electromagnetic model is required to adequately represent the forces at play in a particle–light system. This solution can range from a more complete theory, which uses the Mie solutions to scattering problems involving spherical or elliptical objects, to a simpler case when the particle size is much smaller than the wavelength of the trapping light and is made from a linear, isotropic material. This allows for the use of the dipole approximation in the calculations. The polarizability of a particle in this case gives rise to a dipole moment, $\vec{p}$

$$\vec{p} = \alpha \vec{\mathrm{E}}, \tag{1}$$

where α is the particle's polarization and $\vec{E}$is the electric field. The electrostatic potential generated by a dipole in an electric field is related to this polarizability via $\vec{U} = -\vec{p}.\vec{E}$. Hence, the force, which is the negative gradient of the potential, can be determined

$$\vec{F} = -\nabla U = -\nabla\left(\vec{p}.\vec{E}\right) = -\alpha\nabla\vec{E}^{2}. \tag{2}$$

Because of this polarization dependence, metallic nanoparticles, which, over wavelengths of interest in particle trapping have a much higher polarizability, are often used as targets for trapping at the nanoscale since they require the use of lower optical powers compared to silica or polystyrene particles of the same size. Taking the time average of the field into account, and using the Clausius–Mossotti relationship for a spherical dielectric particle, the so-called gradient force a particle feels is finally given as

$$\vec{F}_{grad} = -\frac{2\pi n_0 r^3}{c}\left(\frac{m^2-1}{m^2+2}\right)\nabla I(\vec{r}), \tag{3}$$

where r is the particle's radius, c is the speed of light, n_0 is the refractive index of the medium, m is the dielectric contrast, i.e. the ratio of the particle's index to the medium's index, and $I(\vec{r})$ is the time-averaged intensity as a function of position, $\vec{r}$. The dielectric contrast plays a role in the trapping strength of optical tweezers, but more interestingly, changing the value of this property can cause the sign of the force to be reversed. If particles of a lower index than their surrounding medium are used, i.e. $m < 1$, the sign of Eq. (3) is seen to change. The origin of the term "*gradient force*" should now be evident from Eq. (3); it is a force that is linearly dependent on the gradient of the intensity and tends to attract particles to regions of higher, or lower, intensity pending the value of the dielectric contrast.

Stable trapping occurs when the net force on a particle is zero and any small displacements from this stable position result in an optical force that resists the motion of the particle away from this position. Typically, traps with a potential depth greater than the thermal limit, i.e. a few k_bT, are required for stable trapping, where k_b is the Boltzmann constant and T is the particle's temperature. A potential depth in the region of $10k_bT$ is often used as a standard value for stable traps.

To complete the discussion on optical forces, one must also include the scattering force felt by a particle that is being bombarded by a flux of photons of wavenumber k. Under the Rayleigh approximation, along with the Clausius–Mossotti relationship, this is given as

$$\vec{F}_{scatt} = \frac{8\pi n_0 k^4 r^6}{3c}\left(\frac{m^2-1}{m^2+2}\right)^2 I(\vec{r})\vec{z}. \tag{4}$$

If the problem is approached using a more rigorous calculation involving the Maxwell stress tensor or Lorentz force, a third force, known as the polarization gradient force, arises out of the calculations; this force is typically not present in trapping systems, but its existence should be noted [23].

3.2. Mie solutions and discrete dipole approximation

For particles of intermediate sizes, between that of the ray optics and Rayleigh regimes, one can apply the Mie solutions [24, 25]. These solutions are the complete solutions to the Helmholtz equation that take the form of an infinite series. The Mie solutions are very important in this size regime. In the Rayleigh regime the force scales as the cube of the particle's radius and this can be shown to be incorrect for larger particles in the ray-optics regime. The Mie solutions help to bridge this gap between the two regimes, while also introducing some new phenomena which would otherwise be unnoticed in the theory. In a paper by Stilgoe et al. [26] a detailed calculation of the trapping forces on particles of varying radii and refractive indices using different numerical apertures is described. A phenomenon known as a Mie resonance occurs in intermediate-sized particles, and this is more prominent in particles with a higher refractive index contrast between them and the medium. The presence of Mie resonances strongly changes the trap strength of optical tweezers, as can be seen from Fig. 1 [26], and should be taken into account when developing tweezers to work at such particle sizes in order to maximize its effectiveness. As can be seen in Fig. 1b, the interference effects can cause the trap strength to oscillate between trapping and nontrapping regions as the particle size is changed, an effect that is absent in the Rayleigh regime.

If the high accuracy of Mie solutions is not required, but work is being done at or near the boundary between the Rayleigh and Mie regimes, the dipole can instead be approximated as a discrete sum of dipoles to reduce the errors arising from the single-dipole approximation.

3.3. Other forces

To fully model an optical manipulation system other forces must be considered, such as the Stokes' drag of a particle and the force due to the random Brownian motion. A

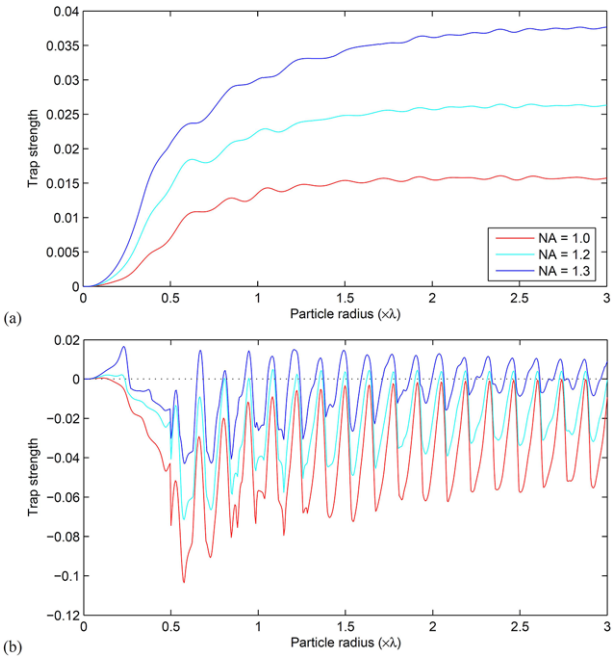

Figure 1 Dependence of the trapping force for (a) polystyrene and (b) diamond particles for a fixed numerical aperture, and particle radii varying between 0 to 3 λ. Note the pronounced interference effects present in the higher refractive index, diamond particles. (Reproduced with permission.[26] 2008, Optics Express).

further discussion of Brownian motion can be found in Section 4.1. The Stokes' drag present in a system can be quite complicated to determine due to the influence of nearby surfaces. For optical tweezers, Faxen's law [27,28] is often used to include the influence of the nearby planar surfaces, such as coverslips, in an experiment. Often these effects can be solved for experimentally by modeling the system as a damped harmonic system and calibrating accordingly.

4. Optical tweezers with free-space laser beams

Modular optical tweezers using free-space Gaussian beams are highly versatile tools that have high trap stiffness when dealing with micrometer- and, to some degree, submicrometer-sized objects. This is a necessary requirement for precise trapping. They also have incredible resolution with respect to position or force measurements on trapped objects. It is this resolution that makes optical tweezers invaluable in the life sciences. Applying this type of optical tweezers to the problem of trapping dielectric particles does have two drawbacks when it comes to trapping smaller particles. The first arises from the diffraction limit, which limits the waist size of a Gaussian beam refracted through a lens. The second drawback is, admittedly, also a side-effect of the diffraction limit; particles of increasingly smaller size require larger gradient forces to trap them. Photons directly exchange energy with particles via scattering; this force is typically called the scattering force and on average acts in the direction of beam propagation. In the Rayleigh regime, the ratio of the gradient force to the scattering force yields an inverse cube dependence on radius. Taking this value at the position of maximal axial intensity gradient yields [4]

$$R = \frac{F_{grad}}{F_{scatt}} = \frac{3\sqrt{3}}{64\pi^5}\frac{n}{\left(\frac{m^2-1}{m^2+2}\right)}\frac{\lambda^5}{r^3\omega_0^2} \geq 1, \qquad (5)$$

where ω_0 is the focal spot size. This puts an upper limit on the particle size, since the gradient force must dominate. However, the time needed for a particle to be trapped must also be longer than the diffusion time out of the trap to ensure efficient trapping. Trapping objects in the nanometer regime requires laser powers that can quickly destroy/denature the samples being trapped. Despite this, optical tweezers systems using focused Gaussian beams remain invaluable tools.

4.1. Optical tweezers basics

The term 'optical tweezers' refers to any optical system that is capable of confining a particle in all three dimensions. The most commonly available system involves the use of free space optical beams to provide a gradient force trap in all directions. Recently, commercial, self-calibrating optical tweezers systems have become available, indicating the rise of interest in the field.

Free-space optical tweezers exist in many different varieties due to their high customizability. As mentioned previously, optical tweezers typically use focused Gaussian beams (Fig. 2) combined with some mechanism that can deflect or otherwise steer the light beam in the focal plane of the tweezers. Some examples include galvanometer-mounted mirror arrays to create multiple trapping sites by rapidly moving the trap center around the focal plane [29], holographic optical tweezers that include a spatial light modulator (SLM) to create different trapping patterns, acousto-optic deflectors, and even diffractive or polarizing elements. Each variation of optical tweezers has advantages and disadvantages. For example, SLMs allow for a higher degree of control and customizability, but have typically low response times [11,30,31]. Both continuous-wave (CW) or pulsed lasers can be used in optical tweezers [32].

The operation of optical tweezers is typically chosen to be in the near-infrared region, primarily because light of wavelengths greater than 800 nm is poorly absorbed by most living matter and, as one moves further into the far-infrared region, absorption from water molecules becomes an issue [33]. For these reasons, light from an Nd:YAG laser at approximately 1064 nm is commonly used for optical trapping. Optical tweezers are capable of resolving subnanometer motion and measuring pN of force [14].

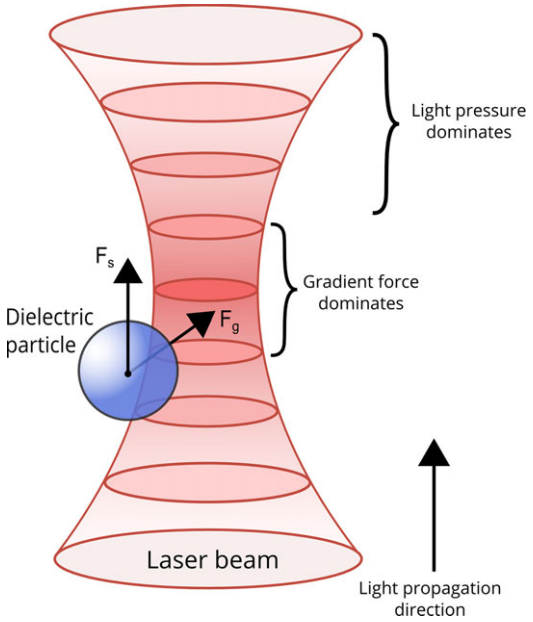

Figure 2 Schematic of a Gaussian beam optical tweezers (red) showing a particle (blue) along with the scattering (F_s) and gradient (F_g) forces that act upon it. The darker shades of red indicate regions of higher intensity.

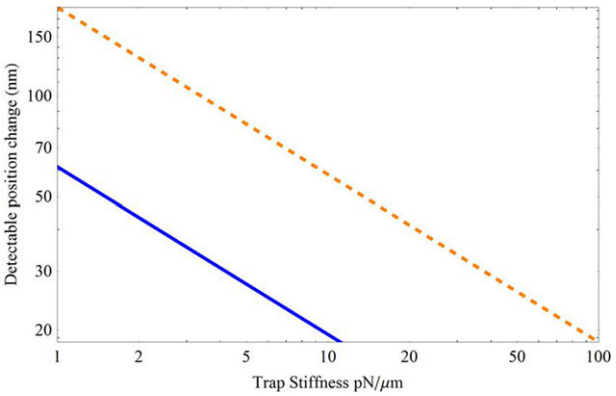

Figure 3 Log-log plot of detectable position change versus trap stiffness at the thermal limit (blue solid line) which corresponds to 68.5% detection efficiency, and three times the thermal limit (orange dashed line) which corresponds to 99.7% detection efficiency.

For optical tweezers in viscous media, the motion of the trapped particle can be well described by an overdamped Langevin model, often termed the "Einstein–Ornstein–Uhlenbeck theory of Brownian motion" [34]. In this overdamped regime, the inertia terms in the Langevin equation become negligible and the power spectrum of the system can be well described. To put it simply, the fundamental operational limit for measurements using optical tweezers, or indeed in any of the systems that will be discussed herein, is due to Brownian noise. This noise is always present and, unlike other measurement-based errors such as laser noise, shot noise, imaging errors, etc., it cannot be circumvented. A particle's motion while trapped in optical tweezers can be described as a harmonic oscillator. Therefore, it is easy to equate the energy of the particle's Brownian motion to the trap's energy using the equipartition theorem, i.e. $\frac{1}{2}k_bT = \frac{1}{2}\kappa\left\langle\chi^2\right\rangle$ [35], where k_b is Boltzmann's constant, T is the temperature, κ is the spring constant of the system, and $\left\langle\chi^2\right\rangle$ is the particle's mean squared displacement from equilibrium. This can be used to determine the fundamental measurement limit for experiments based on optical tweezers. By defining the square root of the mean squared displacement as $\sqrt{\chi^2} = \sqrt{k_bT/\kappa}$, the minimum detectable limit can be determined, as shown in Fig. 3. To measure the trap stiffness, a simple Lorentzian can be fitted to the power spectrum, but this gives errors of 10–20%. Further studies have shown how to increase the accuracy of such a measurement via modification of the Lorentzian fit [36].

The assumption that one can work at this Brownian noise limit is of course, untrue, as there will always be sources of error that cannot be entirely eradicated. One can, however, work extremely close to this limit. Many attempts have been made over the years to reduce noise and increase trapping times in optical tweezers. These approaches range from the use of laser feedback control algorithms to reducing the average laser power and hence the associated noise, to the use of interferometric techniques to enhance sensitivity [13, 37].

Although not discussed in detail in this review, it is worth mentioning that the problems of noise for optical tweezers in vacuum, such as that associated with optically levitated particles, are different. Earlier, we dealt with an overdamped system, but, in vacuum, the system is underdamped as there is no viscous medium to interact with the trapped particle. Aside from the other effects that this has on optical trapping, it also means that the measurement limit now becomes a problem more strongly related to the laser intensity, or, rather, the photon flux. Recoil energy is directly imparted to the particles via interaction with the photons in the laser beam. This is in many ways similar to the laser cooling of atoms in a magneto-optical trap, where the thermal limit comes not from any interaction with residual gases in the vacuum, but rather from the recoil energy of the laser photons.

An influential application of optical tweezers was performed in 1993 by Svoboda et al. [13]. They concluded that kinesin, a type of motor protein found in eukaryotic cells, moved in 8-nm steps. In this early application of optical tweezers, silica beads were coated with kinesin in such a way as to allow only a single active molecule per bead. These beads were then attached to microtubules along which kinesin can move and measurements of the step size were made using overlapping beams from a Wollaston prism. Phase objects, such as silica beads, placed in the overlapping region caused varying degrees of ellipticity in the recombined beam and this effect was used to determine fine movements of the objects. This extra step was required to achieve the 8-nm resolution reported and helped show the versatility of optical tweezers in biology.

4.2. Dual-beam optical tweezers

Single-beam traps are at a disadvantage when compared with dual- or multiple-beam optical tweezers since only one particle can be steered or guided at any given time. Multiple-beam traps can be created numerous ways, such as the time sharing of a single beam using motorized mirror arrays, or the splitting of a single beam via polarization elements to create two individual trapping potentials. A particle suspended in the optical gradient of a beam is somewhat decoupled from the environment, but measurements generally require that a second object, which is directly coupled to the environment via some physical stage or mount, be used. This second particle is subject to many forms of external noise, such as stage drift that often dominates the noise spectrum.

Dual-beam optical tweezers are systems that, effectively, combine two single-beam optical tweezers. This allows one to simultaneously trap two objects and perform differential detection measurements, thereby improving the attainable spatial resolution [10]. Traps of this form existed as early as 1993, although large improvements in stability were shown only about a decade later. Comparing the 8-nm resolution previously obtained [13] to a more recent measurement using a dual-beam trap, an impressive leap in measurement accuracy can be seen, though admittedly this jump was not entirely due to the dual-beam configuration itself.

In 2005, base-pair stepping by RNA polymerase was measured and step sizes of 3.7 Å were distinguishable [14]. This level of high resolution was made possible both through the use of a dual beam tweezers, as well as isolating the system from external air currents via the use of a helium-filled enclosure. The inset of Fig. 4b indicates the drastic drop in noise due to the helium enclosure. By immobilizing both sides of the RNA polymerase with separate optical tweezers, the noise induced by the motion of the stage was effectively removed. The improved signal-to-noise ratio of dual-beam traps has been quantified by Moffitt et al. [38]. The system behaves like a three-spring system consisting of two optical tweezers and a DNA strand as the extra spring. Autocorrelations in the motions of two spheres tethered by a DNA strand, as illustrated in Fig. 4a were measured to determine the 3.7 Å step size. This study showed strong agreement between theory and experiment over the study's chosen parameter range.

Optical tweezers are also used to apply forces. One such example is the combination of an optical trap with a three-color FRET process. In a FRET system, the energy transfer is strongly dependent on the distance between donor and acceptor chromophores [39]. The energy-transfer efficiency is given as:

$$E = \frac{1}{1 + \left(\frac{R}{R_0}\right)^{6'}} \tag{6}$$

where R is the distance between the chromophores and R_0 is a characteristic value called the Förster distance. This Förster distance is where the energy, E, drops to 50% of the maximum and typically the values are in the range of 30–60 Å.

The discovery of fluorescent proteins, which have become ubiquitous in the life sciences, allow direct fluorescence measurements to be made by labeling individual molecular components with different color dyes. This is extremely useful in many fields of study where, for example, the mechanism that needs to be studied is inaccessible due to being part of a minute, complex system. This is true for many biomolecular machines with changing internal conformations. Lee and Hong [16] used this hybrid FRET optical-tweezers system to observe the conformational dynamics of a Holliday junction and the folding dynamics of a DNA hairpin (Fig. 5). Holliday junctions are junctions formed by the intersection of DNA strands, while DNA hairpins are common patterns that can be formed by single DNA strands. Holliday junctions have two distinct conformations (known as ISO1 and ISO2) in the absence of mechanical tension. The authors sought to determine if an applied force showed a bias towards either shape. By labeling different sections of the junction with different dyes, the FRET efficiencies between different pairs were calculated as functions of the applied force and, hence, the shape of the junctions could be deduced. Using a similar technique, folding and unfolding dynamics of a DNA hairpin were studied. The conclusion was that hybrid systems, such as the one discussed in the paper, are readily applicable to many nucleic acid systems.

4.3. Non-Gaussian beam shapes

Alternative approaches to optical tweezing make use of non-Gaussian trapping beams [40]. For example, Tatarkova et al. [41] made use of a zeroth-order Bessel beam generated using an axicon grating. By illuminating the axicon with a slightly converging laser beam they were able to produce a so-called 'washboard' potential with a controllable tilt, i.e. a harmonic potential with a superimposed sinusoidal fluctuation, as illustrated in Fig. 6. When the inclination of the washboard potential exceeded a certain value the particles were drawn to the Bessel beam center.

Optical beams can also have two different types of angular momentum – spin angular momentum and orbital angular momentum (OAM) – both of which can be exploited for particle trapping. Spin angular momentum is related to the polarization of light, whereas OAM is related to the topological phase of light, which gives rise to vortex beams where the phase changes as a function of the beam radius, and can even be transferred to plasmon fields as will be discussed in Section 4 [42–44]. Standing-wave traps generated by counterpropagating Bessel beams have been constructed. Cîzmár et al. [45] successfully trapped particles of diameters from 490 nm to 1000 nm using what they termed a "sliding Bessel standing wave". Using this they constructed an 'optical conveyor belt' by controlling

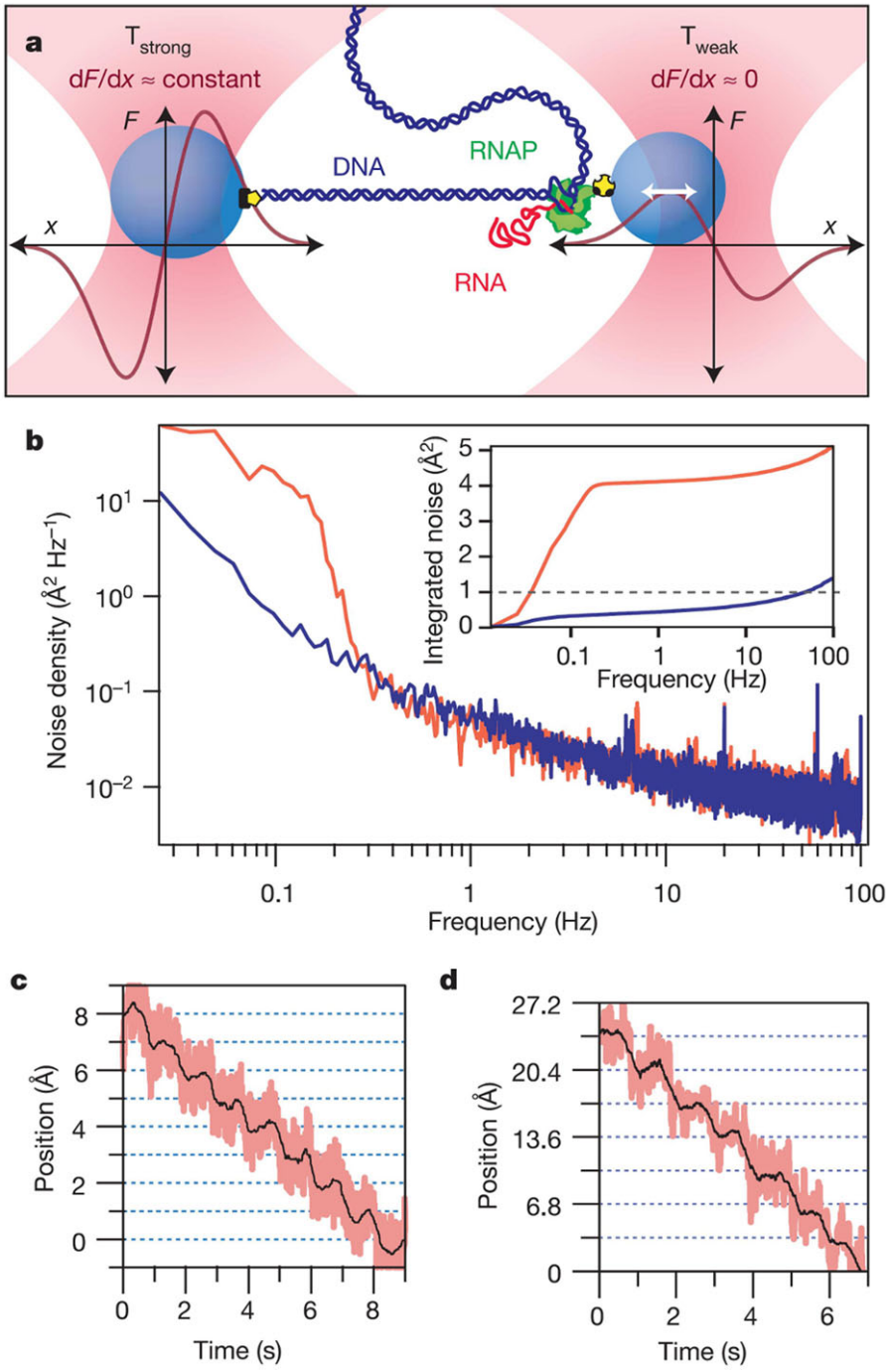

Figure 4 RNA polymerase immobilised using a dual beam optical tweezers and polystyrene beads. T_{strong} and T_{weak} are names given to the traps which refer to them having high and low spring constants respectively. (b) Noise density for helium enclose, blue, and the unenclosed system, red. (c), Steps resolved for a stiffly trapped bead moved in 1 Å increments at 1 Hz. (d) 3.4 Å steps by using a bead-DNA-bead tension of 27 pN then moving T_{strong} in 3.4-A° increments at 1 Hz. (Reproduced with permission.[14] 2005, Nature)

the positions of the nodes and antinodes of the trapping potential generated.

The differences between the two kinds of angular momenta are evident when the effects they have upon particles are considered. Spin angular momentum causes particles to rotate around their axes, whereas OAM can directly impart angular momentum, thereby causing the entire particle to rotate within the field. Furthermore, if the particle is large enough, rotation about an axis is possible with OAM. OAM can be contained within Laguerre–Gaussian (LG) modes, which are frequently used for work in the field. LG beams are particularly useful when fine control of a particle's orientation is required. For example, Dasgupta et al. [18] performed Raman spectroscopy on red blood cells with the help of a Laguerre–Gaussian beam generated from an SLM. The use of Raman spectroscopy techniques combined with optical tweezers has been termed 'Raman tweezers' [19] and is a viable approach that has existed for well over two decades. Optical tweezers have the distinct advantage of being able to make measurements on red blood cells, or

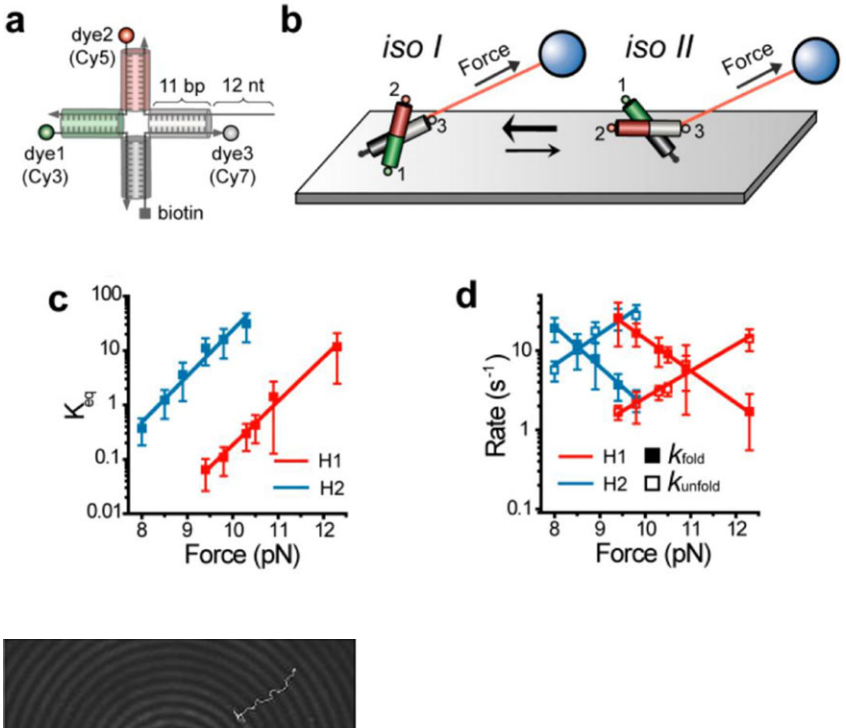

Figure 5 (a) Representative diagram of a Holliday junction. (b) Force is applied to two different conformations of the Holliday junction. (c) The equilibrium constant of the unfolded state (where K_{eq} is the ratio of the unfolded state population to the folded state population) as a function of force, and (d) the rate constants of folding/unfolding reactions as functions of force for H1 (red) and H2 (blue) conformations. (Reproduced with permission.[16] 2013, J. Am. Chem. Soc.)

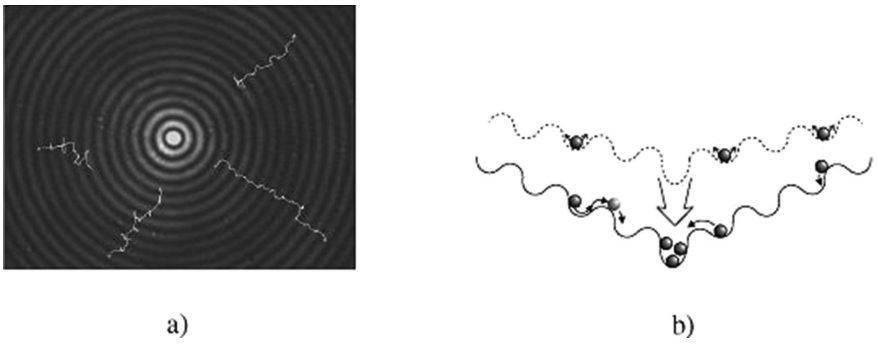

Figure 6 (a) Intensity profile of the zeroth-order Bessel beam produced from an axicon with particle trajectories superimposed upon the image (b) examples of a washboard lattice at two different inclination angles. (Reproduced with permissions.[41] 2003, Phys. Rev. Lett.)

indeed any suitably sized cell, in vitro. Hence, the way a cell behaves during applications of stretching induced stress can be recorded. In the experiment by Dasgupta et al. [18], they showed that LG beams can efficiently trap and control the orientation of blood cells in three dimensions and how this may facilitate polarized Raman spectroscopy of the cells. Larger cells, such as red blood cells, are easier to manipulate with OAM as their bodies can take up a larger portion of the beam allowing for easier rotation.

Certain cells, e.g. E. Coli [46], can be rotated and controlled due to their asymmetric shapes. Spherical particles are, in general, harder to orient accurately. Due to their symmetry, momentum must be imposed via the light's spin or angular momentum. Optical tweezing using cylindrical objects, 1D chains, or birefringent objects has been performed [47]. In 2004, La Porta and Wang [48] published a study that investigated the torque present when birefringent particles were illuminated by an external field. In birefringent materials, the polarization field generated is not aligned with the external electric field, and this produces enough torque to rotate a particle. The authors showed how the position and rotation of a 1-μm quartz particle could be precisely controlled by varying the external field's polarization. Asymmetric objects also rotate in polarization fields

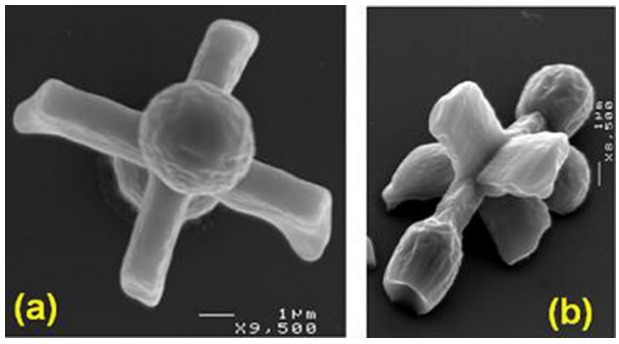

Figure 7 SEM images of a paddle wheel created using two-photon excitation of UV absorbing liquid resins. (Reproduced with permission.[50] 2013, New J. Phys.)

[49]. Asavei et al. [50] microfabricated a paddle wheel, shown in Fig. 7, which could be used in conjunction with a polarized external field to apply controlled fluid flow to specific regions. Many other microfabricated structures have been proposed, and – in some cases – created, to perform specific tasks [51], with an end goal of integrating the fields of micromanipulation and microrobotics.

5. Trapping via integrated optics

Trapping nanoparticles, or submicrometer particles, in subdiffraction-limited regimes can be achieved by using optical near-fields. These can provide high electromagnetic field gradients near dielectric surfaces, opening up attractive avenues of research for optical trapping. Optical near-fields generally take the form of evanescent fields that decay exponentially from their point of origin. The first work that made use of the evanescent fields produced by a dielectric channel waveguide was published in 1996 by Kawata and Tani [52]. Here, the authors used only the evanescent field to propel latex particles of 5.1 μm in diameter along the length of a channeled waveguide at a speed of approximately 5 μm s^{-1} using only 80 mW of input laser power. While the particles propeled were of a relatively large size, it was the first work that highlighted the applicability of evanescent fields to particle trapping. Some of the following applications can be classified as tweezers, since they allow for full 3D confinement of the particle, while others only provide confinement in fewer dimensions.

5.1. Channel waveguides

Evanescent fields that extend beyond the boundary of light-carrying structures become more intense as the dimensions of the waveguide approach the wavelength of the guided light or become smaller [53]. This arises due to the wave nature of light that imposes certain boundary conditions on the structures in which they can exist. Evanescent fields play an indirect role in many plasmonic structures, primarily because they are used to excite SPPs via the Kretschmann configuration (see Section 6.1). However, there are many structures where the evanescent field can be accessed directly to trap particles. The evanescent field from a single beam propagating in an evanescent waveguide provides a gradient force that attracts particles towards the surface, while a simultaneous scattering force is applied in the direction of beam propagation. Hence, single-beam evanescent field traps are useful for guiding particles along the surface of a waveguide, making them ideal for integration with microfluidic systems.

An example of microfluidic/evanescent systems, is described in a paper by Schmidt et al. [54] where they demonstrated how particles could be trapped and propeled using channel waveguides in conjunction with microfluidic channels (Fig. 8). This work provided a clear and concise explanation of the physics at play in optofluidic systems, as well as displaying the trapping and propulsion of particles of varying size. Similarly, Yang and Erickson [55] have analyzed optofluidic particle trapping near waveguides. Building on these works, Ng et al. showed that gold colloidal particles as small as 17 nm could be propeled along a channel waveguide [56]. Using branched channel waveguides, or branched microfluidic channels, other groups have been able to extend these ideas to particle sorting [57, 58]. The attractiveness of these approaches comes from the fact that

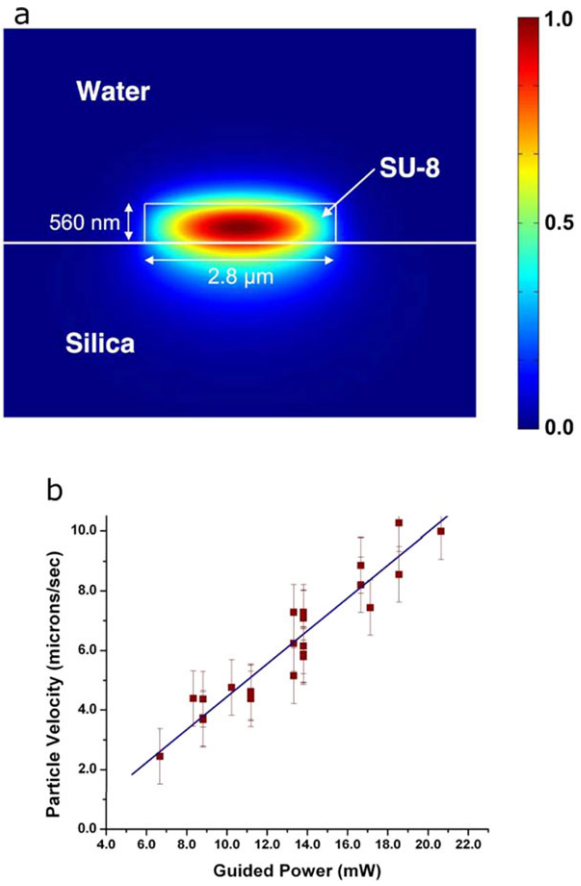

Figure 8 (a) E-field intensity plot of the channel waveguide. (b) Particle velocity versus guided power of a 3 μm particle trapped and propelled along a waveguide. (Reproduced with permission.[54] 2007, Opt. Express)

microfluidic channels and channel waveguides can be run parallel to each other, or even inside each other. Simple waveguides can also be arranged such that they produce resonating structures. Lin et al. [59] showed how microparticles can be trapped above a planar silicon microring resonator with large trapping depths of 25 k_bT.

There is a current trend in scientific research to encourage the development of "lab-on-a-chip" devices. Channel waveguides perfectly fit the requirements of a lab-on-a-chip device as they operate at the correct scale, can be mass produced, and are easily integrated with many existing technologies [60].

5.2. Optical micro- or nanofibers

Optical micro- or nanofibers (MNFs) are optical fibers with micrometer or submicrometer diameters that do not operate in the weakly guided regime. They are sometimes used to trap particles in their evanescent fields [61–64]. MNFs are, generally, manufactured from standard communication-grade optical fibers by heating them until they became malleable, at which point a force is applied from either

side to elongate and taper the heated region until the central (waist) region of the fiber is micrometer or submicrometer in diameter. A more detailed description of this heat-and-pull procedure can be found in the literature [65, 66]. In contrast, channel waveguides typically need to be grown on a substrate that, while allowing for complex geometries to be fabricated, somewhat limits their versatility. For example, some studies in neurobiology require a probe that can reach deep inside tissues in vivo. Very recently, optogenetics has come to the fore in neuroscience, and relies heavily on the use of optical fibers due to their ability to guide light into areas that are inaccessible using other methods [67]. While these techniques do not directly make use of the evanescent field or particle trapping, they emphasize the flexibility that is introduced once one moves from a platform consisting of rigid channel waveguide structures towards the use of tapered fibers. Fiber-based waveguides are capable of trapping and guiding particles as efficiently as their substrate-grown counterparts [62, 68, 69].

The use of a near-field scanning optical microscope to create a fiber optical tweezers (FOT) was realized by Xin et al. [70] and used to reliably trap micrometer-sized particles, but also showed that smaller particles such as yeast, bacteria, and 0.7-μm silica beads could be trapped, albeit with higher laser powers.

To realize a device whose operation is closer to that of optical tweezers, but with only the use of the evanescent fields produced by waveguides, one must consider counterpropagating laser beams [71–73]. Here, a standing wave can be formed that produces a potential landscape that favors the trapping of particles at certain lattice sites defined by the wavelength of light used. In practice, a standing wave is not entirely necessary for successfully immobilizing particles. Lei et al. [74] showed that, by varying the power of two counterpropagating beams, without the formation of a standing wave, particles with a diameter of 710 nm could be transported in either direction along a fiber. This was a useful study as it showed that standing waves are not necessary for the controlled guidance of micro- and nanoparticles along a tapered optical fiber.

Particle sorting using counterpropagating beams of different wavelengths relies on the scattering force's dependence on particle size, refractive index, and the wavelength of light used [75, 76]. Zhang and Li [75] used a subwavelength optical fiber with different wavelengths of light injected at either end (Fig. 9). The difference in scattering for various particle sizes resulted in the particles being sorted by size.

As is the case for optical tweezers, higher-order modes can be used to trap particles in waveguides. MNFs are an ideal platform for this, as they are capable of supporting many higher-order modes [77, 78], including Bessel-beams [79]. Higher-order mode trapping in straight, channel waveguides has been realized [80], but maintaining these modes in tapered fibers has proven to be a difficult process due to the fine degree of control required during the fabrication process, although it has been performed successfully using linearly tapered optical nanofibers [81]. Adiabaticity requirements impose important shape requirements on the taper profile and the dimensions of the fiber at the waist must also be considered. These combined conditions require a more complex tapering system [66] than is usually available to research groups. The use of higher-order modes in fibers for the purposes of atom trapping has been discussed elsewhere [82, 83].

5.3. Slot waveguides

When two waveguides are placed in close proximity to each other, as is the case in slot waveguides, the evanescent fields of the two waveguides overlap, producing a region of increased intensity between them [84]. Yang et al. have published a series of papers [85, 86] where polystyrene and gold particles are trapped in an optofluidic system consisting of a silicon slot waveguide grown on a glass substrate. The small waveguide separation, combined with the overlapping evanescent fields, provides a subdiffraction-limited trapping potential (Fig. 10). The authors were able to trap 75-nm dielectric nanoparticles and λ-DNA molecules using this waveguide system. Lin and Crozier [87] applied this technique to the problem of particle sorting. They used a channel waveguide that ran parallel to a slot waveguide. By introducing a defect, in this case a microsphere that had been fused to the channel waveguide, they were able to 'kick' smaller particles out of the potential formed by the channel waveguide and into the potential generated by the slot waveguide, which had a higher field confinement. Initially, 350-nm and 2-μm particles were guided along the channel waveguide. Upon reaching the defect, the 350-nm particles were pushed more than 250 nm away from the channel waveguide where they were then captured by the potential of the slot waveguide.

The use of evanescent devices to trap and manipulate micro- and nanoparticles continues to be of interest in the scientific community because of their versatility and customizability. Channel waveguide structures can be incorporated into almost any device at the fabrication stage and are produced using common industrial techniques. This makes their potential uses in commercial products more likely than other, more specialized, devices that are produced by nonscalable, multistage techniques.

5.4. Photonic crystal cavities

With the goal of confining light to subdiffraction-limited sizes, many research groups have focused their interest on photonic crystal (PC) cavities. Photonic crystal structures consist of a waveguide which has been periodically patterned to forbid the transmission of specific wavelengths. If, however, one introduces a defect to this periodic lattice it is possible to create a region where frequencies that were previously forbidden are now allowed to propagate. By choosing the defect carefully, a cavity can be set up within the crystal structure [88, 89]. If the wave vector of this new cavity mode is chosen so that it is also a confined mode of the waveguide, both lateral and inplane confinement is possible [90]. Photonic crystal cavities have some interesting

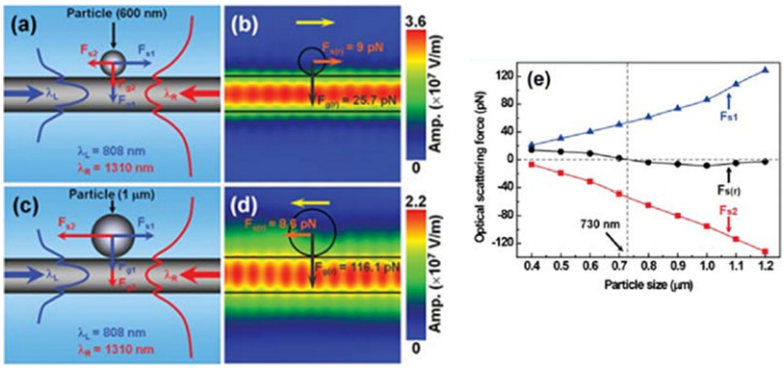

Figure 9 (a-d) Visualisation of the difference in the forces applied to 600 nm and 1000 nm diameter particles due to two different wavelengths counter-propagating along a tapered optical fibre. (b) and (d) are simulation results corresponding to (a) and (c) respectively. (e) A graph of the optical scattering forces on different particle sizes due to different wavelengths. Here, the blue line is the scattering from 808 nm light while the red line shows the scattering from the 1310 nm light, finally, the black line shows the contribution of both fields to the total scattering force acting on the particle. (Reproduced with permission.[75] 2013, Laser Photon. Rev.)

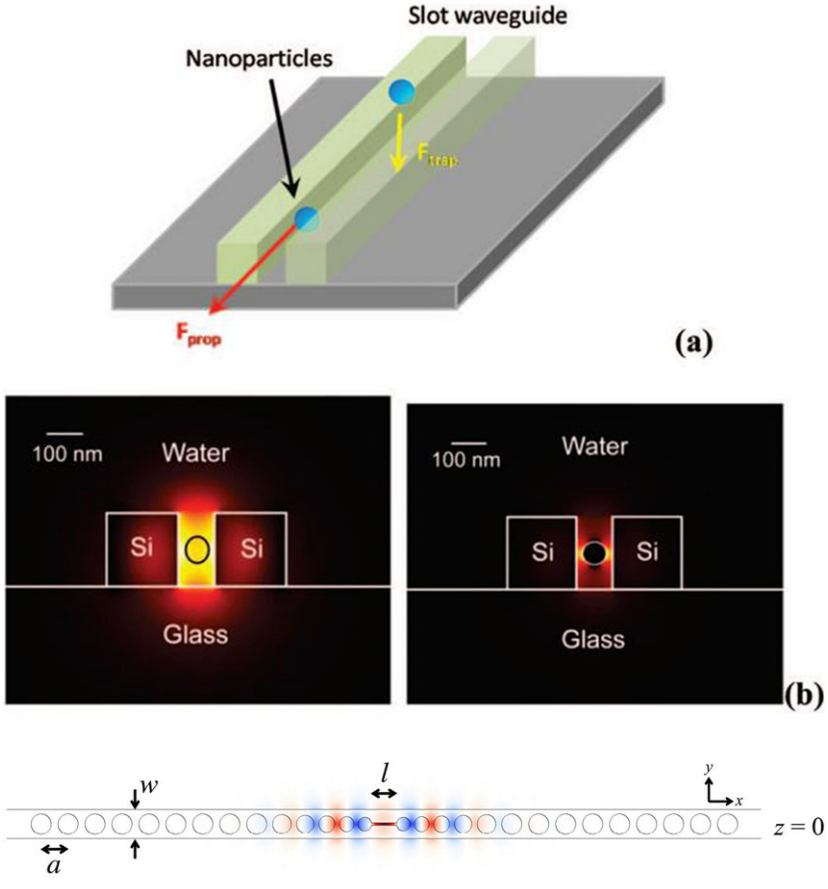

Figure 10 (a) Slot waveguide, (b) electric field intensity profiles for 65 nm polystyrene particles (left), and 100 nm gold particles (right). (Reproduced with permission.[85] 2009, Nano Lett.)

Figure 11 A typical linear photonic crystal cavity showing the field enhancement in the central slotted region. (Reproduced with permission.[90] 2013, Opt. Express)

properties that are advantageous for trapping particles. Robinson et al. [91] showed that the modes present in such structures have "ultrasmall" mode volumes. This leads to extremely high field gradients over subwavelength dimensions; the confinement of the electric field is comparable to the defect size used to create the cavity. A typical PC cavity is shown in Fig. 11.

Particle trapping using photonic crystal cavities was shown to be theoretically possible by Barth and Benson in 2006 [92]. They concluded that, not only could particles of varying sizes be trapped with a PC cavity, but the presence of the particles could shift the cavity resonance, a process known as self-induced back action (SIBA) which is discussed in more detail in Section 6.3. PC cavity devices have distinct advantages over other evanescent field-based devices. For example, Lin et al. [93] showed theoretically that, by tapering the angle of a PC cavity and including a slot, the gradient force could be significantly improved over that given by a waveguide alone, and that a high quality (Q) factor can be maintained.

By tapering a PC cavity, as shown in Fig. 12, an interesting method of controlling a particle's position was achieved [94]. The angle with which such a device is tapered controls the distance along the z-axis at which different wavelengths are reflected. This, in turn, produces trapping potentials at different locations depending on the

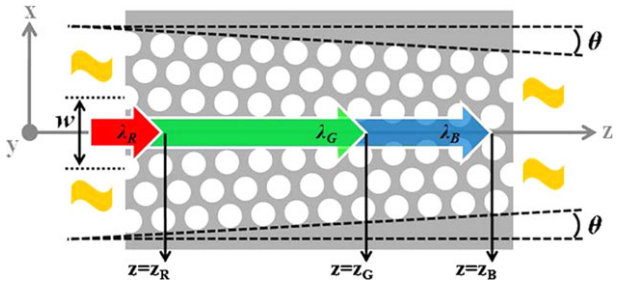

Figure 12 Tapered photonic crystal cavity. z_R, z_G, and z_B are the locations where light of three different colours — red, green, and blue — are reflected. (Reproduced with permission.[94] 2011, Opt. Lett.)

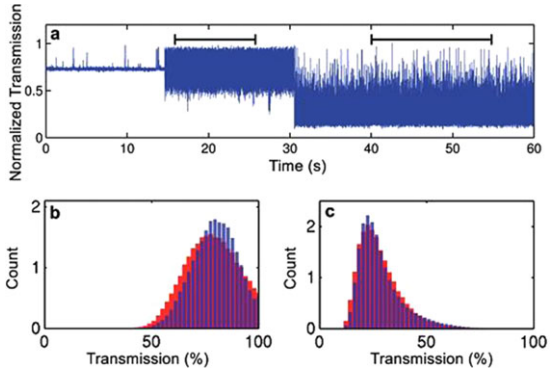

Figure 13 (a) Normalized transmission of the PC cavity system. (b) and (c) are histograms of the data highlighted with the horizontal bars at the left and right of (a) respectively. The histograms of the time series data (red) are given alongside the simulated histogram data (blue). Simulations were performed with a mean particle diameter of 24.8 nm (b) and 30 nm (c). (Reproduced with permission.[100] 2014, Nano Lett.)

frequency of the laser light. Using a tuneable laser source, particles can be moved along the axis of a PC cavity waveguide by gradually varying the wavelength and allowing the trapped particle to follow the changing trap position. Some uncertainity in the particle's position is introduced since the potentials created have multiple minima. However, input powers of 7 mW could, theoretically, trap 50-nm particles stably. PC cavities have also been integrated into optical fibers via femtosecond laser ablation processes, as well as composite systems comprising of MNFs in optical contact with external nanostructured gratings [95, 96]. PC cavities offer an effective way of trapping dielectric particles. Recently, van Leest and Caro [97] were able to stably trap single bacteria of two different species with an inplane trap stiffness of 7.6 pN nm^{-1} mW^{-1}.

Surface traps have also been formed using photonic crystal structures that do not rely on the introduction of a defect. For example, Jaquay et al. [98] used a photonic-crystal structure where the light was incident perpendicular to the apertures. This produced a lattice potential that caused particles to congregate and form large self-assembled arrays, a process that they referred to as light-assisted self-assembly (LATS) [99]. Work performed by Mirsadeghi and Young [100] using PC cavities have shown that they are a useful tool for trapping nanoscale particles and providing a means by which the size of the trapped particle can be determined with nm precision. By introducing a single-mode channel to a PC structure, particles as small as 24 nm were trapped. Analysis of the transmission spectra obtained over a number of trapping events was used to determine the mean diameter of the trapped particles by assuming some variance in the particles' polarizabilities, as shown in Fig. 13. As a particle trapping device, PC cavities are promising and their integration into existing technologies makes them an attractive choice for future progress in the trapping of particles.

5.5. Microlenses

Microlenses with diameters greater than the wavelength of light can also be used to trap particles in regular arrays. Zhao et al. [101] used arrays of 22 μm microlenses to trap 3.1-μm polymer particles. The relative ease of operation and reliability of such a macroscopic device makes it of interest for applications in the life sciences where high optical alignment may not be available. More recently, a similar device was made using femtosecond laser ablation [102].

6. Plasmonic-based devices

As particle sizes become smaller, problems associated with gradient force trapping arise. There are two options to enhance trapping at nanometer scales. One can choose to increase the power to further deepen the optical trap, but this is not usually viable as it is advisable to keep powers at a lower level to reduce noise and lessen power-induced damage to the trapped object. This means that one must increase the confinement of the laser light by some other means. Plasmonic structures have come to the fore in this regime.

The effect of surface plasmons on metallic nanostructures of varying designs is being actively pursued for particle trapping [7,103]. Nowadays, many research groups have access to a wide array of lithography techniques, allowing the creation of arbitrarily shaped designs. Furthermore, access to finite-element and FDTD software packages allow researchers to model how light interacts with plasmonic materials, photonic crystals, III-V semiconductors, etc., to a high degree of accuracy. With this arsenal of tools at hand, it is no surprise that the number of publications in the field has been rising rapidly in the last decade.

6.1. Surface plasmon polaritons and localized surface plasmons

Using plasmonic techniques, light can be concentrated to areas that are significantly below the diffraction limit.

Surface plasmons can be considered differently depending on the geometry of the substrate in question as either localized surface plasmons (LSPs), or as propagating surface plasmon polaritons. For brevity we will refer to the latter simply as surface plasmon polaritons (SPPs). Surface plasmons are the result of coherent electron oscillations on a metal's surface. SPPs are a means of quantifying how they behave on larger metallic surfaces that are capable of supporting propagating plasmon waves. SPPs cannot be directly excited with laser light since they exist as a wave propagating along the dielectric surface interface and their dispersion curves prohibit direct phase matching with an incident laser beam. Instead, they must be excited by an evanescent field. Currently, the most popular method of coupling to SPPs is called the Kretschmann configuration. This configuration makes use of total internal reflection through a glass prism. The required plasmonic structure need only be placed on one face of the prism, thus enabling it to be excited by the evanescent field generated by the reflection of the incident light passed through the prism at the critical angle. LSPs, on the other hand, define how surface plasmons behave on smaller surfaces where the boundary conditions cause confinement of the surface plasmon. LSPs are present in nanoparticles and wavelength-scale plasmonic geometries. Due to spatial confinement, phase matching is relaxed and, therefore, only light matching the correct LSP resonance frequency is required to excite them in a material. SPPs have a wide frequency range over which they can be excited, which is not the case for LSPs.

The form of an SPP is dictated largely by the geometry of the substrate and the input light field. That is not to say they are the only factors; of course, refractive indices and other material properties are important. A recent paper by Tsai et al. [44] showed how an SPP with a topological charge of 2, that is to say an SPP that contains orbital angular momentum, could be produced by using circularly polarized light in combination with a unique surface geometry. By etching an Archimedes spiral into a gold film, they were able to both confine a particle, and impart angular momentum to the particle, thereby causing it to rotate.

Heating due to inevitable ohmic losses in the metal is an intrinsic property of plasmonic devices, especially when devices based predominantly on the excitation of LSP modes are considered. The interaction between laser light and nanoparticles causes the generation of point-like heat sources at locations that depend on factors, such as particle type, beam polarization, and angle of incidence. Intense light fields generated near plasmonic nanostructures are often used to trap particles [104–106]. In some cases, the heat generated by the structures themselves was used to trap particles [107]. Because of this, analyzing heating effects is important. Donner et al. [108] discussed how the plasmon-assisted optofluidics is influenced by the heat produced. In short, this paper concluded that, for isolated nanostructures below 200 nm, the influence of heating is negligible. The authors also state that, to increase the plasmon-assisted fluid motion from tens of nanometers to hundreds of nanometers, structures larger than 1 μm must be used. Larger structures are easily integrated with heat sinks to help quickly dissipate the accumulated heat [109].

A recent study by Roxworthy et al. [110] on the heating effects of a 9×9 array of gold BNAs (bowtie nanoantenna apertures) in a SiO_2/ITO substrate has shown that heat-induced convection currents of greater that 1 μm s^{-1} can be created. The study gives both theoretical and experimental results that are quantitatively in agreement with each other. Seol et al. [111] showed that heating involved with the trapping of gold nanoparticles can also affect the spring constant of an optical trapping system. Because of this heating, they concluded that gold nanoparticles are not recommended when working with biological systems. Despite this, other authors have performed experiments with gold nanoparticles which seem to be in contradiction. For example, Demergis et al. showed ultrastrong binding of metallic nanoparticles via the optical binding force and estimated that there was no heating, contrary to other reported studies on similar systems [112].

6.2. Scalability

Surface plasmon polaritons on metallic surfaces sufficiently larger than the plasmon wavelength can be characterized as SPPs. Under these conditions, it can be assumed that the dispersion curve of the structure approaches that of an infinite metallic film [113]. This relationship is important as it shows that plasmonic-based devices cannot be scaled down ad infinitum. Devices that may work well at a few micrometers cannot be expected to work analogously at the nanometer scale. For example, in an experiment performed by Wong et al. [113], a dielectric channel optical waveguide was integrated with an array of gold micropads of 5 μm diameter and with a pitch of 15 μm. Figure 14 shows a schematic of the system. The authors trapped 5-μm polystyrene beads and yeast cells using an input beam power of 20 mW. This technique works well and relies on the formation of SPPs to create adequate trapping potentials above the discs. A similar paper by Righini et al. [114], where a prism was used to excite the SPPs, showed similar results. It should be obvious that simply downscaling the dimensions will not yield the same results. First, the plasmon will cease to be describable as a SPP once the pad size is reduced sufficiently in size, behaving instead as an LSP, and secondly, the viscous damping of suspended particles is greatly reduced due to the decreased cross section of smaller nanoparticles.

Gold nanopads were used by Chen et al. [115] to trap 500 nm and 100 nm nanoparticles using the LSPs generated in subwavelength disk structures. A seven by seven array of four gold circular nanopads was patterned on an indium titanium oxide substrate and illuminated by a Gaussian beam (Fig. 15). The nanopads were 200 nm in diameter, which produced polarization-dependent LSPs. This work was inspired by the earlier work in [41] and produced a similar washboard-type potential, thus drawing particles towards the center of the plasmonic structure.

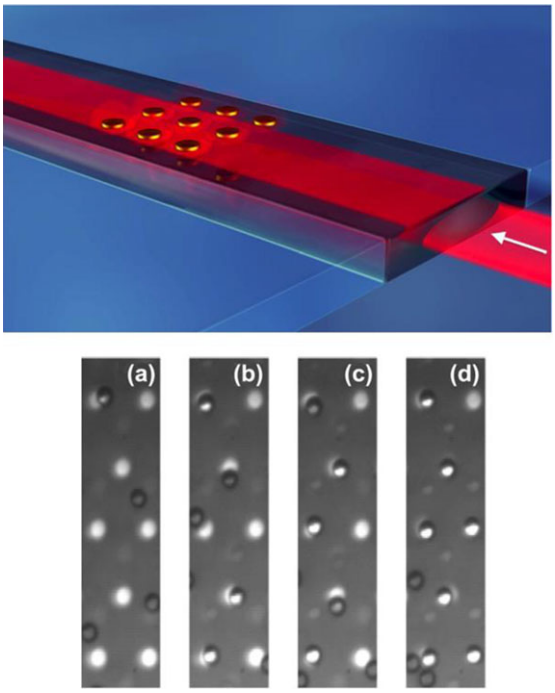

Figure 14 Channel waveguide incorporating a plasmonic gold micropad array. (a) – (d) are a time sequence of images showing the parallel trapping of 5 μm polystyrene beads. (Reproduced with permission.[113] 2011, Appl. Phys. Lett.)

6.3. Self-induced back action

Often, calculations on the trapping capabilities of optical tweezers are done in the absence of any particles. In many cases this is an appropriate choice, as it both simplifies the physics, from a computational viewpoint, and gives quantitatively accurate results. However, as particle sizes become smaller, and lower optical powers are used, it is necessary to include the effect of the dielectric particle on the local electric field, especially when plasmonic effects are present. The effect of a single particle tends to improve certain types of optical trapping via a mechanism called self-induced back action (SIBA). This effect has been studied in various systems, such as plasmonic and photonic crystal cavity systems, as mentioned earlier [116].

SIBA is especially relevant in many plasmonic structures as the effect plays a large role at the scales typically used. Juan et al. [116] trapped 50-nm nanoparticles using 2 mW of power with the help of SIBA. By cutting a 310-nm circular aperture into a 100-nm thick gold film a near-field was generated, which, in the presence of a dielectric particle, created a system that was sensitive to small position variations (Fig. 16). The particle present in the vicinity of the aperture effectively 'saw' a larger hole due to the shifting of the cutoff wavelength, thereby causing higher transmission of light through the aperture. Deviations of the particle from the equilibrium position near the aperture either increased or decreased the net transmission of light through the aperture. The authors showed that the particle's

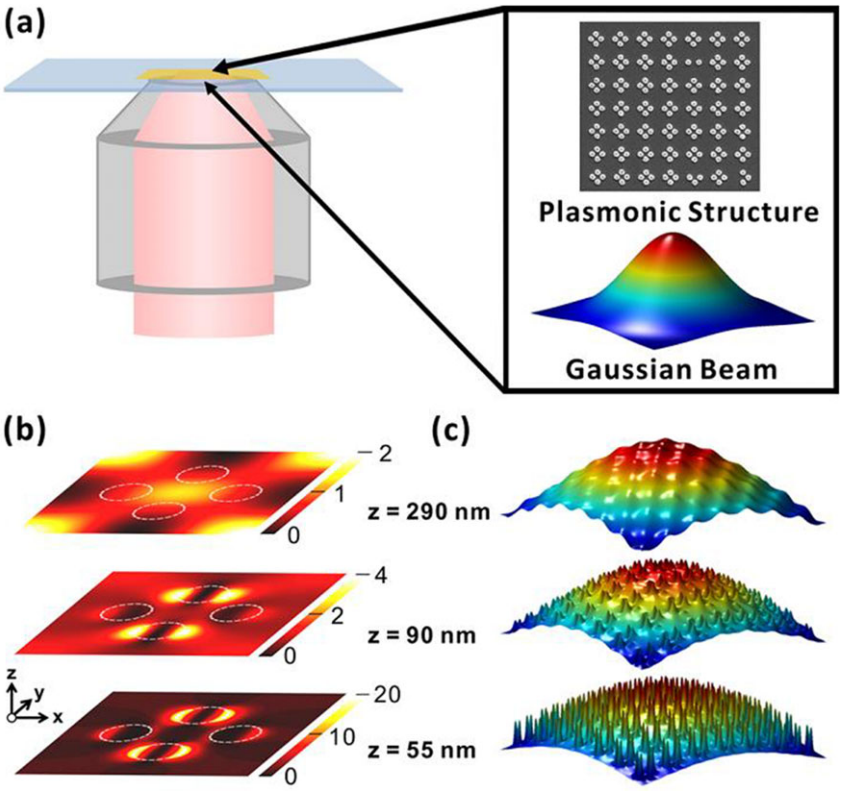

Figure 15 (a) Plasmonic disk array placed on an objective lens. (b) Light intensity at various heights above the disks. (c) Visualisation of the intensity profile at varying heights. (Reproduced with permission.[115] 2013, Nano Lett.)

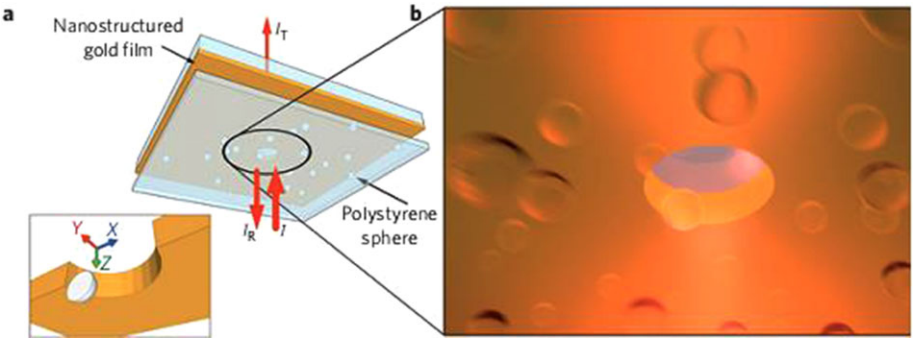

Figure 16 (a) An image showing the structure used to examine self-induced back action. (b) A closer view of the nanohole in the gold substrate. (Reproduced with permission.[116] 2009, Nat. Phys.)

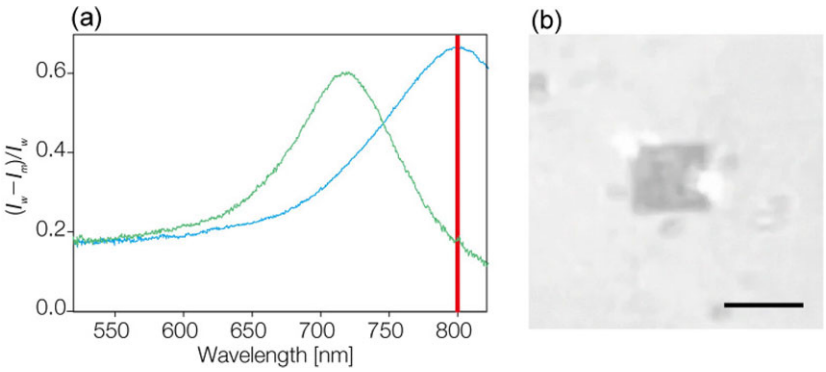

Figure 17 (a) Extinction spectra of a pair of gold nanoblocks with longitudinal (blue) and transverse (green) polarisations. (b) Plasmonic trapping of a 350 nm particle (bright region) using 80 nm $\times$ 80 nm $\times$ 40 nm nanoblocks as the polarisation is shifted between longitudinal and transverse. Scale bar $= 3$ μm. (Reproduced with permission.[117] 2011, Opt. Express)

motion always served to create a force that pushed the particle back to its equilibrium position.

6.4. Superresolution optical trapping

Localized surface plasmons can be used for enhanced trapping well below the diffraction limit. Tanaka et al. referred to this ability as superresolution optical trapping [117]. Their plasmonic structure consisted of only two square gold nanoblocks, as shown in Fig. 17. This paper is indicative of this subfield of plasmonic trapping, in so much as how it highlights the importance of the choice of polarization in LSPs. Two important cases are considered, one parallel to the axis joining the two squares, and one at 90° to this. The two cases highlight the fact that the device has various available modes and, by changing the polarization, specific modes can be excitied individually. The first configuration creates a single high-intensity spot between the two squares, whereas the latter allows for the creation of multiple trapping potentials with a subdiffraction-limit separation. Using gold nanoblocks the authors succeeded in trapping 100-nm polystyrene particles and observed double well potentials with 230 nm separation.

Gold bowtie nanoantenna apertures (BNAs) such as those created by Roxworthy and Toussaint [104] allow for trapping using LSPs (Fig. 18). They created an array of BNAs and, instead of using a standard continuous-wave (CW) laser source, they used a pulsed femtosecond (fs) laser source to trap dielectric and metallic particles. They observed increased trap stiffness over a CW approach while providing the ability to observe nonlinear effects in situ, such as two-photon absorption, second-harmonic generation, etc. The BNA arrays, however, coupled with the fs laser source, caused some of the spheres to adhere to the surface. The effect did not seem to be caused by the melting of the spheres, since the heat generated was not sufficient for this to occur. Rather, the induced heating seemed to attract particles to the BNA surfaces. The authors acknowledged that a theoretical model for optical tweezing using fs laser sources did not yet exist and did not attempt to explain the dynamics of the interaction in such a way. The increased trap stiffness was attributed to the illumination spot size of the laser source. Many BNAs were illuminated at once allowing particles to 'see' the effect of multiple traps, which, in turn, caused the particle's motion within the trap to be describable as acting with an effective trap stiffness with multiple contributions. Once again, fs laser sources are an interesting choice since they have the potential to reduce the overall power transferred to the trapped particles. In this experiment the power levels were three orders of magnitude lower than the optical damage threshold, as reported in [118].

Particles with a high polarizability are good for optical trapping, especially if a high refractive-index contrast between them and the surrounding material can be obtained. J-aggregrates, or Jelley aggregrates to give them their full name, were discovered independently by Scheibe et al. [119], and Jelley in 1937 [120]. J-aggregrates are essentially dye clusters with an absorption band that can be shifted. Zamecnik et al. [121] showed that by functionalizing these

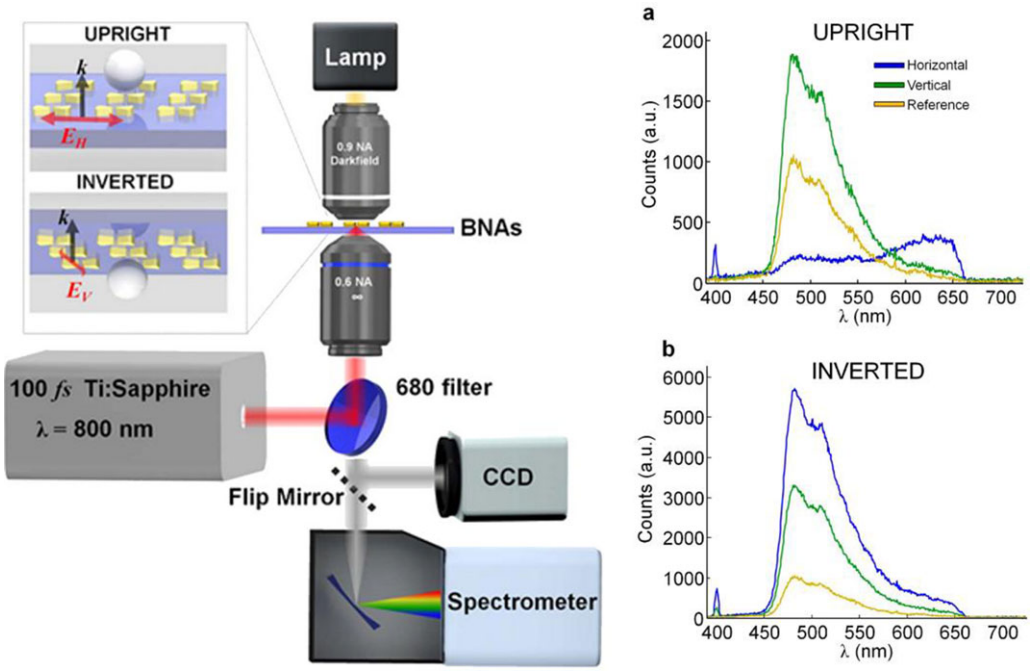

Figure 18 Au bowtie nanoantenna arrays in upright and inverted configuration and the associated experimental setup. Two-photon fluorescence measurements from a trapped fluorescent microsphere are given in (a) the upright orientation and (b) the inverted orientation. Blue and green curves represent the horizontally and vertically-polarized results, respectively. Yellow is a reference signal from a particle trapped on the glass substrate. (Reproduced with permission.[104] 2012, Scientific Reports)

aggregrates onto plasmonic silver nanoparticles interesting effects could be seen. The authors considered a particular type of material, known as ε near-zero materials (ENZ). This is a branch of materials that has an effective ε value near zero when illuminated at certain wavelengths, thereby significantly enhancing the scattering cross section. The permitivity of a medium, ε, is a measure of how much resistance a medium has to an external electric field, which leads to the electric displacement field encountered in Maxwell's equations. The authors targeted this property by combining silver plasmonic nanoparticles with J-aggregrates. By illuminating the particle near the plasmonic resonant wavelength, the electric field was confined within the J-aggregrate, creating a high field in a tightly confined area. The authors used this effect to perform surface-enchanced Raman spectroscopy. ENZ materials have some promising uses in the field of particle trapping.

6.5. Gratings

Gratings etched onto metallic surfaces allow coupling to SPPs since the additional grating vector of the system allows for mode matching of the SPP to the incident light. As we know, light fields can be combined to produce interesting electric-field configurations, and SPPs, being a form of electromagnetic radiation, behave the same. Genevet et al. [122] showed how placing diffraction gratings on a gold surface can generate a plasmonic bottle beam (Fig. 19). When two 2-dimensional planes with intersecting directions of propagation meet, what is known as a cosine Gaussian beam

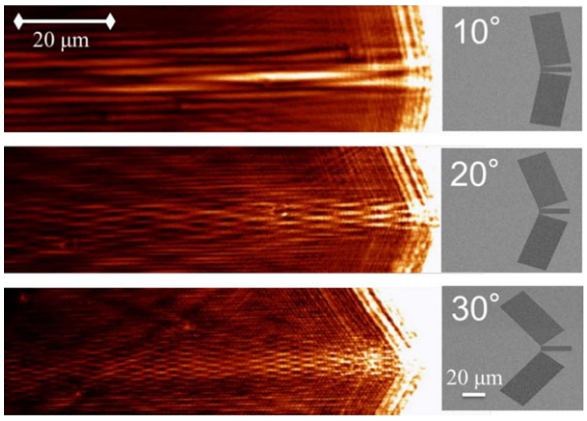

Figure 19 Near-field scanning optical microscopy images of plasmonic bottle beams generated at three different grating configurations. (Reproduced with permission.[122] 2013, Opt. Express)

(CGB) is formed. CGB are similar to Bessel beams since they have a nondiffracting nature in the direction of propagation. The authors applied this theory to SPPs. Using this property they were able to create an intensity profile that could trap particles at the nodes of high intensity.

6.6. Subwavelength apertures

Subwavelength aperture diffraction is, subject to debate, another area where plasmonics may play a role. Previously

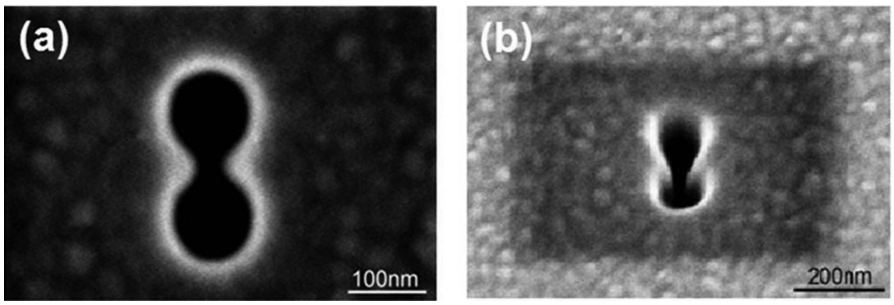

Figure 20 Double-nanohole created using a focussed ion beam in a gold layer. (Reproduced with permission.[126] 2012, Scientific Reports)

accepted theories, such as those by Bethe and Kirchoff, were used to model the propagation of light through apertures in either perfectly conducting screens, or black opaque screens. Given certain conditions these theories worked quite well, but did not provide an adequate explanation of how the light propagated through structures where the dimensions were below the cutoff for any mode to exist. A thorough review of previous and current theories on this type of diffraction is given by Weiner [123]. It was not until 1998 that a theory of plasmon assisted transmission through subwavelength apertures was proposed by Ebbesen et al. [124]. The authors showed that Bethe theory was wholly unsuitable to describe the transmission of light through subwavelength aperture arrays in a silver film. Surpisingly, they showed that transmission increased for wavelengths more than 10 times the diameter of the apertures and, in some cases, more light was transmitted than was directly incident on the apertures. These facts combined indicated that the apertures were more than just passive elements. The authors further showed that the behavior seemed to be independent of hole size and material type, yet had a strong angular dependence that could only be explained by the presence of surface plasmons. While plasmonics may play a role in the transmission through apertures, and for the case of gold materials they most certainly play some part, they are not entirely required to explain the dynamics of light transmission though Bethe apertures and this remains a point of controversy.

Baida and Van Labeke [125] performed work on annular aperture arrays that sought to increase the transmission of light via the same process as described by Ebbesen et al. [124]. Plasmonic double-nanoholes deal with the problem of transmission through subwavelength apertures. A typical double-nanohole is shown in Fig. 20. Using such a system, Zehtabi-Oskuie et al. [126] trapped 20-nm polysterene particles using as little as 3.5 mW of input power. A later analysis of the trapping efficiency was also produced by the same group [127], where they compared the trap stiffnesses obtained for a double-nanohole trap with that of a standard optical tweezers and claimed that similar trap stiffnesses can be obtained, but for particles that are 10 times smaller.

Building on the work by Baida and Van Labeke [125] many groups have pursued coaxial plasmonic waveguide structures for trapping [128–130]. Rodríguez-Fortuno et al. [128] predicted that coaxial plasmonic structures arranged in an array could be used as a negative refractive index material, a property that may be used to produce backwards travelling electromagnetic waves. Highly hybridized structures, such as the device proposed by Liu et al. [129], which combines gold annular aperture arrays with a photoresponsive liquid crystal, can also produce high field gradients in subdiffraction-limited regimes. All of these studies point towards a highly tuneable technique that has promising applications in particle trapping. Saleh and Dionne [131] published a theoretical paper where a gold coaxial plasmonic aperture in a silica fiber could be used to trap particles with sizes less than 10 nm. They also showed that the creation of dual trapping potentials at a distance of 20 nm from the surface is possible.

Subwavelength apertures in gold films can also be used in combination with tapered fibers. For instance, Neumann et al. [132] proposed the use of tapered optical fibers with subwavelength apertures to allow the high transmission of light to subdiffraction-limited spaces. The end face of a near-field scanning optical microscope (NSOM) probe was coated with gold and a focused ion beam was used to etch a 45-nm aperture into the gold layer. The NSOM taper was chosen such that it was near the cut-off diameter for the first excited mode, which was shown to be the case using numerical simulations. A more indepth discussion of the transmission mechanism has been published by Gordon [133]. He showed that transmission through the NSOM was improved by two orders of magnitude. Later, Berthelot et al. expanded on this idea by including a bowtie nanoaperture to the end face of a tapered optical fiber to allow three-dimensional manipulation of 50 nm dielectric objects (Fig. 21) [134]. The fields produced at the output of a half-tapered fiber, similar to an NSOM taper, are also capable of lensing light sufficiently to trap particles without any enhancements from plasmonic apertures.

7. Conclusion and outlook

In this review we have shown how the focus of particle trapping has recently been shifting from the micro- to the nanoscale by highlighting work in the field of optical manipulation, beginning with standard free-space beam-based optical tweezers and ending with more contemporary developments in the field of near-field optical trapping with special importance placed on those methods that circumvent the diffraction limit. It is clear that optical near-fields,

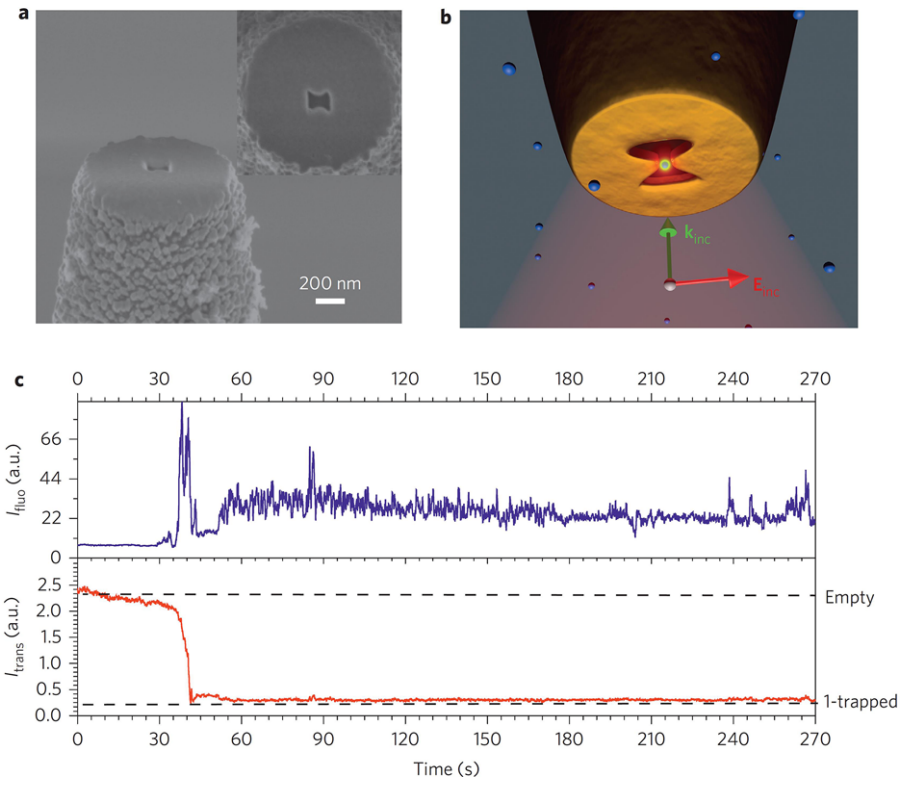

Figure 21 SEM image, (a), and schematic, (b), of an NSOM tip with a bowtie nanoantenna aperture located in the gold layer at the apex. (c) Time series of blue fluorescence from a dyedoped bead (blue line) along with the trapping beam intensity (red). A trapping event occurs at 40 s. (Reproduced with permission.[134] 2014, Nat. Nano)

in all of their forms, are the best solutions for overcoming this problem

Optical near-fields formed at dielectric-cladding interfaces in the form of evanescent fields present a potential path to nanoscale trapping, but, as has been shown, in order to generate the high confinement and required electric fields, simple waveguiding structures, such as ridge waveguides or MNFs, are insufficient. Enhancement of the fields, either through structural modifications, such as photonic crystal cavities, or the addition of plasmonic structures, is necessary to allow submicrometer trapping and manipulation.

The discovery of surface plasmons has arguably provided researchers with one of the most powerful tools to efficiently deal with the problem of trapping at the nanoscale. The low power requirements, high local field enhancements, and flexibility of design have been shown to provide many alternative methods for trapping nanoparticles. An end goal of this line of research is to provide life scientists with full 3D control over minute particles and further developments of the ideas and strategies presented in this paper may ultimately lead to devices that can operate well in the nanoscale regime. If a technique is developed that provides us with the ability to work in the nanoregime with the same degree of control as conventional optical tweezers provide in the microregime this will prove to be a huge boon to the scientific community at large.

Acknowledgements. This work was supported in part by funding from the Okinawa Institute of Science and Technology Graduate University. MS acknowledges the support of JSPS through the Postdoctoral Fellowship for Overseas Researchers scheme.

Received: 6 January 2015, **Revised:** 24 February 2015,
Accepted: 12 March 2015

Published online: 15 April 2015

Key words: Optical trapping, optical tweezers, integrated optics, plasmonics.

References

[1] J. Kepler, De cometis libelli tres : I. Astronomicvs, theoremata continens de motu cometarum ubi demonstratio apparentiarum & altitudinis cometarum qui annis 1607. & 1618. conspecti sunt, ... : II. Physicvs, continens physiologiam comentarum nouam ... : III. Astrologicvs, de significationibus cometarum annorum 1607 and 1618 (typis Andreae Apergeri, sumptibus Sebastiani Mylii bibliopolæ augustani, Avgvstae Vindelicorum, 1619).
[2] J. H. Poynting, Nature **75**, 90 (1906).
[3] T. H. Maiman, Nature **187**, 493–494 (1960).
[4] A. Ashkin, J. M. Dziedzic, J. E. Bjorkholm, and S. Chu, Opt. Lett. **11**, 288–290 (1986).
[5] A. Ashkin, Phys. Rev. Lett. **24**, 156–159 (1970).
[6] J. B. Pendry, Phys. Rev. Lett. **85**, 3966–3969 (2000).
[7] M. L. Juan, M. Righini, and R. Quidant, Nature Photon. **5**, 349–356 (2011).
[8] R. Quidant and C. Girard, Laser Photon. Rev. **2**, 47–57 (2008).

[9] P. C. Ashok and K. Dholakia, Curr. Opin. Biotechnol. **23**, 16–21 (2012).
[10] F. M. Fazal and S. M. Block, Nature Photon. **5**, 318–321 (2011).
[11] M. P. Lee and M. J. Padgett, J. Microsc. **248**, 219–222 (2012).
[12] M. Waleed, S.-U. Hwang, J.-D. Kim, I. Shabbir, S.-M. Shin, and Y.-G. Lee, Biomed. Opt. Exp. **4**, 1533–1547 (2013).
[13] K. Svoboda, C. F. Schmidt, B. J. Schnapp, and S. M. Block, Nature **365**, 721–727 (1993).
[14] E. A. Abbondanzieri, W. J. Greenleaf, J. W. Shaevitz, R. Landick, and S. M. Block, Nature **438**, 460–465 (2005).
[15] N. Mortezaei, B. Singh, E. Bullitt, B. E. Uhlin, and M. Andersson, Sci. Rep. **3**, 3393 (2013).
[16] S. Lee and S. Hohng, J. Am. Chem. Soc. **135**, 18260–18263 (2013).
[17] I. Heller, G. Sitters, O. D. Broekmans, G. Farge, C. Menges, W. Wende, S. W. Hell, E. J. G. Peterman, and G. J. L. Wuite, Nature Meth. **10**, 910–916 (2013).
[18] R. Dasgupta, S. Ahlawat, R. S. Verma, and P. K. Gupta, Opt. Exp. **19**, 7680–7688 (2011).
[19] D. V. Petrov, J. Opt. A: Pure Appl. Opt. **9**, S139 (2007).
[20] I. Amato, Cell **123**, 967–970 (2005).
[21] H. Maruyama, K. Kotani, A. Honda, T. Takahata, and F. Arai, presented at the 10th IEEE Conference on Nanotechnology (IEEE-NANO), 2010 (unpublished).
[22] A. Ashkin, Phys. Rev. Lett. **40**, 729–732 (1978).
[23] S. Albaladejo, M. I. Marqués, M. Laroche, and J. J. Sáenz, Phys. Rev. Lett. **102**, 113602 (2009).
[24] H. C. van de Hulst, Quart. J. Roy. Meteorolog. Soc. **84**, 198–199 (1958).
[25] K.-N. Liou, Appl. Math. Comput. **3**, 331–358 (1977).
[26] A. B. Stilgoe, T. A. Nieminen, G. Knöner, N. R. Heckenberg, and H. Rubinsztein-Dunlop, Opt. Exp. **16**, 15039–15051 (2008).
[27] G. P. Krishnan and D. T. Leighton, Phys. Fluids **7**, 2538–2545 (1995).
[28] A. J. Goldman, R. G. Cox, and H. Brenner, Chem. Eng. Sci. **22**, 637–651 (1967).
[29] K. Visscher, G.J. Brakenhoff, and J. J. Krol, Cytometry **14**, 105–114 (1993).
[30] M. Padgett and R. Di Leonardo, Lab Chip **11**, 1196–1205 (2011).
[31] R. W. Bowman, G. M. Gibson, A. Linnenberger, D. B. Phillips, J. A. Grieve, D. M. Carberry, S. Serati, M. J. Miles, and M. J. Padgett, Comput. Phys. Commun. **185**, 268–273 (2014).
[32] B. Agate, C. Brown, W. Sibbett, and K. Dholakia, Opt. Exp. **12**, 3011–3017 (2004).
[33] K. Svoboda and S. M. Block, Annu. Rev. Biophys. Biomol. Struct. **23**, 247–285 (1994).
[34] Y. Deng, J. Bechhoefer, and N. R. Forde, J. Opt. A: Pure Appl. Opt. **9**, S256–S263 (2007).
[35] B. Lukić, S. Jeney, C. Tischer, A. J. Kulik, L. Forró, and E. L. Florin, Phys. Rev. Lett. **95**, 160601 (2005).
[36] K. Berg-Sørensen and H. Flyvbjerg, Rev. Sci. Instrum. **75**, 594–612 (2004).
[37] A. Balijepalli, J. J. Gorman, S. K. Gupta, and T. W. LeBrun, Nano Lett. **12**, 2347–2351 (2012).
[38] J. R. Moffitt, Y. R. Chemla, D. Izhaky, and C. Bustamante, Proc. Natl. Acad. Sci. **103**, 9006–9011 (2006).
[39] H. Sahoo, J. Photoch. Photobio. C **12**, 20–30 (2011).
[40] M. Woerdemann, C. Alpmann, M. Esseling, and C. Denz, Laser Photon. Rev. **7**, 839–854 (2013).
[41] S. A. Tatarkova, W. Sibbett, and K. Dholakia, Phys. Rev. Lett. **91**, 038101 (2003).
[42] M. Padgett and R. Bowman, Nature Photon. **5**, 343–348 (2011).
[43] L. Allen, M. W. Beijersbergen, R. J. C. Spreeuw, and J. P. Woerdman, Phys. Rev. A **45**, 8185–8189 (1992).
[44] W.-Y. Tsai, J.-S. Huang, and C.-B. Huang, Nano Lett. **14**, 547–552 (2014).
[45] T. Cizmar, V. Garcés-Chávez, K. Dholakia, and P. Zemanek, Appl. Phys. Lett. **86** 174101 (2005).
[46] G. Carmon and M. Feingold, Opt. Lett. **36**, 40–42 (2011).
[47] F. Borghese, P. Denti, R. Saija, M. A. Iatì, and O. M. Maragò, Phys. Rev. Lett. **100**, 163903 (2008).
[48] A. La Porta and M. D. Wang, Phys. Rev. Lett. **92**, 190801 (2004).
[49] S. H. Simpson, D. C. Benito, and S. Hanna, Phys. Rev. A **76**, 043408 (2007).
[50] T. Asavei, T. A. Nieminen, V. L. Y. Loke, A. B. Stilgoe, R. Bowman, D. Preece, M. J. Padgett, N. R. Heckenberg, and H. Rubinsztein-Dunlop, New J. Phys. **15**, 063016 (2013).
[51] D. Palima and J. Glückstad, Laser Photon. Rev. **7**, 478–494 (2013).
[52] S. Kawata and T. Tani, Opt. Lett. **21**, 1768–1770 (1996).
[53] A. W. Snyder and J. Love, Optical Waveguide Theory (Springer, 1983).
[54] B. S. Schmidt, A. H. Yang, D. Erickson, and M. Lipson, Opt. Exp. **15**, 14322–14334 (2007).
[55] A. H. J. Yang and D. Erickson, Nanotechnology **19**, 045704 (2008).
[56] L. N. Ng, B. J. Luff, M. N. Zervas, and J. S. Wilkinson, Opt. Commun. **208**, 117–124 (2002).
[57] K. Grujic, O. G. Hellesø, J. P. Hole, and J. S. Wilkinson, Opt. Exp. **13**, 1–7 (2005).
[58] R. F. Marchington, M. Mazilu, S. Kuriakose, V. Garcés-Chávez, P. J. Reece, T. F. Krauss, M. Gu, and K. Dholakia, Opt. Exp. **16**, 3712–3726 (2008).
[59] S. Lin, E. Schonbrun, and K. Crozier, Nano Lett. **10**, 2408–2411 (2010).
[60] D. Erickson, X. Serey, Y. F. Chen, and S. Mandal, Lab Chip **11**, 995–1009 (2011).
[61] F.-W. Sheu and Y.-S. Huang, Sensors **13**, 2884–2894 (2013).
[62] C. Xu, H. Lei, Y. Zhang, and B. Li, Opt. Exp. **20**, 1930–1938 (2012).
[63] A. Goban, K. S. Choi, D. J. Alton, D. Ding, C. Lacroûte, M. Pototschnig, T. Thiele, N. P. Stern, and H. J. Kimble, Phys. Rev. Lett. **109**, 033603 (2012).
[64] M. Morrissey, K. Deasy, M. Frawley, R. Kumar, E. Prel, L. Russell, V. Truong, and S. Nic Chormaic, Sensors **13**, 10449–10481 (2013).
[65] T. A. Birks and Y. W. Li, J. Lightwave Technol. **10**, 432 (1992).
[66] J. M. Ward, V. H. Le, A. Maimaiti, and S. Nic Chormaic, Rev. Sci. Instrum. **85**, 111501 (2014).
[67] E. Pastrana, Nature Meth. **8**, 24–25 (2011).

[68] G. Brambilla, G. S. Murugan, J. S. Wilkinson, and D. J. Richardson, Opt. Lett. **32**, 3041–3043 (2007).
[69] S. E. Skelton, M. Sergides, R. Patel, E. Karczewska, O. M. Maragó, and P. H. Jones, J. Quant. Spectrosc. Radiat. Transfer **113**, 2512–2520 (2012).
[70] H. Xin, R. Xu, and B. Li, Sci. Rep. **2**, 818 (2012).
[71] C. D. Mellor and C. D. Bain, Chem. Phys. Chem. **7**, 329–332 (2006).
[72] J. Lekner, J. Phys. B: At. Molec. Opt. Phys. **38**, 3849 (2005).
[73] K. Grujic and O. G. Hellesø, Opt. Exp. **15**, 6470–6477 (2007).
[74] H. Lei, C. Xu, Y. Zhang, and B. Li, Nanoscale **4**, 6707–6709 (2012).
[75] Y. Zhang and B. Li, Laser Photon. Rev. **7**, 289–296 (2013).
[76] M. Ploschner, T. Čižmár, M. Mazilu, A. Di Falco, and K. Dholakia, Nano Lett. **12**, 1923–1927 (2012).
[77] A. Petcu-Colan, M. Frawley, and S. Nic Chormaic, J. Nonlinear Opt. Phys. Mater. **20**, 293–307 (2011).
[78] M. Frawley, A. Petcu-Colan, V. G. Truong, and S. Nic Chormaic, Opt. Commun. **285**, 4648 (2012).
[79] T. Cizmar, V. Garcés-Chávez, K. Dholakia, and P. Zemanek, presented at the Proceedings of SPIE Vol. 5514, (2004) (unpublished).
[80] T. Tanaka and S. Yamamoto, Appl. Phys. Lett. **77**, 3131–3133 (2000).
[81] A. Maimaiti, V. G. Truong, M. Sergides, I. Gusachenko, and S. Nic Chormaic, Sci. Rep. **5**, 9077 (2015).
[82] J. Fu, X. Yin, N. Li, and L. Tong, Chin. Opt. Lett. **6**, 112–115 2008.
[83] R. Kumar, V. Gokhroo, K. Deasy, A. Maimaiti, C. Phelan, M. Frawley, and S. Nic Chormaic, New J. Phys. **17**, 013026 (2015).
[84] P. A. Anderson, B. S. Schmidt, and M. Lipson, Opt. Exp. **14**, 9197–9202 (2006).
[85] A. H. J. Yang, T. Lerdsuchatawanich, and D. Erickson, Nano Lett. **9**, 1182–1188 (2009).
[86] A. H. J. Yang, S. D. Moore, B. S. Schmidt, M. Klug, M. Lipson, and D. Erickson, Nature **457**, 71–75 (2009).
[87] S. Lin and K. B. Crozier, Opt. Exp. **20**, 3367–3374 (2012).
[88] B.-S. Song, S. Noda, T. Asano, and Y. Akahane, Nature Mater. **4**, 207–210 (2005).
[89] C. A. Mejia, N. Huang, and M. L. Povinelli, Opt. Lett. **37**, 3690–3692 (2012).
[90] P. Seidler, K. Lister, U. Drechsler, J. Hofrichter, and T. Stöferle, Opt. Exp. **21**, 32468–32483 (2013).
[91] J. T. Robinson, C. Manolatou, L. Chen, and M. Lipson, Phys. Rev. Lett. **95**, 143901 (2005).
[92] M. Barth and O. Benson, Appl. Phys. Lett. **89**, 253114 (2006).
[93] S. Lin, J. Hu, L. Kimerling, and K. Crozier, Opt. Lett. **34**, 3451–3453 (2009).
[94] P.-T. Lin and P.-T. Lee, Opt. Lett. **36**, 424–426 (2011).
[95] K. P. Nayak, P. Zhang, and K. Hakuta, Opt. Lett. **39**, 232–235 (2014).
[96] R. Yalla, M. Sadgrove, K. P. Nayak, and K. Hakuta, Phys. Rev. Lett. **113**, 143601 (2014).
[97] T. van Leest and J. Caro, Lab Chip **13**, 4358–4365 (2013).
[98] E. Jaquay, L. J. Martínez, C. A. Mejia, and M. L. Povinelli, Nano Lett. **13**, 2290–2294 (2013).
[99] C. A. Mejia, A. Dutt, and M. L. Povinelli, Opt. Exp. **19**, 11422–11428 (2011).
[100] S. H. Mirsadeghi and J. F. Young, Nano Lett. **14**, 5004–5009 (2014).
[101] X. Zhao, Y. Sun, J. Bu, S. Zhu, and X. C. Yuan, Appl. Opt. **50**, 318–322 (2011).
[102] J. Yong, F. Chen, Q. Yang, G. Du, H. Bian, D. Zhang, J. Si, F. Yun, and X. Hou, ACS Appl. Mater. Interfaces **5**, 9382–9385 (2013).
[103] R. Quidant, MRS Bull. **37**, 739–744 (2012).
[104] B. J. Roxworthy and K. C. Toussaint, Jr., Sci. Rep. **2**, 660 (2012).
[105] W. Zhang, L. Huang, C. Santschi, and O. J. F. Martin, Nano Lett. **10**, 1006–1011 (2010).
[106] M. Ploschner, M. Mazilu, T. F. Krauss, and K. Dholakia, J. Nanophoton. **4**, 041570 (2010).
[107] C. M. Galloway, M. P. Kreuzer, S. S. Aćimović, G. Volpe, M. Correia, S. B. Petersen, M. T. Neves-Petersen, and R. Quidant, Nano Lett. **13**, 4299–4304 (2013).
[108] J. S. Donner, G. Baffou, D. McCloskey, and R. Quidant, ACS Nano **5**, 5457–5462 (2011).
[109] K. Wang, E. Schonbrun, P. Steinvurzel, and K. B. Crozier, Nature Commun. **2**, 469 (2011).
[110] B. J. Roxworthy, A. M. Bhuiya, S. P. Vanka, and K. C. Toussaint Jr., Nature Commun. **5**, 1713 (2014).
[111] Y. Seol, A. E. Carpenter, and T. T. Perkins, Opt. Lett. **31**, 2429–2431 (2006).
[112] V. Demergis and E.-F. Florin, Nano Lett. **12**, 5756–5760 (2012).
[113] H. M. K. Wong, M. Righini, J. C. Gates, P. G. R. Smith, V. Pruneri, and R. Quidant, Appl. Phys. Lett. **99**, 061107 (2011).
[114] M. Righini, G. Volpe, C. Girard, D. Petrov, and R. Quidant, Phys. Rev. Lett. **100**, 186804 (2008).
[115] K. Y. Chen, A. T. Lee, C. C. Hung, J. S. Huang, and Y. T. Yang, Nano Lett. **13**, 4118–4122 (2013).
[116] M. L. Juan, R. Gordon, Y. Pang, F. Eftekhari, and R. Quidant, Nature Phys. **5**, 915–919 (2009).
[117] Y. Tanaka, and K. Sasaki, Opt. Exp. **19**, 17462–17468 (2011).
[118] M. Righini, P. Ghenuche, S. Cherukulappurath, V. Myroshnychenko, F. J. García de Abajo, and R. Quidant, Nano Lett. **9**, 3387–3391 (2009).
[119] G. Scheibe, L. Kandler, and H. Ecker, Naturwissenschaften **25**, 75–75 (1937).
[120] E. E. Jelley, Nature **139**, 631–632 (1937).
[121] C. R. Zamecnik, A. Ahmed, C. M. Walters, R. Gordon, and G. C. Walker, J. Phys. Chem. C **117**, 1879–1886 (2013).
[122] P. Genevet, J. Dellinger, R. Blanchard, A. She, M. Petit, B. Cluzel, M. A. Kats, F. de Fornel, and F. Capasso, Opt. Exp. **21**, 10295–10300 (2013).
[123] J. Weiner, Rep. Prog. Phys. **72**, 064401 (2009).
[124] T. W. Ebbesen, H. J. Lezec, H. F. Ghaemi, T. Thio, and P. A. Wolff, Nature **391**, 667–669 (1998).
[125] F. I. Baida and D. Van Labeke, Phys. Rev. B: Condens. Matter **67**, 155314 (2003).

[126] A. Zehtabi-Oskuie, J. G. Bergeron, and R. Gordon, Sci. Rep. **2**, 966 (2012).
[127] A. Kotnala and R. Gordon, Nano Lett. **14**, 853–856 (2014).
[128] F. J. Rodríguez-Fortuño, C. García-Meca, R. Ortuño, J. Martí, and A. Martínez, Opt. Lett. **34**, 3325–3327 (2009).
[129] Y. J. Liu, G. Y. Si, E. S. P. Leong, N. Xiang, A. J. Danner, and J. H. Teng, Adv. Mater. **24**, OP131–OP135 (2012).
[130] R. de Waele, S. P. Burgos, A. Polman, and H. A. Atwater, Nano Lett. **9**, 2832–2837 (2009).
[131] A. A. E. Saleh and J. A. Dionne, Nano Lett. **12**, 5581–5586 (2012).
[132] L. Neumann, Y. Pang, A. Houyou, M. L. Juan, R. Gordon, and N. F. van Hulst, Nano Lett. **11**, 355–360 (2010).
[133] R. Gordon, Phys. Rev. A **76**, 053806 (2007).
[134] J. Berthelot, S. S. Acimovic, M. L. Juan, M. P. Kreuzer, J. Renger, and R. Quidant, Nature Nano **9**, 295–299 (2014).

Evanescent field trapping of nanoparticles using nanostructured ultrathin optical fibers

Mark Daly, Viet Giang Truong, and Síle Nic Chormaic*

Light-Matter Interactions Unit, OIST Graduate University, Onna, Okinawa, 904-0495, Japan

*sile.nicchormaic@oist.jp

Abstract: While conventional optical trapping techniques can trap objects with submicron dimensions, the underlying limits imposed by the diffraction of light generally restrict their use to larger or higher refractive index particles. As the index and diameter decrease, the trapping difficulty rapidly increases; hence, the power requirements for stable trapping become so large as to quickly denature the trapped objects in such diffraction-limited systems. Here, we present an evanescent field-based device capable of confining low index nanoscale particles using modest optical powers as low as 1.2 mW, with additional applications in the field of cold atom trapping. Our experiment uses a nanostructured optical micro-nanofiber to trap 200 nm, low index contrast, fluorescent particles within the structured region, thereby overcoming diffraction limitations. We analyze the trapping potential of this device both experimentally and theoretically, and show how strong optical traps are achieved with low input powers.

OCIS codes: (140.7010) Laser trapping; (060.2310) Fiber optics; (220.4241) Nanostructure fabrication.

References and links

1. J. Kepler, *De cometis libelli tres.* (1619).
2. A. Ashkin, "Trapping of atoms by resonance radiation pressure," Phys. Rev. Lett. **40**, 729–732 (1978).
3. A. Ashkin, J. M. Dziedzic, J. E. Bjorkholm, and S. Chu, "Observation of a single-beam gradient force optical trap for dielectric particles," Opt. Lett. **11**, 288–290 (1986).
4. O. M. Maragó, P. H. Jones, P. G. Gucciardi, G. Volpe, and A. C. Ferrari, "Optical trapping and manipulation of nanostructures," Nature Nanotech. **8**, 807–819 (2013).
5. M. Daly, M. Sergides, and S. Nic Chormaic, "Optical trapping and manipulation of micrometer and submicrometer particles," Laser Photon. Rev. **9**, 309–329 (2015).
6. B.-S. Song, S. Noda, T. Asano, and Y. Akahane, "Ultra-high-q photonic double-heterostructure nanocavity," Nature Mat. **4**, 207–210 (2005).
7. P. Jing, J. Wu, G. W. Liu, E. G. Keeler, S. H. Pun, and L. Y. Lin, "Photonic crystal optical tweezers with high efficiency for live biological samples and viability characterization," Sci. Rep. **6**, 19924 (2016).
8. A. Zehtabi-Oskuie, J. G. Bergeron, and R. Gordon, "Flow-dependent double-nanohole optical trapping of 20 nm polystyrene nanospheres," Sci. Rep. **2**, 966 (2012).
9. A. Kotnala and R. Gordon, "Quantification of high-efficiency trapping of nanoparticles in a double nanohole optical tweezer," Nano Lett. **14**, 853–856 (2014).
10. P. A. Anderson, B. S. Schmidt, and M. Lipson, "High confinement in silicon slot waveguides with sharp bends," Opt. Exp. **14**, 9197–9202 (2006).
11. M. Soltani, J. Lin, R. A. Forties, J. T. Inman, S. N. Saraf, R. M. Fulbright, M. Lipson, and M. D. Wang, "Nanophotonic trapping for precise manipulation of biomolecular arrays," Nature Nanotech. **9**, 448–452 (2014).
12. L. Tong, R. R. Gattass, J. B. Ashcom, S. He, J. Lou, M. Shen, I. Maxwell, and E. Mazur, "Subwavelength-diameter silica wires for low-loss optical wave guiding," Nature **426**, 816–819 (2003).

#263072 Received 12 Apr 2016; revised 13 Jun 2016; accepted 14 Jun 2016; published 17 Jun 2016

13. J. Hoffman, S. Ravets, J. Grover, P. Solano, P. Kordell, J. Wong-Campos, L. Orozco, and S. Rolston, "Ultrahigh transmission optical nanofibers," AIP Adv. **4**, 067124 (2014).
14. M. Ploschner, T. Cizmar, M. Mazilu, A. Di Falco, and K. Dholakia, "Bidirectional optical sorting of gold nanoparticles," Nano Lett. **12**, 1923–1927 (2012).
15. O. Brzobohatỳ, M. Šiler, J. Trojek, L. Chvátal, V. Karásek, A. Paták, Z. Pokorná, F. Mika, and P. Zemánek, "Three-dimensional optical trapping of a plasmonic nanoparticle using low numerical aperture optical tweezers," Sci. Rep. **5**, 8106 (2015).
16. M. Geiselmann, M. L. Juan, J. Renger, J. M. Say, L. J. Brown, F. J. G. De Abajo, F. Koppens, and R. Quidant, "Three-dimensional optical manipulation of a single electron spin," Nature Nanotech. **8**, 175–179 (2013).
17. A. Jannasch, A. F. Demirors, P. D. J. van Oostrum, A. van Blaaderen, and E. Schaffer, "Nanonewton optical force trap employing anti-reflection coated, high-refractive-index titania microspheres," Nat Photon **6**, 469–473 (2012). 10.1038/nphoton.2012.140.
18. M. Daly, V. G. Truong, C. Phelan, K. Deasy, and S. Nic Chormaic, "Nanostructured optical nanofibres for atom trapping," New J. Phys. **16**, 053052 (2014).
19. M. Daly, V. G. Truong, and S. Nic Chormaic, "Submicron particle manipulation using slotted tapered optical fibers," in Proceedings of SPIE **9548** Optical Trapping and Optical Micromanipulation XII, (2015), pp. 954812 .
20. M. Daly, V. G. Truong, and S. Nic Chormaic, "Nanostructured tapered optical fibers for particle trapping," in Proceedings of SPIE **9507** Micro-structured and Specialty Optical Fibres IV, (2015), pp. 95070E–95070E6.
21. H. Xin and B. Li, "Targeted delivery and controllable release of nanoparticles using a defect-decorated optical nanofiber," Opt. Exp. **19**, 13285–13290 (2011).
22. A. Maimaiti, V. G. Truong, M. Sergides, I. Gusachenko, and S. Nic Chormaic, "Higher order microfibre modes for dielectric particle trapping and propulsion," Sci. Rep. **5**, 9077 (2015).
23. I. Gusachenko, V. G. Truong, M. C. Frawley, and S. Nic Chormaic, "Optical nanofiber integrated into optical tweezers for in situ fiber probing and optical binding studies," Photonics **2**, 795 (2015).
24. T. Nieddu, V. Gokhroo, and S. Nic Chormaic, "Optical nanofibres and neutral atoms," Journal of Optics **18**, 053001 (2016).
25. S. Skelton, M. Sergides, R. Patel, E. Karczewska, O. Maragó, and P. Jones, "Evanescent wave optical trapping and transport of micro-and nanoparticles on tapered optical fibers," J. Quant Spectrosc. Radiat. Transf. **113**, 2512–2520 (2012).
26. Y. Li, O. V. Svitelskiy, A. V. Maslov, D. Carnegie, E. Rafailov, and V. N. Astratov, "Giant resonant light forces in microspherical photonics," Light: Sci. Appl. **2**, e64 (2013).
27. G. S. Murugan, M. Belal, C. Grivas, M. Ding, J. S. Wilkinson, and G. Brambilla, "An optical fiber optofluidic particle aspirator," Appl. Phys. Lett. **105**, 101103 (2014).
28. M. C. Frawley, I. Gusachenko, V. G. Truong, M. Sergides, and S. Nic Chormaic, "Selective particle trapping and optical binding in the evanescent field of an optical nanofiber," Opt. Exp. **22**, 16322–16334 (2014).
29. C. Cheng, X. Xu, H. Lei, and B. Li, "Plasmon-assisted trapping of nanoparticles using a silver-nanowire-embedded pmma nanofiber," Sci. Rep. **6**, 20433 (2016).
30. R. Yalla, M. Sadgrove, K. P. Nayak, and K. Hakuta, "Cavity quantum electrodynamics on a nanofiber using a composite photonic crystal cavity," Phys. Rev. Lett. **113**, 143601 (2014).
31. J. Knight, G. Cheung, F. Jacques, and T. Birks, "Phase-matched excitation of whispering-gallery-mode resonances by a fiber taper," Opt. Lett. **22**, 1129–1131 (1997).
32. R. Mitsch, C. Sayrin, B. Albrecht, P. Schneeweiss, and A. Rauschenbeutel, "Quantum state-controlled directional spontaneous emission of photons into a nanophotonic waveguide," Nature Commun. **5** (2014).
33. J.-B. Béguin, E. Bookjans, S. Christensen, H. Sørensen, J. Müller, E. Polzik, and J. Appel, "Generation and detection of a sub-poissonian atom number distribution in a one-dimensional optical lattice," Phys. Rev. Lett. **113**, 263603 (2014).
34. S. Kato and T. Aoki, "Strong coupling between a trapped single atom and an all-fiber cavity," Phys. Rev. Lett. **115**, 093603 (2015).
35. R. Kumar, V. Gokhroo, K. Deasy, and S. Nic Chormaic, "Autler-townes splitting via frequency up-conversion at ultralow-power levels in cold rb 87 atoms using an optical nanofiber," Phys. Rev. A **91**, 053842 (2015).
36. A. Watkins, V. B. Tiwari, J. M. Ward, K. Deasy, and S. Nic Chormaic, "Observation of zeeman shift in the rubidium d2 line using an optical nanofiber in vapor," in Proceedings of "8th Ibero American Optics Meeting/11th Latin American Meeting on Optics, Lasers, and Applications," (International Society for Optics and Photonics, 2013), pp. 87850S–87850S.
37. D. Jones, J. Franson, and T. Pittman, "Ladder-type electromagnetically induced transparency using nanofiber-guided light in a warm atomic vapor," Phys. Rev. A **92**, 043806 (2015).
38. H. Xin, R. Xu, and B. Li, "Optical trapping, driving, and arrangement of particles using a tapered fibre probe," Sci. Rep. **2**, 818 (2012).
39. L. Neumann, Y. Pang, A. Houyou, M. L. Juan, R. Gordon, and N. F. van Hulst, "Extraordinary optical transmission brightens near-field fiber probe," Nano Lett. **11**, 355–360 (2010).
40. A. H. Yang, S. D. Moore, B. S. Schmidt, M. Klug, M. Lipson, and D. Erickson, "Optical manipulation of nanoparticles and biomolecules in sub-wavelength slot waveguides," Nature **457**, 71–75 (2009).

#263072 Received 12 Apr 2016; revised 13 Jun 2016; accepted 14 Jun 2016; published 17 Jun 2016

41. M. L. Juan, R. Gordon, Y. Pang, F. Eftekhari, and R. Quidant, "Self-induced back-action optical trapping of dielectric nanoparticles," Nature Phys. **5**, 915–919 (2009).
42. P. Jones, O. Maragó, and G. Volpe, *Optical Tweezers: Principles and Applications* (Cambridge University Press, 2015).
43. T. Ĉižmár, M. Ŝiler, M. Ŝerý, P. Zemánek, V. Garcés-Chávez, and K. Dholakia, "Optical sorting and detection of submicrometer objects in a motional standing wave," Physical Review B **74**, 035105 (2006). PRB.
44. J. Ward, A. Maimaiti, V. H. Le, and S. Nic Chormaic, "Contributed review: Optical micro-and nanofiber pulling rig," Rev. Sci. Instrum. **85**, 111501 (2014).
45. M. Szczurowski, W. Urbanczyk, M. Napiorkowski, P. Hlubina, U. Hollenbach, H. Sieber, and J. Mohr, "Differential Rayleigh scattering method for measurement of polarization and intermodal beat length in optical waveguides and fibers," Appl. Opt. **50**, 2594–2600 (2011).
46. I. Brevik, "Experiments in phenomenological electrodynamics and the electromagnetic energy-momentum tensor," Phys. Rep. **52**, 133–201 (1979).
47. A. van der Horst and N. R. Forde, "Power spectral analysis for optical trap stiffness calibration from high-speed camera position detection with limited bandwidth," Opt. Exp. **18**, 7670–7677 (2010).
48. K. Berg-Sørensen and H. Flyvbjerg, "Power spectrum analysis for optical tweezers," Rev. Sci. Instrum. **75**, 594–612 (2004).
49. É. Roldán, *Irreversibility and Dissipation in Microscopic Systems* (Springer, 2014).
50. R. Kumar, V. Gokhroo, and S. Nic Chormaic, "Multi-level cascaded electromagnetically induced transparency in cold atoms using an optical nanofibre interface," New J. Phys. **17**, 123012 (2015).
51. D. Chang, J. I. Cirac, and H. Kimble, "Self-organization of atoms along a nanophotonic waveguide," Phys. Rev. Lett. **110**, 113606 (2013).

1. Introduction

The concept that light could impart forces to matter can be traced back to early suggestions by Kepler in the 1600s. He observed that the tail of a comet seemed to incongruously point in a direction retrograde to its motion [1]. The tail was seen to point away from the sun and hence the notion of radiation pressure was born. With the advent of coherent light sources, many groups began to make heavy use of optical forces experimentally. For example, Doppler cooling, the precursor to many laser cooling techniques, gave way to the field of atom trapping [2]. Ashkin —often considered to be a pioneer in the field of optical trapping—proposed that Gaussian beams could be used to trap silica microparticles using a technique that would later become known as optical tweezing [3]. At this early stage, it was apparent that optical tweezers had fundamental operational constraints due to the diffraction-limited spot size of the trapping beam. Today, nano-optical techniques, such as near-field optics and plasmonics, provide primary solutions to this problem [4, 5]. Photonic crystal cavities [6, 7], plasmonic double nano-holes [8, 9], slot waveguides [10, 11], and micro-nanofibers [12, 13] are just some of the devices which can confine light locally to regions smaller than achievable using diffraction-limited systems. Aside from modifying how the trapping fields are generated, it is also possible to change the material of the particles to be trapped, thereby reducing the difficulties associated with trapping submicron particles. For example, higher index particles, such as gold nanoparticles [14, 15] are excellent candidates for nanoscale trapping but have associated problems with heat generation. Other high index particles such as nanodiamonds [16] and Titania particles [17] are also easier to trap; however, biologically-relevant materials typically have low refractive indices, thereby negating the trapping advantages associated with higher index particles.

In this article, we discuss a nanostructured, evanescent optical trapping device based on the combination of a slot waveguide with a micro-nanofiber (MNF) [18–20]. MNFs are extremely versatile due to their compact size, enabling them to be integrated noninvasively into many systems, such as optical tweezers [21–23] and cold atom clouds [24]. When light propagates through an MNF, a significant portion of the electric field exists outside the waveguide as an evanescent component, allowing for easy interaction between the guided light field and the surrounding medium. We work with a nanostructured MNF with an overall waist of 1.4 μm guiding light with a wavelength of 980 nm. Previously, unmodified MNFs have been used

#263072 Received 12 Apr 2016; revised 13 Jun 2016; accepted 14 Jun 2016; published 17 Jun 2016

for various experimental configurations such as (i) optical trapping of dielectric particles [25–29], (ii) cavity quantum electrodynamics (cQED) using single quantum emitters [30], (iii) light coupling in and out of whispering gallery resonators [31], and (iv) trapping and probing cold atomic systems [32–35] or atomic vapors [36, 37]. More recently, MNFs have been modified to increase their versatility across a range of fields, through, for example, the incorporation of SNOM tips [38] or extraordinary transmission apertures [39]. Evanescent field trapping has also been realised using what is known as a slot waveguide, as first demonstrated by Yang et al. [40] who trapped 75 nm dielectric nanoparticles. Laser powers of 250-300 mW provided stable trapping against a constant fluid flow. The high refractive index contrast between the Si slot and the surrounding water, along with the small slot separation ($<$100 nm), produced a quasi-TE mode with a large field discontinuity across the boundary that was used for trapping.

While other trapping techniques, such as self-induced back action (SIBA) [41], can confine particles in three dimensions with low optical powers, they lack adequate control over the particle's position. For optical fibers, dynamic three dimensional control over the position of trapped particles becomes difficult, but recent developments using orbital angular momentum carrying beams for particle trapping [42] may soon allow for the spatial translation of particles, whilst still maintaining strong trap stiffnesses.

The slotted tapered optical fiber (STOF) used in this work is a device which exploits the overlapping evanescent fields of a slot waveguide-like structure to further enhance its trapping ability, both for atoms [18] and submicron particle trapping. We sought to create an entirely fiber-based trapping device using evanescent fields to localize particles with a high degree of control in regimes inaccessible to standard MNFs. A nanoscale slot is introduced at the waist of an MNF using focused ion beam (FIB) milling, thereby creating a slot waveguide-like region where the optical forces are greatly enhanced. This provides three dimensional confinement within a small trapping volume, while also providing the potential for one dimensional position control of the trapped particles along the slot through the use of a sliding standing wave, i.e. a particle conveyor belt [43]. Here, we demonstrate trapping of 200 nm silica particles using a STOF. We also show how light transmitted through the fiber pigtails either side of the STOF can be analyzed to determine the trap characteristics. Finite element method (FEM) and finite difference time domain (FDTD) simulations are used to simulate the STOF modes and these are subsequently used to model the forces acting on the particles using perturbative and energy density methods.

2. Experimental setup

Micro-nanofibers and slotted tapered optical fibers

Commercial optical fibers guide light in what is known as the weakly-guided regime, wherein the refractive index contrast between the core of the fiber and the surrounding cladding is quite low ($n_{core} - n_{cladding} < 0.01$). Most of the light is contained within an area defined by the mode field diameter, which is much smaller than the fiber's total cross-sectional area. When an optical fiber is tapered over a heat source such that its diameter is close to, or below, the wavelength of the guided light, the distinction between the core and cladding region is no longer valid. The surrounding medium (in our case, water) becomes the new cladding and the original cladding is now viewed as the core material. These MNFs operate in the strongly guided regime as the refractive index contrast becomes high. The evanescent fields produced in MNFs extend far —when compared to the waveguide dimensions —into the surrounding medium and can interact with particles located at several 100s of nm from the fiber's surface. We work with optical fibers which have been tapered using a heat-and-pull method so that the waist diameter is typically of the order of the wavelength [44].We used a hydrogen-oxygen flame mixed in a 2:1 ratio to provide a clean-burning source. The untapered optical fiber is stripped of its outer

#263072 Received 12 Apr 2016; revised 13 Jun 2016; accepted 14 Jun 2016; published 17 Jun 2016

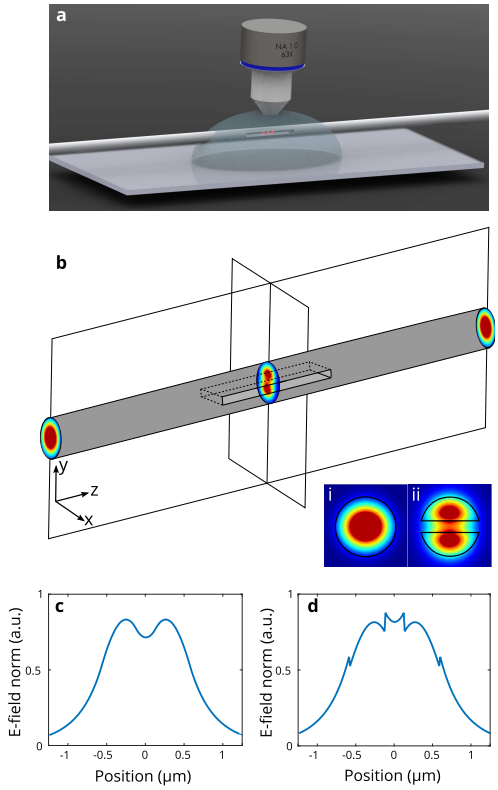

Fig. 1. (a): Representation of the slotted tapered optical fiber (STOF) in a solution of red fluorescent silica nanoparticles. A 63x immersion lens is used to image the system. (b): A schematic showing the STOF section of the optical fiber with the fundamental fiber mode (i) seen at either side of the cavity region and the fundamental STOF mode (ii) at the center. (c) and (d) show typical electric field norm along a line cutting through the origin along y for polarizations parallel to and perpendicular to the slot wall, respectively. The field within the slot can be up to 1.7 times higher than the field at the outer fiber surfaces although variations in the STOF dimensions can drastically alter this. The origin is taken to be at the center of the slot.

acrylic layer and clamped to the stages then placed into the flame. The stages pull both sides of the fiber away from the flame, causing the fiber, which is now in a molten state, to taper. By controlling the speed of the stages, the length of the pull, and the flame size, MNFs with specified diameters can be produced. The MNFs were fabricated from single-mode optical fiber in the 980–1600 nm regime. Slotted tapered optical fibers, or STOFs, are nanostructured MNFs which have had a section of their waist removed. The slotted tapered optical fibers were created using a three step process which involved the initial MNF fabrication process using standard heat-and-pull techniques, an indium tin oxide (ITO) sputter coating process, and finally a focused ion beam milling process to introduce a slot to the MNF. A 5 nm layer of ITO is necessary to provide sufficient charge mitigation at the MNF surface as an uncoated MNF would be subject to large dielectric charging effects during the FIB process, thereby making the subsequent etching of submicron features impossible. This new technique enables us to 'write' high resolution structures directly onto the MNF in a transmission-preserving, three-step process. The STOF geometry is illustrated in Fig. 1.

#263072 Received 12 Apr 2016; revised 13 Jun 2016; accepted 14 Jun 2016; published 17 Jun 2016

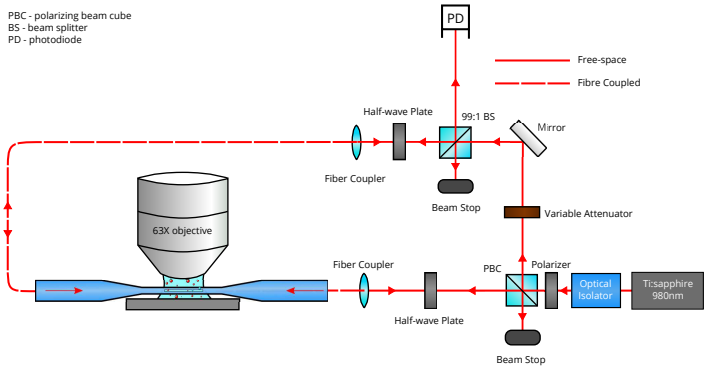

Fig. 2. Optical setup used to trap nanoparticles. 980 nm light from a Ti:sapphire laser is passed through a polarizing beam splitter to split the beam while providing some initial control over the power balance. From here the beams are passed through polarization control optics and finally fiber coupled to the STOF. Transmission data is collected via a photodiode

Field distribution

As expected, the electric fields of a STOF differ greatly from those of a typical tapered fiber. Due to the physical asymmetry introduced to the MNF at the slot region, the polarization of the guided light plays a larger role in the field distribution. To maximize the field at the slot, the polarization must be perpendicular to the walls of the slotted region. This removes the continuity requirement of the electric field at the dielectric boundary, thereby allowing a large portion of the field to exist outside of the waveguide (see Fig.1(d)). The strength of the field at the slotted region depends on a number of parameters: the diameter, the slot width, the polarization and the wavelength of the guided light. We chose a 1.4 μm fiber waist with a slot width of 300 nm. In general, the field strength increases with decreasing slot size, but, since we have an additional requirement that the STOF opening must be large enough to facilitate the entry of submicron particles, the slot width used was the minimal possible while still being practical for particle trapping. When the slot region is excited by the fundamental mode of an MNF, as illustrated in Fig. 1(b) inset (i), a 'fundamental' type mode is excited in either section, see Fig. 1(b) inset (ii). Slot waveguides can exhibit symmetric or anti-symmetric modes depending on the phase difference between the upper and lower sections. The fundamental mode of an MNF has an approximately uniform phase front, so we neglect the possibility of anti-symmetric modes in the following discussion.

Experimental outline

Optical trapping forces are typically divided into two categories in optical trapping experiments. In the dipole approximation, where $[n_p/n_m]ka \ll 1$ where k is the wave number (i.e. $2\pi/\lambda$), a is the radius of the particle, and n_p and n_m are the refractive indices of the particle and medium, respectively, the force can be decomposed into the gradient force ($\mathbf{F}_g \propto \frac{1}{2}\alpha\nabla\mathbf{E}^2$) and the scattering force ($\mathbf{F}_s \propto I(\mathbf{r})\hat{z}$) [42], where α is the real component of the polarizability of the particle, $\mathbf{E}$ is the electric field, and $I(\mathbf{r})$ is the optical intensity. This formalism is not necessarily accurate for all particle sizes, but gives a qualitative and intuitive picture of how the local electric fields affect particles placed within them.

For the case of unidirectional excitation of a STOF waveguide, the gradient force, which

#263072 Received 12 Apr 2016; revised 13 Jun 2016; accepted 14 Jun 2016; published 17 Jun 2016

seeks to pull particles towards regions of high intensity, draws particles towards the walls at the center of the slot, while the scattering force propels particles in the direction of propagation of the trapping laser field. To produce a trap with longitudinal confinement, a standing wave is necessary. This provides an extra degree of confinement for the particles, as well as increasing the overall trap efficiency due to the cancellation of the scattering force components, thereby improving the axial trapping strength. A more in-depth analysis of the trap is made using a combination of FDTD/FEM models and various optical trapping models.

We introduced a low density nanoparticle solution between the water immersion 63x lens and the STOF, shown in Fig. 2. The low density solution was used to prevent large numbers of particles occluding the slot. We used a particle solution of approximately 10^9 particles/ml, equivalent to an average particle occupancy of < 1 over the volume of the slot. Fluorescent nanoparticles were used to increase visibility of the system and we collected data visually, using a high sensitivity, fluorescence camera. Transmission and fluorescence data were also collected through the fiber using either a photodiode (for transmission) or a single photon counting module (for fluorescence).

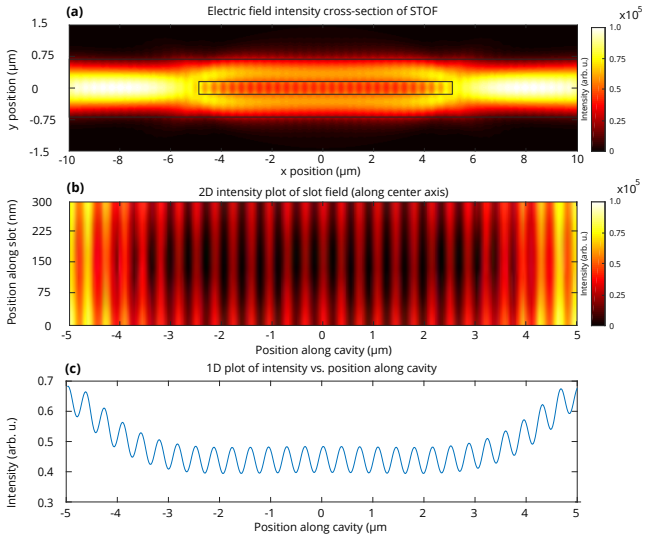

Fig. 3. (a): Results of FDTD analysis showing a cross-section of the STOF. The mode evolves from the fundamental mode of the MNF to the fundamental mode of the STOF at the center and back to the fundamental mode of the MNF with little loss. (b): Electric field intensity within the 10 μm $\times$ 300 nm slot in a 1.4 μm diameter MNF. The field increases in strength near the slot walls. (c): 1D plot of the electric field across the center of the STOF to show the variation in the field as a function of the distance along the cavity. The field stabilizes at the center of the cavity.

Polarization preparation

Polarization preparation of light in an MNF is often a source of contention as temperature and pressure variations (i.e. stresses and strains) along the fiber can cause the polarization to rotate, leading to little correlation between the input and output polarization states. Because of this behavior, polarization measurement methods, such as the observation of Rayleigh scattering along the fiber waist, need to be used [45]. In our experiment, we counter-propagated 980 nm light from a Ti:Sapphire laser through the STOF to provide a 3-dimensional trapping potential.

#263072 Received 12 Apr 2016; revised 13 Jun 2016; accepted 14 Jun 2016; published 17 Jun 2016

The standing wave pattern that was set up within the wave guiding structure extended to the evanescent field, which then interacted with nearby particles to produce a periodic potential within the cavity section of the STOF. Two half-wave plates placed in the path of the two beams gave us fine control over the input polarization states. By monitoring the output at opposite ends of the STOF, we obtained an estimate for the polarization at the slot. However, by directly monitoring the slot region using a 63x water immersion objective lens, we were better able to determine the polarization state at the STOF region via the intensity of the scattered light. When the light was polarized perpendicular to the plane of the slot i.e. along the *y*-axis, scattering was further enhanced due to the increased fraction of light contained within the small region. The slot is viewed in the *yz*-plane where the full slot opening is observed to ensure that the maximum scattering is at the correct polarization state.

3. Numerical analysis

A thorough calculation of the electric fields, using both FDTD and FEM methods, provided us with reliable estimates for the optical forces in the STOF system. The optical fields of the device were calculated both in the presence of, and without, the particles to be trapped. Optical forces on small particles are often described using the dipole approximation, where the size of the particle must be much less than the wavelength of the trapping beams. For 200 nm particles this criterion is not quite satisfied. To this end, we sought to make a comparison between the dipole gradient and scattering forces, and the more standard methods of force calculation for medium-sized particles. The total optical force in mid-sized optical trapping systems, $\mathbf{F}_{MST}$, is often calculated using a surface integral of the dot product of the Maxwell stress tensor, $\mathbf{T}$, with the surface normal, $\mathbf{n}$, such that

$$\mathbf{F}_{MST} = \oint_S (\mathbf{T}.\mathbf{n}) da. \tag{1}$$

Here, da is the unit area element. While this is an accurate method, it can be somewhat difficult to implement when the boundary of the system is ill-defined due to the mesh shape and/or the step size of the FEM/FDTD method used. As an alternative, we used an equivalent form derived from the Minkowski formalism for calculating the force; this method relies on the gradient of the electric permittivity, a value which can be easily extracted from the optical force calculation [46], such that the force is given by

$$\mathbf{F}_{min} = -\frac{1}{4}\varepsilon_0 \iiint_V \mathbf{E}.\mathbf{E}\nabla\varepsilon_r dV, \tag{2}$$

where ε_0 is the permittivity of free space, ε_r is the relative permittivity, $\mathbf{E}$ is the electric field and dV is the unit volume element. Accepted values of the refractive indices of silica and polystyrene at a wavelength of 980 nm were used in all calculations. The effect of the 5 nm layer of indium tin oxide was ignored due to its negligible influence on the MNF modes. Force measurements using data from the FDTD and FEM methods give almost identical results for the trapping forces within the slot except near the slot walls where a maximum discrepancy of 7.6% was found. We assume this discrepancy to be associated with the dynamic meshing of the FEM. To achieve similar resolution near the boundaries of the slot walls in an FDTD calculation, a significant increase in computation time would be required. The dipole approximation for the force calculation proved unreliable in regions where the local gradient was insignificant, but became more accurate as this gradient increased. This method could be improved by considering the particle as a distributed dipole, but this treatment is beyond the scope of this work. FDTD images of the optical fields of the STOF are given in Fig. 3, and a comparison of the trapping forces for different particle locations inside the slot are given in Fig. 4. Considering the close agreement between the FDTD and FEM simulations, we chose to largely model

#263072 Received 12 Apr 2016; revised 13 Jun 2016; accepted 14 Jun 2016; published 17 Jun 2016

the system using the FDTD method due to the reduced memory requirements and regular grid pattern. The dipole approximation,

$$F_{dipole} = \frac{1}{2}\alpha \nabla \mathbf{E}^2, \tag{3}$$

was also used to provide a contrast to the force calculation using the Minkowski formalism. The nature of Mie scattering requires smaller particle dimensions before one can neglect the higher order poles in the multipole expansion, hence the discrepancy between the two methods.

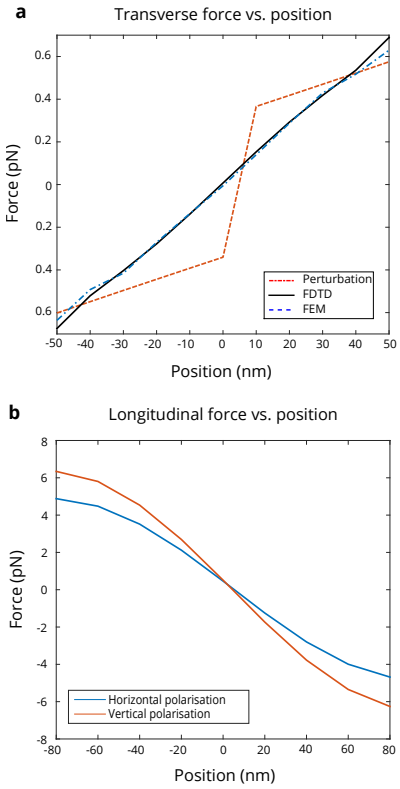

Fig. 4. (a): Forces on a 200 nm particle moving perpendicularly between the upper and lower walls of a STOF as determined using optical fields from FDTD and FEM calculations and Eqn. 2, compared to a perturbative approach using the optical fields of the cavity in the absence of a particle as modeled using the FEM. 1 W of power was used in all simulations. (b): Longitudinal trapping force for two orthogonal polarization states showing the increased trapping forces for the vertical polarization state.

At the ends of the slot, the local electric fields were found to increase due to reflections off the walls. Proposed solutions to this problem involve the introduction of a slot with tapered ends to allow the modes to evolve adiabatically between the MNF and STOF modes. After ≈2 μm the field within the cavity stabilizes, see Fig. 3(c). The trapping forces along the directions which run parallel to the STOF wall (along the *x*- and *z*-axes) are considered to have normal restoring forces, but the trap which runs perpendicularly (along the *y*-axis) between the upper and lower walls of the STOF does not experience a standard restoring force. Here, the optical forces seek to pull particles towards the wall, at which point any restoring character is lost. Instead, we determined the gradient of the force in this direction, indicated by g_y in Table 1.

#263072 Received 12 Apr 2016; revised 13 Jun 2016; accepted 14 Jun 2016; published 17 Jun 2016

4. Results and trap analysis

The small dimensions of the STOF make it hard to image the slot adequately without resorting to SEM imaging; sample images shown in figures 5(a-d). This problem also applies to the much smaller dimensions of the particles we wish to trap. Fluorescence imaging Fig. 5(b), however, allows us to capture live video of the particles' motion; due to the low-light levels, exposure times of $\approx$ 70 ms are required to actually image the particles. This limits our ability to perform Fourier analyses of the visual data since the trap operates at relatively low trap frequencies, requiring prohibitively long data collection times [47]. We can, however, track the particles and bin their positions to observe interesting behavior in their motion Fig. 5(e). With an imaging resolution of 13.3 pixels per micron we were able to track the particles' positions to a high degree of accuracy. Gaussian fitting of the positions showed trapping occurs at regular intervals along the central axis of the STOF. In the bright-field it was difficult to distinguish single particle trapping events from multiple particle trapping, but fluorescent imaging indicates that typically more than one particle is trapped. The dynamics of multiple particle trapping may shed some light on the larger spacing between 'stable' trapping positions. Simulations show that two particles in the trap have non-negligible interactions over distances of approximately 1 μm and this may explain the observation of stable trapping positions which are multiples of the approximately 350 nm standing wave separation, $\frac{\lambda}{2n_{eff}}$, where n_{eff} is the effective refractive index, as evident from the histogram in Fig. 5(f). We also took SEM images of the slot following the experiment. The devices were left to dry overnight in an enclosure. The images show particles on the fiber surface as well as inside the slot. This does not prove that any trapping occurred, but it does indicate that particles can diffuse freely into the slot.

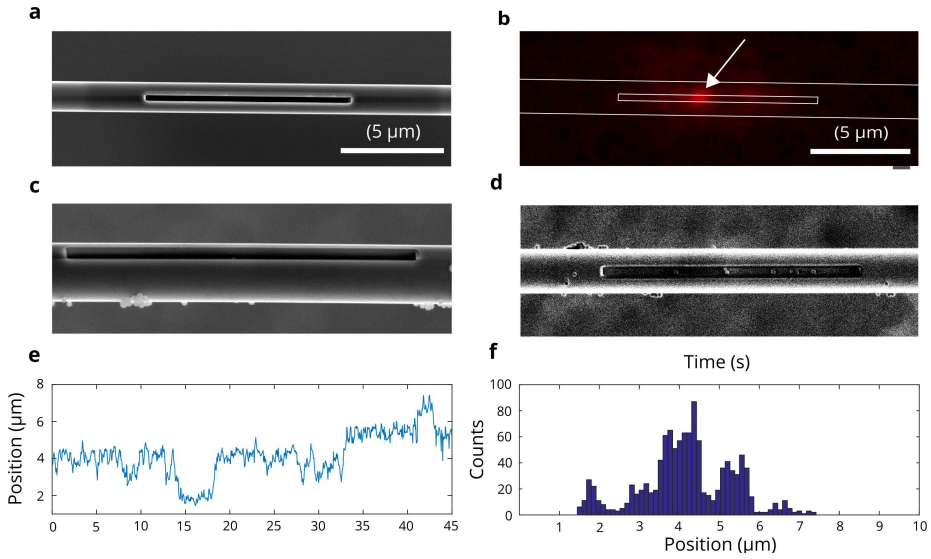

Fig. 5. (a) SEM image of a STOF. (b): Microscope image of a trapped fluorescent particle with an outline of the STOF for clarity (see Visualization 1 & Visualization 2). (c) and (d) show SEM images of the fiber after the experiment was performed. Particles can be seen inside the slot was well as on the surface. (e): Particle position versus time along the *z*-axis of the STOF. The particle is seen to spend most of its time near the slot center. Each pixel was found to correspond to a 100 nm $\times$ 100 nm area and Gaussian fits to the particle center enable high resolution tracking. (f): Histogram of the particle positions given in (e) showing bunching at regular intervals.

#263072 Received 12 Apr 2016; revised 13 Jun 2016; accepted 14 Jun 2016; published 17 Jun 2016

The unrestricted motion of Brownian particles leads to a characteristic $\frac{1}{f^2}$ noise spectrum. In contrast, for a trapped particle, the power spectral density (PSD) follows a Lorentzian distribution, $\frac{A}{f^2+f_c^2}$, which is derived from the Langevin equations of motion [48]. Log-log plots of these data allows one to visually interpret this Lorenztian line-shape as the combination of two regimes which overlap at the corner frequency, f_c. Everything beyond f_c can be viewed as the unbound motion of free Brownian particles and behaves as $\frac{1}{f^2}$, while everything below this represents the restricted motion of the trapped particles [41].

Table 1. **Trap 'Stiffnesses' for Varying Input powers as determined from FDTD analysis**

Trap 'Stiffness'	2 mW	5mW	10 mW
k_x	28 fN μm^{-1}	69 fN μm^{-1}	138 fN μm^{-1}
k_z	202 fN μm^{-1}	510 fN μm^{-1}	1020 fN μm^{-1}
g_y	102 fN μm^{-1}	255 fN μm^{-1}	510 fN μm^{-1}

Throughout the experiment we record the transmission through the STOF during trapping and non-trapping events. Analyzing the power spectral density of this signal can be difficult when low trap frequencies are considered Fig. 6(a). Additionally, our detected signal is coupled to the three non-degenerate trap stiffnesses and it is difficult to distinguish between single-particle and multiple-particle trapping; this adds more noise to our detected signal. To overcome some of these issues, we opt for autocorrelation measurements which are analogous to the PSD, but do not suffer from some of the associated PSD measurement problems [42]. Data was taken in 50 s intervals at a sample rate of 2 kHz. The decay of the autocorrelation with respect to the delay time, given in Fig. 6(b), is not quite exponential (as would be expected for a clean optical trap). The introduction of 'random' forces, can alter the lineshape [49]. We expect fluctuations in the slot walls due to external effects such as air currents etc., while immersed in the particle solution can alter the trapping force on the particles to be sources of these 'random' forces. Despite these contributions, the trap stiffnesses are seen to increase proportionally to the input powers, as determined by closest exponential fits to the data. The increase is directly proportional to the input laser power Fig. 6(c) and give values which are of the same magnitude as the expected theoretical values, Table 1. We instead take the root mean square (RMS) value for the power to adjust for the losses along the fiber and use this power to calculate k_x, k_z, and g_y. The use of the RMS value adjusts the power for adiabatic losses in the taper region of the nanostructured fiber. We assume that the down taper and up taper sections of the STOF are symmetric, therefore losses accrued from both sections should be equal. Hence, we assume that $P_{slot} = \sqrt{T}$, where P_{slot} is the power at the slot and T is the transmission of the fiber. A similar argument can be used for the influence of the slot. Consideration of multiple particle interactions and surface-particle interactions such as the Faxen corrections would reduce this value further. We assume that the longitudinal trap stiffness, k_z, may have a smaller contribution to the measured trap strength since this trap corresponds to motion longitudinally along the fiber which would not result in significant noise contributions in our recorded signal. Additionally, the trap in the y-direction does not have a restoring character which would alter its contributions to the noise spectra. This may point to the x component of the trap being the primary contribution to the measured signal.

5. Conclusions

Micro-nanofibers have recently established themselves as very useful tools in several fields, including optical trapping and cold atom physics [50]. The STOF used in the work reported here

#263072 Received 12 Apr 2016; revised 13 Jun 2016; accepted 14 Jun 2016; published 17 Jun 2016

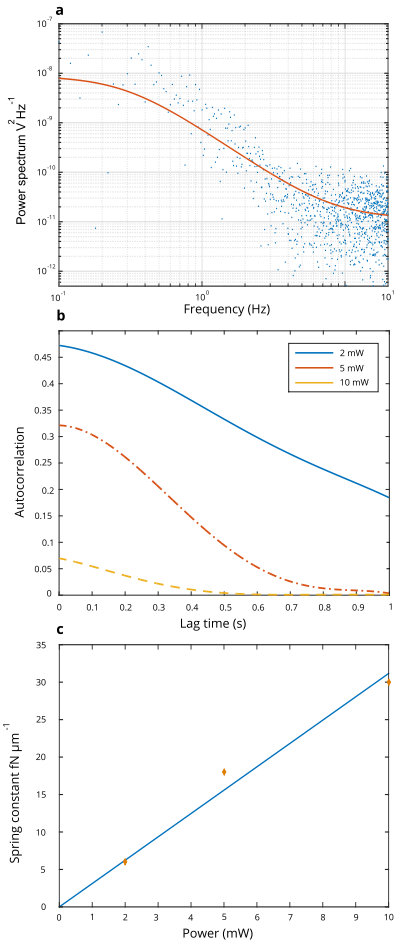

Fig. 6. (a) Power spectrum density of the tranmitted signal for 5 mW of trapping power. A corner frequency of 0.6 Hz is measured.(b) Autocorrelation signals at 2 mW, 5 mW and 10 mW. The observed decrease in the slope of the autocorrelation signal at different powers indicates a linear increase in trap strength with power as is expected. (c) Plot of the Spring constant as determined using the autocorrelation measurement vs. the power in the trapping beams. The subsequent plot is linear with respect to power as predicted.

allowed us to further enhance the effectiveness of MNFs in optical trapping. As a trapping device, the STOF shows promise for particle sizes down to 200 nm with modest trapping powers, albeit with low trap stiffnesses. Trapping of 100 nm polystyrene particles has also been observed, but was not presented here. The flexibility of the fabrication process permits us to make structures with very high resolution, as well as providing a means for *in-situ* scanning electron microscope (SEM) measurements of the device prior to use. This flexibility opens up many avenues of research as it facilitates arbitrary modification of the MNF waist. The unique trapping geometry which confines particles, and potentially atoms, within the slot leads us to believe that spectroscopic measurements are possible by passing probe beams of different wavelengths through the fiber while simultaneously recording the transmission or captured fluorescence at the output pigtail. A substantial improvement to earlier work, such as the self-organization of

#263072 Received 12 Apr 2016; revised 13 Jun 2016; accepted 14 Jun 2016; published 17 Jun 2016

atoms along nanophotonic waveguides [51], should also be possible since light coupling into the STOF is increased compared to for standard optical nanofibers. This study serves as a step towards the realization of more complex applications involving the incorporation of different slot geometries as well as custom MNF Bragg gratings [34] to further enhance the fields of the STOF. Whether as a platform for studying optical binding effects, as an analytical tool, or as a trap for cold, neutral atoms, the STOF has many exciting applications which remain to be investigated.

Acknowledgments

This work was supported by the Okinawa Institute of Science and Technology Graduate University. The authors would like to thank T. Sasaki and L. Szikszai for invaluable technical assistance and V. Brulis (Photon Design) for his insightful comments regarding the FDTD simulations.

#263072 Received 12 Apr 2016; revised 13 Jun 2016; accepted 14 Jun 2016; published 17 Jun 2016

Nanostructured tapered optical fibers for particle trapping

Mark Daly, Viet Giang Truong, and Síle Nic Chormaic*
Light-Matter Interactions Unit, Okinawa Institute of Science and Technology Graduate University, Onna, Okinawa 904-0495, Japan

ABSTRACT

Optical micro- and nanofibers have recently gained popularity as tools in quantum engineering using laser-cooled, neutral atoms. In particular, atoms can be trapped around such optical fibers, and photons coupled into the fibers from the surrounding atoms could be used to transfer quantum state information within the system. It has also been demonstrated that such fibers can be used to manipulate and trap silica and polystyrene particles in the 1-3 μm range. We recently proposed using a focused ion beam nanostructured tapered optical fiber for improved atom trapping geometries[1]. Here, we present details on the design and fabrication of these nanostructured optical fibers and their integration into particle trapping platforms for the demonstration of submicron particle trapping. The optical fibers are tapered to approximately 1-2 μm waist diameters, using a custom-built, heat-and-pull fiber rig, prior to processing using a focused ion beam. Slots of about 300 nm in width and 10-20 μm in length are milled right though the waist regions of the tapered optical fibers. Details on the fabrication steps necessary to ensure high optical transmission though the fiber post processing are included. Fiber transmissions of over 80% over a broad range of wavelengths, in the 700-1100 nm range, are attainable. We also present simulation results on the impact of varying the slot parameters on the trap depths achievable and milling multiple traps within a single tapered fiber. This work demonstrates even further the functionality of optical micro- and nanofibers as trapping devices across a range of regimes.

Keywords: optical nanofibers, optical microfibers, particle trapping, nanostructuring, focused ion beam milling

1. INTRODUCTION

Evanescent field-based devices, particularly those which can be applied in cold atomic gas trapping and particle trapping, have gained popularity in recent decades. The early work, such as the proposed atom trap[2] using the evanescent field at a dielectric-vacuum interface by Ovchinnikov *et al*, spurred much research in the area. More recently, optical micro- and nanofibers (MNFs) have been used extensively in cold atom systems as both a means of trapping and confining atoms to regions around the fiber[3], and as tools to probe atomic systems.[4] MNFs have also been successfully used for propelling and trapping micron- and submicron-sized dielectric particles.[5,6] MNFs can be reliably produced with a high degree of resolution in both their waist radii and the shape of the fiber taper. The advantages to working with an optical field that exists externally to its guiding structure has been recognized by the community, and attempts to increase the utility of such fibers have been proposed and demonstrated in, for example, photonic crystal fibers[7] and modified tapered fiber probes.[8] Here, we propose direct modification of the MNF structure itself in order to enhance the electric field by overlapping two evanescent fields. By removing a rectangular section of the MNF waist using a focused ion beam (FIB), a small cavity is created where the local electric field is increased compared to that of the evanescent field of a regular MNF. A schematic is given in Figure 1. Previously, we proposed fabrication of such a slotted tapered optical fiber (STOF) in the context of atom trapping[1], though applications in the field of optical manipulation are possible. This paper contains details of the fabrication process and the characterization of STOFs.

Figure 1. Schematic of an STOF. Left: Structured area of the STOF showing the rectangular cavity at the waist region. Right: Cross-section of the STOF taken at the dotted region of the image on the left.

Micro-structured and Specialty Optical Fibres IV, edited by Kyriacos Kalli, Jiri Kanka, Alexis Mendez, Proc. of SPIE Vol. 9507, 95070E · © 2015 SPIE · CCC code: 0277-786X/15/$18 · doi: 10.1117/12.2182340

2. FABRICATION

The fabrication procedure for an STOF, as summarized graphically in Figure 2, is a three step process consisting of (i) optical fiber tapering and mounting, (ii) coating, and (iii) FIB milling.

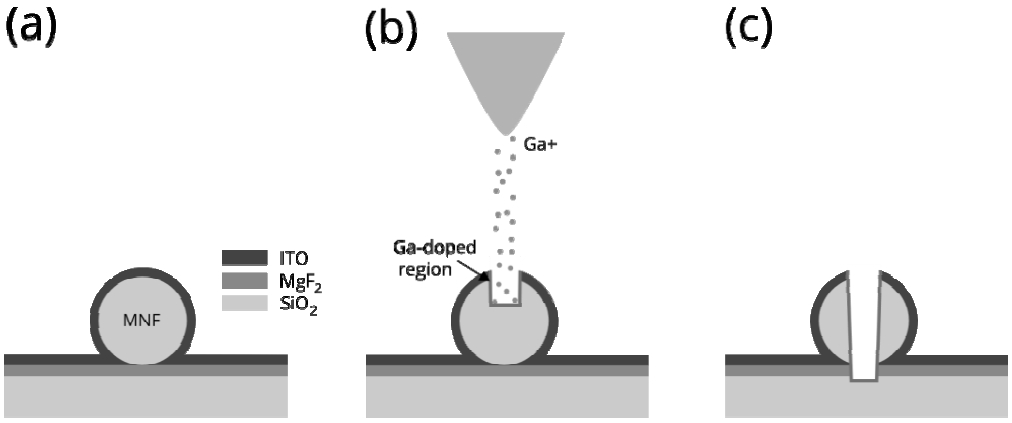

Figure 2. Outline of the fabrication process. (a) A MNF is placed on a microscope slide that has been pre-coated with a thin layer of MgF_2 which is then sputter coated with a 30 nm layer of ITO. (b) Using a focused ion beam, the structure is etched into the MNF. (c) The finished STOF after etching; typically the etch depth is overestimated to ensure complete milling of the cavity.

Tapering process

The first step of the process is tapering. Here, optical tapers must be produced from standard, telecommunications-grade optical fiber. All the STOFs shown in this paper were produced using Thorlabs 1060XP single mode fiber. For our purposes, adiabatically tapered fibers with an exponential taper profile are used. As the higher order modes of the MNF are not desired, more complex taper shapes are not required. Tapering was performed using a heat-and-pull rig; we used both a static, microheater based rig, and a flame-brushed hydrogen/oxygen flame-brushed rig, as described in Ward *et al*.[9] Experimentally, no difference was observed between STOFs produced using either heat-and-pull system.

MNFs with diameters between 1 and 2 μm were produced, and SEM images, which were taken during the fabrication process, show that the MNFs are uniform in diameter over a large (>2 mm) distance. Cleanliness is essential to all steps of the fabrication process; therefore, fabricated MNFs were immediately mounted and transferred to clean containers, and either stored in a vacuum desiccator until they were needed, or immediately transferred to the vacuum chamber of the sputter deposition system for the next step in the process.

Coating process

The MNFs must be mounted on a suitable substrate prior to coating them for the ion beam processing stage; MgF_2 was chosen due to its low refractive index relative to that of the optical fiber's cladding/core indices. This serves to prevent light loss through the coupling of light between the MNF and the higher refractive index microscope slides that are typically used to mount the fibers for optical manipulation experiments. Hence, MgF_2 coated microscope slides were used. During the transfer of the MNF from the heat-and-pull rig to the coated slides, care must be taken to ensure that the fiber is in contact with the slide at the waist region. This step was performed to allow the next coating process to form a semi-continuous layer between the MgF_2 and the MNF fiber (see Figure 2(a)).

To minimize charging effects induced in the dielectric MNFs by the intense incident beam of Ga^+ ions, a thin layer of conductive ITO must be placed over the MNF + MgF_2 system. ITO was chosen due to its high conductivity and high transparency in the 700-1100 nm regime. The layer thickness of ITO is kept extremely thin, approximately 30 nm, to prevent the light from propagating in this new, higher refractive index layer. An ULVAC vacuum sputter deposition system was used to coat the fibers with ITO.

Etching process

After coating, the samples are quickly transferred to the vacuum chamber of the Helios NanoLab™ DualBeam™ 650. The stated operational vacuum for the equipment is between 10^{-2}–10^{-5} Pa, but, to achieve high resolution milling of the samples, they were often left in the vacuum chamber overnight if possible, or for a minimum of two hours, to achieve a vacuum pressure at the lower limit of the operational value of approximately 2×10^{-4} Pa.

Once an adequate vacuum pressure is reached, the etching process can begin. Despite the preventative measures, some small amount of drift may remain in the system. This can be attributed to either dielectric charging, or poor adhesion of the MNF to the MgF_2 surface, resulting in mechanical vibrations of the fiber. To counteract this, the etching process was broken down into short etching periods of a few seconds each. Using a beam voltage of 30 kV, a current of 33 pA, and a dosage of 0.27 m^3 /nC, the etch rate of the MNF was found to be approximately 3.5 nm/s. Between samples, the operational current was found to vary somewhat. The software used for the Helios Nanolab™ DualBeam™ 650 reflects these change in its calculations, so the exact etch rate can be determined on a sample to sample basis. Fibers with slot widths of 300 nm have been fabricated and are shown in Figure 3.

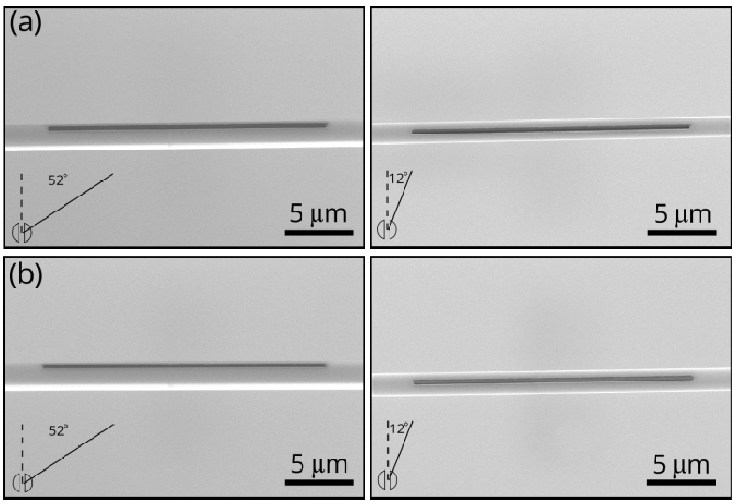

Figure 3. SEM images of two fibers (a) and (b) from two different viewing angles (viewing angles shown on images, solid black line indicates line of sight). Fiber diameters are 1.56 µm and 1.4 µm for (a) and (b), respectively.

3. COMPUTER SIMULATIONS

Both finite element method and eigenmode expansion method solvers were used to determine the operation capabilities of the STOF. The simplest geometry, and the one considered in the fabrication process, is that of a single rectangular slot placed at the waist region of an MNF. The models were used to determine the transmission and reflection of the STOFs over the 600-1100 nm range. This range was chosen to encompass both 780 nm light, a wavelength used in laser-cooling of rubidium, and 1064 nm light, which is frequently used in particle trapping and manipulation. Plots of the electric fields within the fiber are given in Figures 4.

The transmission of the STOFs over the 600 – 1100 nm range was calculated using eigenmode expansion method solvers. To best model the transmission, both TE and TM modes were input into the STOF at both orthogonal polarizations, with the transmission at the output recorded. As the wavelength becomes shorter, the loss across the STOF increases (see Figure 5). Light at lower wavelengths becomes more confined to the central region of the fiber. At the slot region, the flat end faces present a larger obstacle to the evolution of these highly confined fundamental modes to the cavity modes.

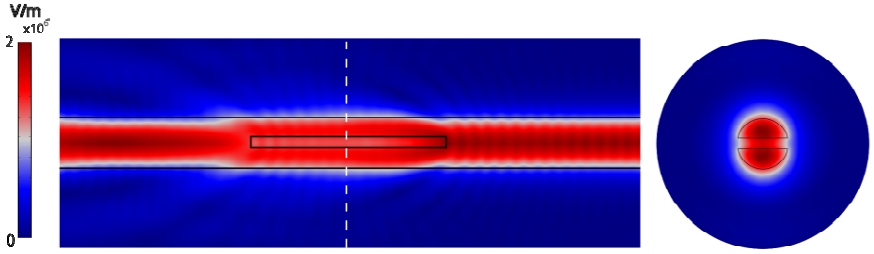

Figure 4. Transversal (right) and longitudinal (left) cross-section, displaying the electric field norms within a STOF. STOF outlines shown in black. Input power: 10 mW. Wavelength: 1064 nm. Polarization: Horizontal with respect to the slot. Refractive index of fiber: 1.4559. Refractive index of surrounding medium: 1. Modelled using COMSOL.

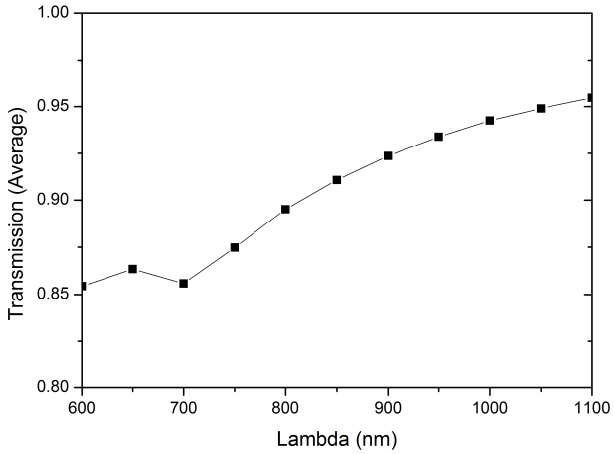

Figure 5. Simulated transmission of a STOF over the 600-1100 nm range. Fiber diameter: 1.4 µm. Slot width: 300 nm.

To increase the STOF's transmission, we modelled cavities with tapered shapes that encourage the adiabatic evolution of the modes in the unperturbed region of the STOF to those present in the slotted region. The simulations show that, by using 'diamond' shaped slots, the loss across the cavity approaches zero for the fundamental modes (see Figure 6).

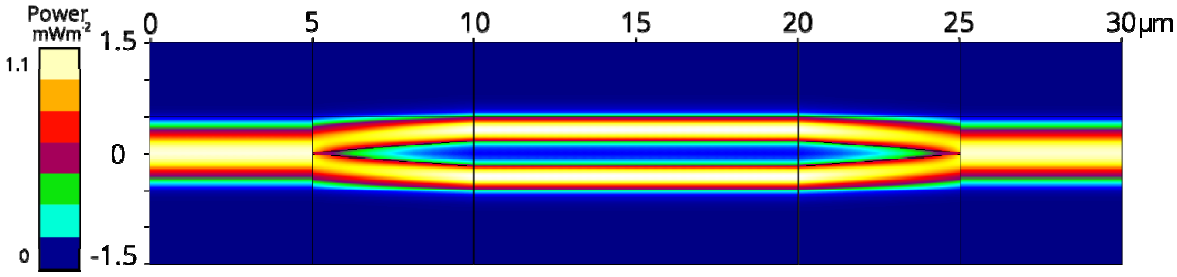

Figure 6. Simulation of a STOF with a diamond shaped slot. The loss approaches zero across the slot as the mode evolution becomes adiabatic. Horizontal scale exaggerated for clarity (all scale units are microns). Fiber diameter 1 µm, slot width 350 nm, taper angle 0.035 radians. Modelled using FIMMPROP.

4. CHARACTERIZATION

Transmission

The removal of the rectangular section of the MNF has, as one would expect, an effect on the STOF's transmission spectra. The presence of the slot introduces a discontinuity in the refractive index along the direction of propagation, and this causes reflections and scattering at the flat end-faces of the slot; this somewhat prevents the adiabatic transition of MNF modes to the STOF modes in the structured region. The experimentally measured transmission of a STOF is shown in Figure 7. While the overall transmission is lower than that predicted in Figure 5, the trend does agree with the simulations. With more careful MNF and STOF fabrication, the transmission should be further increased.

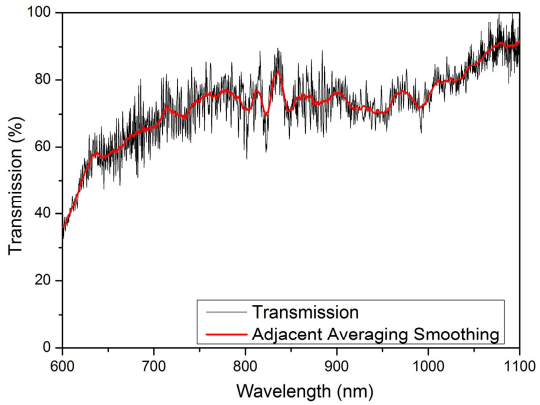

Figure 7. Measured transmission spectrum of a STOF from 600-1100 nm. Fiber diameter: 1.4 μm. Slot width: 300 nm.

Polarization dependence

The field intensity within the cavity is strongly dependent on the polarization, as shown in Figure 8. When the polarization is chosen such that it is perpendicular to the upper and lower walls of the cavity, the field is strongly enhanced due to there being no required continuity of the electric field for this component; hence, there is an increase to the proportion of the field outside the fiber. We used this polarization dependence of the field to determine the polarization at the waist of the STOF. Since the amount of scattered light is higher for the perpendicularly polarized light, the assumption that the transmission was lower at this polarization was made. Experimentally, we have seen that the transmitted power varies by 3-4% with $\pi/2$ periodicity (Figure 8), with the minima assumed to be the positions of highest field intensity within the cavity.

5. CONCLUSION

We have shown that STOFs with a high transmission over a wide range of wavelengths can be fabricated. These STOFs have immediate applications in atom and particle trapping. In cold atomic systems, STOFs can be used both actively and passively either to trap atoms or to collect spontaneously emitted light from atoms trapped within the cavity. The geometry of this fiber-based atom trap allows for increased coupling of the emitted light into the guided modes of the STOF. STOFs can also be used to trap and manipulate dielectric particles as small as 100 nm, providing an improvement in trapping capability when compared to an unmodified MNF. Work on these topics is ongoing. The use of an FIB in the fabrication process allows for high precision milling, thereby enabling feature sizes down to a few tens of nanometers to be milled. Future work will involve the creation of STOFs with multiple cavities and/or cavities which are not rectangular, in order to allow for higher transmission of the fundamental mode.

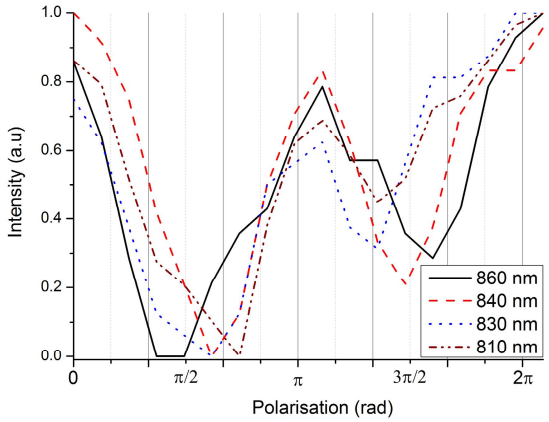

Figure 8. Polarization dependence of the STOF in the range 810-860 nm. Data was taken in 0.35 radian intervals.

ACKNOWLEDGEMENTS

This work was supported by the Okinawa Institute of Science and Technology Graduate University. The authors wish to thank K Deasy for useful discussions and assistance.

REFERENCES

[1] Daly, M., Truong, V. G., Phelan, C. F., Deasy, K., and Nic Chormaic, S.,"Nanostructured optical nanofibres for atom trapping," New J. Phys. 16(5), 053052 (2014).
[2] Ovchinnikov, Y. B., Shul'ga, S. V., and Balykin, V. I.,"An atomic trap based on evanescent light waves," J. Phys. B. At. Mol. Opt. Phys. 24(14), 3173 (1991).
[3] Vetsch, E., Reitz, D., Sague, G., Schmidt, R., Dawkins, S. T., and Rauschenbeutel, A.,"Optical interface created by laser-cooled atoms trapped in the evanescent field surrounding an optical nanofiber," Phys. Rev. Lett. 104(20), 203503 (2010).
[4] Kumar, R., Gokhroo, V., Maimaiti, A., Deasy, K., Frawley, M. C., and Nic Chormaic, S.,"Interaction of laser-cooled ^{87}Rb atoms with higher order modes of an optical nanofiber," New J. Phys. 17, 013026 (2015).
[5] Brambilla, G., Murugan, G. S., Wilkinson, J. S., and Richardson, D. J.,"Optical manipulation of microspheres along a subwavelength optical wire," Optics Letters, 32(20), 3041-3043 (2007).
[6] Maimaiti, A., Truong, V. G., Sergides, M., Gusachenko, I., and Nic Chormaic, S.,"Higher order microfibre modes for dielectric particle trapping and propulsion," arxiv:1409.1665 (2014).
[7] Christensen, C. A., Will, S., Saba, M., Jo, G.-B., Shin, Y.-I., Ketterle, W., and Pritchard, D.,"Trapping of ultracold atoms in a hollow-core photonic crystal fiber," Phys. Rev. A 78(3), 033429 (2008).
[8] Xin, H., Xu, R., and Li, B.,"Optical trapping, driving, and arrangement of particles using a tapered fibre probe," Sci. Rep. 2, 818 (2012).
[9] Ward, J. M., Le, V. H., Maimaiti, A., and Nic Chormaic, S., "Optical micro- and nanofiber pulling rig," Rev. Sci. Instrum. 85, 111501 (2014).

Submicron particle manipulation using slotted tapered optical fibers

M. Daly[a], V.G. Truong[a], and S. Nic Chormaic[a]

[a]Light-Matter Interactions Unit, Okinawa Institute of Science and Technology Graduate University, Onna, Okinawa 904-0495, Japan;

ABSTRACT

The use of optical micro- and nanofibers has become commonplace in the areas of atom trapping using neutral atoms and, perhaps more relevantly, the optical trapping and propulsion of micro- and nanoscale particles. It has been shown that such fibers can be used to manipulate and trap silica and polystyrene particles in the 1-3 μm range using either the fundamental or higher order modes of the fibers, with the propulsion of smaller particle sizes also possible through the use of metallic and/or high index materials. We previously proposed using a focused ion beam nanostructured tapered optical fiber for improved atom trapping geometries; here, we present the details of how these nanostructured optical fibers can be used as a platform for submicron particle trapping. The optical fibers are tapered to approximately 1.2 μm waist diameters, using a custom-built, heat-and-pull fiber rig prior to processing using a focused ion beam. Slots of approximately 300 nm in width and 10-20 μm in length are milled clean though the waist regions of the tapered optical fibers. High fiber transmissions ($> 80\%$) over a broad range of wavelengths (700-1100 nm) are observed. We present simulation results for the trapping of submicron particles and experimental results on the trapping of 200 nm particles. This work demonstrates even further the functionality of optical micro- and nanofibers as trapping devices across a range of regimes.

Keywords: Near-field trapping, optical trapping, sub-micron trapping, optical fibers, tapered optical fibers, micro- and nanofibers, nanostructuring

1. INTRODUCTION

Particle manipulation and cold atom traps have benefited from the rise in popularity of evanescent field-based devices over the last few decades. Some of the earliest work by Ovchinnikov et al.[1] discussed the trapping of cold, neutral atoms through their interaction with the evanescent field formed at a dielectric-vacuum interface of counterpropagating laser beams. The realization that the evanescent light field at dielectric interfaces could interact with atoms and/or particles eventually led to the use of optical micro- and nanofibers (MNFs) as a means of producing these fields.[2,3] MNFs have been used in cold atom systems as both a means of trapping and confining atoms to regions around the fiber,[4,5] as well as in particle manipulation systems as a way of propelling, trapping, and sorting micro and nanoparticles.[6,7] Today, MNFs can be reliably produced to a high degree of accuracy in both their waist radii and the overall shape of the transition region of the fiber taper.[8] Advances in the fabrication methods of MNFs have allowed researchers to create fibers with extremely high transmission values, sometimes $> 99.95\%$,[9] for the fundamental mode of the fiber. Research groups have also succeeded in efficiently propagating higher order modes through MNFs.[10] With little left to optimize in the fabrication process, the focus of certain groups has drifted to the modification of standard waveguiding structures; devices such as photonic crystal cavities and photonic crystal fibers allow for high field intensities with low mode volumes to exist.[11,12] Our proposed device involves the bulk modification of an MNF through the removal of a rectangular cavity at the waist region, as shown in Figure 1. By removing a section of the MNF waist using a focused ion beam (FIB), a small cavity is created where the local electric field is increased[13] as compared to that of the evanescent field of a regular MNF. This slotted tapered optical fiber (STOF), was previously proposed in the context of atom trapping[14] due to its appealing characteristics as both a means to trap atoms as well as providing a tool for efficiently collecting fluorescence light from the trapped atoms. In this paper we show how STOFs can be used as a platform to trap submicron particles, namely 200 nm silica beads. We show how the evanescent field present at the cavity region of a STOF can trap a large cluster of submicron particles.

Further author information: (Send correspondence to M. Daly)
M. Daly: E-mail: mark.daly@oist.jp

Optical Trapping and Optical Micromanipulation XII, edited by Kishan Dholakia, Gabriel C. Spalding
Proc. of Vol. 9548, 954812 · © 2015 SPIE · CCC code: 0277-786X/15/$18 · doi: 10.1117/12.2189168

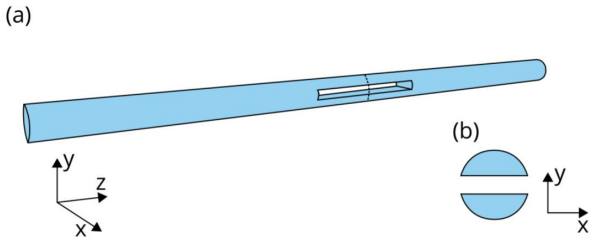

Figure 1. Schematic drawing of a STOF. (a) The overall structure at the waist of the MNF; (b) A cross-section of the STOF at the dotted line in (a).

2. SLOTTED TAPERED OPTICAL FIBERS

MNFs are created by pulling standard optical fiber over a heat source until the diameter at a central 'waist' region is reduced to near, or below, the wavelength of the input light. Much literature has been published on the fabrication process and their use has become widespread across a broad range of topics.[15]

A slotted tapered optical fiber consists of an MNF which has had its waist region altered through the introduction of a rectangular cavity. The presence of a cavity effectively breaks the symmetry of the MNF at the waist, resulting in the strong polarization dependency of the electric field at this location. Light which arrives at the slot region with a polarization aligned along the y-direction, as given in the coordinate system in Figure 1, produces a region with high electric field intensity within the cavity. This increased intensity can be used to trap and manipulate particles. The fabrication process involves coating an MNF with indium titanium oxide (ITO) — which is a conductive, transparent material, and is used to mitigate the charging effects of the dielectric — followed by etching using a focused ion beam. The end result is a STOF, see Figure 2, with high transmission in the 700–1100 nm wavelength range. Transmissions of >90% are routinely obtained at a wavelength of 980 nm.

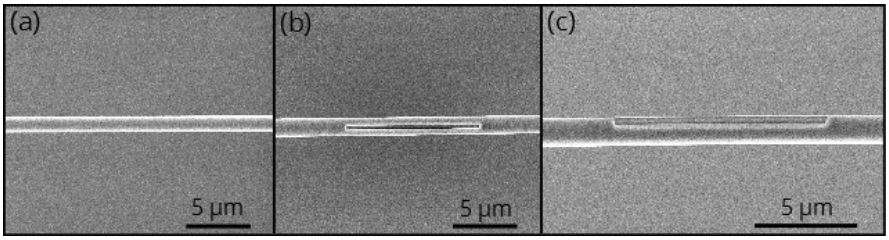

Figure 2. SEM images of a fabricated STOF. (a) MNF pre-milling; (b) MNF post-milling; (c) MNF post-milling viewed at 52° to the slot face. Fiber diameter 1.2 μm, slot width 300 nm, and slot length 10 μm.

3. EXPERIMENTAL METHOD AND RESULTS

We used STOFs with fiber diameters of 1.2 μm, slot widths of 300 nm, and slot lengths of 10 μm. We chose these parameters as they provide adequate electric fields for the trapping of submicron particles as determined from finite element models. In addition to the electric field requirement, the slot width was also chosen for the more practical reason of allowing the particles enough room to enter and exit the cavity without sticking to the walls. Other combinations of diameters and slot widths can be used to trap smaller or larger particles as required. Small variations in the STOFs due to the fabrication process are not considered in this paper.

A Ti:Sapphire laser tuned to a wavelength of 980 nm was used as the trapping beam. The STOFs were created from Thorlabs 1060XP single mode optical fiber; this fiber is single mode in the 980–1600 nm range. A simplified layout of the experiment is given in Figure 3. The STOF was mounted onto a soda glass microscope slide with an optically thick coating of magnesium fluoride (MgF_2) to prevent light coupling between the fiber and the slide itself. Instead of an inverted optical setup, we opted for a water immersion lens to allow us to obtain clean images of our system as well as enabling us to observe fluorescence from the fluorescent nanoparticlesin situ. Solutions

of fluorescent 200nm silica particles with varying levels of concentration were used in this experiment. The solutions were added to the STOF in two different ways; the first involved pipetting 100 μl of solution between the immersion lens and the STOF. The second method made use of a LabSmith μprocess automated injection system to inject a controlled volume of colloidal nanoparticle solution into a droplet of ultrapure water that had been previously pipetted onto the sample. A small fraction of the transmitted power was redirected towards a photodiode and a single photon counting module. The data were recorded using a National Instruments DAQ card. Trapping was simultaneously monitored using a CCD camera through the water immersion lens.

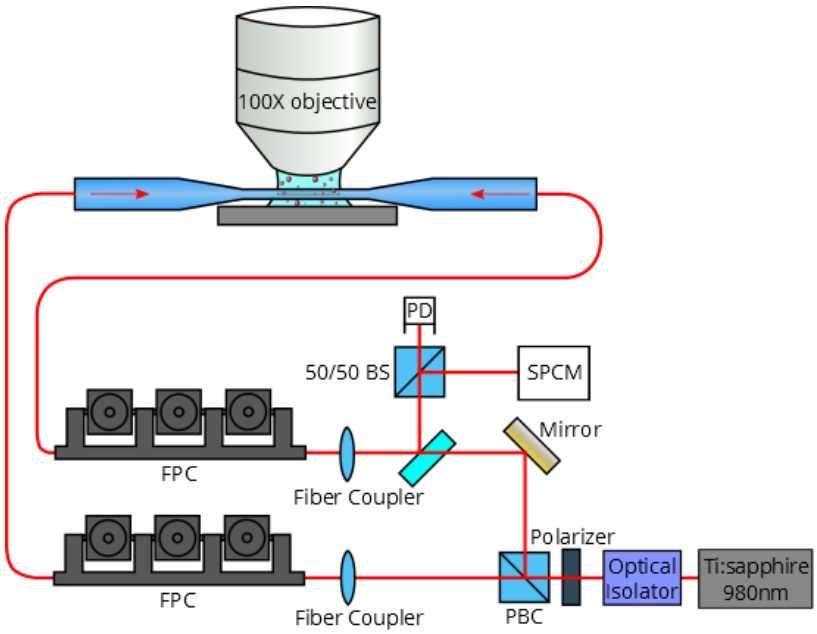

Figure 3. Diagram of the experimental setup. PBC: polarizing beam splitting cube, FPC: fiber polarization control, PD: photodiode, SPCM: single photon counting module, BS: beam splitter.

Finally, trapping was observed for the nanoparticles. Using a variable attenuator, the power in the counter-propagating beam was slowly increased during the experiments and measurements of the power spectral density were taken for (i) counter propagating beams and (ii) single direction beams in order to observe the change between trapping via a standing wave potential and the lack of trapping when using a single beam. Distinct differences in the trapping can be seen between low and high density solutions, though we only present the results for high densities here. Initially 100 nm particle solutions were used and individual trapping events were observed for low density solutions, whereas for 200 nm particles, large scale trapping was seen for more dense particle solutions. Ostensibly, this may be linked to the increased gradient force, since, assuming similar laser conditions, it should be eight times higher for 200 nm particles since the gradient force is volume dependent in the Rayleigh approximation. A sequence of images taken from a video recording of 200 nm particle trapping is shown in Figure 4. The particles form a large cloud around the slot area and it rapidly disperses once the laser is blocked. Thermophoretic forces were considered and further experimentation needs to be performed to determine the nature of the observed trapping. Evidence of trapping using low concentrations of silica has also been seen, but is not presented here as further study needs to be performed.

4. CONCLUSIONS

We show that STOFs can be used to trap 200 nm particles using modest powers. For the trapping of 200 nm particles, as shown in Figure 4, a total power of 30 mW was used; the total power is the sum of the power in the balanced, counterpropagating beams. Experimentally, traps with low spring constants have been observed, but the inclusion of microfluidic channels could help to increase this by removing sources of transmission loss

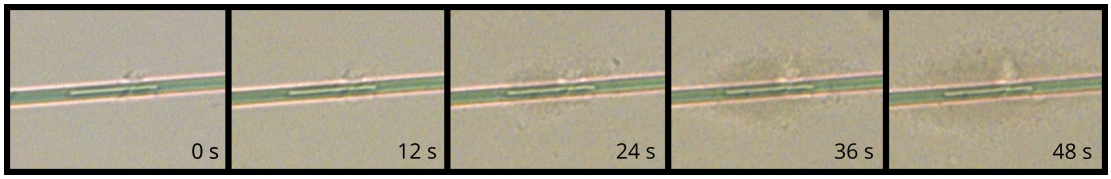

Figure 4. Still images taken from a video showing the trapping of 200 nm particles using a total power of 30 mW.

attributed to particles attaching to the surface of the fiber along the full length of the taper transition as well as isolating the STOF somewhat from the outside environment. Further investigation of the trapping capabilities of STOFs needs to be performed to clarify the process through which particles are trapped and to also confirm, at least for the large arrangement of nanoparticles, that the particles are indeed trapped within the slot as well as outside. Additionally, the seemingly long range trapping outside of the slot for 200 nm particles could serve as a potential test bed for optical binding since the extent of the particle assembly is well beyond the decay length of the evanescent field.

5. ACKNOWLEDGMENTS

This work was supported by funding from the Okinawa Institute of Science and Technology Graduate University.

REFERENCES

[1] Ovchinnikov, Y. B., Shul'ga, S. V., and Balykin, V. I., "An atomic trap based on evanescent light waves," *Journal of Physics B: Atomic, Molecular and Optical Physics* **24(14)**, 3173 (1991).

[2] Le Kien, F., Balykin, V. I., and Hakuta, K., "Atom trap and waveguide using a two-color evanescent light field around a subwavelength-diameter optical fiber," *Physical Review A* **70(6)**, 063403 (2004).

[3] Balykin, V. I., Hakuta, K., Le Kien, F., Liang, J. Q., and Morinaga, M., "Atom trapping and guiding with a subwavelength-diameter optical fiber," *Physical Review A* **70(1)**, 011401 (2004).

[4] Goban, A., Choi, K. S., Alton, D. J., Ding, D.,Lacroute, C.,Pototschnig, M., Thiele, T., Stern, N. P., Kimble, H. J., "Demonstration of a state-insensitive, compensated nanofiber trap," *Physical Review Letters* **109(3)**, 033603 (2012).

[5] Vetsch, E., Reitz, D., Sagué, G., Schmidt, R., Dawkins, S. T., Rauschenbeutel, A., "Optical interface created by laser-cooled atoms trapped in the evanescent field surrounding an optical nanofiber," *Physical Review Letters* **104(20)**, 203603 (2012).

[6] Zhang, Y., and Li, B., "Particle sorting using a subwavelength optical fiber," *Laser & Photonics Reviews* **7(2)**, 289–296 (2004).

[7] Brambilla, G., Murugan, G. S., Wilkinson, J. S., and Richardson, D. J., "Optical manipulation of microspheres along a subwavelength optical wire," *Optics Letters* **32(20)**, 3041–3043 (2013).

[8] Ward, J. M., Maimaiti, A., Le, V. H., and Nic Chormaic, S., "Contributed review: Optical micro- and nanofiber pulling rig," *Review of Scientific Instruments* **85(11)**, 111501 (2014).

[9] Hoffman, J. E., Ravets, S., Grover, J. A., Solano, P., Kordell, P. R., Wong-Campos, J. D., Orozco, L. A., and Rolston, S. L., "Ultrahigh transmission optical nanofibers," *AIP Advances* **4(6)**, 067124 (2014).

[10] Frawley, M. C., Petcu-Colan, A., Truong,V.G., and Nic Chormaic, S., "Higher order mode propagation in an optical nanofiber," *Optics Communications* **285(23)**, 4648–4654 (2012).

[11] Nayak, K. P., Zhang, P., and Hakuta, K., "Optical nanofiber-based photonic crystal cavity," *Optics Letters* **39(2)**, 232–235 (2014).

[12] Christensen, C. A., Will, S., Saba, M., Jo, G.-B., Shin, Y.-I., Ketterle, W., and Pritchard, D., "Trapping of ultracold atoms in a hollow-core photonic crystal fiber," *Physical Review A* **78(3)**, 033429 (2008).

[13] Daly, M., Truong, V. G., and Nic Chormaic, S., "Nanostructured tapered optical fibers for particle trapping," *SPIE Proceedings* **4(6)**, 067124 (2014).

[14] Daly, M., Truong, V. G., Phelan, C. F., Deasy, K., and Nic Chormaic, S., "Nanostructured optical nanofibres for atom trapping," *New Journal of Physics* **16(5)**, 053052 (2014).

[15] Birks, T. A.,Li, Y. W., "The shape of fiber tapers," **10(4)**, 432–438 (1992).